2022

Novel approaches to assess cellular interactions and their role in the pathology and treatment of lymphoproliferative disorders

Frend, Frances Hilary Rose

http://hdl.handle.net/10026.1/20077

http://dx.doi.org/10.24382/497
University of Plymouth

Copyright Statement

Novel approaches to assess cellular interactions and their role in the pathology and treatment of lymphoproliferative disorders

Frances Hilary Rose Frend

MBio Biomedical Science with associated BSc (Hons) Biomedical Science

A thesis submitted to the University of Plymouth in partial fulfilment for the degree of

DOCTOR OF PHILOSOPHY

Peninsula Medical School

April 2022

ACKNOWLEDGEMENTS

AUTHOR'S DECLARATION

At no time during the registration for the degree of Doctor of Philosophy has the author been registered for any other University award without prior agreement of the Doctoral College Quality Sub-Committee.

Work submitted for this research degree at the University of Plymouth has not formed part of any other degree either at the University of Plymouth or at another establishment.

Word count of main body of thesis: 58,126

Signed...................................

Date.......... 14th April 2022 ....

ABSTRACT

Frances Hilary Rose Frend

Novel approaches to assess cellular interactions and their role in the pathology and treatment of lymphoproliferative disorders

Background: Migration and homing are essential to B-lymphocyte mediated immunity, and are driven by rapid, directed, and appropriate reorganisation of the actin cytoskeleton. Important observations have linked the cytoskeletal-rearrangements made by leukaemic B-lymphocytes of chronic lymphocytic leukaemia (CLL) to disease pathology. In particular, cytoskeletal alterations mediated by B-cell receptor (BCR) engagement or chemokine-binding are recognised to be central to the migration of CLL cells to lymphoid tissues, where they engage in the complex cellular and molecular interactions that underlie their survival, proliferation, and drug resistance. Further emphasising this importance, has been the observation that highly effective small molecule inhibitors that target key components of the BCR signalling machinery, such as Bruton's tyrosine kinase (BTK), disrupt the migratory behaviour of CLL cells, and that this may, at least in part, underlie their clinical effect.

Detailed characterisation of the highly dynamic cytoskeletal alterations in CLL may, therefore, inform novel therapeutic interventions, particularly for subsets with unmet clinical needs, such as those with mutations affecting the tumour protein P53 (*TP53*), ataxia telangiectasia mutated (*ATM*), or Notch receptor 1 (*NOTCH1*) genes, which are all more frequent in *IGHV*-unmutated disease. This work describes the development of techniques to characterise and quantify morphological responses to inhibitors, aiming to produce a quantitative description of cytoskeletal changes relating to specific signalling pathways, and to suggest rational drug combinations in the disorder.

Methods: Primary CLL cells were cultured at high density with autologous T-lymphocytes and monocytes in the presence of specific signal inhibitors. The morphological responses of leukaemic cells were determined using a range of microscopic techniques, including scanning electron microscopy, and immunocytofluorescent detection of cytoskeletal and plasma

membrane components. Cytoskeletal alterations were evaluated via computer-aided morphometric analyses of cell shape parameter, homotypic cellular interactions, and migration, generating a precise description of changes to the polymerised F-actin cytoskeleton and cell behaviour.

Matrigel™ matrix models were combined with transmission electron microscopy to study cellular morphology within a 3D tumour microenvironment (TME)-like setting. Immunogold labelling of specific proteins within neoplastic lymphocytes was performed to allow visualisation of protein localisation changes in response to signal inhibition at the ultrastructure level.

Results: This study tested inhibitors targeting different signalling pathways as a 'proof of principle' evaluation to determine whether the morphological and behavioural responses induced could be effectively distinguished from one another and quantitatively described.

Inhibition of BTK by ibrutinib resulted in uniform populations of globular cells with retained polarity and, consequently, increased amoeboid motility. BTK blockage is recognised to impair integrin-mediated retention of leukaemic cells within tissue niches, leading to the observed peripheral blood lymphocytosis seen in CLL patients receiving ibrutinib. Reduced integrin-mediated motility was associated with impaired homotypic cellular interactions within *IGHV*-mutated cases specifically, indicating that this subgroup may have a greater dependency on elongated-type migration for permitting pro-survival cellular contact than their *IGHV*-unmutated counterparts.

Disruption of Rho-associated protein kinase 1 (ROCK1) activity by Y-27632 lead to impaired actomyosin-mediated retraction of cytoskeletal processes. Loss of the ROCK1-induced cytoskeletal asymmetry required for effective cell migration resulted in reduced CLL cellular interactions; however, CXCL12-driven motility was attenuated in *IGHV*-mutated cases alone.

The Abelson kinase 1 (ABL1) inhibitor imatinib caused CLL cells to acquire a globular phenotype with frequent microvilli, similar to that of B-lymphocytes isolated directly from the

peripheral blood. Transient cellular interactions were markedly reduced by imatinib, whereas elongated-type motility, being a largely ABL1-independent process, was unaltered.

The morphological and behavioural responses of CLL cells were compared to those observed in mantle cell lymphoma (MCL) cell lines. These cells lines, which were utilised as a surrogate model for BTK inhibitor sensitivity in CLL, demonstrated that the establishment of anterior-posterior morphology, mediated by the activity of ROCK1 and ABL1, is essential for effective trafficking of B-lymphocytes to protective niches, regardless of ibrutinib sensitivity.

Blockage of NOCTH1 signalling by gamma-secretase inhibitors (GSIs) PF-03084014 and R04929097 resulted in varying morphological responses, possibly indicating differences in NOTCH1 activation between CLL cases. Despite chemotaxis being identified as a key NOTCH1-regulated process, CLL and *NOTCH1*-mutated MCL cells demonstrated enhanced directional transmigration with GSI treatments. MCL cell lines were utilised to model the effects of GSI sensitivity in CLL. In contrast, *NOTCH1*-unmutated MCL cells displayed unaltered migration with PF-03084014 pre-treatment, consistent with reports of low GSI sensitivity in MCL cells exhibiting unmutated *NOTCH1*, and reduced chemotaxis with R04929097.

The developed 3D *ex vivo* culture system preserved CLL cell viability, migration, and dynamic cellular interactions, as demonstrated by flow cytometry and time-lapse live-cell imaging. Interrogation with transmission electron microscopy enabled high-resolution visualisation of cell morphology within a TME-like setting; however, further optimisation of immunogold labelling of effector proteins is required.

Conclusion: Using novel imaged-based morphometric analyses, distinct signal inhibitor-induced cytoskeletal adaptations were identified in CLL B-lymphocytes. This approach may be applied to prognostically-defined subgroups or resistant cases to provide in-depth characterisation of morphological responses to novel therapeutic agents and to assess treatment responses within the TME. These observations, when combined with transcriptional data, may allow more effective combinational targeting of behavioural signatures unique to the patient and, thus, improve treatment outcomes in the disease.

TABLE OF CONTENTS

LIST OF FIGURES

LIST OF TABLES

LIST OF ABBREVIATIONS

°C	Degree Celsius
2D	Two-dimensional
3'	3 prime
3D	Three-dimensional
3'-UTR	3 prime-untranslated region
A	Adenine
ABC	Ammonium bicarbonate
ABL	Ableson kinase
ACN	Acetonitrile
ADAM	A disintegrin and metalloproteinase
AKT	Protein kinase B
AML	Acute myeloid leukaemia
ANK	Ankyrin
APRIL	A proliferation inducing ligand
APS	Ammonium persulphate
Arg	Abl-related gene
ARP2/3	Actin-related protein 2/3
ARPC1-5	Actin-related protein 2/3 complex 1-5
ATM	Ataxia telangiectasia mutated
BAFF	B-cell activating factor
BAFF-R	BAFF-receptor
BCA	Bicinchoninic acid
BCL-2	B-cell lymphoma 2
BCMA	B-cell maturation antigen
BCR	B-cell receptor
BIRC3	Baculoviral AP repeating containing 3
BLIMP-1	B-lymphocyte-induced maturation protein-1
BLNK	B-cell linker
BM	Bone marrow
BMS	Bristol-Myers-Squibb
BMSC	BM stromal cells
bp	Base pair
BSA	Bovine serum albumin
BTK	Bruton's tyrosine kinase
BTKi	BTK inhibitor
C	Cytosine
Ca^{2+}	Calcium ion
CCL(3, 4, 12, 19, 22)	C-C motif chemokine ligand
CCND1	Cyclin D1 gene
CCR(1,3,7)	C-C motif chemokine receptor
CD(4, 5, 8, 14, 19, 20, 23, 31, 34, 33, 38, 39, 40, 45, 79A/B, 107, 138, 160, 244)	Cluster of differentiation

CD40L	CD40 ligand
CLL	Chronic lymphocytic leukaemic
CO_2	Carbon dioxide
CoA	Coactivations
Co-IP	Co-immunoprecipitation
CR2	Complement receptor 2
CST	Cell Signalling Technology
CXCL(12, 13)	C-X-C motif chemokine ligand
CXCR(4)	C-X-C motif chemokine receptor
DAG	diacylglycerol
DAPI	4',6-diamidino-2-phenylindole
DBSCAN	Density-Based Spatial Clustering of Applications with Noise
Del(11q)	Deleted of long arm of chromosome 11
Del(13q14)	Deletion of long arm of band 14 of chromosome 13
Del(17p)	Deletion of short arm of chromise 17
dH_2O	Deionised water
DLBCL	Diffuse large B-cell lymphoma
DLEU2	Deleted in lymphocytic leukaemic 2
DMSO	Dimethyl sulphoxide
DNA	Deoxyribonucleic acid
dNTP	Deoxynucleoside triphosphate
DSMZ	Deutsche Sammlung von Mikroorganismen und Zellkulturen GmbH
DUSP22	Dual specificity phosphate 22
ECM	Extracellular matrix
EDTA	Ethylenediaminetetraacetic acid
EGF	Epidermal growth factor
eIF4E	Eukaryotic translation initiation factor 4E
EM	Electron microscopy
ERK	MEK-extracellular signal-regulated kinase
ERM	Ezrin, radixin and moesin
Eu	Euchromatin
FBS	Foetal bovine serum
FBXW7	F-box protein F-box/WD repeat-containing protein 7
FCR	Fludarabine, cyclophosphamide and rituximab
FDC	Follicular dendritic cell
FH2	Formin homology 2
FITC	Fluorescein isothiocyanate
G	Guanine
g	Gram
G519	Granta-519
GSI	γ-secretase inhibitor
h	Hour
HBSS	Hank's balanced salt solution
HCl	Hydrochloric acid

HD	Heterodimerisation domain
He	Heterochromatin
HPLC	High-performance liquid chromatography
HRP	Horseradish peroxidase
IC_{50}	Half-maximal inhibitory concentration
IgHV	Immunoglobulin heavy chain variable region
IL	Interleukin
INF	Interferon
IP3	Inositol 1,4,5-trisphosphate
IS	Immunological synapse
ITAMS	Immunoreceptor tyrosine-based activation motifs
ITK	IL-2-inducible kinase
kDa	Kilodaltons
kV	Kilovolt
LYN	lck/yes novel tyrosine kinase
M	Molar
m/z	Mass to charge ratio
MAML	Mastermind-like
MAP3K14	Mitogen-activated protein kinase kinase kinase 14
MAPK	Mitogen-activated protein kinase
MBL	Monoclonal B-lymphocyte lymphocytosis
MCL	Mantle cell lymphoma
MCL-1	Myeloid cell leukaemia 1
M-CLL	CLL exhibiting mutated *IGHV*
MEK	Mitogen-activated protein kinase kinase
min	Minute
mir	microRNA
mL	Millilitre
MLC	Myosin light chain
MM	Multiple myeloma
mM	Millimolar
mm	Millimetre
MMP9	Matrix metallopeptidase 9
mTOR	Mechanistic target of rapamycin
N/A	Not applicable
N/D	Not determined
Na	Sodium
NaCl	Sodium chloride
NaOH	Sodium Hydroxide
N-EC	NOTCH1 extracellular subunit
NF-κB	Nuclear factor kappa light chain enhancer of activated B-cell
ng	Nanogram
NGS	Next generation sequencing
NHL	Non-Hodgkin lymphoma
N-ICD	NOTCH1 intracellular domain

nL	Nanolitre
NLC	Nurse-like cell
nM	Nanomolar
nm	Nanometre
NOTCH1	Notch receptor 1
NS	Not significant
N-TMIC	NOTCH1 transmembrane and intracellular subunit
Nu	Nucleolus
ORR	Overall response rate
OS	Overall survival
p120	p120RasGAP
p190	p190RhoGAP-A
PB	Peripheral blood
PBMC	Peripheral blood mononuclear cells
PBS	Phosphate buffered saline
PCR	Polymerase chain reaction
PD-1	Programmed cell death protein-1
PE	Phycoerythrin
PEST	Proline-glutamate-serine-threonine-rich
PFH	Paraformaldehyde
PI3K	Phosphoinositide 3-kinase
PIP	Protein-protein interaction
P-IP	Post-immunoprecipitation
PIP2	Phosphatidylinositol 4,5-bisphosphate
PKC	Protein kinase C
PLCγ2	Phospholipase Cγ2
PVDF	Polyvinylidene difluoride
R/R	Relapsed or refractory
RAC(1,2)	Ras-related C3 botulinum toxin substrate
RAM	RBP-Jκ associated molecule
RAS	Rat sarcoma proteins
RBP-Jκ	Recombination signal binding protein for immunoglobulin kappa J region
Rho	Ras homologous
RhoA	Ras homolog gene family, member A
RIPA	Radioimmunoprecipitation assay buffer
RNA	Ribonucleic acid
ROCK1	RHO-associated protein kinase 1
ROR(1,2)	Receptor Tyrosine Kinase Like Orphan Receptor
rpm	revolutions per minute
RT	Room temperature
SDS	Sodium dodecyl sulphate
SDS-PAGE	Sodium dodecyl sulphate–polyacrylamide gel electrophoresis
SEM	Scanning electron microscopy
SERCA	Sarco/endoplasmic reticulum calcium-ATPase

SHM	Somatic hypermutation
SLL	Small lymphocytic lymphoma
SOX11	SRY-box transcription factor 11
STAGE	Stop-and-go-extraction
STAT3	Signal transducer and activator of transcription 3
STRING	Search Tool for the Retrieval of Interacting Genes/Protein
SYK	Spleen tyrosine kinase
T	Thymine
TACI	Transmembrane activator calcium modulator and cyclophilin ligand interactor
TAD	Transactivation domain
T-ALL	T-lymphocyte acute lymphoblastic leukaemia
TBE	Tris borate EDTA
TBET	Transcription factor T-box 21
TBS	Tris buffered saline
TBST	Tris buffered saline with 0.1% Tween-20
TEMED	N, N, N', N'-Tetramethylethylenediamine
TFA	Trifluoroacetic acid
TM	Transmembrane domain
TME`	Tumour microenvironment
TN	Treatment-naïve
TNF	Tumour necrosis factor
TP53	Tumour protein 53
UM-CLL	CLL exhibiting unmutated *IGHV*
V	Volts
VCAM1	Vascular cell adhesion molecule 1
$V_H D J_H$	V, D and J gene segments for the IgHV
VLA-4	Very late antigen-4
$V_L J_L$	V and J gene segments for the light chain variable region
WAS	Wiskott-Aldrich syndrome
WASP	WAS protein
WAVE	WAS protein family verprolin-homologous protein
WIP	WASP interacting protein
Wnt5a	Wnt Family Member 5A
WT	Wild-type
x*g*	Times gravity
ZAP70	Zeta chain of T-cell receptor associated protein kinase 70
β-ME	β-mercaptoethanol
μL	Microlitre
μM	Micromolar

CHAPTER 1 – INTRODUCTION

1.1. CHRONIC LYMPHOCYTIC LEUKAEMIA

Chronic lymphocytic leukaemia (CLL) is characterised by a clonal proliferation of mature-appearing cluster of differentiation (CD)5^{+} CD23^{+} B-lymphocytes and the accumulation of these neoplastic lymphocytes in the bone marrow (BM), peripheral blood (PB) and secondary lymphoid tissues.[1] It is the most frequent haematological cancer in the Western hemisphere, with 20,110 new cases of CLL diagnosed in the US in 2017.[2] In the UK, 3,541 new CLL cases were diagnosed in 2017.[3] The incidence rate of CLL is approximately two-times higher for men than for women and increases with age; the median age at diagnosis ranges from 70-72 years.[4,5] The prevalence and mortality of CLL are likely to increase further due to demographic changes in society (i.e., ageing population) in the near future, making this currently incurable disease (in virtually all cases) an important public health issue.[6] A family history of CLL is an additional risk factor; first-degree relatives of CLL patients have an 8.5-fold increased risk of developing the disease.[7]

Common features of CLL include lymphadenopathy, hepatosplenomegaly, constitutional symptoms (e.g., weight loss, sweats, fatigue), BM failure and recurrent infections. However, most patients are asymptomatic at diagnosis.[8] Patients with CLL exhibit a heterogeneous clinical course, with some patients surviving decades without treatment and other exhibiting rapid disease progression despite early therapeutic intervention.[9–12] Several molecular/biological features have been identified as robust predictors of treatment-free survival and overall survival (OS) in newly diagnosed CLL cases.

1.2. THE BIOLOGICAL CHARACTERISTICS OF CLL

CLL can be divided into two main subgroups which differ in their clinical and biological behaviour. These subgroups are distinguished by whether CLL cells have undergone somatic hypermutation (SHM) in the variable region of the immunoglobulin heavy chain (IgHV) gene or whether the IgHV resembles that of germ-line.[13]

Each B-lymphocyte carries a distinct B-cell receptor (BCR) that is formed through rearrangement of V, D and J gene segments for the IgHV (V_HDJ_H) and V and J gene segments for the light chain variable region (V_LJ_L) during B-lymphocyte maturation in the BM (Figure 1.1). During an immune response, the BCR repertoire is further increased within germinal centres by the introduction of somatic mutations in the rearranged V_HDJ_H and V_LJ_L segments that code for the antigen binding site of the receptor.[14] The antigen-driven somatic hypermutation process introduces single nucleotide exchanges into the rearranged immunoglobulin variable regions, at a rate of 10^{-3} base pair per generation,[15] via error-prone repair of deoxyribonucleic acid (DNA) strand breaks (reviewed in Di Noia and Neuberger[16]). SHM results in B-lymphocytes with enhanced antigen-binding affinity that go on to proliferate in the presence of the antigen. B-lymphocytes with receptors that no longer recognise the antigen or recognise autoantigens are typically eliminated via apoptosis[17] (Figure 1.2).

CLL cells that express a mutated *IGHV* are thought to originate from post-germinal centre B-lymphocytes that have experienced SHM and, in some cases, also immunoglobulin class-switching, similar to normal B-lymphocytes during an immune response to an antigen. CLL cells expressing an unmutated *IGHV* are thought to have not undergone differentiation in germinal centres[13] (Figure 1.2). Patients with CLL cells exhibiting an unmutated *IGHV* (UM-

CLL) usually have a more-aggressive disease than patients with CLL cells that express a mutated *IGHV* (M-CLL).[18,19]
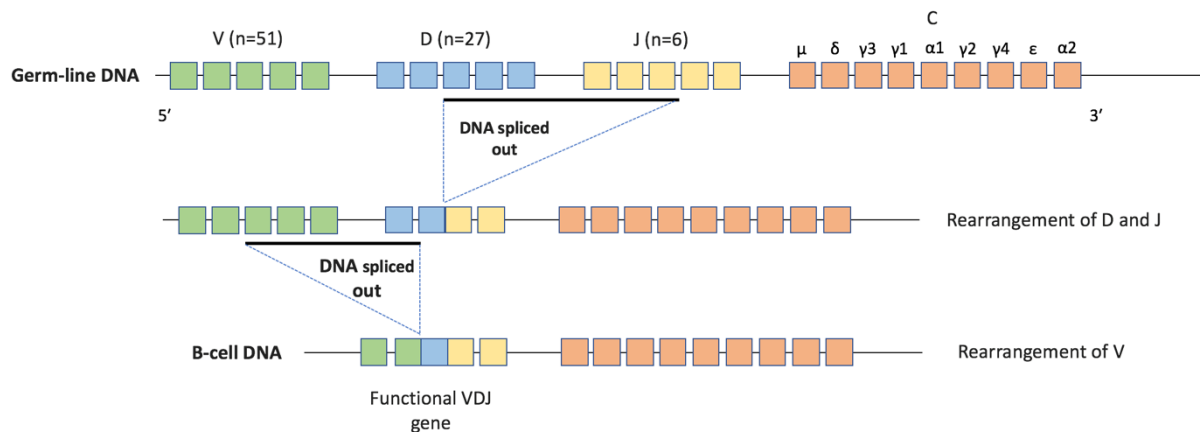
Figure 1.1: Rearrangement of V, D and J segments in developing B-lymphocytes. Genes encoding the variable region of the BCR heavy and light chains are rearranged in a step-wise manner. Firstly, 1 of the 27 D gene segments in the germ-line DNA is linked with one of the six J genes. Next, 1 of the 51 V segments joins the rearranged DJ segments to produce a functional $V_H DJ_H$ variable region gene. The rearranged gene is transcribed, spliced, and translated into an immunoglobulin heavy chain protein. Similar rearrangement events occur at the L chain locus in pre-B-lymphocytes, although they involve only two gene segments ($V_L J_L$). Each B-lymphocytes uses different $V_H DJ_H$ and $V_L J_L$ rearrangement products to create a unique B-lymphocyte receptor structure. This figure is based on information taken from Lydyard *et al.*[14]

In line with the clinical diversity seen between UM-CLL and M-CLL, there are key biological differences between the two groups. *IGHV* mutational status appears to affect CD38 and zeta chain of T-cell receptor associated protein kinase 70 (ZAP70) expression, telomere length, activation of key signalling pathways and the likelihood of carrying or acquiring deleterious genetic aberrations.[18,20–22] Studies show that the BCR signalling pathway is more readily activated in CLL cells that express ZAP70 and have unmutated *IGHV*.[23,24]
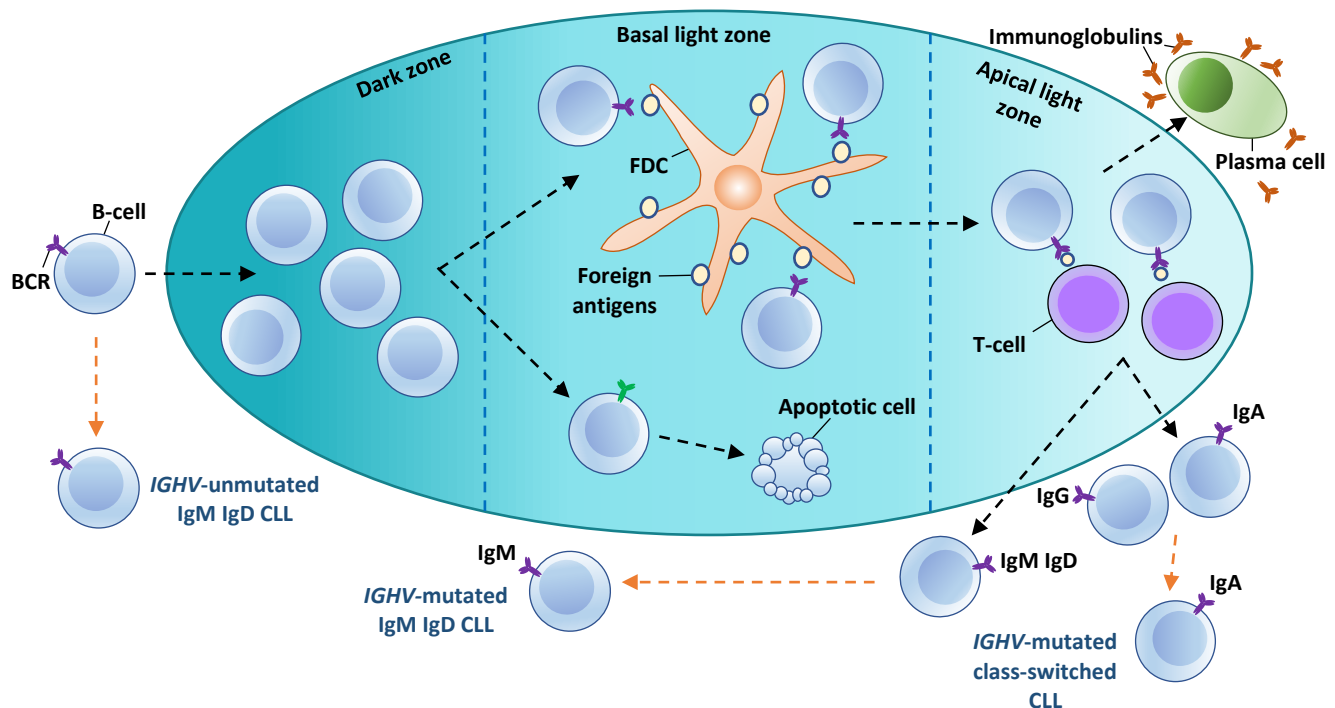
Figure 1.2: Cellular origins of CLL cells. Following T-lymphocyte-dependent stimulation, normal naïve B-lymphocytes (IgM^{high} IgD^{low}) enter secondary lymphoid organs and aggregate to form histological structures known as germinal centres. Within the dark zone, activated B-lymphocytes down-regulate BCRs and undergo rapid clonal expansion, acquiring mutations in the V_HDJ_H and V_LJ_L segments encoding the IgHV and immunoglobulin light chain variable regions, respectively, with each round of cell division. B-lymphocytes then pass into the basal light zone where they re-express BCRs and bind to a foreign antigen presented on the surface of follicular dendritic cells (FDC). B-lymphocytes that have gained BCR affinity-increasing mutations receive a temporary survival signal, whereas B-lymphocytes with undesirable mutations (i.e., BCRs no longer recognise the antigen) are typically removed via apoptosis. Selected B-lymphocytes, which have bound the antigen fragment on their cell surface, proceed to the apical light zone and receive a permanent survival signal from antigen-specific T-lymphocytes. Following multiple rounds of proliferation, SHM and selection, affinity-matured B-lymphocytes finally differentiate into plasma cells producing oligoreactive/monoreactive immunoglobulins or memory B-lymphocytes. UM-CLL is thought to originate from B-lymphocytes which have not experienced SHM within germinal centres. In contrast, M-CLL is most likely derived from affinity-matured B-lymphocytes which may have undergone class-switch recombination and express immunoglobulin isotypes other than IgM and IgD (e.g., IgG or IgA). This figure is based on information taken from Chiorazzi and Ferrarini[25] and Kipps *et al.*[13]

CLL cells, particularly UM-CLL cases, have a biased *IGHV* usage and carry 'stereotyped' BCRs, which carry V_HDJ_H and V_LJ_L segments with highly similar complementarity-determining region 3 structural features (e.g., length, amino acid sequence, and unique amino acid residues at precise points of recombination).[26–28] Approximately 1.3% of all CLL patients express surface immunoglobulins that are virtually identical.[29] This limited *IGHV* combinational diversity strongly suggests that CLL B-lymphocytes recognise common antigens and that constitutive antigen-driven signalling plays a crucial part in CLL leukaemogenesis.[13]

1.3. CHROMOSOMAL ALTERATIONS IN CLL

Approximately 80% of CLL patients exhibit aberrations affecting at least one of four common chromosomal regions. These abnormalities act as independent prognostic markers, identifying patients with rapidly progressing disease and an adverse clinical outcome[6] (Figure 1.3). Although UM-CLL and M-CLL display the same chromosomal aberrations, the incidence of high-risk abnormalities is higher in patients exhibiting unmutated *IGHV*.[30]

Deletions of the long arm of chromosome 13, specifically involving band 13q14 [del(13q14)], represent the most frequently observed cytogenetic alteration in CLL (evident in >50% of all cases) and is the sole aberration associated with a benign disease course.[6] Two microRNAs (ribonucleic acid) genes, microRNA (*mir*)-*15a* and *mir-16-1*, have been identified as being located within the deleted 13q14 region.[31] Targeted deletion in mice of the *mir-15a/16-1* locus [and the non-coding RNA gene deleted in lymphocytic leukaemia 2 (*DLEU2*)] resulted in the full replication of CLL-associated phenotypes observed in humans,[32] suggesting that mir-15a and -16-1 play a key pathophysiological role in CLL leukaemogenesis.

Approximately 20% of advanced disease stage CLL cases display deletions of the long arm of chromosome 11 [del(11q)].[33,34] This deletion affects band 11q22.3-q23.1, which typically contains the ataxia telangiectasia mutated (ATM) gene.[35] *ATM* encodes for a serine/threonine protein kinase that activates cell cycle checkpoint signalling and, consequently, induces apoptosis in response to DNA double-stand breaks.[36] Correspondingly, patients carrying a del(11q) clone typically have more rapid disease progression, bulky lymphadenopathy and reduced OS.[9] Del(11q) is rarely found in CLL patients with early-state disease.[37] Recently, a high incidence of deletion/mutation of the baculoviral IAP repeat containing 3 (BIRC3) gene, which is located at 11q22, has been reported. BIRC3 is a negative regulator of the pro-cell proliferation nuclear factor kappa light chain enhancer of activated B-cell (NF-κB) signalling pathway, facilitating proteasomal degradation of mitogen-activated protein kinase kinase kinase 14 (MAP3K14).[38,39] However, Rose-Zerilli *et al.*[40] confirmed that *ATM* dysfunction rather than *BIRC3* deletions/mutations predict survival in del(11q) CLL cases.

Trisomy 12 is identified in around 7-17% of all CLL cases.[9,30,33,34] The mechanisms by which this chromosomal aberration contributes to CLL pathogenesis are largely unknow and its initial association with an intermediate prognosis[9] remains a matter of debate. The incidence of trisomy 12 does not increase with disease progression[33,34,41] and the results of the CLL8 trial showed that the response rate and OS for patients with trisomy 12 treated with chemoimmunotherapy was particularly favourable.[42]

Deletions involving the short arm of chromosome 17 [del(17p)] are found in 4-8% of chemotherapy-naïve patients.[9,11,12,42] This chromosomal abnormality almost always involves the loss of band 17p13, which contains the tumour suppressor gene tumour protein p53 (*TP53*).[35,43] The clinical course of CLL patients harbouring a del(17p) clones is characterised by

marked resistance against chemoimmunotherapy regimens, such as chemotherapy combined with anti-CD20 antibodies, rapid disease progression and significantly reduced OS.[42,44] The majority of CLL cases with del(17p) display mutations in the remaining *TP53* allele (>80%).[45] *TP53* mutations in isolation from del(17p) are much rarer; however, they are also associated with an adverse clinical outcome.[10,11,46]

No. at Risk

17p deletion	23	18	13	8	5	4	1	0	0	0	0	0	0	0	0	0
11q deletion	56	53	47	43	33	27	20	15	10	4	2	2	1	0	0	0
12q trisomy	47	44	41	29	24	17	14	13	12	11	4	3	2	1	1	0
Normal	57	51	45	37	30	27	20	17	12	11	6	5	2	2	1	1
13q deletion as sole abnormality	117	117	106	91	80	63	45	36	24	16	12	11	3	1	1	0
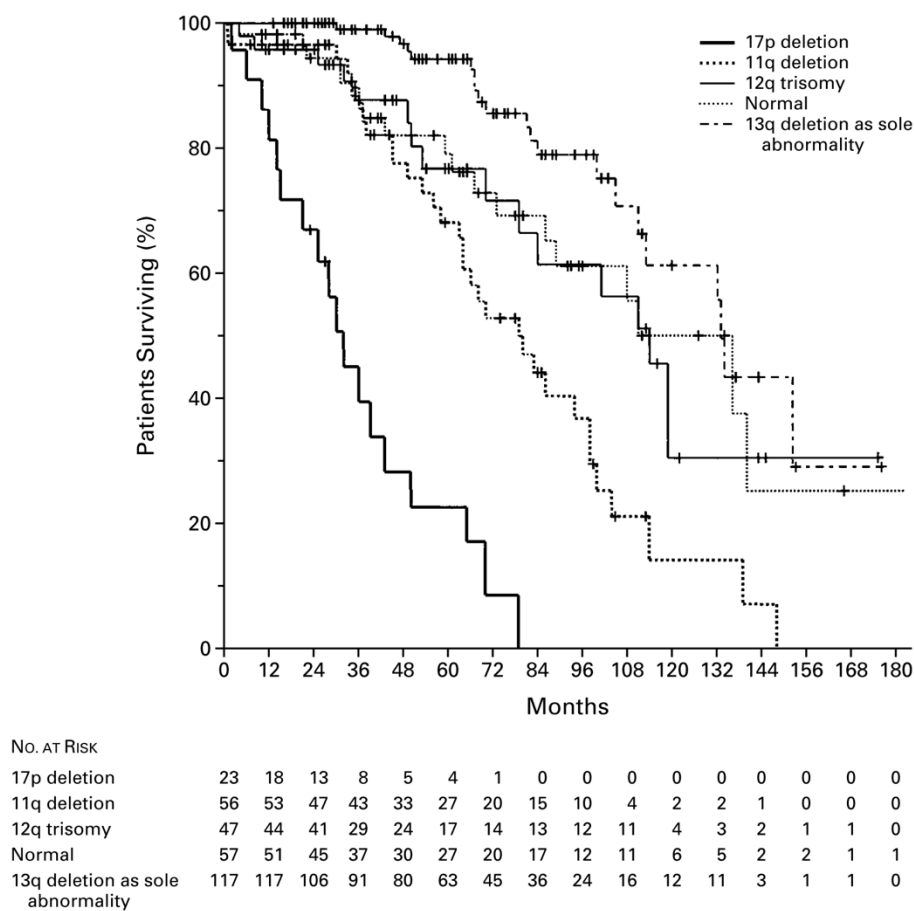
Figure 1.3: Survival of CLL patients with chromosomal aberrations. The survival times from the date of diagnosis of CLL patients with one of four common cytogenetic abnormalities [del(13q), del(11q), del(17p) and trisomy 12] or normal karyotype were compared. The median times of survival for patients with del(17p), del(11q), trisomy 12, normal karyotype or del(13q) were 32, 79, 114, 111, and 133 months, respectively. Reproduced with permission from Döhner *et al.*[9], Copyright Massachusetts Medical Society.

1.4. SOMATIC MUTATIONS IN CLL

Recently, the application of whole-exome sequencing to CLL has transformed our understanding of the genomic landscape of the disease. In addition to the above-mentioned chromosomal aberrations, recurrent somatic mutations have repeatedly been observed in genes involved in DNA damage signalling and repair (e.g., *TP53* and *ATM*), RNA processing and export (e.g., splicing factor 3b subunit 1 gene and exportin 1 gene), inflammatory pathways (e.g., myeloid differentiation primary response gene 88), chromatin modification (e.g., chromodomain helicase DNA binding protein 2 gene), WNT signalling[47–49] (an evolutionarily conserved pathway regulating key aspects of cell fate determination, cell migration and polarity, neural patterning and organogenesis during embryonic development),[50,51] and the pro-survival NF-κB signalling pathway (e.g., BIRC3).[52] However, the Notch receptor 1 (NOTCH1) gene, which encodes a ligand-activated transcription factor, has now emerged as the most commonly mutated gene in CLL at diagnosis, with approximately 10-15% of patients harbouring a NOTCH1 mutation.[47,53–56] CLL cases with a NOTCH1 mutation express a constitutively active form of the protein.[47,54] Interestingly, expression of NOTCH1 target genes has also been described in CLL patients lacking an activating mutation.[57] Thus, alterations in the NOTCH1 signalling pathway likely represent a novel oncogenic process in CLL leukaemogenesis.

1.4.1. NOTCH1 PROTEIN STRUCTURE AND PATHWAY

NOTCH1 belongs to a family of four single-pass type I transmembrane receptors (NOTCH1-4) and five ligands (Delta-like 1, 3 and 4, and Jagged 1 and 2).[58] It exists as a noncovalently linked heterodimer, composed of an amino-terminal extracellular subunit (N-EC), and a carboxy-terminal transmembrane and intracellular subunit (N-TMIC) subunit, at the cell surface.[59] The

N-EC subunit consists of thirty-six epidermal growth factor (EGF)-like repeats, required for receptor ligation, and three LIN-12/NOTCH repeats, which prevent ligand-independent activation of the receptor by stabilising the heterodimerisation domain. The N-TMIC contains a transmembrane region followed by the NOTCH1 intracellular domain (N-ICD). The N-ICD includes a series of ankyrin (ANK) repeats, a recombination signal binding protein for immunoglobulin kappa J region (RBP-Jκ) associated molecule (RAM) domain, a transactivation domain, nuclear localisation signals and a proline-glutamate-serine-threonine-rich (PEST) domain, which regulates protein stability and proteasomal degradation of active NOTCH1[58,60] (Figure 1.4A).

NOTCH1 signalling is initiated when the NOTCH1 receptor binds to cognate ligands expressed on an adjacent cell. Both the NOTCH1 receptor and Jagged/Delta ligands are membrane-bound and therefore, signalling is short range.[58] However, cellular projections enriched with NOTCH ligands may function in long-range NOTCH signalling.[61,62] Interaction of the receptor with its ligands triggers two consecutive proteolytic cleavages: (i) an extracellular juxtamembrane cleavage by a disintegrin and metalloproteinase (ADAM) metalloproteinase, that occurs in the heterodimerisation domain; and (ii) an intramembrane cleavage by the γ-secretase complex, which is composed of presenilin, Aph-1 homology A γ-secretase subunit, nicastrin and presenilin enhancer protein 2.[58,63] These cleavage steps release the active N-ICD which translocates to the nucleus and forms a short-lived transcription complex with DNA-binding proteins RBP-Jκ, mastermind-like (MAML) proteins and other coactivators, switching on expression of NOTCH target genes[64] (Figure 1.4B).
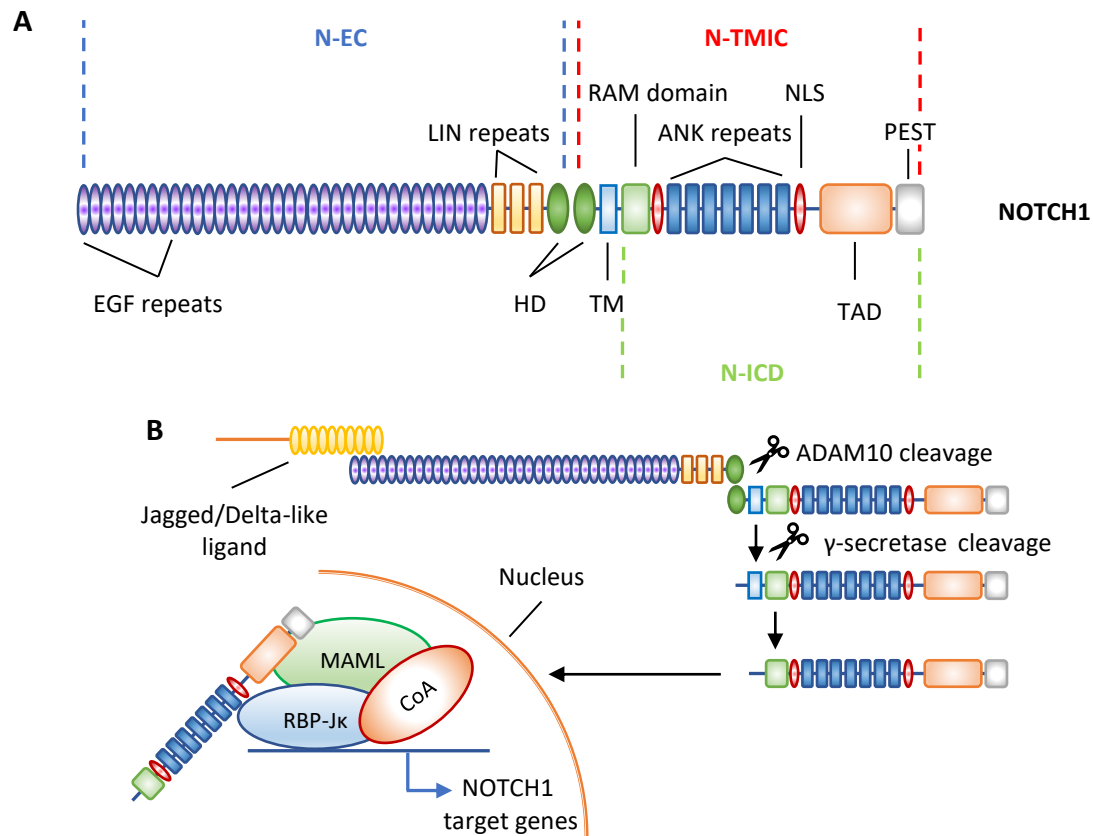
Figure 1.4: NOTCH1 protein structure and signalling pathway. (A) The NOTCH1 receptor is a heterodimer consisting of an N-EC subunit and N-TMIC subunit. The N-EC subunit includes numerous EGF-like repeats, three negative regulatory LIN repeats and the heterodimerisation domain (HD), which non-covalently binds the two subunits. The N-TMIC contains the transmembrane domain (TM) and the N-ICD, which is made up of a RAM domain, nuclear localisation signals (NLS), seven ANK repeats, a transactivation domain (TAD) and a PEST domain. The PEST domain is required for proteasomal degradation of the active N-ICD. (B) Cognate interaction between NOTCH1 and its ligands (Jagged/Delta-like) triggers two sequential proteolytic cleavages of NOTCH1. Firstly, ADAM metalloproteinase cleaves NOTCH1 within the HD domain, releasing the N-TMIC subunit. The N-TMIC then acts as a substrate for the γ-secretase complex. Cleavage by the γ-secretase complex generates the N-ICD, the signalling portion of the receptor, which translocates to the nucleus and recruits the transcription factor RBP-Jκ, the MAML proteins and other coactivators (CoA), switching on expression of NOTCH1 target genes. This figure is based on information taken from Rosati et al.[60] and Lobry et al.[58]

NOTCH1 signalling is terminated via ubiquitination of a 'degron' site on the carboxyl-terminal end of the NOTCH1 PEST domain, followed by proteasome-dependent degradation of the active N-ICD.[65,66] To date, only one E3 ligase, the F-box protein F-box/WD repeat-containing protein 7 (FBXW7), has been shown to specifically target the N-ICD for degradation by the proteasome. To allow successful FBXW7-substrate binding, the target protein degron site must first be phosphorylated at a key threonine residue.[67] Threonine phosphorylation is mediated by cyclin dependent kinase 8[68] and possibly integrin-liked protein kinase.[69]

1.4.2. NOTCH1 MUTATIONS AND PROGNOSIS IN CLL

The oncogenic potential of deregulated NOTCH1 signalling is well demonstrated in T-lymphocyte malignancies. In 1991, Ellisen *et al.*[70] identified a translocation in T-lymphocyte acute lymphoblastic leukaemia (T-ALL) that results in fusion of the 3 prime (3') end portion of *NOTCH1*, containing the N-ICD, on chromosome 9 to the enhancer and promotor elements of the T-cell receptor beta gene on chromosome 7 [t(7;9)(q34;34.4)]. This translocation results in overexpression of a constitutively active form of NOTCH1, leading to impaired cell differentiation and malignant transformation; however, it is found in less than 1% of T-ALL cases.[70,71] More recently, Weng *et al.*[72] has shown that more than 50% of T-ALL cases exhibit activating NOTCH1 mutations.

Initial interest in NOTCH1 signalling in the context of CLL emerged from observations that, in contrast to their normal counterparts, CLL B-lymphocytes constitutively express the NOTCH1 receptor, as well as its ligands. This suggests the existence of a paracrine feedback loop, responsible for the constitutive NOTCH1 signalling activation that contributes to CLL survival and resistance to apoptosis.[73] Furthermore, co-culture of CLL cells with stromal cells, which express several NOTCH ligands, has been shown to support CLL survival and resistance to

chemotherapy via stromal cell-mediated NOTCH1 signalling.[74] Subsequent studies revealed a 2-base pair [bp; cytosine (C) and thymine (T) nucleotides] frameshift deletion (c.7541_7542delCT) within the CLL NOTCH1 gene[54,75] which had significant prognostic implications.[76] Unlike T-ALL *NOTCH1* mutations which typically affect the heterodimerisation domain, resulting in ligand-independent receptor activation,[72] this 2-bp frameshift deletion in CLL cells is localised within exon 34 and generates a premature stop codon resulting in truncation of the carboxyl-terminal PEST domain (P2514fs*4).[54,75,77] The truncated NOTCH1 protein lacks the domains required for FBXW7-induced NOTCH1 proteasomal degradation (Figure 1.5), leading to an increase in the half-life of the N-ICD and, consequently, aberrantly prolonged NOTCH1 signalling in CLL cells harbouring this mutation.[54,60,77]

The advent of next-generation sequencing (NGS) technology revealed additional frameshift mutations/truncations that affect different nucleotides within exon 34 and disrupt the function of the carboxyl-terminal PEST domain, but they occur with a much lower frequency than that of the canonical c.7541_7542delCT mutation.[53,54,78,79] Additionally, the NOTCH1 TAD and ANK repeats are subjected to frameshift nonsense mutations (Figure 1.5), typically generating premature stop codons, in CLL cells at low frequency.[80]

In 2015, Puente *et al.*[53] identified recurrent transition [c.*7668+371A (adenine)>G (guanine), c.*7668+378A>G] and transversion (c.*7668+380A>C) mutations in the 3' untranslated region (3'-UTR) of *NOTCH1* (Figure 1.5) within CLL cases and cases of the CLL-precursor state known as monoclonal B-lymphocyte lymphocytosis (MBL). These non-coding variants occur at low frequency (4-5%) in CLL cohorts[81,82] and create new splice acceptor sites that favour alterative NOTCH1 RNA splicing events, leading to the removal of 158 coding bases from the PEST

domain sequence and, thus, increase N-ICD stability as in the case of the c.7541_7542delCT mutation.[53]
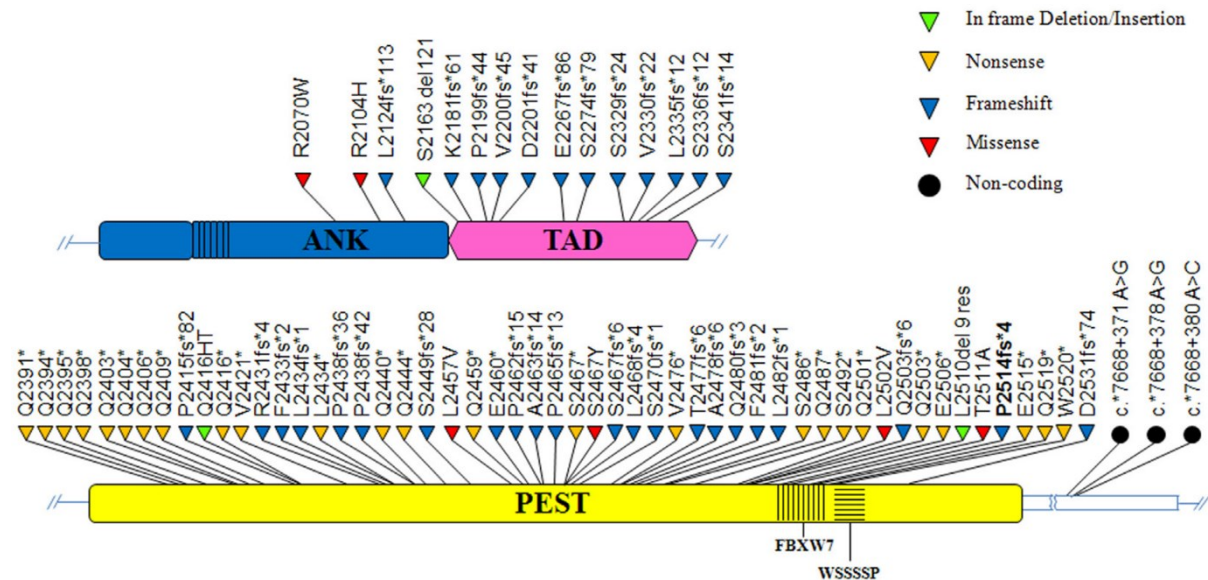
Figure 1.5: NOTCH1 mutations in CLL. The position of in frame deletion/insertion (green triangles), nonsense (orange triangles), frameshift (blue triangles), missense (red triangles) and non-coding (black circles) mutations within the *NOTCH1* ANK/TAD domains and PEST domains of CLL cells. The FBXW7 and WSSSSP degron sequences, which are required for NOTCH1 proteasomal degradation, are shown within the PEST domain. Adapted with permission from Rosati *et al.*[60], Copyright: © 2018 Rosati, Baldoni, De Falco, Del Papa, Dorillo, Rompietti, Albi, Falzetti, Di Ianni and Sportoletti.

Regardless of their location within the gene, all *NOTCH1* mutations were associated with a poor prognosis (i.e., reduced time-to-first treatment and OS) compared to wild-type patients in large retrospective analyses.[47,53–55,80,81] The adverse clinical outcomes of these patients could possibly be explained by the strong correlation of mutated-*NOTCH1* with other poor prognostic markers. Indeed, *NOTCH1* mutations are particularly prevalent in patients with chemorefractory CLL (20.8%), progression to Richter transformation (31%) or clinically aggressive UM-CLL (17.9% versus 3.7% in M-CLL).[47] Richter syndrome is the development of

an aggressive lymphoma, mainly diffuse large B-cell lymphoma (DLBCL), in a proportion of patients with CLL. Richter transformation is characterised by rapidly progressing disease and an extremely poor prognosis (reviewed in Rossi *et al.*[83]). A high *NOTCH1* mutation rate has also been described in aggressive (UM-CLL/ZAP70^{+}) CLL cases with trisomy 12 (41.9% of cases),[84] suggesting that sustained NOTCH1 signalling plays a key role in the pathogenesis of CLL within this subset. However, the use of *NOTCH1* mutational status as an independent prognostic biomarker remains debated.[56,85]

1.4.3. DOWNSTREAM EFFECTS OF NOTCH1 ALTERATION IN CLL

Although NOTCH1 potentially plays a key role in the clinical course of CLL, the specific function of this protein in leukaemogenesis remains poorly understood. An integrated RNA-sequencing and chromatin immunoprecipitation-sequencing analysis of the NOTCH1-dependent CLL transcriptional signature revealed that NOTCH1 activation results in upregulation of a broad range of transcripts, independent of *NOTCH1* mutational status. Upregulated genes included known NOTCH1 targets such as hairy and enhancer of split/hair and enhancer of split-related with YRPW motif gene family members, the deltex E3 ubiquitin ligase 1 gene, the NOTCH-regulated ankyrin repeat-containing protein gene, cytokine-chemokine and pro-survival signalling pathway members, in addition to genes involved in immune and signalling cascades required for the development and activation of B-lymphocytes. NOTCH1 signalling also induces transcription of itself and its ligand Jagged 1, again suggesting that a positive feed-back loop of NOTCH1 activation exists within CLL[57] (Figure 1.6).
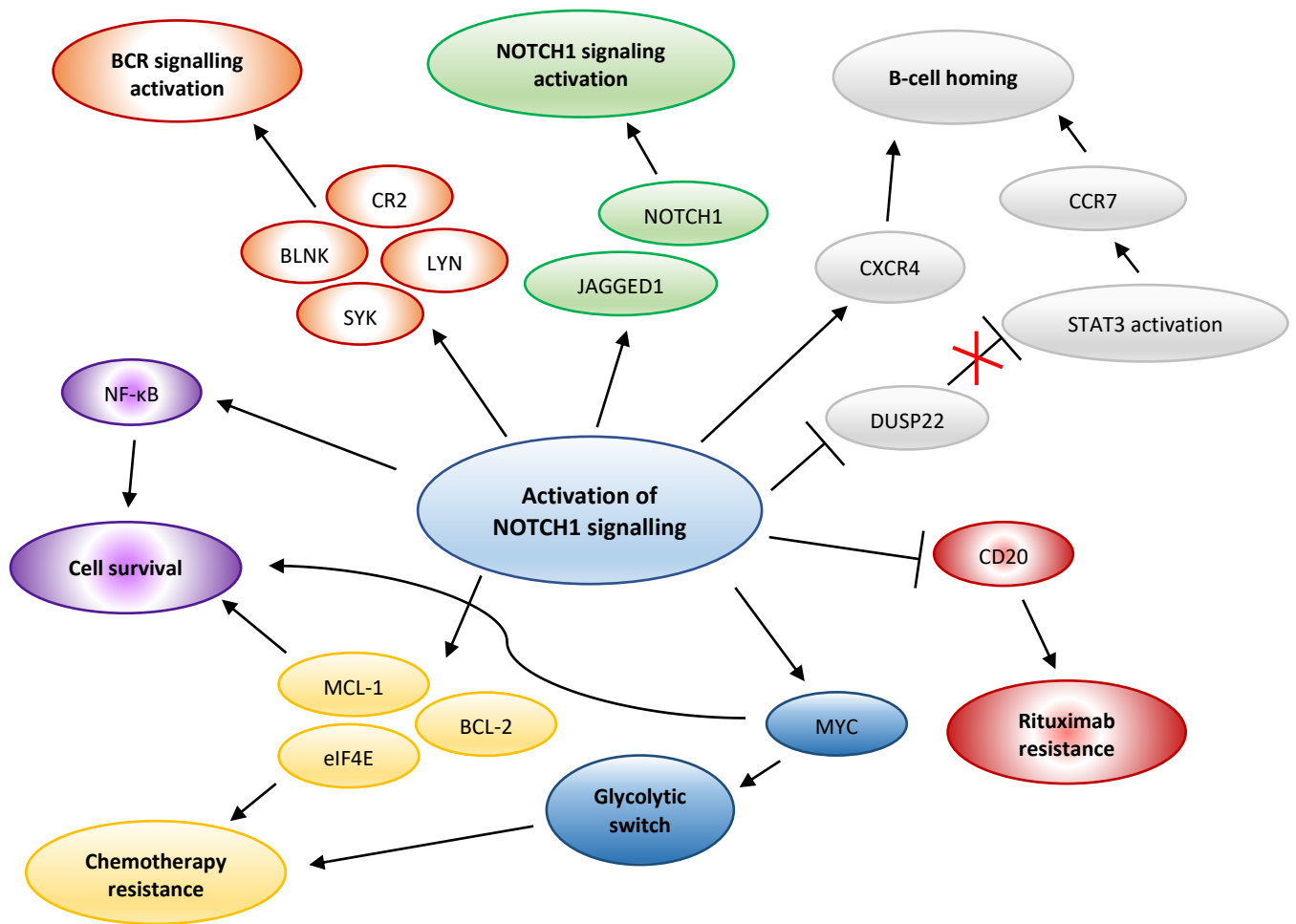
Figure 1.6: Downstream effects of NOTCH1 signalling in CLL cells. NOTCH1 activation results in a broad range of biological effects in CLL cells, independent of *NOTCH1* mutational status. The NOTCH1 transcriptional signature includes several genes with specific functions in B-lymphocyte physiology. Amongst these are genes required for BCR signalling, such as upstream pathway members lck/yes novel tyrosine kinase (LYN), spleen tyrosine kinase (SYK), B-cell linker (BLNK) and complement receptor 2 (CR2), and downstream effectors mitogen-activated protein kinase (MAPK) and NF-κB. Increased activity of NF-κB play a key role in CLL pathogenesis by promoting malignant B-lymphocyte survival. In addition, CLL cell survival is sustained by NOTCH1-mediated expression of anti-apoptotic proteins myeloid cell leukaemia 1 (MCL-1), B-cell lymphoma 2 (BCL-2) and eukaryotic translation initiation factor 4E (eIF4E), all of which are implicated in CLL pathogenesis. NOCTH1 signalling also upregulates the expression of genes regulating CLL cell homing to secondary lymphoid organs, with reduced expression of dual specificity phosphatase 22 (DUSP22), which in turn leads to constitutive activation of signal transducer and activator of transcription 3 (STAT3). STAT3 signalling increases expression of C-C motif chemokine receptor (CCR)7, which mediates C-C motif chemokine ligand (CCL)19-driven chemotaxis. In contrast, C-X-C motif chemokine receptor (CXCR)4 is a direct targeted of NOTCH1 signalling and its upregulation promotes migration towards accessory cells producing C-X-C motif chemokine ligand (CXCL)12. NOTCH1 signalling induces expression of itself as well as its ligands (Jagged 1 and Delta-like protein 1), suggesting that a positive NOTCH1 activation feed-back loop exists in CLL cells. Finally, lower CD20 expression and reduced anti-CD20-mediated cell lysis has been described in NOTCH1-mutated CLL cells and possibly contributes to rituximab resistance. Adapted with permission from Rosati *et al.*[60], Copyright: © 2018 Rosati, Baldoni, De Falco, Del Papa, Dorillo, Rompietti, Albi, Falzetti, Di Ianni and Sportoletti.

By comparing the transcriptome of cells expressing wild-type *NOTCH1* to that of cells lacking the gene, chemotaxis was highlighted as one of the main NOTCH1-regulated processes. Indeed, primary CLL cells carrying clonal NOTCH1 mutations showed higher levels of CCR7 expression and more efficient migration towards CCL19 (the ligand of CCR7) than cells with subclonal *NOTCH1* mutations, mediated via altered methylation of the tumour suppressor gene *DUSP22*. Methylation-dependent downregulation of *DUSP22* led to constitutive phosphorylation (and activation) of STAT3, which in turn is a transcriptional regulator of *CCR7*.[86] Furthermore, the combination of PF-03084014, a clinically relevant NOTCH1 inhibitor, and fludarabine downregulated expression of genes involved in invasion and chemotaxis in *NOTCH1*-mutated cells, including the matrix metallopeptidase 9 (MMP9) gene, which promotes integrin-mediated CLL invasion, and the interleukin (IL)-32 and Ras-related C3 botulinum toxin substrate (RAC)2 genes.[87,88]

IL-32 is a member of the focal adhesion protein complex and can bind to integrins,[89] whereas the Ras homologous (Rho) GTP(guanosine triphosphate)ase RAC2 is required for actin reorganisation and efficient chemotaxis.[90,91] Rho genes have also been shown to be consistently upregulated in T-ALL and are involved in T-ALL cell migration.[92] Consequently, *NOTCH1*-mutated CLL cells displayed reduced actin (a key component of the cytoskeleton) polymerisation, and CXCL12-induced migration and invasion following treatment with PF-03084014 and fludarabine. These effects were specific for *NOTCH1*-mutated cells and did not occur in unmutated cases.[88] As CCL19 and CXCL12 regulate CLL cell homing,[93,94] these studies suggest that *NOTCH1*-mutated CLL cells may favour recirculation to lymphoid organs, where signals produced by accessory cells promote malignant B-lymphocyte proliferation and provide protection from apoptosis,[94] two features associated with a more aggressive disease

progression. This is further supported by NOTCH1-dependent transcriptional profile analyses showing that *CXCR4*, which encodes a chemokine receptor highly expressed in CLL cells and relevant for the chemotaxis of leukaemic cells towards CXCL12-producing accessory cells,[95] is a direct target of NOTCH1 signalling in CLL.[57]

1.4.4. INHIBITORS OF NOTCH1

Given that numerous studies have demonstrated recurrent mutations in haematological malignancies, including CLL, the NOCTH1 signalling pathway has become a promising therapeutic target in recent years.[96] Several novel strategies targeting NOTCH1 in leukaemia and lymphoma have been developed, such as antibodies that block NOTCH1 ligand-receptor interactions, inhibitors that impair the trafficking of mutated NOTCH1 receptors, and small molecules that block γ-secretase cleavage of the N-TMIC, or the assembly of the N-ICD transcription complex.[96]

Targeting Extracellular NOTCH1: Canonical NOTCH1 signalling is activated in a ligand-dependent manner.[58] Therefore, monoclonal antibodies that recognise the juxtamembrane negative regulatory region within the N-EC domain and, subsequently, block cognate receptor-ligand interactions and ADAM metalloprotease-mediated release of the N-TMIC have been explored in malignancies with NOTCH1 activation.[96–99] For example, OMP-52M51 (brontictuzumab), an anti-human NOTCH1 monoclonal antibody generated by immunising mice with a NOTCH1 protein fragment comprising of the LIN repeats and HD, effectively impaired Delta-like protein 4-induced activation of NOTCH1 signalling *in vitro*. Additionally, OMP-52M51 extended survival by 29 days and >67 days in two patient-derived xenograft T-ALL models exhibiting HD and PEST domain mutations, respectively. The anti-leukaemia effects of OMP-52M51 correlated with markedly reduced expression of NOTCH1 target genes

in vivo.[100] In a subsequent phase I dose escalation and expansion study (NCT01778439) in previously treated haematological malignancies [including CLL, mantle cell lymphoma (MCL) and T-ALL], just one of the five patients with activating *NOTCH1* mutations achieved stable disease as best response after 101 days of OMP-52M51 therapy.[101] Although, agents targeting NOTCH1 receptor-ligand binding are generally well tolerated; they have shown limited anti-tumour efficacy in clinical trials.[101–103]

Targeting mutated NOTCH1 trafficking: Inhibition of sarco/endoplasmic reticulum calcium-ATPase (SERCA) channels results in concurrent depletion of calcium ion (Ca^{2+}) stores within the endoplasmic reticulum and elevated cytosolic Ca^{2+}. Disrupted intracellular Ca^{2+} homeostasis leads to endoplasmic reticulum stress and, ultimately, cell death via activation of downstream signalling pathways.[96,104] Thus, SERCA has been identified as a potential target in the treatment of malignancies. Interestingly, the non-competitive SERCA inhibitor Thapsigargin, an organic compound isolated from the roots of *Thapsia garganica*, selectively inhibited mutated NOTCH1 receptor trafficking to the cell surface and induced cell cycle arrest in *NOTCH1*-mutated T-ALL cells.[98,104] The folate-thapsigargin conjugate JQ-FT, designed to prevent cardiac toxicity secondary to impaired Ca^{2+} homeostasis by leveraging the high dependency of leukaemic cells on folate metabolism, diminished cell proliferation, N-ICD expression, and transcription of NOTCH1 target genes in a T-ALL murine model displaying a frequently observed (in human disease) *NOTCH1* PEST domain mutation.[105] In CLL, the US Food and Drug Administration approved Ca^{2+} channel antagonist bepridil demonstrated anti-leukaemia efficacy associated with reduced transmembrane NOTCH1 and N-ICD levels, independent of *NOTCH1* mutational status or the presence of cytogenetic alterations. Furthermore, in a xenotransplant model of CLL, bepridil markedly reduced leukaemic cell

infiltration in the spleen. However, the leukaemic BM cell population was not significantly altered with bepridil treatment.[106] Despite the encouraging results obtained in *in vitro* studies and animal models,[98,104–106] the efficacy of Ca^{2+} channel inhibitors in treating haematological malignancies has yet to be assessed in clinical trials.

Targeting the N-ICD complex: NOTCH1 signalling initiation results in two consecutive proteolytic cleavages that release the active N-ICD. Following translocation to the nucleus, the N-ICD forms a short-lived transcription complex with DNA-binding proteins RBP-Jκ, MAML proteins and other CoA, switching on expression of NOTCH target genes.[58,64] Therefore, protein-protein interaction (PPI) inhibitors that target assembly of the NOTCH1 transcription complex in the nucleus have been developed. The PIP inhibitor soluble α-Helix-constrained 'stapled' peptide derived from mastermind-like 1 repressed *NOTCH1*-dependent gene expression, associated with decreased leukaemic cell proliferation in a panel of T-ALL cell lines *in vitro* and a *NOTCH1*-mutated murine T-ALL model.[107] An open-label, multicentre, non-randomised phase I/IIa dose escalation and expansion study (CB103-C-101) of CB-103, an oral PIP inhibitor which demonstrated anti-tumour efficacy and tolerability in various *NOTCH1*-dependent pre-clinical tumour models, is currently recruiting patients with advanced, metastatic or R/R solid tumours and haematological malignancies for whom no standard therapy exists.[108–110]

Targeting the γ-secretase complex: γ-secretase inhibitors (GSIs), originally developed to reduce the generation of Aβ polypeptides in the amyloid plaques of Alzheimer's disease,[111] have been extensively utilised in NOTCH1-dependent cancers.[96,112] Cleavage by the γ-secretase complex releases the active N-ICD[58,63,64] and, thus, represents a key step in the NOTCH1 signalling pathway. Rosati *et al.*[73] first reported that GSI treatment increased

spontaneous CLL cell apoptosis and concomitantly decreased NOTCH1 expression in a concentration-dependent manner. Results from several subsequent pre-clinical studies have further demonstrated the potential therapeutic benefits of GSIs in treating CLL.[86,88,113,114] Despite promising *in vitro* studies, to date, no clinical trials have assessed the efficacy of GSI therapy in patients with CLL. However, several GSI trials have been conducted in T-ALL.

The first trial in seven patients with relapsed T-ALL and one acute myeloid leukaemia case evaluated the anti-leukemic effects of the potent oral GSI MK-0752 [half-maximal inhibitory concentration (IC_{50}) of approximately 50nM] over 2 to 56 days. The trail was terminated due to disease progressions, or the development of gastrointestinal toxicity in most participants at a dose of 300 mg/m^2,[115] resulting from disrupted intestinal homeostasis due to simultaneous GSI-induced inhibition of both NOTCH1 and NOTCH2.[116,117] GSIs are pan-NOTCH inhibitors blocking the proteolysis of all NOTCH receptors, albeit unequally.[112] One *NOTCH1*-mutated patient had a transient response, achieving a 45% reduction in tumour mass at 28 days as best response (150 mg/m^2) before progressing.[115]

In a subsequent phase I study, patients with relapsed or refractory (R/R) T-ALL (three cases) or T-lymphocyte lymphoblastic lymphoma (five cases) received the non-competitive, reversible GSI PF-03084014 (Nirogacestat) at 150 mg twice daily. One heavily pre-treated, *NOCH1*-mutated T-ALL patient achieved complete remission lasting approximately 3 months. Nausea and vomiting were the most frequent adverse events reported.[118] Diarrhoea was typically low grade and not treatment-limiting[118] as previously reported with other GSIs.[115,119]

Knoechel *et al.*[120] observed a complete haematological response in a patient with R/R early T-lymphocyte precursor ALL following treatment with GSI Bristol-Myers-Squibb (BMS)-906024 at 6 mg once per week in 4-week cycles.[120] Furthermore, a phase I trial incorporating

twenty-five R/R T-ALL or T-lymphocyte lymphoblastic lymphomas cases reported that eight of the patients had a ≥50% reduction in BM blasts when administered BMS-906024 weekly (4-6 mg), with three patients displaying 98-100% clearance of BM blasts. Adverse events, including anaemia, thrombocytopaenia and diarrhoea, were generally tolerable.[121]

Despite encouraging clinical results, overall, GSI are considered to have severe gastrointestinal toxicity and limited anti-leukemic activity as a monotherapy, providing only transient or partial responses. Therefore, no GSI has been approved for use in patients with T-ALL. However, combination therapies, incorporating GSI with other apoptosis-inducing or immune-modulating agents, may be an alternative treatment option in malignancies with increased NOTCH1 activity. For example, in a T-ALL xenograft mouse model, a combination of GSI MRK-003 at a non-efficacious dose and the mechanistic target of rapamycin (mTOR) inhibitor rapamycin increased the mean survival period of mice by more than 50 days compared to MRK-003 or vehicle alone.[122] Histological analysis demonstrated that xenograft mice co-treated with GSI dibenzazepine plus dexamethasone show normal goblet cell numbers within the duodenum and preservation of the intestinal epithelium architecture.[123] Thus, suggesting that glucocorticoids can abrogate the GSI-induced toxicity within the gastrointestinal track. An additional synergistic effect of GSI and glucocorticoid treatment was reversal of glucocorticoid resistance in T-ALL cells. A glucocorticoid-resistant T-ALL cell line with activated NOTCH1 showed only minimal loss of viability when treated with high concentrations of dexamethasone (up to 1×10^{-5} M). In contrast, dexamethasone plus GSI Compound E (100 nM) effectively induced cell death, with an IC_{50} value of 7.7×10^{-8} M for dexamethasone.[123]

With regards to CLL, PF-03084014 was shown to enhance the cytotoxic effect of fludarabine in *NOTCH1*-mutated cells, despite the introduction of pro-survival stimuli, possibly by reducing fludarabine-mediated activation of NF-κB.[88] Furthermore, a combination of BMS-906024 and ibrutinib had synergistic anti-leukaemic effects in CLL cases exhibiting deleterious *TP53* mutations, promoting down-regulation of N-ICD activation and CXCR4 expression, and, consequently, reduced transcription of the oncogenic transcription factor c-MYC and CXCL12-mediated migration, respectively.[113]

1.5. THE B-LYMPHOCYTE CYTOSKELETON

The cytoskeleton of eukaryotic cells is composed of three categories of filaments: (i) microfilaments (diameter: 4-7nm), made up of predominantly actin; (ii) intermediate filaments (diameter: 8-11nm), formed by at least five distinct classes of proteins; and (iii) microtubules (diameter: 25nm), consisting of tubulin (reviewed in Fletcher and Mullins[124]). The cytoskeleton is involved in numerous basic cellular functions, including cell shape, motility, mitosis, and organelle movement.

B-lymphocyte migration and homing, which are essential features of B-lymphocyte mediated immunity, both require the rapid reorganisation of the plasma membrane and cytoskeleton. Dynamic shape changes involving the cytoskeleton are also crucial for intra-and extravasation of B-lymphocytes through blood vessels during homing to and from lymphoid organs during an immune response (reviewed in Vicente-Manzanares and Sánchez-Madrid[125]). Indeed, even partial loss of cytoskeletal integrity in lymphocytes can cause increased susceptibility to infections and cancer. For example, Wiskott-Aldrich syndrome (WAS), a primary immunodeficiency characterised by immune dysregulation, eczema, thrombocytopaenia with small platelets and lymphoid malignancies, results from a deficiency of the WAS protein

(WASP), an important regulator of the actin cytoskeleton in haematopoietic cells, or the WASP interacting protein (WIP).[126–130]

The mechanical functions of the B-lymphocyte cytoskeleton require the dynamic, but highly regulated, polymerisation of actin monomers into helical actin filaments [filamentous actin (F-actin)].[125] In all cell types, nucleation factors are responsible for the generation of new F-actin, including the actin-related protein 2/3 (ARP2/3) complex and formins[131].

Formins are single polypeptide, multidomain proteins that generate filaments directly from actin monomers by encircling energetically unstable actin dimers and/or trimers with their dimeric formin homology 2 (FH2) domains[132] (Figure 1.7A). Formins remain bound to F-actin and move processively as it elongates.[133–136] Some formins can also form bundles of F-actin,[137,138] sever or depolymerise actin filaments.[139,140] In contrast, the ARP2/3 complex, which is composed of seven polypeptides [actin-related protein 2/3 complex subunit 1-5 (ARPC1-5), ARP2 and ARP3], binds to the side of a pre-existing actin filament and produces a daughter filament that branches out at an angle of 70°, thereby generating highly branched actin filaments that create 'dendritic' networks[131,141,142] (Figure 1.7B). Nucleated filaments can be elongated or disassembled from either their 'barbed' or 'pointed' ends, but the processes are (ten-times) faster at the barbed end, giving the filament directionality.[143–146] The activity of nucleators, capping proteins, which bind to the barbed end and prevent further elongation, and actin-severing proteins, regulate the length of filaments. The combined actions of these actin-binding proteins, along with cross-linkers, which create complex actin networks by joining filaments, produce a range of specialised structures that are required for cellular functions.[131,147]
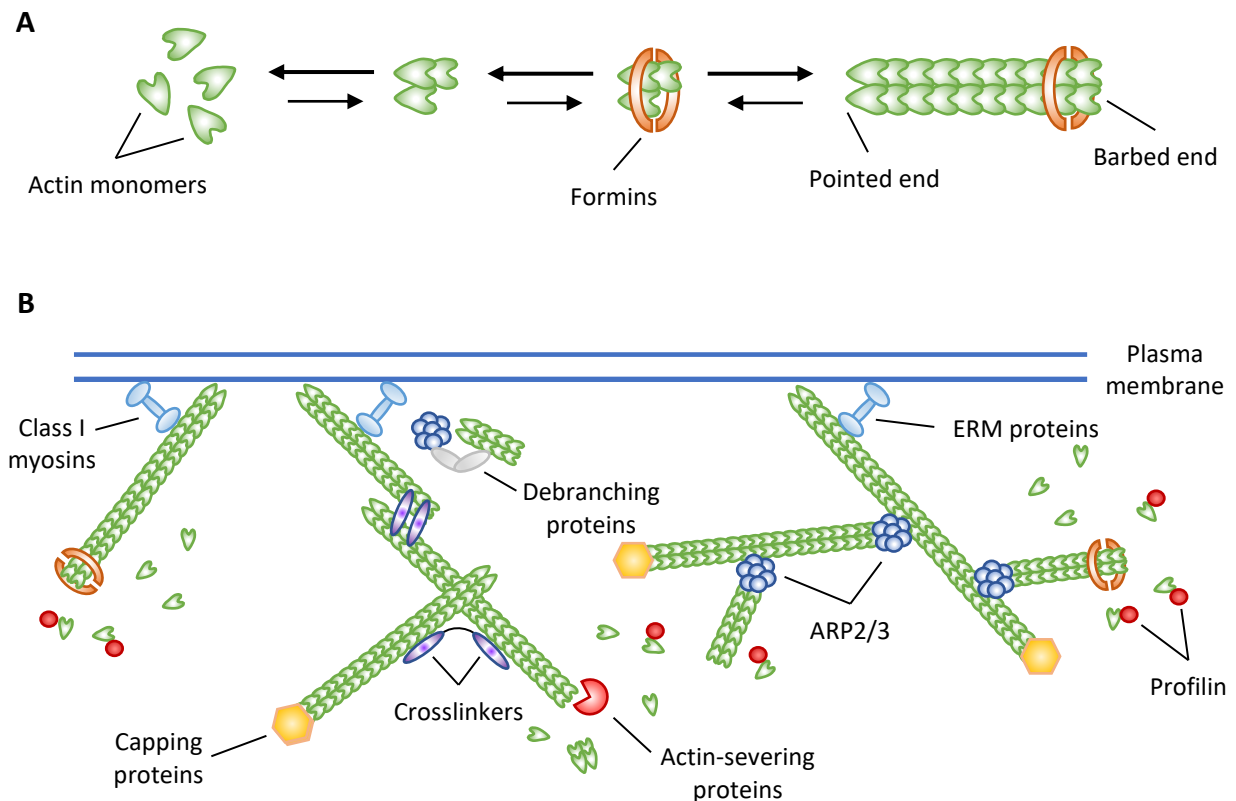
Figure 1.7: Polymerisation of actin filaments within the B-lymphocyte cortical cytoskeleton. (A) Actin monomers self-assemble into helical F-actin filaments; however, the initial formation of dimeric and trimeric complexes is highly unfavourable. Nucleation factors such as formins and the ARP2/3 complex overcome the unfavourable dimerisation and/or trimerisation steps to begin rapid filament elongation. Filaments can be polymerised or depolymerised from either end, but both processes are faster at the barbed end than the pointed end. (B) Within the cortical cytoskeleton, the ARP2/3 complex nucleates a new filament (at an angle of 70°) from the side of a pre-existing filament, creating dendritic networks along with crosslinker proteins. Formins generate filaments directly from monomers and then progresses with the barbed end as it elongates. In non-muscle cells, profilin enhances the unidirectional elongation of filaments by adding actin monomers to the barbed end only. The size and structure of the actin cytoskeleton is regulated by capping proteins (inhibit the elongation of F-actin by binding to its barbed end), actin-severing proteins (depolymerise filaments), and debranching proteins (remove daughter filaments generated by ARP2/3). The complex actin network is attached to the plasma membrane through several linker proteins, including ezrin, radixin and moesin (ERM) proteins and class I myosins. This figure is based on information taken from Chhabra and Higgs[131], Fletcher and Mullins[124] and Tolar[147].

The area directly underneath the plasma membrane, the cortex, is a key site of actin reorganisation. The cortical cytoskeleton, which is a meshwork of short actin filaments approximately 100nm thick with a pore size of approximately 50nm[148] (generated by the activity of both formins and ARP2/3) is extremely dynamic and can turnover in less than a minute (min).[148,149] In B-lymphocytes, the cortical cytoskeleton is a key target of the BCR and chemokine receptors. Antigen- or chemokine-induced signalling pathways lead to a burst of actin polymerisation against the plasma membrane which pushes the membrane outwards generating a range of protrusive structures.[147] These structures are broadly divided into two groups: (i) sheet-like protrusions such as lamellipodia/lamella, which are observed during crawling cell motility and spreading; and (ii) finger-like protrusions such as filopodia and microvilli[131] (Figure 1.8). Adherent filopodia extend from the lamellipodial sheet and are believed to be involved in chemotaxis,[150] possibly through enrichment of activated integrins at their tips,[151] and cell-to-cell communication; whereas, microvilli are non-adherent and may act to segregate cell surface proteins on lymphocytes.[152] BCR-triggered remodelling of the actin cytoskeleton can also induce the formation of the immunological synapse (IS)[147] and deformation of the membrane inwards to mediate endocytosis.[153,154]

In addition to pushing the membrane outwards, actin reorganisation also produces cortical tension. This tension is produced by class II non-muscles myosins (non-muscle myosin IIA in lymphocytes), which are motor protein that assemble into mini-filaments, containing numerous mechanically active heads on each side.[155,156] These myosin heads bind to F-actin (typically, linear actin filaments; however, myosin can also act on branched filaments within the cortical meshwork) and by exerting power strokes, slide two actin filaments towards the

centre of the myosin mini-filament, thus contracting the actin cytoskeleton and generating tension.[157]
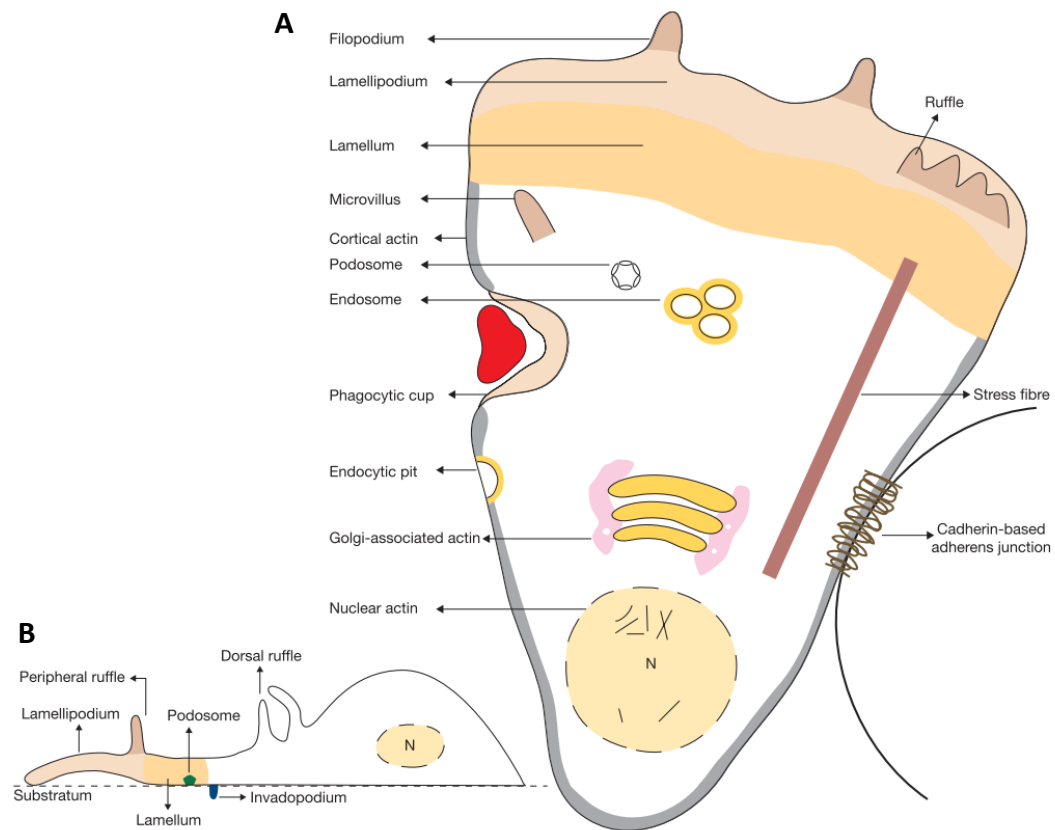
Figure 1.8: Actin-based structures in eukaryotic cells (A) A hypothetical eukaryotic cell, undergoing directional cell migration and attached to a neighbouring cell via a cadherin-based adherens junction. (B) A side view of a migrating cells. Several key cytoskeletal features are shown, including microvilli, ruffles (peripheral and dorsal), filopodia, weakly adherent lamellipodia and stress fibres. Image taken from Chhabra and Higgs.[131] Reproduced with permission from Springer Nature.

In CLL the organisation or function of different cytoskeletal components has long been recognised as having unique and unusual features. CLL cells exhibit impaired cell motility,[158] decreased capping of multivalent ligands,[159] the formation of podosomes instead of conventional adhesion plaques,[160] enhanced susceptibility to microtubule-disrupting drugs[161,162] and reduced expression of vimentin,[163] an intermediate filament responsible for maintaining the rigidity of circulating leucocytes.[164] More recently however, drugs which target BCR signalling pathways have highlighted the importance of understanding cytoskeletal-directed behaviour.

1.6. CLL AND THE TUMOUR MICROENVIRONMENT

Important observations have now emerged that link the cytoskeleton of neoplastic CLL lymphocytes to disease pathology. These include the recognition that chemokine-driven cytoskeletal reorganisation is central to the migration of CLL cells into lymphoid organs[125] where they engage in complex, yet incompletely defined, cellular and molecular interactions with accessory cells, such as T-lymphocytes, monocyte-derived nurse-like cells (NLCs) and BM stromal cells (BMSCs), which collectively are referred to as the 'tumour microenvironment (TME)' (Figure 1.9). Within tissue niches, CLL cells also display transient homotypic cell contact.[165] These CLL-CLL and CLL-TME interactions are crucial for leukaemic cell survival, with pure preparations of CLL B-lymphocytes undergoing cell death within 24 hours (h) of culture at standard density.[166] Apoptosis is prevented by the introduction of supportive cells,[167,168] or by culture of leukaemic cells at high density with PB mononuclear cells.[165,166] Thus, effective modelling of the TME has become a highly relevant field of research in recent decades (explored in detail in Chapter 5).
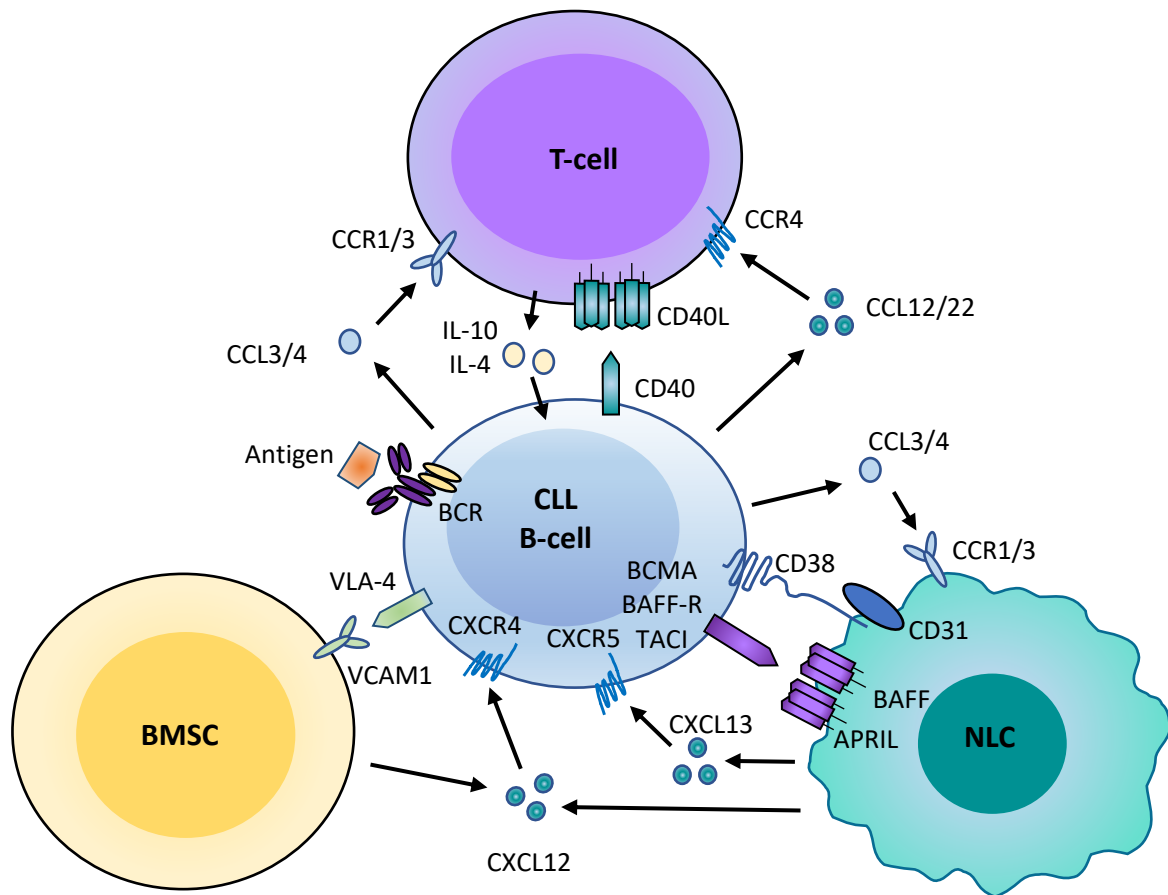
Figure 1.9: Cellular and molecular interactions in the CLL TME. CLL cell homing and retention within lymphoid organs is primarily mediated by CXCL12 (secreted by BMSCs and NLCs) binding to CXCR4. Once in tissues, integrins, particularly α4β1 [also known as very late antigen-4 (VLA-4)], expressed on the CLL cell surface, facilitate cell-to-cell adhesion via respective ligands [vascular cell adhesion molecule 1 (VCAM1) and fibronectin] on BMSCs, which contributes to CLL cell survival. In turn, CLL cells secrete chemokines, such as CCL3 and CCL4, that recruit T-lymphocytes and monocytes to the TME. Activated T-lymphocytes provide CLL cells with antigen-dependent proliferative and pro-survival signals via CD40 ligand (CD40L)-CD40 engagement and the production of various cytokines (e.g., IL-4 and IL-10). Activated CLL cells can then secrete more chemokines (CCL12 and CCL22) which recruit additional T-lymphocytes to lymphoid organs. Within the TME, monocytes differentiate into NLCs which express tumour necrosis factor family members B-cell activating factor (BAFF) and a proliferation inducing ligand (APRIL). BAFF and APRIL support CLL cell survival by binding to their corresponding receptors [B-cell maturation antigen (BCMA), BAFF-receptor (BAFF-R) and transmembrane activator calcium modulator and cyclophilin ligand interactor (TACI)] on CLL cells. NLCs also aid in the migration of CLL cells into tissues via the production of CXCL13. The interaction of CD38 on CLL cells with BMSC- and NLC-expressed CD31 activates ZAP-70 and downstream pro-survival pathways. Stimulation of the BCR complex (BCR, CD79A and CD79B) induces downstream signalling pathways, and may increase the responsiveness of CLL cells to cellular and molecular signals provided by the CLL TME. This figure is based on information taken from Burger[95] and Burger and Gribben.[94]

1.6.1. BONE MARROW STROMAL CELLS

In the BM, stromal cells maintain normal haematopoietic precursor cells in specialised 'niches' which are close to the marrow vasculature system.[169] In CLL, BMSCs function in a similar fashion, creating niches in which CLL cells are nourished and protected from cytotoxic agents in a contact-dependent manner.[170,171] Indeed, CLL lymphocytes have a high affinity for BMSCs: *in* vitro co-culture with BMSCs results in the rapid adhesion and spontaneous migration of a fraction of CLL cells beneath the BMSCs, inducing a cobblestone-like appearance. This phenomenon is termed pseudoemperipolesis and is highly dependent upon CXCR4 and integrin $\alpha4\beta1$ expression by neoplastic cells.[172,173]

The cross-talk between CLL and BMSCs is bi-directional, with BMSCs becoming activated by platelet-derived growth factor secreted by CLL cells.[174] The binding of platelet-derived growth factor to its cognate receptor present on the BMSC membrane triggers down-stream signalling pathways leading to increased vascular endothelial growth factor expression.[175] Vascular endothelial growth factor promotes neovascularisation, a process associated with disease progression in many malignancies.[176] The positive correlation shown between platelet-derived growth factor and vascular endothelial growth factor expression in CLL patients, particularly those with rapidly progressing or late stage disease was therefore expected.[175] Additionally, directed contact of CLL cells with BMSCs results in expression of protein kinase C (PKC)-βII and the subsequent activation of NF-κB signalling in BMSCs, both of which are required for BMSCs to support CLL cell survival.[177]

1.6.2. NURSE-LIKE CELLS

NLCs, which differentiate from blood monocytes following prolonged co-culture with CLL cells at high-density, attract CLL cells to the TME by secreting CXCL12 and CXCL13,[167,178] and

provide leukaemic cells with contact-dependent protection from spontaneous or drug-induced apoptosis via factors such as APRIL, BAFF,[179] CD31 (also known as platelet endothelial cell adhesion molecule-1) and plexin-B1.[180] *In vivo,* NLCs have been identified in the spleen and secondary lymphoid tissues of CLL patients,[181] and murine models have highlighted the importance of NLCs for disease progression.[182,183] DNA microarray analyses of CLL cells co-cultured *in vitro* with NLCs demonstrated relatively homogenous gene expression profiles, which were similar to those observed for leukemic cells isolated from lymph nodes, with the induction of several genes involved in TME interactions, including *CCL3, CLL4* and *BCMA*, in addition to up-regulation of BCR signalling target genes.[184,185]

1.6.3. T-LYMPHOCYTES

The neoplastic CLL cells should be subject to immune-destruction by allogeneic or autologous T-lymphocytes; however, it is becoming increasingly clear that defective interactions with T-lymphocytes may permit neoplastic cells to escape immunological destruction during leukaemogenesis. T-lymphocytes in CLL display changes in the expression of genes involved in cytoskeletal formation,[186] resulting in defective actin polymerisation and consequently, impaired IS formation with antigen presenting cells – an abnormality that can be reversed with lenalidomide (an immunomodulatory drug) treatment.[187] Similar alterations in gene expression are also induced in healthy T-lymphocytes after co-culture with CLL cells, demonstrating that it is the neoplastic cells that are inducing these changes.[186] T-lymphocytes also exhibit an 'exhausted' phenotype characterised by increased expression of exhaustion markers CD244, CD160, programmed cell death protein-1 (PD-1) and B-lymphocyte-induced maturation protein-1 (BLIMP-1).[188]

In contrast to the phenotype observed in virally induced exhaustion, CLL T-lymphocytes show increased interferon (INF)-γ and tumour necrosis factor (TNF)-α production, increased expression of transcription factor T-box 21 (TBET) and normal IL-2 production, possibility protecting CLL from entering apoptotic cell death. Exhausted CD8^{+} T-lymphocytes cannot effectively eliminate CLL cells due to an inability to co-localise Granzyme B with CD107A - a prerequisite for successful IS formation.[188] Finally, signals emanating from CD4^{+} T-lymphocytes can induce antigen-dependent leukaemic cell proliferation (via CD40L engagement in combination with IL-21[189]) in additional to promoting CLL survival (via IFN-γ, IL-4 and CD40L).[190–192]

1.7. THE BCR COMPLEX AND SIGNALLING PATHWAYS

B-lymphocytes are a crucial component of the adaptive immune system, having two main functions: (i) participating directly in the humoral immune response by producing antibodies; and (ii) facilitating the initiation of the T-lymphocyte immune response by selectively internalising and presenting processed antigens to naïve and memory T-lymphocytes. These two functions of B-lymphocytes are both achieved through the activation of the BCR.[193]

In addition to playing a key role in the adaptive immune response, BCR signalling is essential for normal B-lymphocyte development. There are several possible cellular responses that may be mediated by the BCR, such as apoptosis, proliferation, and differentiation into plasma cells or memory B-lymphocytes.[193] However, BCR signalling is also used by B-cell malignancies, including CLL, to drive proliferation, growth, and survival.[194] Inhibitors targeting BCR-related pathways have, therefore, emerged over the past few decades as novel therapies for the treatment of B-lymphocyte malignancies.

The BCR (Figure 1.10) is composed of a ligand-binding moiety, the antigen-specific transmembrane immunoglobulin [either IgM, IgD (naïve B-lymphocytes), IgG (memory B-lymphocytes), IgA or IgE], non-covalently bound to the signal transduction moiety, the Igα (also known as CD79A)/Igβ (also known as CD79B) heterodimer.[195,196] CLL cells predominantly co-express IgD and IgM, albeit at lower levels than their normal counterparts; CLL cases exhibiting class-switched immunoglobulins are infrequent.[13]

Engagement of the BCR by soluble or membrane-bound antigens induces migration and aggregation of the membrane immunoglobulins,[197] leading to phosphorylation of the cytoplasmic immunoreceptor tyrosine-based activation motifs (ITAMs) of CD79A and CD79B[198,199] by SRC family kinases including LYN, and SYK.[200–202] This phosphorylation event is the moment of BCR signalling cascade activation and results in the recruitment of numerous kinases and adaptor proteins, including phosphoinositide 3-kinase (PI3K), Bruton's tyrosine kinase (BTK) and B-cell linker (BLNK).[203]
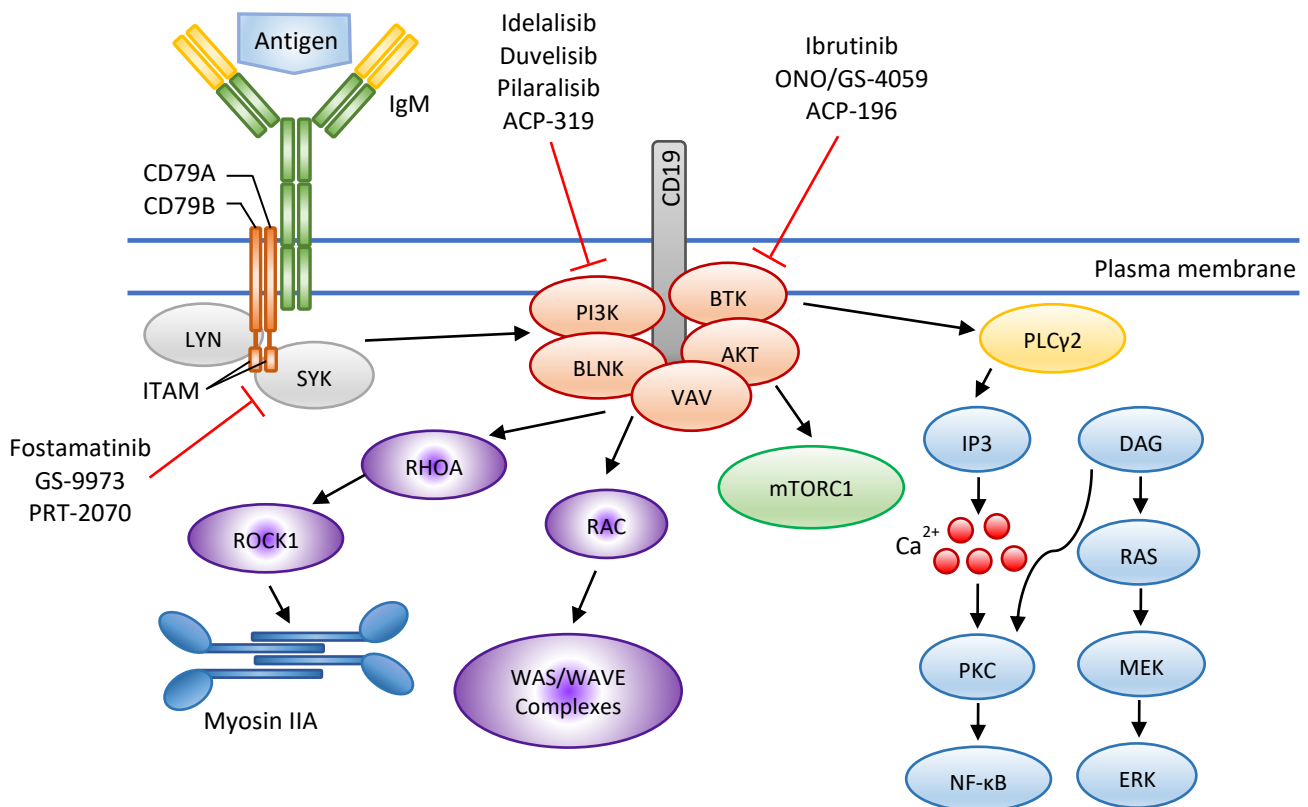
Figure 1.10: The BCR complex and signalling pathway. The receptor for antigens on B-lymphocytes is a surface membrane immunoglobulin. Initially, cells express IgM and then IgD; however, B-lymphocytes can undergo class switching. The immunoglobulin functions as the antigen-binding domain, whilst the non-covalently associated CD79A/CD79B heterodimer acts as the signalling component. After an antigen engages the BCR, SRC family kinases LYN and SYK phosphorylate the ITAMs within the cytoplasmic tails of CD79A and CD79B. This then triggers the recruitment of a multi-component 'signalosome', comprising of PI3K, BLNK, AKT, BTK and Vav proteins. CD19 (a co-receptor for BCR) is essential for PI3K activation. Activated BTK then phosphorylates phospholipase Cγ2 (PLCγ2), which catalyses the hydrolysis of phosphatidylinositol 4,5-bisphosphate (PIP2) into inositol 1,4,5-trisphosphate (IP3) and diacylglycerol (DAG). This leads to Ca^{2+} release from the endoplasmic reticulum and, subsequently, PKC-mediated activation of the NF-κB signalling pathway. DAG also activates the mitogen-activated protein kinase kinase (MEK)/MEK-extracellular signal-regulated kinase (ERK) signalling pathway via rat sarcoma proteins (RAS). Additional effects of BCR signalling include activation of mTORC1. mTORC1 plays a key role in coordinating anabolic and catabolic processes in response to diverse nutritional and environmental cues. The activation of BLNK, CD19 and Vav proteins results in the activation of WAS protein and WAS protein family verprolin-homologous protein (WAVE) complexes via GTPase RAC. The WAS and WAVE proteins induce actin polymerisation, leading to reorganisation of the cytoskeleton. Ras homolog gene family, member A (RhoA), activated through VAV2, initiates actin polymerisation in addition to stimulating myosin contractility via Rho-associated protein kinase 1 (ROCK1). Inhibitors of BTK, SYK and PI3K are shown. Note that this figure summarises the main proteins and interactions that are involved in the BCR signalling pathway but is not an exhaustive description of all signalling pathways or molecule involved. This figure is based on information taken from Kipps *et al.*,[13] Tolar[147] and Woyach *et al.*[203]

Following phosphorylation of the ITAMs, BLNK is recruited and rapidly phosphorylated by SYK.[203] Activated BLNK is required for phosphorylation of BTK by SYK,[204] whilst LYN can phosphorylate BTK directly.[205] Activation of BTK enables it to phosphorylate its direct substrate PLCγ2, which catalyses the hydrolysis of PIP2 into IP3 and DAG.[197] In turn, this event leads to Ca^{2+} mobilisation by IP3, and DAG-mediated PKC activation,[203] followed by the subsequent induction of transcription factors necessary for B-lymphocyte proliferation, differentiation, antigen presentation, cytokine and antibody production, and migration.[203,206] Targets of BCR signalling include ERK and NF-κB signalling pathways,[203] and Rho-family GTPases, RAC1 and RhoA, which facilitate chemotaxis by coordinating extension of the leading edge and retraction of the lagging tail, respectively.[147,207]

1.8. MODULATING CYTOSKELETAL RESPONSES IN CLL

1.8.1. BTK AND BTK INHIBITORS

BTK, an early component of BCR signalling pathway (Figure 1.10), has been implicated in the development of B-lymphocyte lymphoproliferative disorders, including CLL, follicular lymphoma, MCL, acute lymphoblastic leukaemia and DLBCL.[194] Pre-clinical and clinical studies have shown that inhibiting the action of BTK, a member of the TEC family of non-receptor tyrosine kinases, has been highly effective in the treatment of in several B-lymphocyte malignancies.[208–210] Perhaps of more clinical importance, however, are observations that relate the cytoskeleton directly to the response to BTK inhibitors (BTKi).

Ibrutinib (Imbruvica®, Pharmacyclics) is a first-in class, orally active, small molecule inhibitor of BTK. The molecule binds covalently to the cysteine-481 residue at the active site of BTK,[208] irreversibly inhibiting tyrosine-223 autophosphorylation and downstream signalling cascades[211] (Figure 1.10). The presence of a cysteine residue within the catalytic site is an

interesting feature; only nine other kinases possess cysteine at comparable sites.[208] The selective inhibition of BTK and other TEC kinases combined with the restricted expression of BTK to B-lymphocytes, therefore, enhances the specificity of ibrutinib.

Originally, ibrutinib (previously known as PCI-32765) was developed by Celera Genomics and later Pharmacyclics as a targeted therapy in both rheumatoid arthritis and lymphoma.[208,211] *In vitro* assays showed that ibrutinib inhibited tyrosine-223 phosphorylation at very low concentrations (IC_{50}: 0.5 nM).[208] Following oral administration, ibrutinib was rapidly absorbed (median time to maximum serum concentrations: 1-2 h) and eliminated (terminal half-life: 4-8 h).[209] In a phase I study, ibrutinib displayed greater than 95% occupancy of the BTK active site for up to 24 h after oral administration in patients with R/R B-lymphocyte malignancies. Ibrutinib was generally well tolerated, with most adverse effects being mild in severity. Significant myelosuppression was not seen with ibrutinib treatment. Furthermore, no cumulative toxicity was seen with repeated dosing. [209] However, significant toxicities, including bleeding, diarrhoea, arthralgia, neutropenia and atrial fibrillation were observed in some patients[209,210,212,213] and likely resulted from low nanomolar inhibition of other kinases.[208,211,214–216] More selective BTKi, with comparable activity to ibrutinib have, therefore, been developed such as tirabrutinib (ONO/GS-4059)[217] and acalabrutinib (formally known as ACP-196; trade name CALQUENCE®).[218] Due to its significant clinical efficacy in several mature B-lymphocyte malignances, ibrutinib was awarded 'Breakthrough Drug' status[219] and approval by the US Food and Drug Administration for the treatment of R/R MCL in 2013, for CLL in 2014 and for Waldenström's macroglobulinaemia in 2015 . Ibrutinib has since been approved in Europe for the treatment of R/R MCL and several patient groups with CLL and Waldenström's macroglobulinaemia.

1.8.2. CLINICAL STUDIES WITH IBRUTINIB

In the initial phase I study conducted by Advani *et al.*[209] durable, objective responses (mean PF survival of 13.6 months) were demonstrated in R/R B-lymphocyte malignancies, particularly in MCL (79%) and CLL/small lymphocytic lymphoma (SLL) (69%). Results from the subsequent phase Ib/II trial showed long-term efficacy and durable responses with single-agent ibrutinib, with estimated 5-year progression-free survival (PFS) rates of 92% in treatment-naïve (TN) and 44% in R/R patients; the median OS had not been reached in either group at the time of follow-up. High overall response rates (ORR) were observed in patients with high-risk molecular features. In particular, an ORR of 79% was seen in R/R patients with del(17p).[210] Although the median PFS and OS in the R/R del(17p) subgroup were less robust (26 and 57 months, respectively) than those obtained in patients with other high-risk cytogenetic abnormalities,[210] they still compared favourably to the PFS and OS seen in patients with del(17p) (R/R or TN) receiving fludarabine, cyclophosphamide and rituximab (FCR) chemoimmunotherapy,[42] or alemtuzumab (anti-CD52 monoclonal antibody) alone[220] or in combination with steroids.[221] The follow-up data obtained at up to 7 years of this phase Ib/II trail was also encouraging, with sustained PFS and OS rates demonstrated in TN (estimated 7-year rates: 80% and 75%, respectively) and R/R (estimated 7-year rates: 32% and 52%, respectively) groups.[222]

In the open-label, multicentre phase III RESONATE trail, comparing ibrutinib to ofatumumab (anti-CD20 monoclonal antibody) in R/R CLL/SLL patients, medium PFS was not reached in the ibrutinib group whereas it was 8.1 months in the group receiving ofatumumab. Significantly prolonged PFS in the ibrutinib group compared to the ofatumumab group was observed regardless of high-risk clinical characteristics or molecular features. However, severe adverse effects were more frequent in patients receiving ibrutinib.[223]

The phase III RESONATE-2 trail, which compared ibrutinib against chlorambucil in a 1:1 randomisation in TN CLL/SLL patients older than 65 years, demonstrated superior 5-year PFS and OS rates in ibrutinib-treated patients (estimated rates: 70% and 83%, respectively) compared to chlorambucil recipients (estimated rates: 12% and 68%, respectively). The PFS benefits of ibrutinib over chlorambucil were observed across all patient subgroups, including those with high-risk molecular features. Patients with del(17p) were excluded from this trail as chlorambucil was not considered an appropriate alternative in this subgroup; however, some patients displayed *TP53* mutations.[224] Data regarding ibrutinib as a monotherapy for the treatment of TN and R/R CLL/SLL and ibrutinib used in combination with other therapeutic agents (Table 1.1) continue to look promising.

Table 1.1: Inclusion criteria and PFS in phase III trials of ibrutinib combinational therapies in TN and R/R CLL

Clinical trial	Inclusion criteria	Ibrutinib arm	CIT* arm	Ibrutinib arm PFS	CIT arm PFS
ECOG-ACRIN[225]	Untreated CLL/SLL Patients aged 70 years or younger Patients able to tolerate FCR Patients with del(17p) excluded	Ibrutinib + Rituximab	FCR[†]	89%	73%
iLLUMINATE[226]	Untreated CLL/SLL Patients aged 65 years or older Patients younger than 65 years with coexisting conditions Patients with del(17p) or *TP53* mutations included	Ibrutinib + Obinutuzumab	Chlorambucil + Obinutuzumab	79%	31%
ALLIANCE[227]	Untreated CLL Patients aged 65 years or older Patients with del(17p) or *TP53* mutations included	Ibrutinib + Rituximab Ibrutinib alone	Bendamustine + Rituximab	88% 87%	74%
HELIOS[228]	R/R CLL or SLL Patients with del(17p) excluded Patients previously treated with BTKi, bendamustine-containing regimes (within 24 months) or HSCT[§] excluded	Ibrutinib + Bendamustine + Rituximab	Placebo + Bendamustine + Rituximab	79%	24%

*CIT, chemoimmunotherapy.

[†] FCR, fludarabine, cyclophosphamide, rituximab chemoimmunotherapy.

[§]HSCT, haematopoietic stem-cell transplant.

1.8.3. THERAPEUTIC MODE OF ACTION OF IBRUTINIB

Despite the clinical success of ibrutinib, its therapeutic mode(s) of action is still poorly understood. However, a particular feature of ibrutinib treatment was that a significant lymphocytosis was observed concomitantly with a rapid reduction in lymphadenopathy, and represented the egress of tissue-resident malignant cells into the PB.[212,229]

A lymphocytosis was typically seen in ibrutinib-treated CLL patients by 7 days (78% of cases), peaking at a medium of 4 weeks and then slowly decreasing to baseline level over several months (approximately 8 months).[212] In contrast, the transient lymphocytosis seen in MCL patients receiving ibrutinib (34% of cases) generally resolved quicker, peaking at a medium of 4 weeks and falling to near baseline after approximately 3 months.[229] Similar responses have also been observed in clinical trials of inhibitors of SYK (R788/fostamatinib)[230] and PI3K (CAL-101).[231]

Through its inhibition of BTK, ibrutinib inhibits several downstream pro-survival signalling pathways, as demonstrated by its ability to reduce phosphorylation of ERK, protein kinase B (AKT) and PLCγ,[211,232] and expression of NF-κB target gene, NF-κB p50, in the nucleus of CLL cells;[233] however, rapid apoptosis of circulating neoplastic cells was not seen.[234] The tumour regression seen in CLL (and possibly MCL) patients treated with ibrutinib is thought to be caused by 'death by deprivation' rather than a direct cytotoxic effect on malignant B-lymphocyte. Inhibition of α4β1-mediated adhesion and reduced migration towards chemokines[235–237] may be key factors in the development of lymphocytosis following ibrutinib treatment and would deprive malignant cells of the crucial TME signals they need to survive. Furthermore, an on-target effect of ibrutinib was the rapid reduction in serum levels of key chemokines (e.g., IL8, CCL3, CCL4 and CCL22) that are secreted by CLL cells in response to,

among others, BCR and CD40 signalling.[238] Inflammatory cytokines secreted by accessory cells were also significantly reduced following ibrutinib treatment,[238] suggesting widespread changes in the behaviour of accessory cells within the TME.

In addition to inhibiting BTK, ibrutinib was active against IL-2-inducible kinase (ITK) at clinically achievable concentrations.[239] ITK is a member of the TEC-kinase family expressed in T-lymphocytes and NK cells, and is an essential component for signalling from the T-cell receptor.[240] By irreversibly inhibiting the activity of ITK, ibrutinib drives a T-lymphocyte helper 1-selective pressure in CD4$^+$ T-lymphocyte populations, which may promote immunosurveillance of leukaemic cells.[239] Moreover, ibrutinib reduced CLL cell-mediated T-lymphocyte activation and pseudoexhaustion, as indicated by reduced surface expression of human leucocyte antigen-DR, CD39 and PD-1, along with decreased secretion of T-lymphocyte-derived cytokines.[238] As the TME plays a crucial role in CLL leukaemogenesis, further studies are needed to detail precisely how ibrutinib modulates both CLL cell behaviour and the TME, and inform the rationale design of combination therapies.

1.8.4. RESISTANCE TO BTKI IN CLL

Although durable responses are observed in the majority of R/R CLL cases, approximately 13-43% of ibrutinib recipients develop disease progression on current follow-up.[212] Two distinct types of resistant disease have been described which have important clinical implications: (i) CLL with early progression (i.e., less than 12 months of ibrutinib initiation) which is typically due to Richter transformation; and (ii) CLL with late progression (i.e., more than 12 months) which is frequently associated with *BTK* and *PLCγ2* mutations.[241–243] Treatment of Richter transformation remains largely ineffective and outcomes are dismal (median OS: 3 months).[244] In contrast, patients without transformation may be rescued by shifting to an

alternative novel therapy such as venetoclax (BCL2 inhibitor),[245] entospletinib (SYK inhibitor)[246] or idelalisib/duvelisib (PI3K inhibitors).[247,248] Mutations of *BTK* and *PLCγ2* in a real-life setting have been reported in 57% and 13% of CLL patients receiving ibrutinib, respectively.[249] Whole-exome sequencing analysis of patients with late progression demonstrated an acquired cysteine-to-serine mutation in BTK (*BTK*[C481S]) at the binding site of ibrutinib (Cys-481).[250,251] Several activating mutations have been described in PLCγ2, the kinase immediately downstream of BTK in the BCR signalling cascade (Figure 1.10).[250,252,253]

On a structural level, the *BTK*[C481S] mutation results in loss of covalent binding, allowing reversible instead of irreversible ibrutinib binding.[250,251] Using functional assays, Woyach *et al.*[250] showed that inhibition of recombinant BTK[C481S] by ibrutinib was 25-fold less than that of wild-type BTK, indicating that the affinity of ibrutinib for BTK is significantly decreased by the C481S mutation. Impaired BTK[C481S] inhibition by ibrutinib subsequently leads to re-activation of BCR signalling, as demonstrated by restored BTK and ERK activity at the time of disease progression, expression of BCR target genes and increased cell proliferation.[232] This increased malignant B-lymphocyte proliferation likely leads to worsening lymphadenopathy in CLL patients, and may indicate clinical disease progression. Additional BTK mutations at cysteine-481 and other residues have also been associated with ibrutinib resistance in R/R CLL cases. However, some of these variants are present at only low variant allele frequencies.[252–254]

In contrast to the *BTK*[C481] mutation, which leads to diminished BTK inhibition by ibrutinib,[250,251] *PLCγ2* mutations are all potentially gain-of function mutations, allowing the induction of PLCγ2 activity independent of BTK.[250] Thus, PLCγ2 mutations could potentially allow autonomous BCR signalling, regardless of BTK activity. BTK and *PLCγ2* can occur

concurrently[250,253] and may cause issues when selecting an alternative therapy. Ibrutinib resistance has also been attributed to deletions in short arm of chromosome 8 (in combination with driver mutations),[252] gain of the short arm of chromosome 2,[255] and clonal evolution of residual CLL cells maintaining competent PI3K/ART/ERK signalling pathways under ibrutinib, in addition to BTK-independent non-conical NF-κB signalling.[256]

1.8.5. RHOA/ROCK AND ROCK INHIBITION

Contraction of the cell body and focal adhesion are highly dependent on actomyosin contractility.[257] Stress fibre assembly and contraction of the cytoskeleton, which are both controlled by myosin II, are predominantly mediated by the GTPase RhoA and its key downstream effectors, protein kinases of the ROCK family.[258] RhoA-activated ROCK increases myosin-based contractility both by inactivating myosin light chain (MLC) phosphatase through phosphorylation and by directly phosphorylating MLC.[259] ROCK is believed to mediate bundling of F-actin filaments and clustering of extracellular matrix (ECM)-ligated integrins, via this increased contractility, to produce stress fibres and focal adhesions.[260]

In addition to regulating cytoskeletal contractility, the RhoA/ROCK signalling pathway plays an important role in permitting effective cell migration.[257,261] Cellular transmigration is crucial for development, immune responses, and wound healing[261] as well as tumour cell invasion and metastasis.[262–266] Proper cell movement is elicited by dynamic reorganisation of the cortical cytoskeleton; specifically, polymerisation and assembly of a mesh-like actin network at the leading edge and RhoA/ROCK-mediated actin bundling and actomyosin-based contraction at the lagging tail.[257] Inhibition of RhoA or ROCK resulted in impaired migration, but not attachment, of leucocytes[267–269] and smooth muscle cells.[270] Furthermore, monocytes treated with Y-27632, a selective ROCK inhibitor, or electroporated with C3 exoenzyme, which

specifically inhibits RhoA with little effect on other Rho family members, displayed long

unretracted tails, correlating with significantly reduced cell migration.[267] These findings

confirm the importance of the RhoA/ROCK pathway in permitting effective cellular

movement, and indicate that inhibitors of this signalling axis may be useful for suppressing

metastasis in sold tumour[262–266] and preventing trafficking of malignant lymphocytes to

lymphoid tissues in CLL.

1.8.6. ABL KINASES AND ABL INHIBITION

Abelson kinase (ABL) family nonreceptor kinases have been the focus of intense research ever

since a reciprocal translocation between chromosomes 9 and 22, generating a constitutively

active ABL mutant, was identified as the initiating oncogenic event in chronic myeloid

leukaemia.[271,272] These proteins, which include mammalian ABL1 and Abl-related gene (Arg),

coordinate several key biological processes such as development of the immune and nervous

systems, apoptosis, cell morphogenesis, and responses to genotoxic stress. However, the

most prominent and well-characterised signalling pathways that are regulated by ABL family

kinases lead to changes in the cytoskeleton and, subsequently, alterations in cell spreading

and migration. ABL family kinases activate numerous downstream effector proteins which

directly or indirectly modulate F-actin turnover, including WASP and WAVE family members,

the GTPase RAC1, haematopoietic lineage cell-specific protein, and cortactin (reviewed in

Bradley and Koleske[273]).

Following appropriate stimulation, cells rapidly initiate ABL kinase-induced actin

polymerisation at the plasma membrane generating a range of protrusive structures.[273]

Indeed, platelet-derived growth factor-treated fibroblasts deficient in ABL1 and/or Arg

displayed significantly reduced dorsal and peripheral ruffling, which was restored by re-

expression of the kinases.[274,275] Likewise, fibroblasts lacking ABL or Arg exhibited reduced generation of filopodial projections[276] and lamellipodial protrusions[277,278] during fibronectin-activated cell spreading. Additionally, *Arg*^{-/-} fibroblasts showed dramatically increased RhoA-mediated stress fibre formation leading to increased cell contractility.[279] Collectively, these studies highlight the key role of ABL family kinases in transducing diverse extracellular signals into cytoskeletal rearrangements that have profound effects on cell morphology and behaviour.

Despite being highly expressed in CLL,[280] the relevance of ABL1 to leukaemogenesis and to the maintenance of malignant B-lymphocytes is not yet well understood. ABL1 expression is crucial for normal lymphocyte development and function. This has been demonstrated by lymphopenia and splenic/thymic atrophy in *ABL1*^{-/-} mice,[281,282] in addition to defective actin polymerisation and lamellipodial spreading at the IS during T-lymphocyte activation in *ABL1* knockout murine models.[283] Interestingly, the ABL1-inhibitor imatinib impaired chemokine-independent CLL cell migration *in vitro* and markedly reduced cytoskeleton polarisation.[165] Furthermore, imatinib sensitised CLL cells to the cytotoxic effect of chlorambucil at clinically achievable concentrations.[284] Elucidating how ABL family kinases regulate cytoskeletal changes and, consequently, CLL cell behaviour and survival is highly relevant to the development of novel therapeutic strategies.

1.9. SUMMARY OF INTRODUCTION AND AIMS OF THESIS

CLL is a currently incurable lymphoproliferative disorder of mature B-lymphocytes. It is well established that interactions within the TME, facilitated through BCR- and chemokine-controlled reorganisation of the cytoskeleton, play a major role in the homing, proliferation, survival, and drug resistance of CLL cells. Small molecule inhibitors which interfere with the

migration and adhesion of leukaemic cells, particularly the BTKi ibrutinib, have emerged as highly effective therapies in TN and multiple R/R patients with CLL. However, less durable responses are seen in high risk patients with CLL. The PFS of patients with del(17p) and del(11q) was 26 months and 51 months, respectively.[222] Furthermore, the exact mechanism of action(s) of ibrutinib and related signal-inhibitory drugs remains unclear. A more detailed understanding of the role of the cytoskeleton in CLL pathogenesis and treatment responses, gained by evaluating, developing, and implementing tools by which behavioural alterations can be quantitatively assessed, may, therefore, have substantial importance to inform new therapeutic interventions or combinational therapies.

This thesis will build upon the previous work of the Plymouth University Haematology Research Group, UK, and will explore the function of cytoskeletal structures within the TME. Specifically, this work will evaluate the effects of therapeutic interventions, particularly the BTKi ibrutinib, on the behaviour and cytoskeletal adaptations of leukaemic cells within two-dimensional (2D) and three-dimensional (3D) culture systems. Inhibitors of ABL1 and ROCK will also be employed as they provide well-characterised, contrasting effects on the cortical cytoskeleton. Impaired ABL1 signalling typically prevents extension of the cytoskeleton,[165] whereas disruption of the RhoA/ROCK pathway leads to the accumulation of long unretracted processes.[267] Thus, these signal inhibitors will be useful positive/negative controls during the optimisation and selection of tools to evaluate CLL cytoskeletal changes. In addition, they may provide insight into the pathways underlying the morphological responses of neoplastic lymphocytes treated with BTKi or NOTCH1 inhibitors. Furthermore, due to a lack of representative immortalised CLL cells, the MCL cell lines REC-1 (BTKi-sensitive; *NOTCH1*-mutated) and G519 (BTKi-resistant; *NOTCH1*-unmutated) will be utilised as a surrogate model

to explore the effects of BTKi sensitivity or *NOTCH1* mutational status on behavioural responses induced by signal inhibition (discussed in Chapters 4 and 6, respectively). Specifically, the aims of this thesis were:

- To evaluate, develop, and apply tools for the quantitative assessment of cytoskeletal changes in neoplastic B-lymphocytes.

- To use optimised tools to explore key elements of the morphological response of CLL cells to small molecule inhibitors, linking cytoskeletal changes to alterations in migration and homotypic cellular interactions within 2D culture systems.

- To compare the morphological and behaviour responses of prognostically relevant subgroups of CLL, with particular focus on *IGHV*-mutated and *IGHV*-unmutated CLL cases.

- To develop a 3D *ex vivo* culture system that reflects the CLL TME and can be combined with high resolution microscopy for the study of CLL morphology and protein localisation.

- To assess the role of NOTCH1 in mediating cytoskeletal responses of neoplastic B-lymphocytes in 2D and 3D culture systems.

CHAPTER 2 – MATERIALS AND METHODS

2.1. REAGENTS AND BUFFERS

2.1.1. CELL CULTURE

Complete culture media

50 millilitres (mL) of foetal bovine serum (FBS; 16140071, Gibco™) and 5mL of penicillin-streptomycin (10,000 units/mL; 15140122, Gibco™) added into 445mL of RPMI 1640 growth media with GLUTAMAX™ (61870044, Gibco™).

Freezing media [90% (v/v) FBS, 10% (v/v) dimethyl sulphoxide (DMSO)]

2mL of DMSO (25-950-CQC, Corning™) added into 18mL of FBS (10500064, Gibco™).

1X Phosphate buffered saline (PBS)

1 tablet of PBS (12821680, Fisher BioReagents™) dissolved in 100mL of deionised water (dH$_2$O).

1X Trypsin-ethylenediaminetetraacetic acid (EDTA)

5mL of 10X trypsin-EDTA [0.5% trypsin, 5.3 millimolar (mM) EDTA 4Na (sodium); 15400054, Gibco™] diluted with 45mL of sterile 1X PBS.

100mM EDTA solution

1.86 grams (g) of EDTA disodium salt dihydrate (E/P140/48, Fisher Chemical™) dissolved in 40mL of dH$_2$O and pH adjusted to 7.4 with sodium hydroxide (NaOH). Total volume brought up to 50mL with dH$_2$O.

10% (v/v) Triton X-100 solution

500 microlitres (µL) of Triton™ X-100 (T8787, Sigma-Aldrich) added into 4.5mL of dH$_2$O.

Radioimmunoprecipitation assay buffer (RIPA) lysis buffer [20mM Tris, 150mM sodium chloride (NaCl), 1mM EDTA, 1% (v/v) Triton X-100]

790mg of Tris base (T1503, Sigma-Aldrich) and 900mg of NaCl dissolved in 75mL of dH$_2$O, and pH adjusted to 7.4 with concentrated hydrochloric acid (HCl). Ten millilitres of 10% Triton X-100 solution, 2.5mL sodium deoxycholate and 1mL of 100mM EDTA added into the solution. Total volume brought up to 100mL with dH$_2$O. Protease (P8340, Sigma-Aldrich) and phosphates (P5726, Sigma-Aldrich) inhibitors added at 10μL/mL before use.

1 molar (M) Tris-HCl, pH 8.0

12.11g of Tris base dissolved in 70mL of dH$_2$O and pH adjusted to 8.0 with concentrated HCl. Total volume brought up to 100mL with dH$_2$O.

3M NaCl

17.53g of NaCl dissolved in 70g of dH$_2$O. Total volume brought up to 100mL with dH$_2$O.

Low stringency lysis buffer [10mM Tris, 0.14M NaCl, 0.5% (v/v) Triton X-100]

1mL of 10% Triton X-100 solution, 0.2mL of 1M Tris-HCL (pH 8.0) and 0.93mL 3M NaCl added into a 50mL falcon tube. Total volume brought up to 20mL with dH$_2$O. Protease and phosphates inhibitors added at 10μL/mL before use.

2.1.2. IMMUNOCYTOFLUORESCENCE

Fixation buffer [4% (w/v) paraformaldehyde (PFH)]

0.4g of PFH (P/0840/53, Fisher Chemical) dissolved in 9.6mL of 1X PBS at 60°C. Stored at -20°C once dissolved.

Permeabilisation Buffers [0.1% or 0.2% (v/v) Triton X-100]

0.1% Triton X-100: 10μL of Triton X-100 added into 9990μL of 1X PBS.

0.2% Triton X-100: 20µL of Triton X-100 added into 9980µL of 1X PBS.

Blocking solution [1% (w/v) bovine serum albumin (BSA)]

0.1g of BSA (BP9701-100, Fisher BioReagents™) dissolved in 10mL of 1X PBS.

2.1.3. 1D SDS-PAGE, WESTERN BLOTTING AND IMMUNOHYBRIDISATION

10% (w/v) Sodium dodecyl sulphate (SDS) solution

10g of SDS (BP166-5, Fisher Bioreagents™) dissolved into 90mL of dH_2O.

10% (w/v) Ammonium persulphate (APS) solution

100mg of APS (A3678, Sigma-Aldrich) dissolved into 1mL of dH_2O. Stored at -20°C once dissolved.

1.5M Tris-HCL, pH 8.8

18.17g of Tris base dissolved in 70mL of dH_2O and pH adjusted to 8.8 with concentrated HCl. Total volume brought up to 100mL with dH_2O.

0.5M Tris-HCL, pH 6.8

6g of Tris base dissolved in 60mL of dH_2O and pH adjusted to 6.8 with concentrated HCl. Total volume brought up to 100mL with dH_2O.

10X Tris buffer (0.24M Tris, 1.91M glycine)

30.2g of Tris base and 144g of glycine dissolved in 800mL of dH_2O. Total volume brought up to 100mL with dH_2O.

10X Tris buffered saline (TBS), pH 7.6

24.2g of Tris base and 80.06g of NaCl dissolved in 800mL of dH_2O and pH adjusted to 7.6 with concentrated HCl. Total volume brought up to 100mL with dH_2O.

1X Running buffer [24mM Tris-HCL, 191mM Glycine, 0.1% (w/v) SDS]

100mL of 10X Tris buffer diluted with 890mL of dH₂O. Total volume brought up to 1000mL with 10% SDS solution and pH adjusted to 8.3 with concentrated HCl.

1X Transfer buffer [24mM Tris-HCl, 191mM Glycine, 20% (v/v) methanol]

100mL of 10X Tris buffer diluted with 700mL of dH₂O. Total volume brought up to 1000mL with 100% methanol and pH adjusted to 8.3 with concentrated HCl.

0.5% (w/v) Bromophenol blue

0.05g of bromophenol blue (B0126, Sigma-Aldrich) dissolved in 10mL of dH₂0.

Laemmli sample buffer (SDS reducing buffer)

Depending on the concentration of protein obtained during cell lysis, lysates were diluted 1 in 2 or 1 in 5 with 2% or 5% Laemmli sample buffer, respectively (Table 2.1).

Table 2.1: Composition of 2% and 5% Laemmli sample buffers

Reagent	Volume used (mL)	
	2% buffer*	5% buffer†
dH₂O	3.55	1.80
0.5M Tris-HCL, pH 6.8	1.25	2.50
10% SDS solution	2.00	2.00
Glycerol	2.50	2.50
0.5% Bromophenol blue	0.20	0.20

*Before use 5% (v/v) of β-mercaptoethanol (β-ME; M3148, Sigma-Aldrich) was added to the desired volume of 2% Laemmli sample buffer.

†Before use 10% (v/v) of β-ME was added to the desired volume of 5% Laemmli sample buffer.

Wash buffers

1X TBS: 10mL of 10X TBS (pH 7.6) added into 90mL of dH$_2$O.

1X TBST: 100mL of 10X TBS (pH 7.6) and 1mL of Tween-20 (P9416, Sigma-Aldrich) added into 900mL of dH$_2$O.

Blocking buffer and antibody dilution buffer

5% (w/v) BSA in 1X TBST: 1g of BSA added into 20mL of 1X TBST.

5% (w/v) non-fat dry milk powder in 1xTBST: 1g of non-fat milk powder (M7409, Sigma-Aldrich) added into 20mL of 1X TBST.

Resolving gels

Gels containing varying acrylamide/bis-acrylamide concentrations were used to yield the optimal separation and resolution of the proteins of interest (Table 2.2).

Table 2.2: Composition of acrylamide/bis-acrylamide resolving gels

Reagent	Volume used (mL)*	
	7% gel	**12% gel**
dH$_2$O	15	10
Acrylamide/bis-acrylamide 37.5:1, 30% solution[†]	7	12
1.5M Tris, pH 8.8	7.5	7.5
10% SDS solution	0.3	0.3
10% APS solution	0.15	0.15
TEMED[‡]	0.015	0.015

* Total volume of all reagents: 20mL (2 gels).

[†] Acrylamide/bis-acrylamide 37.5:1, 30% solution (J61505.AP, Alfa Aesar™).

[‡] TEMED (*N, N, N', N'*-Tetramethylethylenediamine; T9281, Sigma-Aldrich).

Stacking Gel

4% stacking gels were used throughout this study (Table 2.3).

Table 2.3: Composition of 4% acrylamide/bis-acrylamide stacking gels

Reagent	Volume used (mL)*
dH$_2$O	4.02
Acrylamide/bis-acrylamide 37.5:1, 30% solution	0.870
0.5M Tris, pH 8.8	1.670
10% SDS solution	0.667
10% APS solution	0.33
TEMED	0.0067

*Total volume of all reagents: 20mL (2 gels).

2.1.4. SCANNING ELECTRON MICROSCOPY

0.1M Cacodylate buffer, pH 7.2

10.7g of Na cacodylate dissolved in 250mL of dH$_2$O and pH adjusted to 7.2 with concentrated HCl. Total volume brought up to 500mL with dH$_2$O.

Scanning electron microscopy (SEM) fixative solution [2.5% (v/v) glutaraldehyde in 0.1 M cacodylate buffer, pH 7.2]

2.5mL of glutaraldehyde (BP2548-1, Fisher BioReagents™) added into 50mL of 0.1 M cacodylate buffer. Total volume brought up to 100mL with 0.1 M cacodylate buffer.

2.1.5. MASS SPECTROMETRY

50mM Ammonium bicarbonate (ABC)

200mg of ABC (09830, Sigma-Aldrich) dissolved in 50mL of high-performance liquid chromatography (HPLC) grade water. Prepared fresh and remaining solution discarded.

Reduction buffer (10mM dithiothreitol)

7.7mg of dithiothreitol (D9779, Sigma-Aldrich) dissolved in 5mL of HPLC grade water. Prepared fresh and remaining solution discarded.

Alkylation buffer (50mM 2-chloroacetamide)

23.35mg of 2-chloroacetamide (C0267, Sigma-Aldrich) dissolved in 5mL of 50mM ABC and store in the dark. Prepared fresh and remaining solution discarded

2% (v/v) Trifluoroacetic acid (TFA)

1mL of TFA (T/3258/PB05, Fisher Chemical) diluted in 49mL of HPLC grade water.

Buffer A [0.5% (v/v) acetic acid, 1% (v/v) TFA]

40mL of HPLC grade water, 250µL of acetic acid (A/0406/PB08, Fischer Chemical) and 500µL of TFA added to a 50mL falcon tube and the total volume brought up to 50mL with HPLC grade water.

Buffer B [80% (v/v) acetonitrile, 0.5% (v/v) acetic acid, 1% TFA]

40mL of acetonitrile (A/0626/17, Fischer Chemical), 250µL of acetic acid and 500µL of TFA added to a 50mL falcon tube and the total volume brought up to 50mL with HPLC grade water.

Digestion buffer [12.5 nanograms (ng)/µL trypsin]

1 vial of trypsin (20µg; V5111, Promega) dissolved in 1.6mL of 50mM ABC. Prepared fresh and remaining solution discarded.

2.1.6. GENOMIC DNA EXTRACTION, AGAROSE GEL ELECTROPHORESIS AND DNA PURIFICATION FOR SEQUECNING

QIAGEN® Protease stock solution*

1 vial of lyophilised QIAGEN® Protease dissolved in 1.2mL of protease solvent.

Buffer AL*

Lysis buffer containing chaotropic salt (guanidine hydrochloride). Mixed thoroughly by inverting before use.

Buffer AW1*

Wash buffer containing chaotropic salt (guanidine hydrochloride) and supplied as concentrate. Diluted with 25mL of ethanol (96-100%) before use.

Buffer AW2*

Wash buffer supplied as concentrate and diluted with 30mL of ethanol (96-100%) before use.

[*All provided in the QIAamp® DNA Blood Mini Kit (51104, Qiagen)]

1X Tris borate EDTA (TBE)

100mL of 10X TBE (B52, Thermo Fisher) added into 900mL of dH$_2$O.

2% (w/v) Agarose gel

3g of agarose (12841680, Fisher Bioreagents) dissolved in 150mL of 1X TBE with heat. Once cooled to approximately 50°C, 3µL of X10,000 GelRed® Nucleic Acid Gel Stain (1 in 50,000 dilution; 41003, Biotium) was added.

DNA loading dye

6X DNA loading dye buffer containing SDS (B7024S, New England Biolabs).

Monarch® gel dissolving buffer†

Gel dissolving buffer supplied at the recommended working concentration.

Monarch® DNA wash buffer†

Wash buffer supplied as concentrate and diluted with 20mL of ethanol (96-100%) before use.

[†All provided in the Monarch® DNA Gel Extraction Kit (T1020, New England Biolabs)]

2.2. CELL AND GENERAL CULTURE

PB samples from patients fulfilling standard diagnostic and immunophenotypic criteria for CLL[6,285] were collected by the Haematology medical staff at University Hospitals Plymouth NHS trust (Plymouth, UK). Informed consent for all samples used in this study was obtained (Integrated Research Application System project ID number: 145245) in accordance with the regulatory approval granted by the NHS Health Research Authority National Research Ethics Service Committee East of England – Cambridge East.

The human MCL cell line Granta-519 (G519) was purchased from Deutsche Sammlung von Mikroorganismen und Zellkulturen GmbH (DSMZ) (Braunschweig, Germany). The human MCL cell line REC-1 was a kind gift from Martin Dyer (Leicester University, UK). MCL is a mature B-lymphocyte chronic lymphoproliferative disorder. The REC-1 cell line was chosen due to it representing an excellent model to assess responses to the TME, BTKi sensitivity and BCR stimulation. In contrast, G519 cells are resistant to BTKi.[286] The characteristics of the selected MCL cell lines are summaries in Table 2.4.

The human T-ALL cell line JURKAT (ACC 282) was purchased from DSMZ. The JURKAT cell line does not exhibit activating mutations of *NOTCH1* (i.e., wild-type); however, it has been shown

to produce high levels of N-ICD compared to other T-ALL cells lines and is resistant to GSI treatment.[287]

Primary cells and cell lines were all cultured in complete culture media (section 2.1.1) and maintained in a humidified incubator at 37°C with 5% carbon dioxide (CO_2).

Table 2.4: Characteristics of MCL cell lines used in this study.

Cell line	Origin	Diagnosis	Exhibits the t(11;14) translocation?*	Expresses CCND1/cyclin D1?
G519	PB	High-grade B-lymphocyte non-Hodgkin lymphoma (NHL) (leukaemic transformation of MCL, stage IV)	Yes	Yes
REC-1	Lymph node/PB	B-lymphocyte NHL (diffuse large cell progressing to transformed MCL, blastoid variant)	Yes	Yes

*The characteristic hallmark of MCL is the oncogenic t(11;14)(q13;q32) translocation which juxtaposes the proto-oncogene cyclin D1 gene (*CCND1*) on chromosome 11 (11q13) to the *IGHV* gene on chromosome 14 (14q32), resulting in overexpression of cyclin D1.[288,289]

2.2.1. PERIPHERAL BLOOD MONONUCLEAR CELL ISOLATION

PB mononuclear cells (PBMCs) were isolated from EDTA whole blood samples via density-gradient centrifugation with Ficoll-Paque PLUS™ media (17-1440-02, GE Healthcare) according to the manufacturer's instructions within 12 h of collection. Briefly, blood was slowly layered onto an equal volume of Ficoll-Paque PLUS™ media in a 50mL falcon tube (Sarstedt; held at a 45° angle) and centrifuged at 400 times gravity (x*g*) for 30 min at room temperature (RT), with zero brake speed. Using a Pasteur pipette, the PBMCs were extracted

from the interface between the Ficoll-Paque PLUS™ media and plasma (Figure 2.1), and then added to a fresh 50mL falcon tube. The cells were washed with 1X PBS, and the supernatant was discarded. The cell pellet was resuspended in 10mL of complete culture media and a cell count preformed (section 2.2.4). PBMCs were either seeded at $1x10^7$ cell/ml into 24-well plates for immediate use or stored in liquid nitrogen (-196°C) (section 2.2.2).
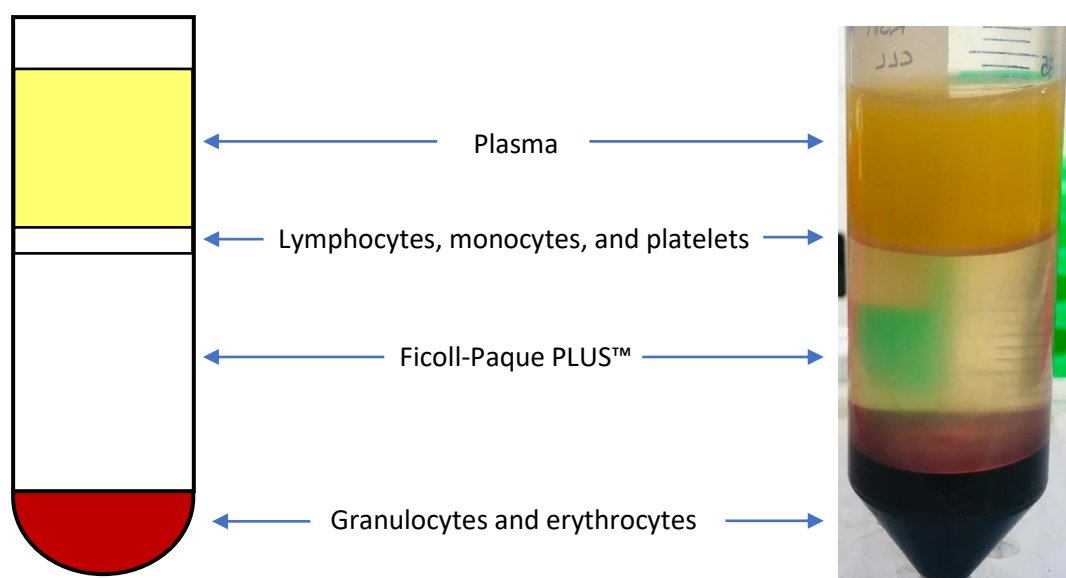
Figure 2.1: **Isolation of CLL PBMCs via density-gradient centrifugation over Ficoll-Paque PLUS™ media.**

2.2.2. CELLULAR CRYOPRESERVATION

Cell lines and primary PBMCs were centrifuged at 200x*g* for 5 min at RT and the cell pellets re-suspended in 1mL of freezing media (section 2.1.1). For cell lines, $5x10^6$ cells were aliquoted into 2mL CryoPure tubes. For primary PBMCs, $2x10^7$, $5x10^7$, and $1x10^8$ cells were aliquoted into 2mL CryoPure tubes. Cells were frozen gradually (1°C per min) to -80°C in a

cryopreservation container filled with isopropyl alcohol and then stored in liquid nitrogen (-196°C) for future use. Cell pellets were prepared at $1x10^8$ and $2x10^7$ for protein assays and were 'snap' frozen at -80°C.

Cryopreserved PBMCs were thawed from liquid nitrogen in a 37°C water bath and transferred to a 50mL falcon tube. To remove the DMSO, 9mL of pre-warmed complete culture media was slowly added to the 1mL of cells and centrifuged at 200xg for 5 min at RT. The supernatant was discarded, and the cell pellet re-suspended in 1mL of complete culture media. The cell suspension was made up to 5mL with complete culture media and transferred to a $25cm^2$ vented flat-bottom culture flasks.

2.2.3. CULTURE OF CELL LINES

MCL cell lines (G519 and REC-1) and JURKAT cells were grown in $25cm^2$ or 75^2 vented flat-bottom culture flasks. Cells were passaged 2-3 times per week depending on their doubling times, to maintain optimal cell density. After 28 culture passages, the cells were discarded, and fresh aliquots obtained from liquid nitrogen[286] (section 2.2.2) to minimise passage-dependent effects, particularly the development of considerable genomic instability and, consequently, phenotypic and genotypic heterogeneity.[290–292]

2.2.4. ASSESSMENT OF CELL NUMBER

A cell count was performed by adding 40µL of cell suspension to an equal volume of 0.4% trypan blue solution (15250061, Gibco™). Ten microliters of the cell/trypan blue solution was then loaded onto a dual-chamber cell counting slide (1450011, Bio-Rad) and the number of viable cells determined using the TC20™ automated cell counter (1450102, Bio-Rad), according to the manufacturer's instructions.

2.3. ASSESSMENT OF CELL SHAPE

To observe changes in the shape of neoplastic cells, three techniques were utilised: cytoskeletal staining, plasma membrane staining and SEM. Cell adhesion was enhanced by coating coverslips with fibronectin – a multifunctional, extracellular matrix glycoprotein present in many tissues, including the lymph nodes, spleen and vascular endothelium (reviewed in Pankov and Yamada[293]). All experiments described used fibronectin-coated coverslips (section 2.3.1).

2.3.1. COATING COVERSLIPS WITH FIBRONECTIN

Sterile coverslips (13mm diameter; MIC3336, Scientific Laboratory Supplies) were placed into a 24-well plate (Sarstedt) and coated with 100µL of fibronectin (F2006, Sigma-Aldrich) [1000µg/ml stock diluted to 40µg/ml with sterile 1X Hank's balanced salt solution (HBSS; 14175046, Gibco™)] at 4°C overnight. The fibronectin was removed and $1x10^6$ cells in 1mL of RPMI media (no FBS or antibiotics added) was placed onto each coverslip. Cells were allowed to adhere for up to 4 h at 37°C with 5% CO_2.

2.3.2. FIXING CELLS WITH PARAFORMALDEHYDE

The media was removed from the 24-well plate and 500µL of 4% PFH (section 2.1.2) added to each coverslip. The cells were fixed at RT for 15 min and then washed with 1X PBS three times for 5 min each.

2.3.3. CYTOSKELETAL STAINING: F-ACTIN

Adhered cells were fixed using PFH (section 2.3.2) and permeabilised for 5 min at RT using 200µL of 0.1% Triton-X (section 2.1.2). The coverslips were washed twice for 5 min with 1X PBS and then blocked for 30 min at RT using blocking solution (section 2.1.2). The blocking

solution was removed and 5µL of Texas-Red™-X Phalloidin (T7471, Invitrogen™) (diluted into 200µL of fresh blocking solution) was added to each coverslip. The coverslips were incubated in the dark at RT for 20 min and then washed, air-dried, and mounted onto glass slides (section 2.3.7).

2.3.4. CYTOSKELETAL STAINING: VIMENTIN

Adhered cells were fixed using PFH (section 2.3.2) and permeabilised for 5 min at RT using 200µL of 0.2% Triton-X (section 2.1.2). The coverslips were washed twice for 5 min with 1X PBS and then blocked for 1 h at RT using blocking solution (section 2.1.2). The blocking solution was removed, and the coverslips washed once in 1X PBS for 5 min. The coverslips were incubated with the anti-vimentin antibody (ab92547, Abcam) (1 in 500 dilution in fresh blocking solution) at 4°C overnight. Coverslips were washed twice for 5 min with 1X PBS then incubated with the Alexa Fluro 488 antibody (ab150077, Abcam) (1 in 1000 dilution in fresh blocking solution) for 30 min at RT in the dark. The coverslips were then washed, air-dried, and mounted onto glass slides (section 2.3.7).

2.3.5. IMMUNOFLUORESCENCE DOUBLE STAINING: F-ACTIN AND VIMENTIN

For double immunofluorescence staining of both vimentin and F-actin, the staining was carried out as stated in section 2.3.4 with the following exception: 5µL of Texas-Red™-X Phalloidin (diluted into 200µL of fresh blocking solution) was added to each coverslip 10 min into the 30 min incubation with the Alexa Fluro 488 antibody. The coverslips were then washed, air-dried, and mounted onto glass slides (section 2.3.7).

2.3.6. STAINING PLASMA MEMBRANE COMPONENTS

Adhered cells were fixed using PFH (section 2.3.2) and the coverslips blocked for 1 h at RT using blocking solution (section 2.1.2). Following a wash for 5 min with 1X PBS, the coverslips

were incubated with fluorescein isothiocyanate (FITC)-conjugated CD20 (PN IM1456, Beckman Coulter) and CD45 (A07782, Beckman Coulter), and phycoerythrin (PE)-conjugated CD40 (PN IM1936U, Beckman Coulter) monoclonal antibodies (1 in 100 dilution in blocking solution) for 20 min at RT in the dark. The coverslips were then washed, air-dried, and mounted onto glass slides (section 2.3.7).

2.3.7. MOUNTING COVERSLIPS

Coverslips were washed quickly twice with 1X PBS and once with dH_2O. Following air-drying overnight at RT, the coverslips were mounted onto glass slides using 10µL of ProLong Gold Antifade Mountant with DAPI (4',6-diamidino-2-phenylindole; P36966, Molecular Probes™) and cured overnight in the dark at RT. The edges of the coverslips were sealed with a thin layer of nail polish and the slides stored at 4°C.

2.3.8. FLUORESCENT MICROSCOPY

Fluorescent staining was observed on a Leica TCS SPE Confocal Microscope using the LAS X software (version 3.1.2.16221). Images were acquired using a HC PL APO oil x63/1.30 objective on a 2048x2048 pixel resolution format and images were saved in a .lif file format. Six focal planes (also known as a Z-stack) were collected for each image and merged to create a maximum intensity projection image. Three laser wavelengths were used for signal capture: a 405nm violet laser for DAPI signal; a 488nm blue laser for Alex Fluor 488, FITC and PE signal; and a 561nm green laser for Texas- Red-X signal.

2.3.9. *IN VITRO* DRUG TREATMENTS

To observe changes in cell shape in response to clinically relevant small molecule inhibitors, CLL cells were treated with 100nm and 1µM ibrutinib, 20µM Y-27632 2HCL (a selective ROCK1 inhibitor) and 10µM imatinib mesylate (an inhibitor of ABL) for 30 min, 1 h or 4 h. Cells were

treated with 10µM R04929097 and 1µM PF-03084014 for 72 h. Drug concentrations were based on published work[88,294–297] and previous work conducted by the Haematology Research Group (University of Plymouth, UK; unpublished work). Following incubation, the treated cells were processed for analysis by SEM (section 2.3.10) or analysis of cellular interactions (section 2.4).

2.3.10. SCANNING ELECTRON MICROSCOPY

Adhered cells were fixed in approximately 500µL of pre-warmed (37°C) standard SEM fixative solution (section 2.1.4) for 1-2 h at RT. The coverslips were washed in 1X PBS three times for 5 min and the cells dehydrated through an ethanol series, beginning with 30% and changing to solutions of 50%, 70%, 90% and two times 100%. Coverslips were left in each ethanol change for 10 min. The dehydrated coverslips were dried in a critical point dryer and mounted (off centre) on metal stubs using double sided sticky pads. A small amount of silver paint was placed onto the edges of the coverslips and left to dry completely. The coverslips were sputter coated with either 1-2 nanometre (nm) of chromium or 5nm of gold. Processed samples were viewed with a JEOL 7001 F SEM with an accelerating voltage of 15 kilovolts (kV) and images captured using the supporting software. Images were saved in a .tif file format.

2.3.11. IMAGE ANALYSIS USING IMAGEJ

Images acquired using the Leica SPE confocal microscope and SEM were analysed using ImageJ 2.0.0 software. Using ImageJ, .lif files were split into three channels: blue (DAPI staining), green (Alex Fluro 488 and FITC) and red (Texas-Red-X and PE). Using the 'threshold' tool, the red and green channels were then segmented into features of interest and background by setting lower and upper threshold values. Features of interest were displayed in black and the background in white, generating a binary image. The threshold values of

greyscale SEM images were set directly after converting images into an 8-bit format. Using the 'ROI Manger' tool, single cells were selected, and their area, perimeter and circularity measured (Figure 2.2). For SEM image analyses, all single cells within six fields of view at x1000 were measured for each treatment condition.

2.3.12. STATISTICAL ANALYSIS

Data were exported to GraphPad Prism V (version 8) for statistical analysis. Frequency distribution histograms show the number of cells observed within certain ranges (bins) of values. The bin sizes were optimised for perimeter (2µm bins), circularity (0.08 bins) and area ($2µm^2$ bins) histograms to allow distinct cell populations to be identified. Exact *p*-values were calculated using the non-parametric Mann-Whitney U test for unpaired data sets. The tests were performed with a 95% confidence interval.

	Area	Perim.	Circ.
1	19.664	18.036	0.760
2	21.270	21.682	0.569
3	16.018	15.635	0.823
4	15.410	15.612	0.795
5	18.195	16.104	0.882
6	18.503	17.047	0.800
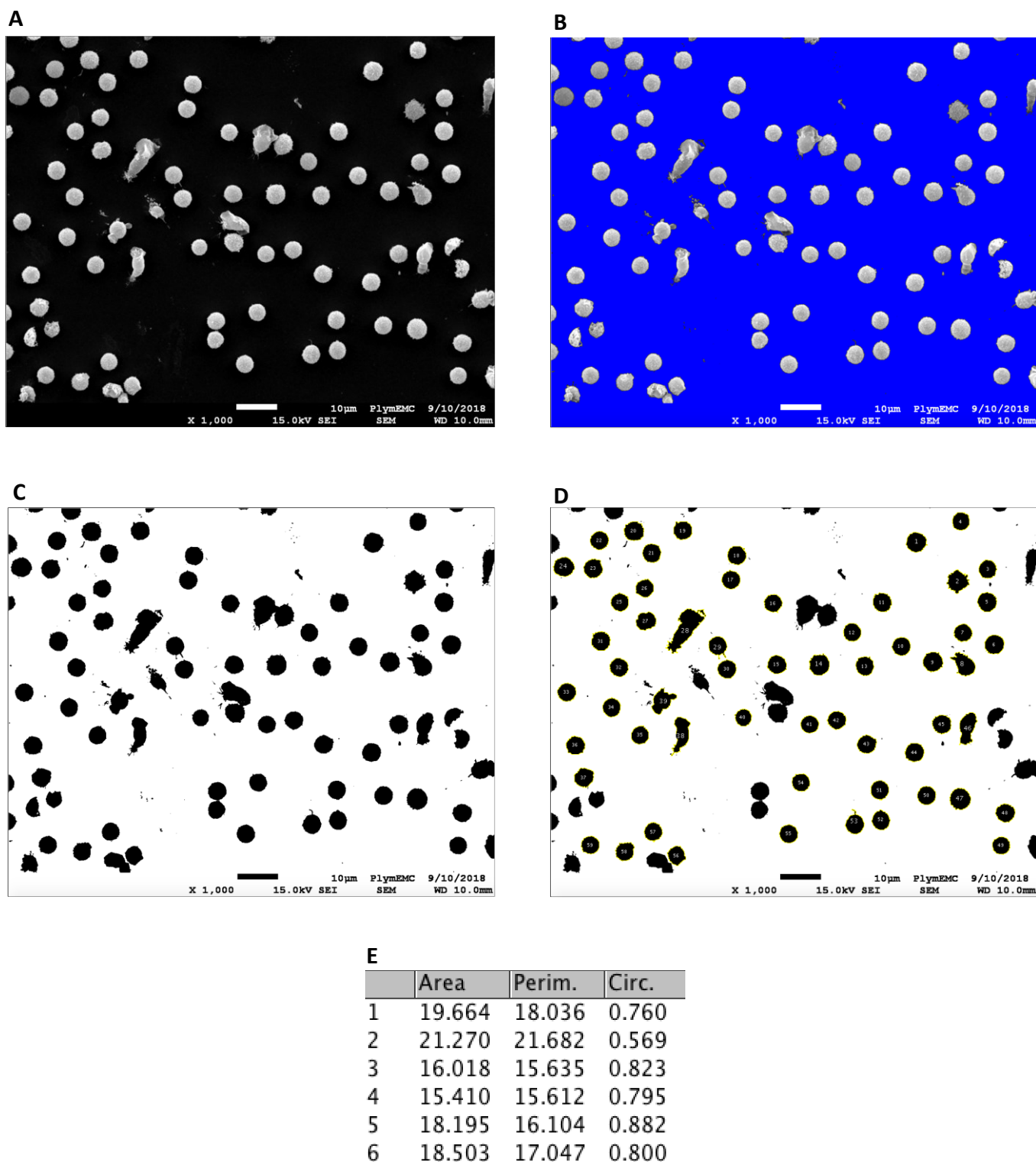
Figure 2.2: Analysis of SEM images. Using ImageJ, an 8-bit black and white SEM image (A) was converted to binary image by adjusting the threshold (B). Individual cells within the binary image (C) were then selected using the ROI Manager tool (D) and their area, perimeter and circularity measured (E). The scale was set by measuring the scale bar shown in the image.

2.4. ANALYSIS OF CELLULAR INTERACTIONS

To determine the effect of signal inhibitors on cellular interactions, the Density-Based Spatial Clustering of Applications with Noise (DBSCAN) analysis[298–300] was utilised.

2.4.1. STAINING AND IMAGING CELLS FOR CLUSTERING ANALYSIS

Cells were adhered to fibronectin-coated coverslips as described in section 2.3.1 with the following exception: $1x10^6$ cells were allowed to adhere coverslips for 1 h 37°C with 5% CO_2. Adhered cells were fixed as stated in section 2.3.2, and F-actin and vimentin stained as defined in section 2.3.5. Coverslips were mounted and cell nuclei counter stained with DAPI as described in section 2.3.7. Fluorescent staining was observed as outlined in section 2.3.8 with the following exception: images were acquired using an ACS APO 10x/0.30 dry objective on a 2048x2048 pixel resolution format and images were saved in a .lif file format.

2.4.2. IMAGE PROCESSING USING IMAGEJ

The protocol for processing images for DBSCAN analyses using ImageJ was kindly provided by Dr John Burthem (University of Manchester, UK) and was based on work by Bankhead.[301]

Using ImageJ, .lif files were split into three channels: blue (DAPI staining), green (Alex Fluro 488) and red (Texas-Red-X). Only the blue channel was needed for clustering analyses. The DAPI images were converted to 8-bit grayscale images and using the 'Brightness/Contrast' tool, adjusted to give good contrast between lymphocyte nuclei and the background.

Preparing the images for processing: Using the 'Auto threshold' tool (method: Moments; 'white objects on a white background' option selected), grayscale images were converted to black-and-white. Background signal was removed using the 'Subtract background' tool (rolling ball radius: 50 pixels; background type: sliding paraboloid) and then images converted

back to black-and-white using the 'Auto threshold' tool (method: Moments; 'white objects on a white background' option selected).

Setting the cell size criteria: A line was drawn across the diameter of a lymphocyte nuclei using the 'line' tool. This line was then estimated to be 10μm (approximate size of a lymphocyte) using the 'Set scale' tool (known distance: 10μm; pixel aspect ratio: 1; unit of length: μm; 'global' selected).

Generating a binary Image: Using the 'Invert' tool, images were converted to black cells on a white background. Clumps of cells were split into individual cells using the 'Watershed' tool; however, not all clumps were separated correctly. Cell nuclei that were clearly still joined were manually separated by using the 'line' tool and 'Delete' command to draw separating lines. Using the 'Ultimate points' tool, followed by the 'Make binary' and 'Dilate' tools, images containing single points which represented individual lymphocyte nuclei were created.

Determining the co-ordinates of each point: The 'Centre of mass' option was selected within the 'Set measurement' tool. The x- and y-coordinates of each of the points was determined using the 'Analyze particles' tool (show: outlines; 'display results' and 'clear results' options selected). Data were exported as .cvs files which could be directly used in R for clustering analyses.

2.4.3. DBSCAN ANALYSIS USING RSTUDIO

DBSCAN analyses were carried out using the R (version 3.6.1) and RStudio (version 1.2.1335) programs with the Dbscan[299] and tidyverse[302] packages. The protocol for performing DBSCAN analyses using R and RStudio was kindly provided by Dr John Burthem (University of Manchester, UK). For clustering analyses, all single cells within three fields of view at x10

were counted for each treatment condition. DBSCAN analyses were exported as hull plots for visualisation of homotypic cellular interactions within CLL cell populations (Figure 2.3).

2.4.4. STATISTICAL ANALYSIS

Data were exported to GraphPad Prism V (version 8) for statistical analysis. Graphs show the total number of cells within clusters (cluster sizes: 1, 2, 3, 4 and 5+). Exact *p*-values for DMSO vs treatment for each case were calculated using the Chi-square test. The tests were performed with a 95% confidence interval. Error bars represent standard error of the mean.
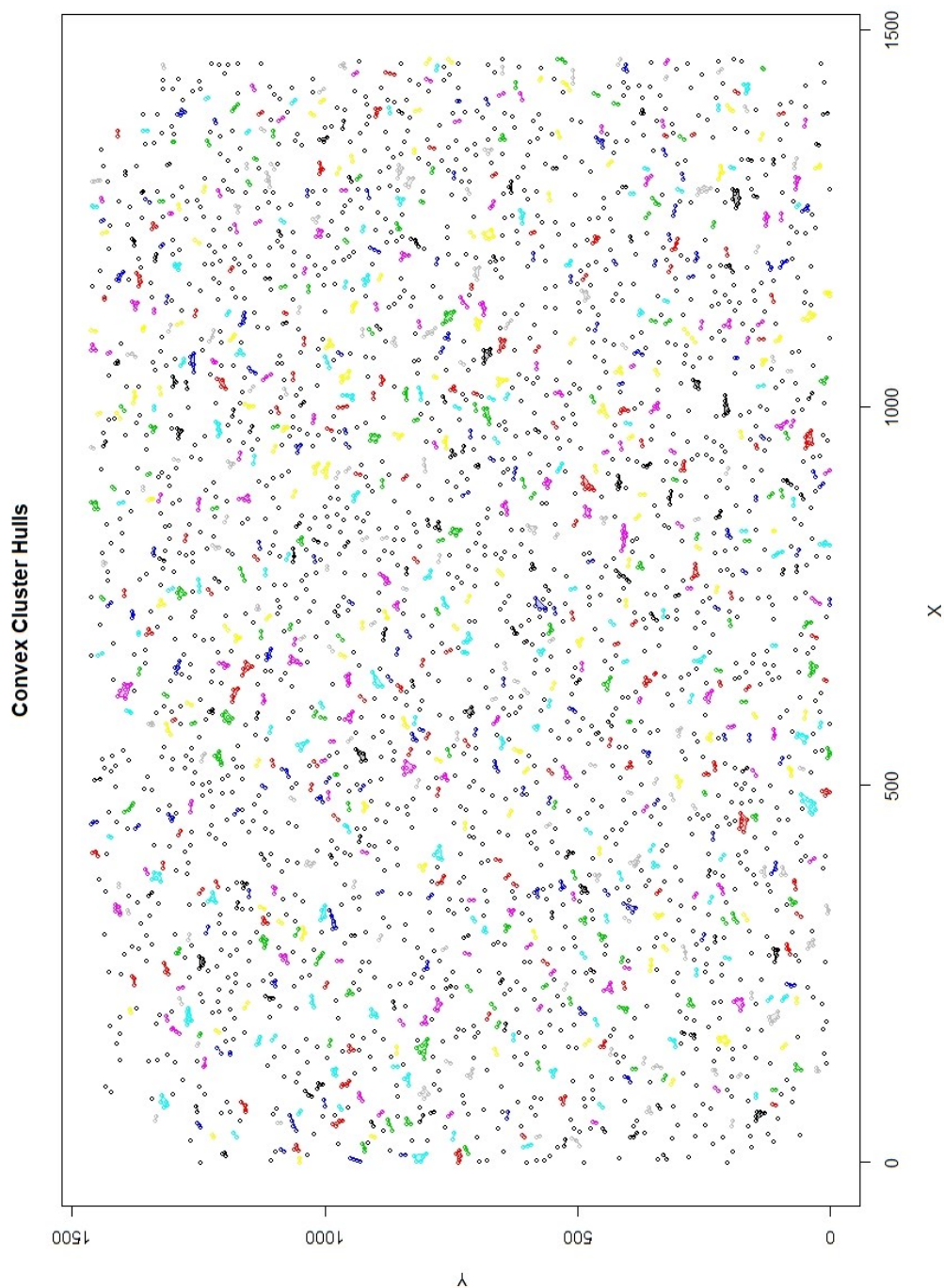
Figure 2.3: Hull plot of homotypic cellular clusters with CLL populations. To determine the effect of small molecule inhibitors on cellular interactions, the DBSCAN analysis was utilised. Results of DBSCAN analyses were exported as hull plots for visualisation of cellular clusters within untreated (control) and treated CLL populations.

2.5. TRANSWELL MIGRATION ASSAYS

To observe changes in the migration response of CLL cells to CXCL12 following treatments with clinically relevant small molecule inhibitors, the Transwell migration assay was utilised.

2.5.1. SETTING UP TRANSWELL PLATES

Prior to performing migration assays, Transwell™ Multiple Well Plates with Permeable Polycarbonate Membrane Inserts (3421, Corning™) were allowed to equilibrate according to the manufacturer's instructions. Briefly, 600µL of RPMI media (no FBS or antibiotics added) was placed into each well and 100µL of RPMI media (no FBS or antibiotics added) was placed into each Transwell insert. The plate was then incubated overnight at 37°C with 5% CO_2.

2.5.2. PERFORMING MIGRATION ASSAYS

CLL cells were pre-treated with signal inhibitors as described in section 2.3.9 with the following exceptions: $1x10^6$ cells were treated with small molecule inhibitors (DMSO, ibrutinib, Y-27632 and imatinib) for 30 min or GSIs for 72 h. Following incubation, the treated cells were centrifuged at 200xg for 5 min and the supernatant removed. The cell pellets were gently resuspended in 100µL of fresh RPMI media (no FBS or antibiotics added) containing the signal inhibitors at the appropriate concentrations (section 2.3.9). The media was removed from each well and Transwell insert. Chemokine gradients were created by adding fresh RPMI media (no FBS or antibiotics added), containing the signal inhibitors at the appropriate concentrations (section 2.3.9) and 200ng/mL CXCL12 (300-28A, Peprotech) into each well. The cells ($1x10^6$ cells in 100µL) were added into each Transwell insert. The plate was incubated for 4h at 37°C with 5% CO_2. Following incubation, the media and any cells that had migrated were removed from the wells and transferred to fresh Eppendorf tubes. The cells were centrifuged at 200xg for 5 min and the supernatant removed. The cell pellets were

resuspended in 200μL of 4% PFH (section 2.1.2), briefly vortexed and incubated at RT for 10 min. One thousand microlitres of sterile 1X PBS was then added into each Eppendorf and centrifuged at 200xg for 5 min. The supernatant was removed, and the cell pellets resuspended in 600μL of sterile 1X PBS. The fixed cells were stored at 4°C. To allow the CLL cell populations to be correctly identified during flow cytometry analyses, 5x10^6 untreated CLL cells were also fixed with 4% PFH as outlined above.

2.5.3. FLOW CYTOMETRY ANALYSIS

Transwell migration assay results were acquired using a BD Accuri™ C6 flow cytometer (Becton Dickinson) and supporting BD Accuri™ CFLow Plus software (Becton Dickinson).

For migration analyses, a 2D plot of forward/side scatter was generated and the number of events in 5 min counted (327μL) using the fast flow rate (66μL/min; 22μm core). Flow cytometry data were exported as .fcs file for analysis in FlowJo (version 10.4).

Using the FlowJo software, the viable untreated CLL cells were separately gated from dead cells within 2D plots of forward/side scatter (Figure 2.4A). These gates were then applied to all corresponding .fcs files (Figure 2.4B). The number of events within each gate was determined and multiplied by 1.83 to determine the total number of migrating cells within the 600μL of 1XPBS. This data was then normalised against the total number of migrating DMSO-treated cells to give a relative migration value for each drug treatment.
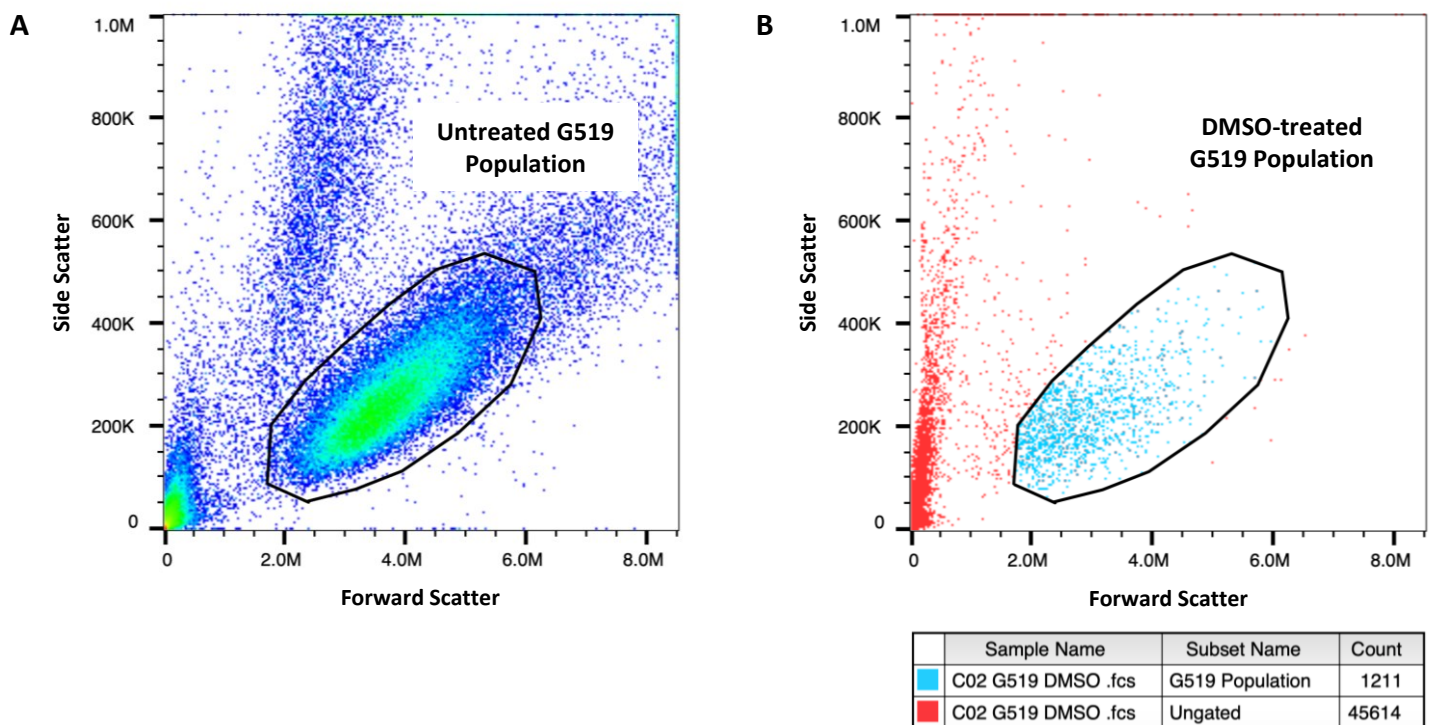
Figure 2.4: Analysis of Transwell migration assay. Using FlowJo, the viable, untreated malignant cell population was separately gated from the dead cell population in 2D plots of forward/side scatter (A). This gate was then applied to all corresponding .fcs files and allowed the number of viable migrating cells to be determined for each drug treatment (B).

2.5.4. STATISTICAL ANALYSIS

Data were exported to GraphPad Prism V (version 8) for statistical analysis. Graphs show the CXCL12-driven cell migration for each drug treatment relative to the migration of DMSO-treated cells. Exact *p*-values for DMSO vs treatment for each case were calculated using the t-test test for unpaired data sets with Welch's correction. The tests were performed with a 95% confidence interval. Error bars represent standard error of the mean.

2.6. BIOCHEMICAL ASSAYS

2.6.1. CELL LYSIS

For cell lysis two buffer were utilised: RIPA buffer and low stringency lysis buffer. RIPA buffer was used for standard protein extraction for western blot analyses, whereas low stringency lysis buffer was used to extract protein for co-immunoprecipitation (Co-IP). RIPA buffer is a higher stringency lysis buffer containing the ionic detergent SDS which denatures the protein(s) of interest and may disrupt protein-protein interactions, thus making it unsuitable for Co-IP. The low stringency lysis buffer is a non-denaturing, low-salt buffer that utilises the non-ionic detergent Triton X-100. This low stringency buffer is less likely to interfere with protein-protein interactions whilst still allowing the recovery of protein complexes with low solubility.[303]

Whole cell protein extracts were prepared by lysing snap frozen cell pellets in either RIPA buffer or low stringency lysis buffer (section 2.1.1) (100µL of lysis buffer was used per $1x10^7$ cells). The cells were incubated on ice for 30 min with brief vortexing at 10-min intervals. The lysed cells were pelleted by centrifugation at full speed at 4°C for 10 min and the supernatant containing the extracted proteins transferred to new Eppendorf tubes. The total protein concentration was quantified (section 2.6.2) and the cell lysates then stored at -20°C.

2.6.2. PROTEIN QUANTIFICATION

Total protein concentrations were estimated using the BCA (Bicinchoninic acid) Protein Assay Reagent Kit (23227, Thermo Scientific), according to the manufacturer's instructions. Briefly, one BSA ampule was diluted in a step-wise manner to create set of protein standards (ranging from 0-2000µg/mL). RIPA buffer without protease and phosphatase inhibitors added was

used as the diluent. Ten microliters of each protein standard was added in triplicate to a 96-well plate to construct a standard curve.

Cell lysates were diluted 1 in 5 and 1 in 10 in either RIPA or low stringency lysis buffer (section 2.1.1), to bring the total protein concentration within the detection range of the kit (125-2000µg/mL). Ten microliters of diluted lysate was added in duplicate to the 96-well plate. Two hundred microliters of working reagent (BCA reagent A and BCA reagent B, mixed at a ratio of 50:1) was added to each sample, including the protein standard. The plate was incubated at 37°C for 30 min and the mean absorbance values of the samples measured at 562nm using a microplate reader. The total protein concentration of each lysate was calculated using the plotted standard curve. A multiplication factor of 5 or 10 was applied to the resulting protein concentration to account for the initial 1 in 5 or 1 in 10 dilution of the lysates, respectively.

2.6.3. CO-IMMUNOPRECIPITATION

For Co-IP, $1x10^8$ cell pellets were lysed in low stringency buffer (section 2.6.1) and the total protein concentration estimated (section 2.6.2). For each immunoprecipitation, the stated quantity of protein (diluted into 200µL of low stringency buffer with inhibitors added) was used.

Prior to use, the required volume(s) of Dynabeads™ protein G (10003D, Invitrogen™) were pre-washed. Briefly, the beads were aliquoted into a 1.5mL Eppendorf tube and placed into a magnetic separator (7017S, Cell Signalling Technology). The clear buffer was removed and 500µL of low stringency lysis buffer (without inhibitors; section 2.1.1) added to each Eppendorf tube. The beads were resuspended by vortexing before being placed back into the magnetic separator. The clear buffer was removed, and the beads resuspended in 500µL of

low stringency lysis buffer. The pre-washed beads were placed into the magnetic separator and the clear buffer removed.

To eliminate any non-specific binding to the beads, a pre-clearing step was performed prior to immunoprecipitation. The diluted cell lysate was added to 20µL of pre-washed beads and incubated with rotation at 4°C for 30 min. The magnetic beads were then pulled out of solution using the magnetic separator and the pre-cleared lysate transferred to a fresh Eppendorf tube containing 20µL of pre-washed beads. This pre-clearing step was repeated three times in total.

Immunoprecipitation was performed indirectly by adding antibodies specific to the protein of interest to the pre-cleared diluted cell lysate at concentrations indicted on the data sheets and incubating with rotation overnight at 4°C. Normal rabbit IgG was added to pre-cleared diluted cell lysate (at the same final concentrations as the test antibodies) as a control. Following incubation, the lysate-antibody mixture was added to 50µL of pre-washed beads and incubated with rotation at RT for 20 min.

The lysate-antibody mixture was placed into the magnetic separator and the beads bound to the protein(s) of interest, drawn to the side of the Eppendorf tube. The post-immunoprecipitation (P-IP) fraction (i.e., remaining solution) was transferred to a new Eppendorf tube for SDS-PAGE (sodium dodecyl sulphate-polyacrylamide gel electrophoresis) analysis to ensure the immunoprecipitation had been successful. The beads were washed 5 times in 200µL of low stringency lysis buffer (without inhibitors) and finally resuspended in 30µL of 2X Laemmli buffer (section 2.1.3). The beads and P-IP fractions were stored at -20°C.

Prior to SDS-PAGE analysis, the protein complex was separated from the beads by adding 5% β-ME to each sample and heating at 95°C. The beads were pelleted by centrifugation at 14,000 revolutions per minute (rpm) and the supernatant (containing the released protein) collected.

2.6.4. GEL PREPARATION, SAMPLE LOADING AND SDS-PAGE

A fresh resolving gel was prepared (section 2.1.3) and poured into the 1.0 or 1.5mm chamber between two glass casting plates assembly in a Mini-PROTEAN® Tetra Cell Casting Module (1658021, Bio-Rad). The gel was poured up to three quarters of the taller back plate and left to polymerise for 45-60 min. The resolving gel was overlaid with 1mL of dH_2O while setting to prevent gel shrinkage. A fresh 4% stacking gel (section 2.1.3) was prepared and poured on top of the set resolving gel until it began to overflow. A 10 or 15 well comb was inserted into the chamber and the gel left to polymerise for 30-45 min. The glass plates containing the set gel were placed into a Mini-PROTEAN® Tetra Electrode Assembly (1658037, Bio-Rad). The Tetra module was placed into a gel tank and the inside of the module filled with 1X running buffer (section 2.1.3). The tank was also filled with 1X running buffer to the indicated level. The comb was removed.

Cell lysates were diluted with dH_2O into fresh Eppendorf tubes to achieve equal protein concentrations between all samples. Proteins were denatured by adding an equal volume of 2X Laemmli buffer containing 5% BME (section 2.1.3) to the diluted lysates and heating at 95°C for 5 min.

Cell lysates were loaded into individual wells of the stacking gel along with 5µL of protein standard (1610374, Bio-Rad) used as a marker to identify proteins based on their molecular weight. Cell lysates were separated at 70 volts (V) using a power pack (Bio-Rad) until the

proteins were running uniformly through the stacking gel (approximately 30 min). The voltage was then increased to 140V for 1 h so that the protein could be separated based on their molecular weight.

2.7. WESTERN BLOTTING

Following 1D SDS-PAGE, separated proteins were transferred from the gel onto polyvinylidene difluoride (PVDF) membrane (1620264, Bio-Rad). The membrane was prepared by immersing in 100% methanol until transparent (approximately 10-15 sec). The membrane was then rinsed in dH_2O and left to soak in cold 1X transfer buffer (section 2.1.3) for 20 min along with fibre pads, filter paper and the gel. The transferring apparatus was assembled as shown in Figure 2.5. The mini gel holder cassette was closed and placed inside a Mini Trans-blot central core unit (Bio-Rad) and placed inside the blotting tank. A magnetic flee was placed in the bottom of the tank and a frozen blue cooling placed inside the front of the tank. The tank was filled with 1X transfer buffer to the indicated mark and placed on a magnetic stirrer plate set to a low-medium speed. The proteins were transferred at 100V using a power pack for 90 min.

2.7.1. IMMUNOHYBRIDISATION

The membrane was rinsed briefly in 1X TBS and incubated in blocking buffer (section 2.1.3) at RT for 1 h. The membrane was washed in 1X TBST (section 2.1.3) for 10 min, then twice more for 5 min each. The membrane was then incubated with primary antibody (diluted in blocking buffer) at 4°C overnight. The membrane was washed three times in 1X TBST for 10 min each to remove non-specific binding of the primary antibody. The membrane was then incubated with a secondary antibody conjugated to horseradish peroxidase (HRP) at RT for 1

h. The membrane was washed in 1X TBST for 15 min, then twice more for 10 min each to remove non-specific binding of the secondary antibody.
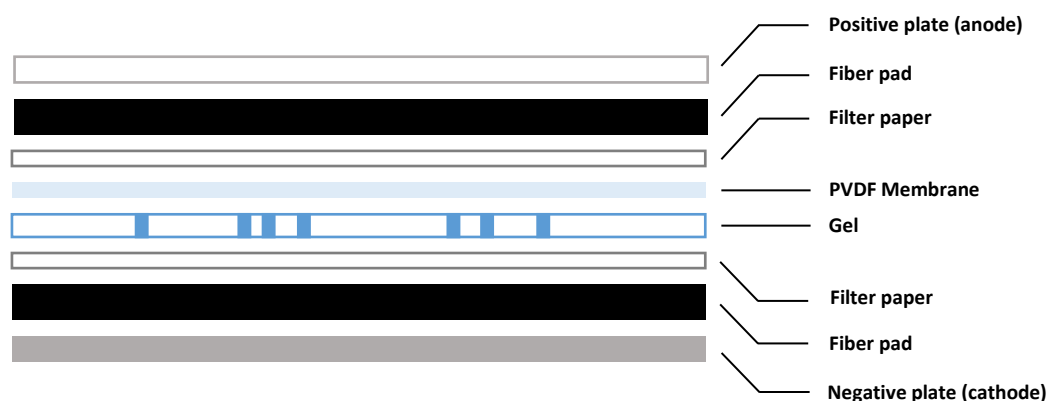
Figure 2.5: Assembly of the transferring apparatus. All transfer components were left to soak in cold 1X transfer buffer for 20 min before being assembled. A fibre pad was placed onto the negative plate of the mini gel holder cassette, followed by filter paper and the separating gel. A piece of PVDH membrane was then carefully placed onto the gel and any air bubbles removed by rolling a sterile 15mL falcon tube across the surface of the membrane. Filter paper followed by a fibre pad was then placed onto the membrane and the positive plate of the gel holder brought into position by closing the cassette.

2.7.2. DETECTION AND ANALYSIS

Protein bands were visualised by incubating the membrane with enhanced chemiluminescence™ (ECL™; RPN2106, GE Healthcare) or ECL™ prime (RPN2232, GE Healthcare) western blotting detection reagents for 1 or 5 min, respectively. The membrane was placed in an Amersham™ Hypercassette™ Autoradiography cassette (RPN11643, Cytiva) and X-ray film (34089, Thermo Scientific™) placed on top of the membrane (performed in a

dark room). The cassette was closed, and the film developed for the required length of time. The film was developed with a Compact X4 Xograph Imaging system (Xograph Healthcare Ltd.)

2.8. PREPARATION OF MASS SPECTROMETRY SAMPLES

Co-IP was performed as described in section 2.6.3. For one-dimensional electrophoretic separation, a 7% resolving gel and 4% stacking gel was prepared (section 2.1.3). To minimise contamination of the samples, the reagents used to make the gels (excluding the polymerising agents TEMED and APS) were drawn into a 20mL sterile plastic syringe (15829152, Fisherbrand™) and filtered into a sterile 50mL falcon tube through a sterile 0.2µm polyethersulfone syringe filter (15206869, Fisherbrand™). All equipment used, including falcon tubes, Eppendorf tubes, pipette tips and glass plates, was unautoclaved, and soaked in 100% methanol and left to air dry. Following the addition of the polymerising agents, the gels were poured and 1D SDS-PAGE performed as stated in section 2.6.4.

A volume of 30µL of each Co-IP sample was added to a 10 well gels as shown in the template below (Figure 2.6). Each IP sample was surrounded by wells containing only 2X Laemmli buffer (section 2.1.3) to prevent cross-contamination from other samples or the ladder when cutting. The gel was stained overnight with ProtoBlue Safe Colloidal Coomassie Blue (G-250, National Diagnostics), a mass spectrometry compatible stain. An adequate volume of stain to cover the gel was prepared by mixing ProtoBlue with 100% ethanol (9:1 ratio). Following incubation, the gel was rinsed repeatedly with dH$_2$O to remove excess stain.
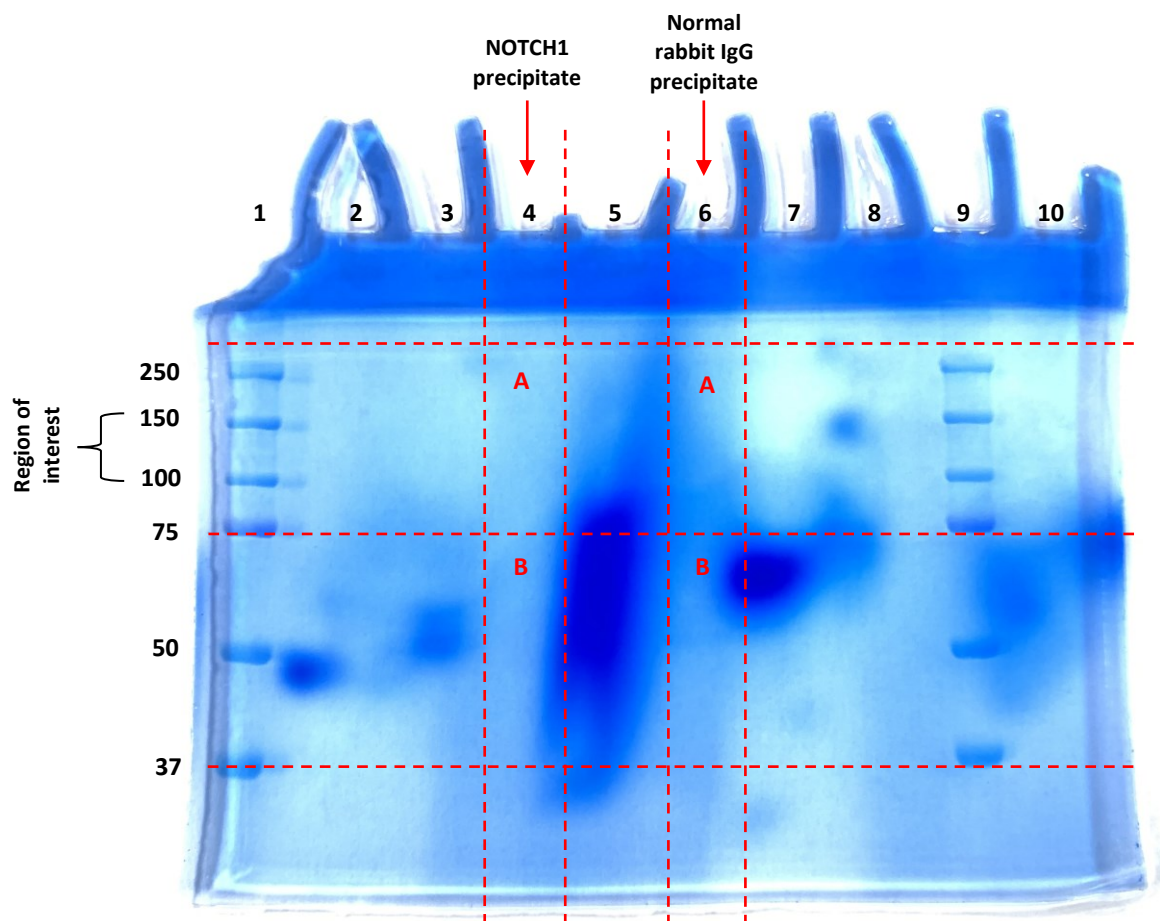
Figure 2.6: Example of a gel after separation of NOTCH1 Co-IP samples. Following separation of precipitates via electrophoresis, the agarose gel was stained overnight with ProtoBlue Safe Colloidal Coomassie Blue and cut in the approximate positions shown. Each gel segment (A or B) was then cut into smaller pieces (approximately 3mm³) and placed into a sterile, labelled Eppendorf tubes. The pieces were then processed for mass spectrometry analysis. Sections A were the regions of interest as the N-TMIC region is approximately 120kDa (kilodaltons). The Precision Plus Protein Dual Colour Standards (1610374, Bio-Rad) were included as references (Lanes 1 and 9). Lanes 2 and 3, 30µL of 2X Laemmli buffer; Lane 4, anti-NOTCH1 (D1E11) XP® primary antibody (3608, CST) precipitate; Lane 5, 30µL of 2X Laemmli buffer; Lane 6, normal rabbit IgG antibody (2729, CST) precipitate; Lanes 7, 8 and 10, 30µL of 2X Laemmli buffer.

2.8.1. BAND/LANE EXCISION

After running the Co-IP samples, the gel was transferred to the surface of a large glass plate. The wells from the stacking gel were used as a guide to identify each lane. As shown in Figure 2.6, the Co-IP lanes were cut vertically and horizontally to produce two gel segments per lane using sterile 10A surgical scalpels (0502, Swann-Morton™). A new scalpel was used for every cut. Each gel segment was then cut into cubes approximately 3mm^3 in size before being placed into a labelled Eppendorf tube.

2.8.2. IN-GEL DIGESTION OF PROTEINS

Throughout the in-gel digestion procedure enough reagent to completely cover the gel pieces was added to each Eppendorf tube, unless otherwise stated. The composition of all reagents is described in section 2.1.5.

Equilibration and destaining: To remove contaminants and staining, a mixture of 100% acetonitrile (ACN) and ABC (1:3 ratio) was added to the gel pieces and incubated at 37°C for 15 min on a Thermomixer (600rpm). The liquid was removed and the incubation with the ACN and ABC mixture repeated. Following removal of the liquid, ACN was added to the gel pieces and incubated at RT for 5 min. The liquid was then discarded.

Reduction: Reduction buffer was added to the gel pieces and incubated at 56°C for 20 min on a Thermomixer (600rpm). The liquid was then discarded.

Shrinking: ACN was added to the gel pieces and incubated at RT for 5 min. The liquid was discarded and the incubation with ACN repeated.

Alkylation: Alkylation buffer was added to the gel pieces and incubated in the dark at RT for 20 min. The liquid was discarded.

Equilibration: ACN was added to the gel pieces and incubated at RT for 5 min. The liquid was discarded. ABC was added to the gel pieces and incubated at RT for 5 min. The liquid was discarded. ACN was added to the gel pieces and incubated at RT for 5 min. The liquid was discarded, and the incubations with ACN and ABC repeated.

Rehydration and digestion: One hundred microliters of sample digestion buffer was added to the gel pieces and incubated at RT for 15-20 min. ABC was added to cover the gel pieces and incubated at RT for 30 min. After the incubation, more ABC was added as needed to ensure that the gel pieces remained submerged during the overnight incubation at 37°C.

Peptide extraction: The Eppendorf tubes were briefly centrifuged to collect liquid and then sonicated for 15-20 sec. Twenty microliters of 2% TFA was added to the gel pieces and incubated at RT for 20 min on a ThermoMixer (14000rpm). The Eppendorf tubes were briefly centrifuged, and the liquid transferred to new labelled Eppendorf tubes. Enough Buffer B to cover the gel pieces was added and the samples incubated at RT for 20 min on a ThermoMixer (14000rpm). The Eppendorf tubes were briefly centrifuged, and the liquid transferred to fresh labelled Eppendorf tubes.

Concentration: The extracted peptide solution was transferred to a vacuum centrifuge (Eppendorf Concentrator Plus™) and incubated at 30°C on the vacuum concentrator setting until the volume was reduced to approximately 20-40μL. The peptide solution was then diluted 1:1 with 2% TFA and stored at -20°C until the 'peptide clean-up' step was performed.

2.8.4. STAGE TIP ASSEMBLY

Stop-and-go-extraction (STAGE) tips were prepared using a C18 disc (high performance extraction disk) (66883-U, Sigma-Aldrich). Using a small piece of wire and a 200μL pipette tip

with the end cut off, a small circle of C18 disc was removed. The C18 piece was then placed into a new 200µL pipette and packed down using the wire. A gap of approximately 5mm was left between the end of the tip and the C18 piece. A hole was then made in the lid of an Eppendorf tube that was big enough to allow the STAGE tip to be inserted, but also suspended the end of the tip approximately 10mm from the bottom of the Eppendorf tube. One STAGE tip was prepared per peptide sample.

2.8.5. PEPTIDE CLEAN-UP

Throughout the peptide clean-up procedure all centrifugation steps were performed at 5000xg for 10-15 min, or until all of the added liquid has passed through the C18 piece in the STAGE tip, unless otherwise stated.

Peptide capture: STAGE tips were placed into a centrifuge and 100µL of 100% methanol added into each tip. The STAGE tips were then briefly centrifuged (30-60 sec) to ensure the C18 piece was adequately packed. If the methanol immediately travelled through the tip and into the Eppendorf tube, it was discarded, and a fresh STAGE tip prepared. Appropriately packed STAGE tips were then centrifuged until the methanol had completely passed through the C18 piece. Fifty microliters of Buffer B was added to each tip and centrifuged. Fifty microliters of Buffer A was added to each tip and centrifuged. Fifty microliters of Buffer A was added to each tip and centrifuged. Following centrifugation at RT at 1000xg, the peptide solutions were added to individual STAGE tips and centrifuged. Fifty microliters of Buffer A was then added to each tip and centrifuged.

Elution: To elute the peptide from the C18 piece, 20µL of Buffer B was added to each STAGE tip and pressure applied to the tip using a syringe filled with air. The pressure pushed the liquid through the C18 piece and into a new Eppendorf tube. The elution step with 20µL of

Buffer B and the syringe was then repeated and the corresponding eluted peptide solutions pooled.

Concentration: The eluted peptide solutions were transferred to a vacuum centrifuge and incubated at 30°C on the vacuum concentrator setting until the volume was reduced to approximately 8µL. Buffer A was then added to produce a final volume of approximately 45-50L. The concentrated peptide solutions were transfer to 0.5mL glass reaction vials and stored at -20°C until mass spectrometry analysis was performed.

2.9. LIQUID CHROMATOGRPAHY-MASS SPECTROMETRY

Liquid chromatography-mass spectrometry and data analysis was kindly performed by Dr Vikram Sharma (University of Plymouth, UK) and was based on work by Suárez-Cortés *et al.*[304] and Cox *et al.*[305]

Briefly, concentrated peptides were separated on a Dionex™ UltiMate™ 3000 RSLC Nano Flow System (Thermo Scientific). Three microlitres of sample [in 0.1% TFA and acetonitrile (2% ACN in 0.1% TFA)] was loaded onto an Acclaim™ PepMap™ 100 C18 HPLC Trap Column [particle size: 3µm; diameter: 100µm; length: 20mm (Thermo Scientific)] at a flow rate of 5µl/min, bypassing the analytical column. Elution of bound peptides was performed with the trap column in line with an Acclaim™ PepMap™ 100 C18 Nano Column [particle size: 3µm; diameter: 75µm; length: 250 millimetres (mm); 100 Å (Thermo Scientific)] (i.e., analytical column) with a linear gradient of 96% Buffer A and 4% Buffer B to 60% Buffer A and 40% Buffer B at a constant flow rate of 300 nanolitres (nl)/min over 60 min. The eluent from the analytical column was directed to a Proxeon Nanospray ESI source (Thermo Fisher) operating in positive ion mode and analysed using an Orbitrap Velos Pro FTMS (Thermo Fisher). The Orbitrap Velos Pro instrument underXcalibur2.1 software was operated in the data-

dependent mode to automatically switch between single and tandem acquisition (MS/MS). Mass spectra of intact peptides [mass to charge ratio (*m/z*) 350-1600] with an automated gain control accumulation target value of 1,000,000 ions were acquired with a resolution of 60,000. The ten most intense charged ions were sequentially isolated and fragmented in the linear ion trap by collision induced dissociation at a target value of 10,000 or maximum ion time of 200 milliseconds. A dynamic exclusion of ions previously sequenced within 45'' was applied. Precursor ions with a charge sate of one and unassigned charge sate ions were excluded from sequencing. Typical mass spectrometric conditions included: 2.3 kV spray voltage; no sheath and auxiliary gas flow; 275°C capillary temperature; 30% normalised collision induced dissociation collision energy for MS2 in LTQ. The ion selection threshold was 10,000 counts for MS2. An activation q = 0.25 and activation time of 30 milliseconds were utilised.

2.9.1 MASS SPECTROMETRY DATA ANALYSIS BY MAXQUANT

Peptides and proteins were identified from mass spectrometry data by Andromeda via automated database searching of all MS/MS spectra against a curated target/decoy database [forward and reversed version of the Human protein sequence database (https://www.uniprot.org/proteomes/UP000005640) (last modified June, 2021)] containing all Human protein entries from UniProt SwissProt and TrEMBL databases. The search parameters included: cysteine carbamidomethylation as a fixed modification; N-acetyl protein, deamidation and methionine oxidisation as variable modifications. Precursor tolerance was 6 ppm in MS mode with 0.5 Da in MS/MS mode. Resulting Andromeda peak list-output files were automatically uploaded to inbuilt MaxQuant software modules for

further processing and label free quantitation. A maximum false discovery rate of 1% was fixed for output files.

2.10. PREPARATION OF DNA FOR SANGER SEQUENCING

The reagents and buffers used to produce high-quality polymerase chain reaction (PCR) products for Sanger Sequencing are described in section 2.1.6.

2.10.1. GENOMIC DNA EXTRACTION

Genomic DNA extracts were prepared by lysing snap frozen cell pellets using the QIAamp DNA Mini Blood Kit following the manufacturer's instructions (QIAamp® DNA Blood Mini Kit [51104, Qiagen]). Briefly, 20µL of QIAGEN Protease was added into 1.5mL Eppendorf tubes. Two hundred microlitres of sample ($5x10^6$ cells in PBS) was then added into the Eppendorf tubes along with 200µL of Buffer AL. The samples and Buffer AL were mixed thoroughly to yield homogenous solutions by pulse-vortexing for 15 s. Following a 10 min incubation at 56°C, 200µL of ethanol (96-100%) was added to the Eppendorf tubes and the solution mixed by pulsed-vortexing for 15 s. The mixtures were added into QIAamp Mini spin columns and centrifuged at 6000x*g* for 1 min. The columns were then placed into fresh 2mL collection tubes and the filtrate discarded. Five hundred microlitres of Buffer AW1 was added into the columns and centrifuged at 6000x*g* for 1 min. The columns were then placed into fresh 2mL collection tubes and the filtrate discarded. Five hundred microlitres of Buffer AW2 was added into the columns and centrifuged at max speed (approximately 20,000x*g*) for 3 min. The columns were then placed into fresh 2mL collection tubes (filtrate discarded) and centrifuged at max speed for 1 min. The columns were then placed into fresh 1.5mL Eppendorf tubes and the filtrate discarded. Two hundred microlitres of AE buffer was added into the columns and incubated at RT for 5 min to increase DNA yield. The columns were centrifuged at 6000x*g* for

1 min. An additional elution step was performed by placing the columns into fresh 1.5mL Eppendorf tubes and adding 200µL of AE buffer. The columns were then centrifuged at 6000x*g* for 1 min. The spin columns were finally discarded, leaving the purified DNA in the Eppendorf tubes.

The DNA was quantified using a NanoDrop 2000 spectrophotometer (ND-2000, Thermo Scientific). The purity of each DNA sample was determined from the ratio of absorption at 260nm and 280nm. The DNA was considered pure at a ratio of approximately 1.8. DNA extracts were stored at -80°C.

2.10.2. POLYMERASE CHAIN REACTION (PCR)

IGHV genes were amplified from genomic DNA by multiplex PCR. The primers, consisting of 7 oligonucleotides, were generated in the Framework 1 and 2 regions, and were designed to anneal to their corresponding VH segments (VH1-VH7) with minimal-to-no mismatches. The primer set was used in combination with a single JH consensus primer, designed to anneal to all JH segments with the same binding efficiency. The primer set design and the rationale behind the multiplex approach is described in van Dongen *et al.*[306]

Oligonucleotide sequences are shown in Table 2.5. All primer were purchased from Merck Life Science. Stock solutions of 300µM were prepared in nuclease-free water (Fisher Scientific, BP2484-100) and stored at -20°C. A primer mix (final concentration of each primer: 2µM) was prepared using nuclease-free water as required and stored at -20°C.

Table 2.5: Oligonucleotides used to amplify IGHV genes from genomic DNA.

Primer	Melting Temp (°C)	Sequence*	GC Content (%)
Vh1 FR1	73.70	GGCCTCAGTGAAGGTCTCCTGCAAG	60.00
Vh2 FR1	73.10	GTCTGGTCCTACGCTGGTGAAACCC	60.00
Vh3 FR1	76.30	CTGGGGGGTCCCTGAGACTCTCCTG	68.00
Vh4 FR1	75.30	CTTCGGAGACCCTGTCCCTCACCTG	64.00
Vh5 FR1	70.60	CGGGGAGTCTCTGAAGATCTCCTGT	56.00
Vh6 FR1	74.70	TCGCAGACCCTCTCACTCACCTGTG	60.00
Vh7 FR2	82.20	TTGGGTGCGACAGGCCCCTGGACAA	64.00
JH	68.10	CCTACCTGAGGAGACGGTGACC	63.64

*Primers were designed by van Dongen *et al.*[306]

Prior to experimentation, the primer annealing temperature was optimised. Annealing temperatures of 59, 60 or 61°C were tested. One hundred microlitre PCR reactions were set up using the primer mix, *Taq* PCR Core Kit (201223, Qiagen) and extracted genomic DNA. Details of the reaction mix are listed in Table 2.6. IGHV genes were amplified using a GSTROM thermal cycler (Applied Biosystems), following the cycle sequence outlined in Table 2.7. The PCR products were analysed by agarose gel electrophoresis.

Table 2.6: PCR reaction mix used to amplify IGHV genes from genomic DNA.

Reagent*	Volume/reaction (µL)	Final Concentration
10X PCR Buffer[†]	10	1X
dNTP mix (10 mM each)	2	200µM of each dNTP
Primer mix	10	0.2µM of each primer
Taq DNA Polymerase (5 units/µL)	0.5	2.5 units/reaction
5X Q-solution	20	1X
Template DNA	8	Approximately 200ng
Nuclease-free water	49.5	N/A[‡]
Total Volume	100	

*10X PCR Buffer, dNTP (deoxynucleoside triphosphate) mix, *Taq* DNA Polymerase and 5X Q-solution all supplied in the *Taq* PCR Core Kit (201223, Qiagen).

[†] Contains 15mM $MgCl_2$.

[‡] N/A, not applicable.

Table 2.7: PCR cycle sequence for optimised primer annealing.

Step	Temperature (°C)	Time	Number of cycles
Heated lid	112	N/A*	N/A
Automatic hot start	95	10 min	1
Initial denaturation	95	7 min	1
Denaturation	95	45 sec	
Annealing	59	90 sec	35
Extension	72	30 sec	
Final Extension	72	10 min	1
Hold	4	Infinite	N/A

*N/A, not applicable.

2.10.3. AGAROSE GEL ELECTROPHORESIS

A 2% agarose gel was prepared in a clean, glass flask and heated until the agarose was completely dissolved. To visualise the DNA, GelRed® Nucleic Acid Gel Stain was added once the mixture had cooled to approximately 50°C. The gel mixture was then poured into a gel tray and a 15 well comb added. The gel was left to set for at least 30 min before loading the samples.

To track the migration of the PCR products during electrophoresis, the samples were mixed with 6X loading dye (1 in 6 dilution) and then loaded into the wells of the agarose gel. A DNA ladder was also loaded onto the gel. The samples were electrophoresed through the gel at a constant voltage of 150V for approximately 1 h or until the samples had almost migrated the length of the gel. Following electrophoresis, PCR products were visualised using a PXi 4 imaging system (Syngene), aided by the GeneSys programme (Syngene).

2.10.4. DNA EXTRACTION FROM AGAROSE GEL

PCR products were extracted from the agarose gel using the Monarch® DNA Gel Extraction Kit (T1020, New England Biolabs) following the manufacturer's instructions. Briefly, DNA fragments were excised from the agarose gel using sterile 10A surgical scalpels (0502, Swann-Morton™). A new scalpel was used for every cut. Excess agarose was removed, and the gel slices placed into separate Eppendorf tubes (which had previously been weighed). The Eppendorf tubes containing the gel slices were weighed and the weight of the gel slice calculated. Four volumes of Monarch Gel Dissolving Buffer was added to each gel slice (e.g. 400µL per 100mg agarose) and incubated at 50°C for 10 min, or until the gel was completely dissolved. Spin columns were inserted into collection tubes and the samples loaded into the columns. The columns were centrifuged at 16,000xg for 1 min and the filtrate discarded. The

columns were reinserted into the collection tubes and 200μL of DNA Wash Buffer added into each column. The columns were centrifuged at 16,000x*g* for 1 min and the filtrate discarded. The columns were reinserted into the collection tubes and 200μL of DNA Wash Buffer added into each column once again. The columns were centrifuged at 16,000x*g* for 1 min and the filtrate discarded. The columns were transferred to clean Eppendorf tubes and 6μL of DNA Elution Buffer added to the centre of the matrix. The columns were incubated at room temperature for 1 min and then centrifuged at 16,000x*g* for 1 min. The spin columns were finally discarded, leaving the purified DNA fragments in the Eppendorf tubes.

The DNA fragments were quantified using a NanoDrop 2000 as described in section 2.10.1 and stored at -80°C.

2.10.5. SANGER SEQUENCING

Sanger sequencing of extracted DNA fragments was performed by Eurofins Genomics. Prior to sequencing, 15μL of each PCR product (5ng/μL) was prepared using nuclease-free water in separate Eppendorf tubes. Two microlitres of the JH primer (stock concentration: 10μM) was then added into each Eppendorf tube (17μL final volume). A prepaid barcoded TubeSeq Label (3094-000PPB, Eurofins Genomics) was then attached to each tube and the samples sent (at RT) to Eurofins Genomics (Ebersberg, Germany) for Sanger sequencing.

Downloadable sequencing results were provided by Eurofins Genomic as .ab1 files. These files were imported into Unipro UGENE (version 36) for alignment against the IGHV gene reference sequence (https://www.ncbi.nlm.nih.gov/gene?Db=gene&Cmd=DetailsSearch&Term=3492). For sequence alignment, the 'Sanger data analysis' tool was utilised with the 'Trimming quality threshold' set to 30, 'Mapping min similarity' set to 30%, and 'Read name in result alignment' set to 'File name'. Within Unipro UGENE, sequences were trimmed to remove

poor quality reads, typically seen at the beginning and end of sequences, and peaks within the chromatograms check to ensure the correct nucleotides had been assigned. Analysed sequences were exported as .FASTA files, which were then imported to IMGT/V-QUEST (http://www.imgt.org/IMGT_vquest/input). IMGT/V-QUEST is an integrated alignment tool for the immunoglobulin and TCR nucleotide sequences and compares the germline/rearranged sequences with the IMGT reference directory sets.[307] Cases with ≥98% sequence homology to the *IGHV* germline sequence were classified as UM-CLL cases, whereas cases with <98% homology to *IGHV* germline sequence were classified as M-CLL.[306]

CHAPTER 3 – OPTIMISING AND EVALUATING TECHNIQUES FOR QUANTITATIVE MEASUREMENT OF CYTOSKELETAL-MEDIATED SHAPE-CHANGE IN CLL CELLS

3.1. INTRODUCTION

It is well established that interactions with accessory cells within the TME, facilitated through BCR- and chemokine-driven reorganisation of the B-lymphocyte cytoskeleton, control key aspects of CLL pathogenesis.[94,125] BCR aggregation leads to activation of Rho family members through BTK-mediated recruitment of the guanine nucleotide exchange factor VAV. The Rho family GTPases activate cytoskeletal regulators that coordinate F-actin turnover and remodelling, permitting leukemic cell proliferation, migration, and IS formation, via stabilisation of the ARP2/3 complex, and activation of formins and ROCK.[147] Thus, BTKi have emerged as highly effective therapies in the treatment of CLL.[209,210,222–224] However, a proportion of responding CLL cases develop resistance and eventually, relapse.[243,244] The exact mechanism of action of BTKi is currently unknown. Evidence suggests that the tumour regression seen in CLL patients receiving BTKi may result from the deprivation of crucial TME growth and survival signals via inhibition of CLL migration and adhesion.[235–237] This indicates a need to further investigate the cytoskeletal response underlying the cellular sensitivity of CLL cells to BTKi, so that alternative treatments targeting specific resistance mechanisms can be used.

Due to difficulties in directly quantifying changes in cytoskeletal organisation, previous studies have instead focused on surrogate 'downstream' markers such as cell adhesion, proliferation, and survival. However, advances in cell labelling and software developments now allow a high level of semi-automated quantitative assessment of cytoskeletal changes.

This chapter describes the optimisation and use of microscopy techniques to quantitatively characterise the morphological features of the CLL cytoskeleton. The aim was to define these features to allow the identification of specific mechanical responses to BTKi and other small molecule inhibitors, which may ultimately, inform novel combinational therapies.

Using SEM, combined with ImageJ morphometric analysis, it was possible to identify unique morphological populations formed following treatment of CLL cells with small molecule inhibitors.

3.2. SUMMARY OF EXPERIMENTAL METHODS

The methods employed in this chapter involve the general culture of patient-derived CLL cells *ex vivo* (section 2.2.1) and MCL cell lines (section 2.2.3). These cells were adhered to fibronectin-coated coverslips (section 2.3.1-2) and their cytoskeletal features assessed by immunofluorescent staining of F-actin, vimentin, and plasma membrane proteins (section 2.3.3-8), and SEM (2.3.10) combined with morphometric ImageJ analysis (2.3.11).

Following optimisation, the specific morphological responses of CLL cells to treatment with the small molecule inhibitors ibrutinib, Y-27632 and imatinib (section 2.3.9) were determined using SEM.

A table of fluorophore-conjugated antibodies/probes used in this chapter is shown below (Table 3.1).

All data generated through ImageJ analyses were exported to GraphPad Prism™ Version 5 software for graphical representation and statistical analysis (section 2.3.12). The specific statistical tests employed are described in the figure legends of each experiment.

Table 3.1: Fluorophore-conjugated antibodies and probes.

Antibody/probe	Species	Application*	Product number	Supplier	Concentration
Texas Red™-X Phalloidin	N/A	IF	T7471	Invitrogen™	1 in 40
Anti-vimentin (EPR3776)	Rabbit	IF	Ab92547	Abcam	1 in 500
Anti-rabbit IgG H&L Alexa Fluor® 488	Goat	IF	Ab150077	Abcam	1 in 1000
Anti-human CD20-FITC	Mouse	IF	IM1456	Beckman Coulter	1 in 100
Anti-human CD40-PE	Mouse	IF	IM1936U	Beckman Coulter	1in 100
Anti-human CD45-FITC	Mouse	IF	A07782	Beckman Coulter	1 in 100
FITC IgG2a, κ Isotype Control (G155-178)	Mouse	IF	555573	Becton Dickinson	1in 100
PE IgG1, Isotype control (MOPC-21)	Mouse	IF	559320	Becton Dickinson	1 in 100

*IF, immunofluorescence.

3.3. ESTABLISHING THE SUITABILITY OF IMMUNOFLUORESCENT STAINING FOR QUANTITATIVE MEASUREMENT OF CLL SHAPE PARAMETERS

F-actin and plasma membrane labelling methods both demonstrated varying levels of staining between the main cell body and filopodial projections, which prevented accurate quantitative measurement of CLL shape parameters due to loss of all but the largest, most intensely stained membrane protrusions during image processing.

3.3.1. ASSESSMENT OF F-ACTIN STAINING IN CLL CELLS

To characterise and quantify the morphically features of the neoplastic B-lymphocyte cytoskeleton, three CLL cases were seeded onto fibronectin-coated coverslips and allowed to adhere for 1 h. Cells were fixed, and F-actin stained with Texas-Red™-X Phalloidin. In CLL cells, F-actin was concentrated around the periphery of the cell in the cortex underlying the plasma membrane (Figure 3.1). Bundles of aligned actin filaments formed filopodia – slender, tapering extensions of the plasma membrane (arrows in Figure 3.1). Filopodia were more frequent on motile cells, where they emanated from the trailing edge and adhered to the substratum or other cells. Varying levels of F-actin staining were observed, with the cortical cytoskeleton staining intensely and thin filopodia staining weakly due to their small size.

Although polymerised actin structures could be visualised, the difference in staining intensity resulted in loss of all but the largest filopodial protrusions during binary image generation (arrows in Figure 3.2A-C). The bases of the protrusions, where they integrate with the rest of the cytoskeleton, were still present in binary images and could be used to estimate the prevalence of filopodia on CLL cells; however, large proportions of the structures were still missing. This would have resulted in the inaccurate measurement of shape parameters (i.e., decreased cell area and perimeter, and increased cell circularity) during ImageJ analyses. It was, therefore, determined that F-actin staining was not the optimal tool for quantitative

measurement of morphological features of the CLL cytoskeleton. Despite this, F-actin could

still be used to qualitatively assess changes in the cortical cytoskeleton.
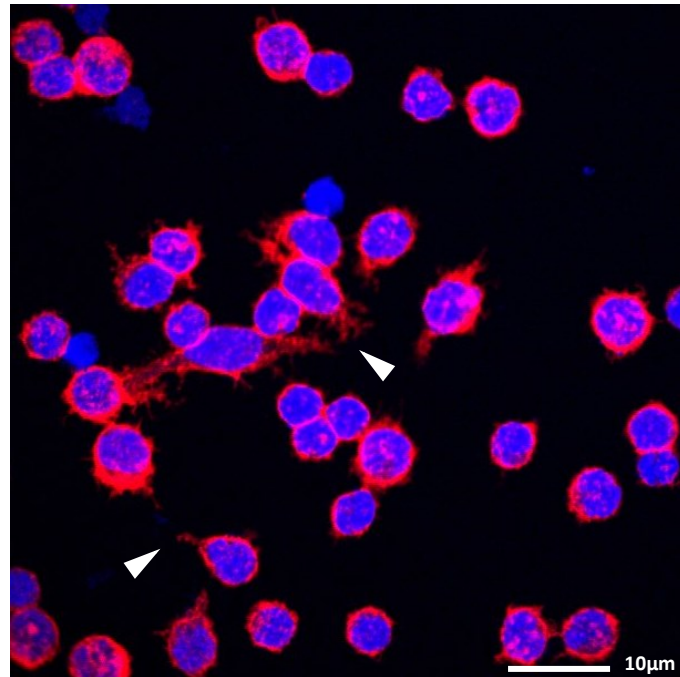
Figure 3.1: **The actin cytoskeleton in patient-derived CLL cells.** F-actin staining was evaluated using Texas Red-X Phalloidin (red) in isolated patient-derived CLL cells, after culture for 6 days. Cells were allowed to adhere for 1 h before being fixed and stained. Arrows indicate filopodial projections. DNA was counterstained with DAPI (blue). The Z-stacks was acquired using a Leica SE Confocal Microscope with the use of a 63x oil objective and merged to create a maximum intensity projection image.

Texas Red-X Phalloidin   **Binary Image**
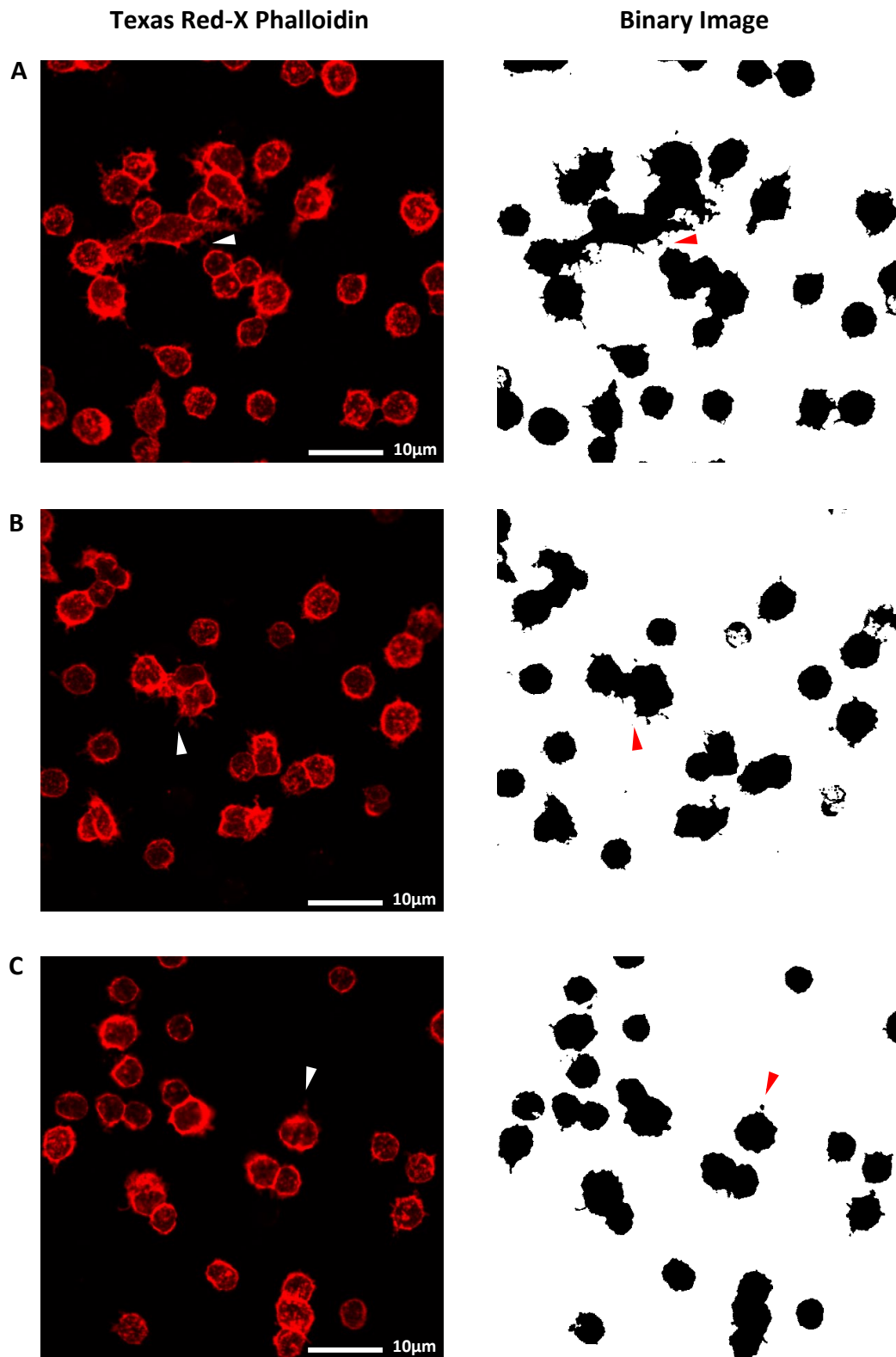
Figure 3.2: Binary image generation using Texas Red-X Phalloidin staining of F-actin in CLL cells. Using ImageJ, binary images were generated by thresholding the F-actin staining within cells from three CLL cases. The white arrows indicate small, thin filopodial protrusion which were lost (red arrows) during binary image generation due to weaker F-actin staining than the rest of the cortical cytoskeleton.

97

3.3.2. ASSESSMENT OF STAINING OF PLASMA MEMBRANE COMPONENTS IN CLL CELLS

As an alternative to F-actin cytoskeleton staining, the suitability of cell membrane staining (with fluorophore-conjugated monoclonal CD20, CD45 and CD40 antibodies; Table 3.1) for the quantitative measurement of morphological features of the CLL cytoskeleton was determined.

CD20 (human B-lymphocyte-restricted differentiation antigen) is a non-glycosylated phosphoprotein that is expressed on mature naïve B-lymphocytes until terminal differentiation to BM plasma cells.[308,309] In CLL, clusters of CD20 were observed around the periphery of the cell, with weaker staining observed on filopodial protrusions and peripheral ruffles (Figure 3.3A). Varying levels of CD20 staining were seen between CLL cells.

CD45, a receptor-like tyrosine phosphatase, is the most abundantly expressed phosphatase on the surface of cells of the myeloid, T-lymphocyte and B-lymphocyte lineages.[310] In line with this, intense staining was observed at the periphery of CLL cells, with weaker staining observed on cytoplasmic extensions (Figure 3.3B). Whereas varying levels of CD20 expression were found, the expression of CD45 was similar amongst CLL cells; highlighting it crucial role in regulating tyrosine kinase signalling by dephosphorylating members of the Src family kinases.[310]

The transmembrane phosphoprotein CD40 is expressed on resting B-lymphocytes and its interaction with CD154, expressed on antigen-activated CD4$^+$ helper T-lymphocytes, promotes BCR-induced B-lymphocyte survival.[191] Weak CD40 staining was located at the cell periphery, with weak-to-absent staining of filopodia (Figure 3.3C).

CD Marker Staining **Binary Image**

A — CD20

B — CD45

C — CD40
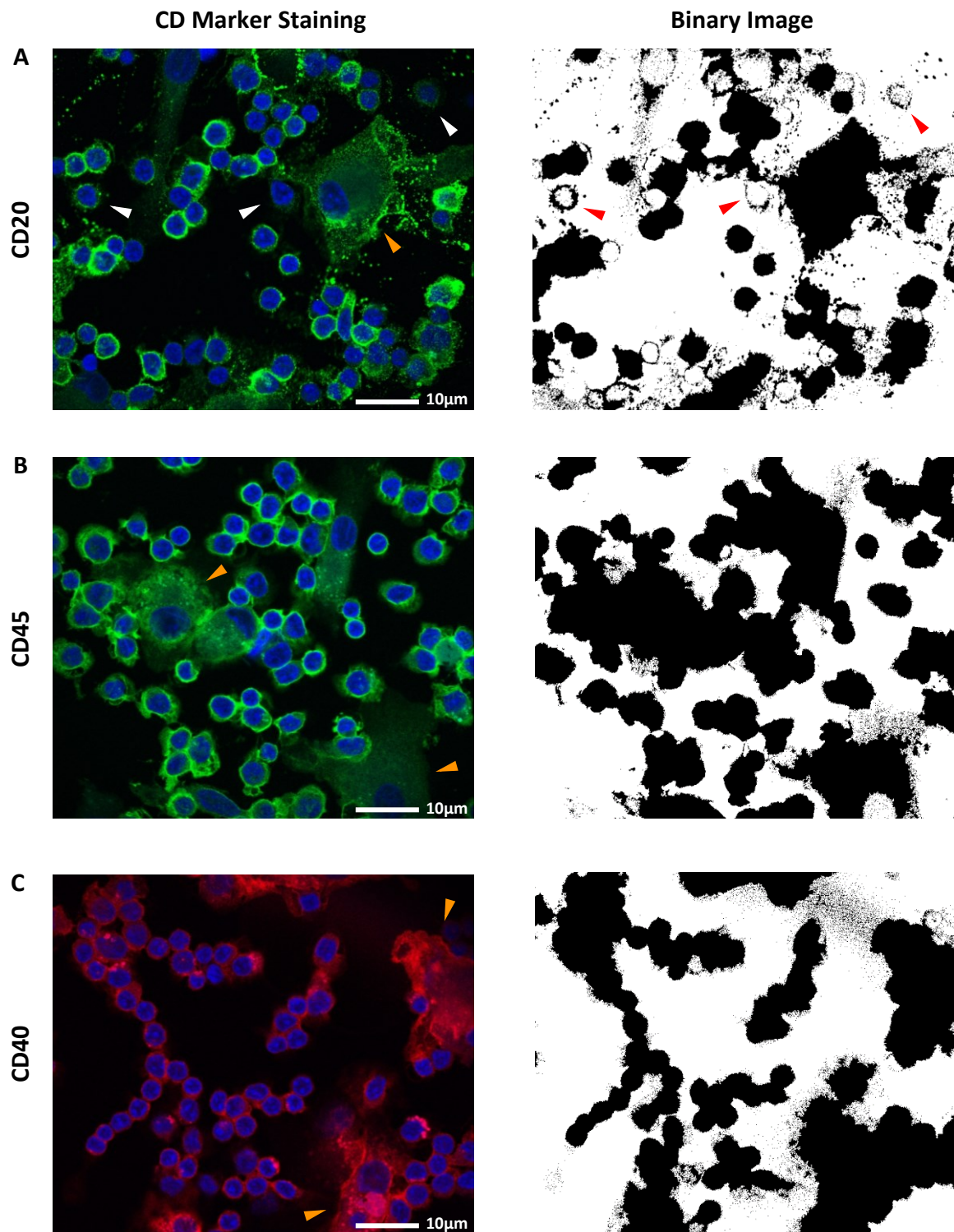
Figure 3.3: Staining of CLL surface markers. Following 6 days culture, CLL cells were fixed and stained using FITC-conjugated CD20 (PN IM1456; Beckman Coulter) (A) and CD45 (A07782; Beckman Coulter) (B), and PE-conjugated CD40 (PN IM1936U; Beckman Coulter) (C) monoclonal antibodies (1 in 100 dilution). DNA was counterstained with DAPI (blue). Z-stacks were acquired using a Leica SE Confocal Microscope with the use of a 63x oil objective and merged to create maximum intensity projection images. Binary images were generated in ImageJ by thresholding the green (FITC) or red (PE) channels. White and red arrows indicate cells that were lost during binary image generation due to the speckled appearance of CD20 staining. Large monocyte-derived NLCs can also be seen in images (orange arrows).

As with F-actin staining, thresholding CD20, CD45 and CD40 staining in ImageJ resulted in binary images that lacked thin filopodial protrusions (Figure 3.3A-C). This was due to weaker staining of membrane projections (i.e., filopodia) than the rest of the plasma membrane. Some cells were also lost due to the speckled appearance of CD20 staining at the cell edge (white arrows in Figure 3.3A). Consequently, surface membrane staining did not provide any significant benefits over F-actin staining in the quantitative determination of CLL shape parameters.

3.3.3 ASSESSMENT OF VIMENTIN STAINING IN CLL CELLS

Vimentin is the major intermediate filament found in leucocytes, where it contributes to their rigidity whilst circulating. The controlled collapse of vimentin may also be an essential process in chemokine-induced extravasation.[164] To observe the structure of vimentin filaments within CLL cells, immunocytofluorescent staining was utilised. Vimentin filament within the MCL cell lines REC-1 and G519 were also visualised.

In both CLL cells and the MCL cell lines, vimentin formed a complex network of 'basket- like' filaments, concentrated in the thin perinuclear region from which filaments radiated out towards the cell surface (Figure 3.4). In migrating CLL cells, vimentin was concentrated in posterior attachment points and was absent from anterior lamellipodia (arrows in Figure 3.4). Apparent independence between vimentin filaments and the distribution of F-actin was also observed, with vimentin bundles not extending into thin filopodial protrusions or ruffles. Interestingly, vimentin staining was only observed in approximately 48% of REC-1 cells (data not shown), whilst it was seen (in varying levels) in the majority of CLL and G519 cells; suggesting that its role in REC-1 cells may be cell cycle regulated or link to cell motility.
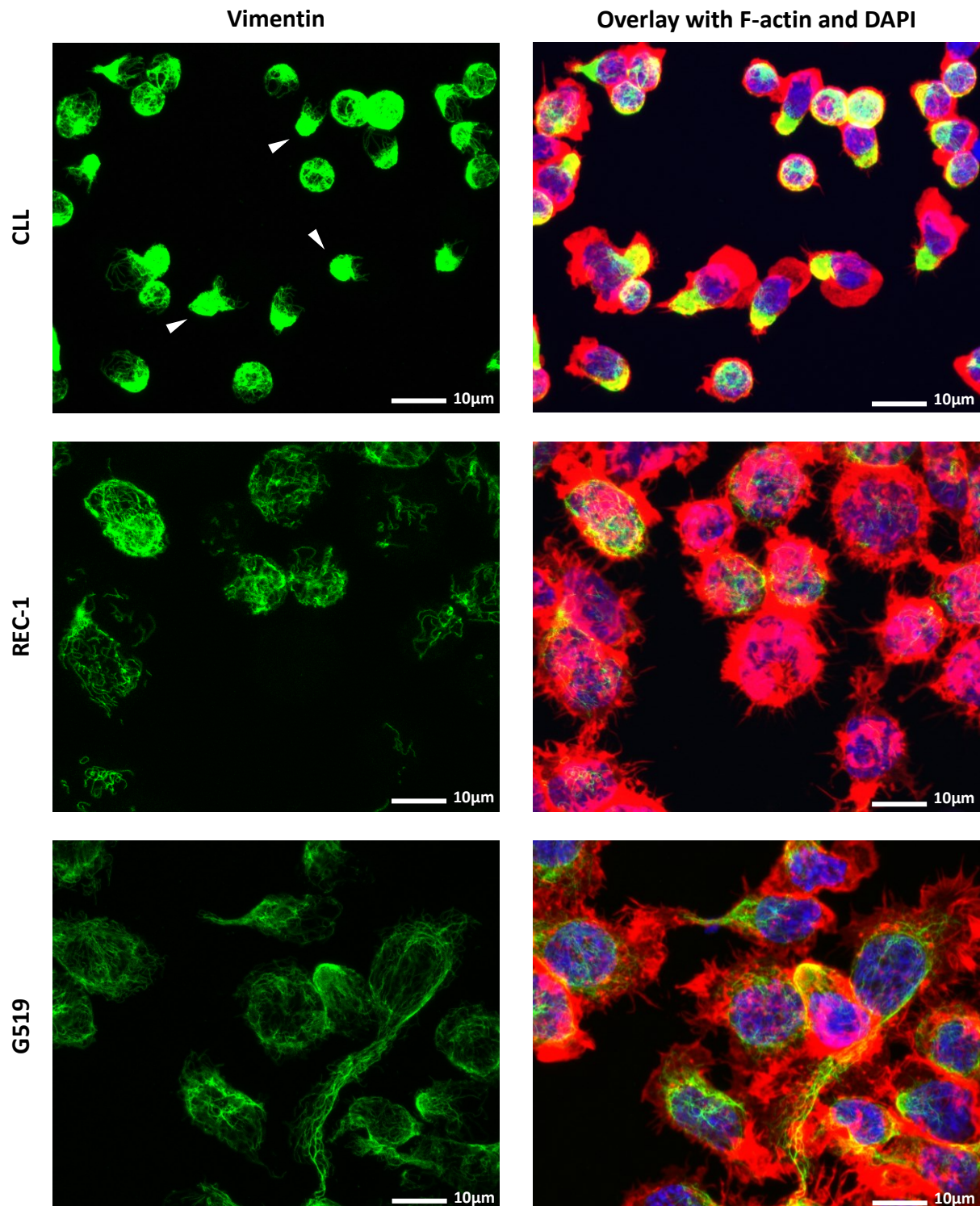
Figure 3.4: Distribution of vimentin and F-actin filaments in CLL, REC-1 and G519 cells. Following 6 days culture, patient-derived CLL cells were fixed and stained with the monoclonal anti-vimentin antibody (ab92547, Abcam) (1 in 500 dilution), followed by staining with Alexa Fluor 488 (ab150077, Abcam) (1 in 1000 dilution; green). The MCL cell lines, REC-1 and G519, were also stained for vimentin. DNA and F-actin were counterstained with DAPI (blue) and Texas Red-X Phalloidin (red), respectively. Z-stacks were acquired using a Leica SE Confocal Microscope with the use of a 63x oil objective and merged to create maximum intensity projection images. Vimentin was concentrated in posterior attachment points of motile CLL cells (white arrows).

Although vimentin cannot be used for binary image generation and quantitative measurement of shape parameters, changes in the unique distribution of filaments in response to clinically relevant therapeutics can be qualitatively assessed.

3.4. ESTABLISHING THE SUITABILITY OF SEM FOR QUANTITATIVE MEASUREMENT OF CLL SHAPE PARAMETERS

CLL cells display a range of different morphologies that could be visualised and quantitatively assessed using SEM combined with ImageJ analyses.

3.4.1. OPTIMISATION OF THE SPUTTER COATING PROCESS

Although SEM can image almost all types of materials, certain specimens require an extra step during sample preparation to enable high-quality images to be obtained. Sputter coating is the standard method for preparing non-conductive or poorly conducting samples for observation by SEM and involves coating the specimen with an additional thin layer of conductive material.[311] In order to test the ability of SEM to visualise morphological features of the CLL cell cytoskeleton, an initial experiment was designed to determine the optimal sputter coating material, 1-2nm of chromium or 5nm of gold, for the preparation of poorly conducting CLL samples for observation by SEM.

When a material cannot effectively conduct the impacting electrons to ground, it is said to be 'charging'. This build-up of electrical potential in the sample can result in detrimental artefacts such as abnormal contrast, and image deformation and shift.[311] The dark bands and image shift observed in chromium-coated cells (Figure 3.5A) were the result of charging and could not be eliminated by recoating the specimen with an additional layer of 1-2nm of chromium or decreasing the accelerating voltage of the electron beam (images not shown).
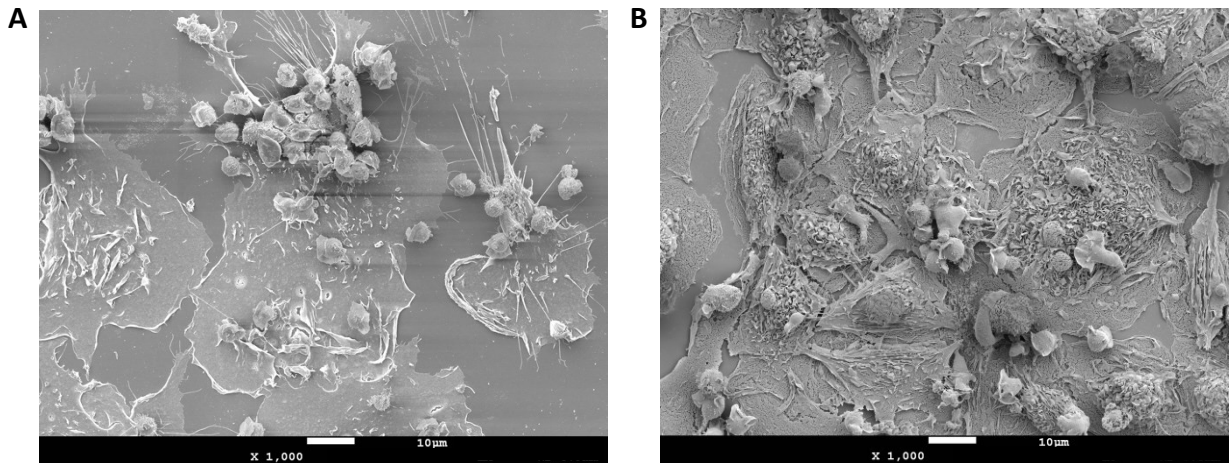
Figure 3.5: Scanning electron microscopy image of CLL cells. Following 6 days culture, CLL cells were adhered to fibronectin-coated coverslips for 4 h, fixed and either sputter coated with 1-2nm of chromium (A) or 5nm of gold (B) during sample processing. Cells were observed using a JEOL 7001 F SEM and images were captured using the supporting software. Large monocyte-derived NLCs can also be observed.

Samples sputter coated with gold did not exhibit charging artefacts (Figure 3.5B). Gold has more effective electrical conduction characteristics than chromium and, therefore, impacting electrons were successfully able to escape from the specimen. The larger grain size of gold, which can limit its use in high-resolution coating,[312] was not found to be an issue in this study, as the maximum magnification used (5000x) was not sufficient to resolve individual gold particles. Coating the specimens with gold produced high-resolution images with good contrast. A range of cytoskeletal features could be observed in detail, including ruffles, and thin microvilli and filopodial projections (Figure 3.6). Thus, gold was selected as the sputter coating material to be used in all subsequent experiments involving the observation of neoplastic B-cells by SEM.
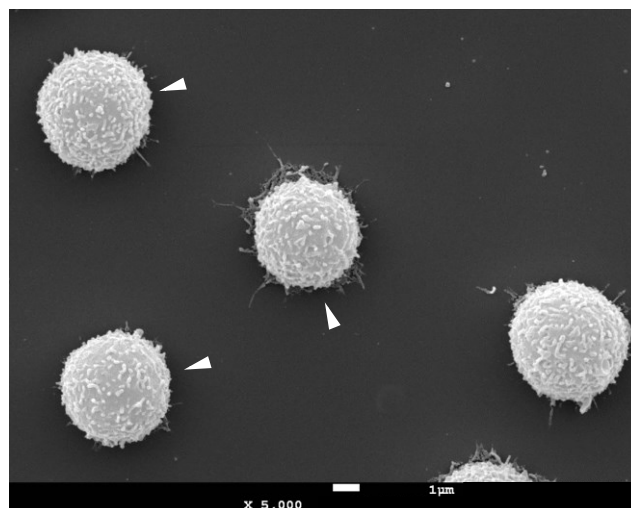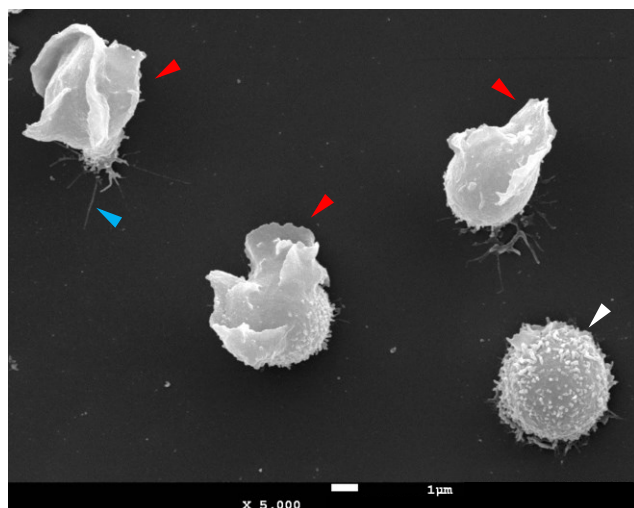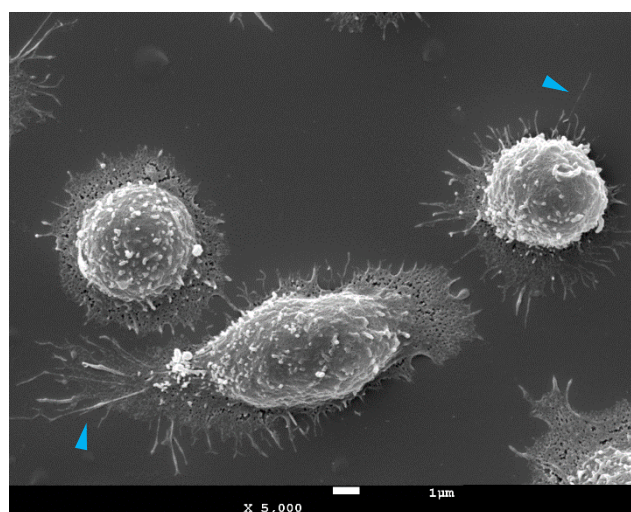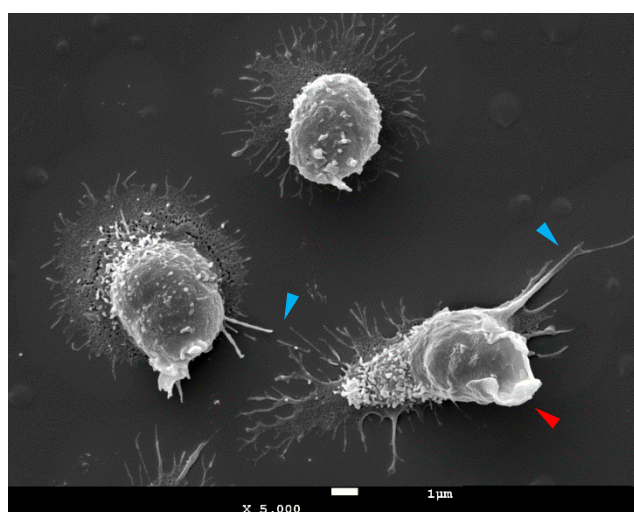
Figure 3.6: Cytoskeletal features of resting CLL cells. Following 6 days culture, cases CLL-01 and CLL-27 were adhered to fibronectin coverslips for 4 h, fixed and sputter coated with 5nm of gold. Cells were processed, observed using a JEOL 7001 F SEM and images were captured using the supporting software. A range of cytoskeletal features can be observed within CLL populations, including densely packed microvilli (white arrows), fine filopodia (blue arrows) and ruffles (red arrows). Images were taken at 5000x so that cytoskeletal features could be seen in detail.

3.4.2. QUANTITATIVE MEASUREMENT OF CONTROL CLL SHAPE PARAMETERS

Although SEM provided high-resolution images of CLL cytoskeletal features, the suitability of these images for quantitative measurement of shape parameters still needed to be determined. This was established by ImageJ analyses and graphical representation of CLL cell morphologies. The characteristics of the CLL case used for this initial experiment are summarised in Table 4.2.

SEM provided high-resolution grey-scale images of DMSO-treated CLL-01 cells. A range of different morphological features could be seen, including microvilli, filopodial and peripheral ruffles (Figure 3.7A). Due to good contrast between the light grey cells and the dark background, binary images could be easily generated. Unlike with the immunofluorescent staining previously mentioned, there was little difference in the shade (of grey) of the main cell body and cytoskeletal projections and, therefore, after thresholding, these features were still present in binary images (arrows in Figure 3.7A).

As the binary images accurately reflected the cell morphologies present in original SEM images, the shape parameters of individual cells within six fields of view could be accurately measured. Morphometric data was used to create frequency distribution histograms showing the number of cells observed within certain ranges (bins) of values (Figure 3.7B). The bin sizes were optimised for perimeter (2µm bins), circularity (0.08 bins) and area (2µm^2 bins) histograms to allow the distinct cell populations (small, highly circular cells or larger, more irregular cells) observed in SEM images to be identified.
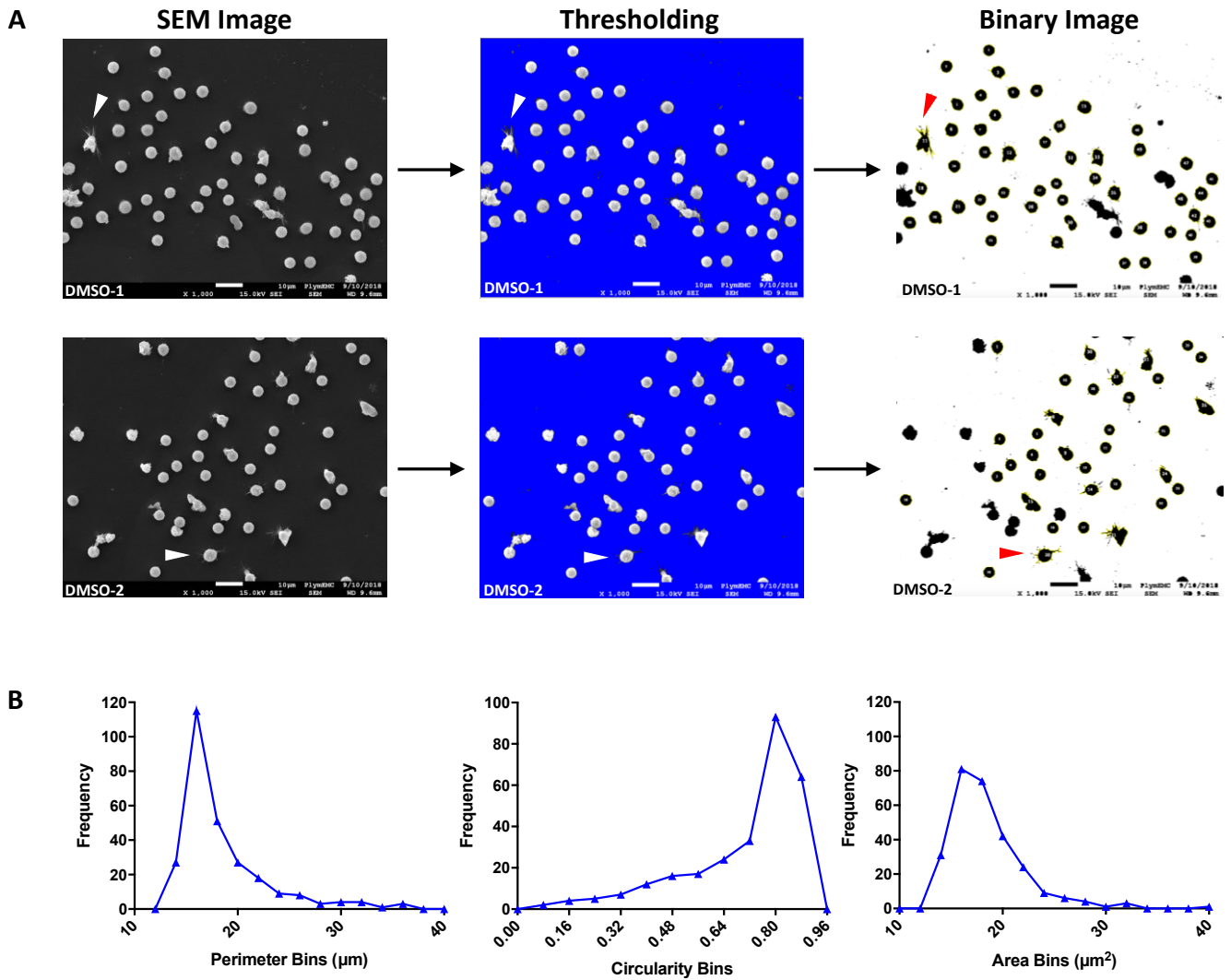
Figure 3.7: Binary images generation using SEM images and measurement of shape parameters. (A) Following 6 days culture, CLL-01 cells were treated with DMSO for 1 h, fixed and processed. Cells were observed using a JEOL 7001 F SEM at 1000x and images were captured using supporting software. By thresholding on cells within .tif images, binary images which contained thin filopodial protrusions and microvilli were generated (white and red arrows). Single cells within six field of view at 1000x were then selected and their shape parameters (perimeter, circularity, and area) measured. (B) Morphometric data was transferred to GraphPad Prism™ for graphical representation as frequency distribution histograms showing the number of cells observed within certain ranges (bins) of values.

3.5. EVALUATING CLL MORPHOLOGICAL RESPONSES FOLLOWING TREATMENT WITH SMALL MOLECULE INHIBITORS

Distinct morphological populations were formed following the treatment of CLL cells with small molecule inhibitors. Cytoskeletal changes were seen early (1 h) with ibrutinib and Y-27632, whereas imatinib showed morphological changes at all time points.

3.5.1. DETERMINING THE EFFECTS OF SMALL MOLECULE INHIBITORS ON THE CLL CYTOSKELETON

To begin establishing how the CLL cytoskeleton is changed by inhibition of BCR signalling, a CLL case was treated with ibrutinib for 1 h prior to observation by SEM. The case was also treated with two small molecule inhibitors, imatinib (an ABL1 inhibitor) and Y-27632 (an inhibitor of ROCK1). The effect(s) of these signal inhibitors on cytoskeletal morphology are well characterised and would aid in the identification of pathways that may be involved in the shape changes observed following ibrutinib treatment, and possibly inform novel combinational therapies for the treatment of CLL. The characteristics of the CLL case used for this SEM experiments are summarised in Table 4.2.

Using structural fixation followed by SEM, high quality images were obtained that allowed quantitative measurement of shape parameters (perimeter, circularity, and area). These measures then permitted the graphical representation and statistical comparison of different cells shapes formed in response to signal protein inhibition and suggested changes in neoplastic cell behaviour (Figure 3.8).

At 1 h, DMSO-treated (control) cells formed one main population composed of small (perimeter and area approximately 16μm and 16μm^2, respectively), highly circular (circularity approximately 0.80) cells. The remaining cells were more irregular with larger perimeters and areas. This can also be seen in the SEM images, with numerous globular cells displaying many

fine surface microvilli. They also produced fine horizontal filopodia across the adhesion surface which were polarised in their distribution. The larger, more irregular cells had broad, anterior lamellipodia with prominent peripheral ruffles and most likely represented motile cells due to their posterior attachment points and front-tail polarity. Filopodia are defined as thin, finger-like projections which typically protrude from the leading edge of motile cells and are adhered to the substratum or neighbouring cells. In contrast, lamellipodia are broad, surface-attached, sheet-like membrane protrusions, starting at the leading edge and extending back towards the cell body. Lamellipodia are observed during cell spreading and crawling migration.[131]

BCR signalling, meditated by BTK in addition to other signalling proteins, is a central process in B-lymphocyte cytoskeletal rearrangements.[313] Histograms showed a significant shift towards smaller, more circular cells with ibrutinib treatment (100nM and 1µM). However, the morphology of ibrutinib-treated cells was largely similar to control cells. Ibrutinib-treated cells were predominantly globular and exhibited surface microvilli, which were decreased in number compared to control cells. Filopodial projects extended from ibrutinib-treated cells, particularly motile cells with clear front-tail polarity. Given that ibrutinib inhibits a broad kinome and similar effects on cell shape were observed at both concentrations tested, 100nM ibrutinib treatment was selected for future experiments based on the maximum achievable dose *in vivo* of 400nM[209,314] and to avoid unwanted off-target effects.
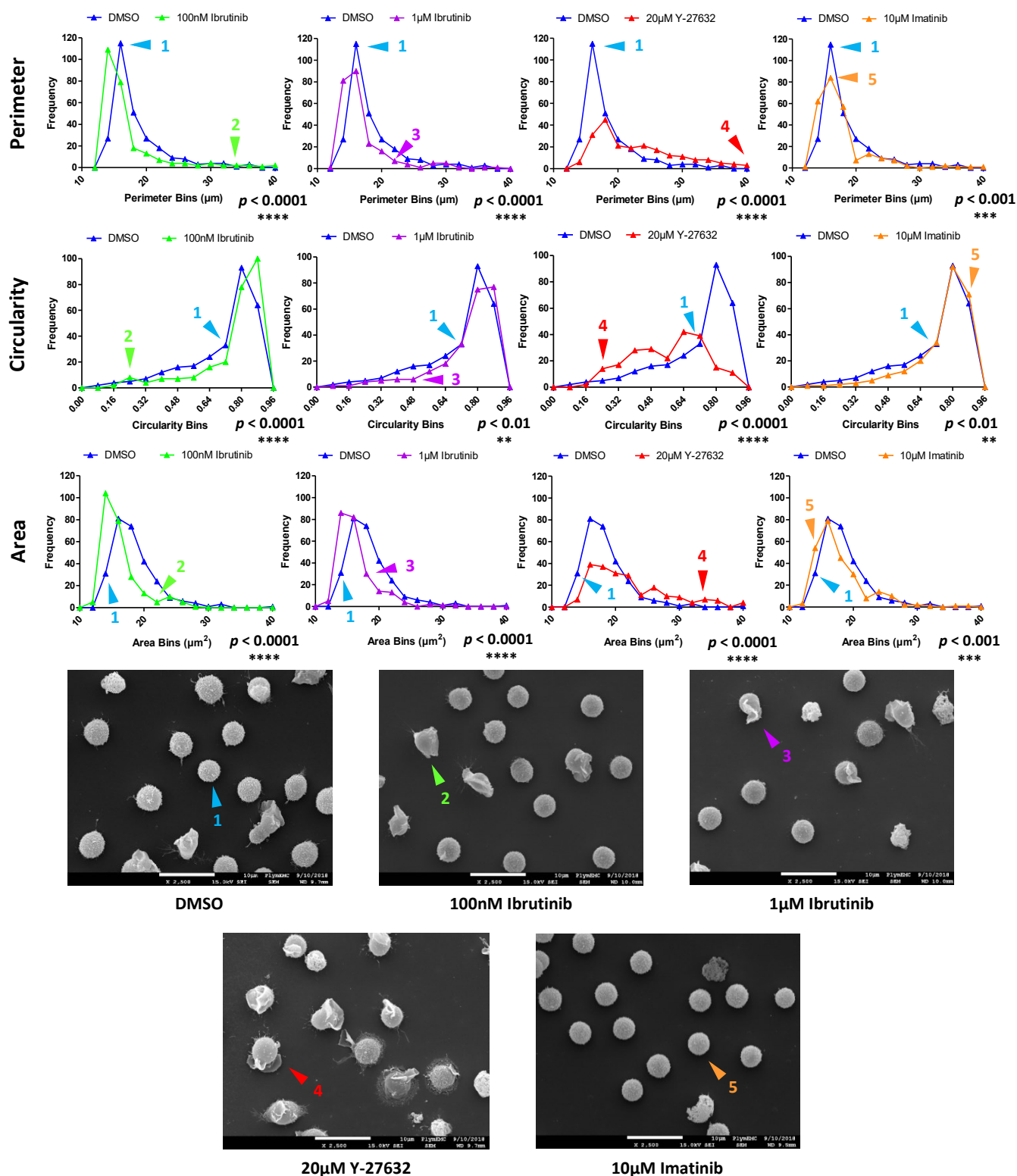
Figure 3.8: Effects of small molecule inhibitors on CLL cell shape. Following 6 days culture, CLL-01 cells were treated with either DMSO, ibrutinib, Y-27632 or imatinib for 1 h, fixed and processed. Cells were observed using a JEOL 7001 F SEM at 1000x and 2500x, and images were captured using supporting software. Binary images were generated from 1000x .tif images using ImageJ, and the perimeter, circularity and area of cells measured. Frequency distribution histograms were created using GraphPad Prism. *p*-values for DMSO vs treatments were calculated using the Mann-Whitney U test. Arrows represent the position of specific cells on frequency distribution histograms. Images were taken at 2500x so that cytoskeletal features could be seen in detail.

ROCK plays a crucial role in mediating rearrangements of the cytoskeleton downstream of the small GTPase Rho. In particular, Rho regulates stress fibre formation and focal adhesion which confer contractibility of a cell.[315] In line with this, larger and more irregular cells which lacked posterior attachment points were observed with Y-27632 treatment compared to DMSO. Microvilli were spare-to-absent from the surface of Y-27632-treated cells. However, filopodia and ruffles were both frequent and non-polarised.

ABL1 has a major role in regulating F-actin organisation in lymphocytes and is known to support cell motility and filopodia formation.[283] Imatinib treatment resulted in a significant decrease in neoplastic cell perimeter and area, with an increase in circularity. Interestingly, imatinib-induced shape changes resembled those observed in BTK-treated CLL cells. Cells displayed numerous, short microvilli, similar to those seen on control cells following ABL1 inhibition. However, imatinib-treated cells did not form fine filopodial protrusion like DMSO-treated cells.

3.5.2. ESTABLISHING THE EFFECTS OF SMALL MOLECULE INHIBITORS ON THE CLL CYTOSKELETON OVER TIME

To model how the observed changes in CLL cell shape, mediated by signal protein inhibition, evolved during the culture period, three CLL cases (Table 4.1-2) were fixed at 30 min, 1 h and 4 h time points. The results for the individual cases being discussed in this section are shown in Figure 3.9-11. Exact *p*-values for DMSO vs small molecule inhibitor treatment at each time point are listed in Table 3.2-4.
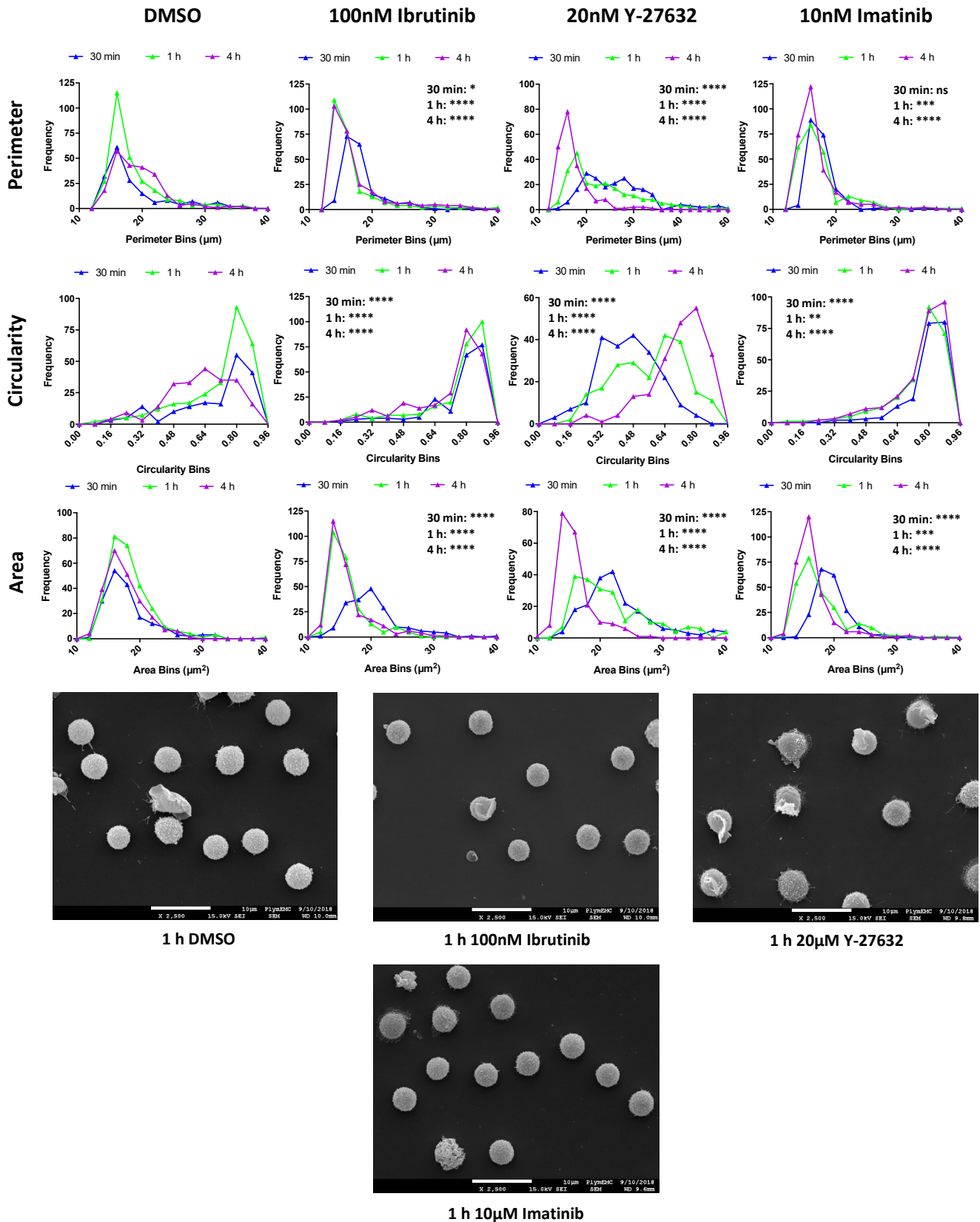
Figure 3.9: Effects of small molecule inhibitors on CLL-01 cell shape. Case CLL-01 was treated with signal inhibitors for 30 min, 1 h and 4 h, and then fixed. Cells were observed using a JEOL 7001 F SEM at 1000x and 2500x, and images were captured using supporting software. Binary images were generated from 1000x .tif images using ImageJ, and the perimeter, circularity and area of cells measured. Frequency distribution histograms were created using GraphPad Prism. *p*-values for DMSO vs treatments for each time point were calculated using the Mann-Whitney U test. ****$p < 0.0001$; ***$p < 0.001$; **$p < 0.01$; *$p < 0.05$; not significant (ns) $p > 0.05$.
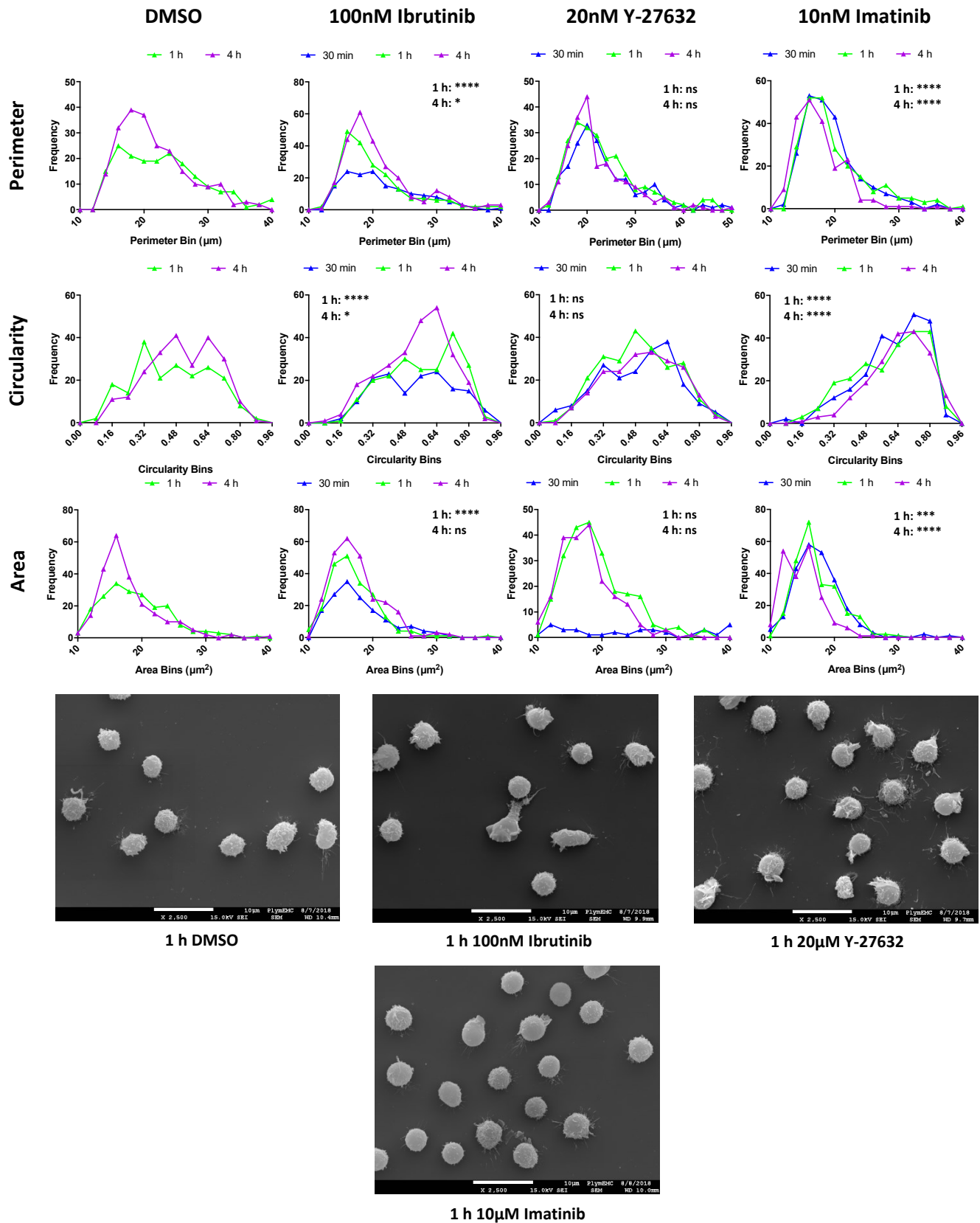
Figure 3.10: Effects of small molecule inhibitors on CLL-02 cell shape. Case CLL-02 was treated with signal inhibitors for 30 min, 1 h and 4 h, and then fixed. Cells were observed using a JEOL 7001 F SEM at 1000x and 2500x, and images were captured using supporting software. Binary images were generated from 1000x .tif images using ImageJ, and the perimeter, circularity and area of cells measured. Frequency distribution histograms were created using GraphPad Prism. *p*-values for DMSO vs treatments for each time point were calculated using the Mann-Whitney U test. ****$p < 0.0001$; ***$p < 0.001$; **$p < 0.01$; *$p < 0.05$; not significant (ns) $p > 0.05$. The 30 min data points for DMSO-treated CLL-02 cells could not be obtained as issues during sample preparation resulted in prominent structural artefacts.

CLL cells treated with 100nM ibrutinib showed variable changes in area and perimeter compared to DMSO-treated cells (Table 3.2-4). However, the general trend for all CLL cases was to become one population (Figure 3.9-11). The circularity of all CLL cells was predominately increased at later time points (1 h and 4 h) compared to control cells. The BTKi-treated CLL cases also displayed a slight decrease in the number of microvilli, and the number and length of filopodia.

Extensive filopodia networks and ruffles were observed following Y-27632 treatment (30 min and 1 h); indicating that retraction of cytoplasmic projections and establishment of front-tail polarity, which are both important for effective cell migration, had been impaired (Figure 3.9-11). Generally, cells treated with Y-27632 displayed an early response, with an increase in perimeter reflecting the frequent filopodial extensions seen in SEM images at 30 min and 1 h (Table 3.2-4). However, not all cases responded in the same way. Y-27632-treated CLL-02 cells showed no significant change in shape parameters despite frequent long filopodia, and ruffles being observed in SEM images; whereas CLL-03 exhibited a delayed response which was quite marked in terms of changes in filopodial extension. Circularity did not accurately reflect the morphological changes seen following Y-27632 treatment.

Imatinib treatment resulted in relatively uniform neoplastic cell populations that were highly circular at all time points compared to DMSO-treated cells (Figure 3.9-11; Table 3.2-4). Cell perimeter and area were also predominantly decreased. The morphology seen in SEM images confirmed the lack of irregularity and/or polarity. Despite ABL1 roles in filopodia formation,[283] inhibition by imatinib did not prevent the formation of filopodial projections by CLL-02 cells.
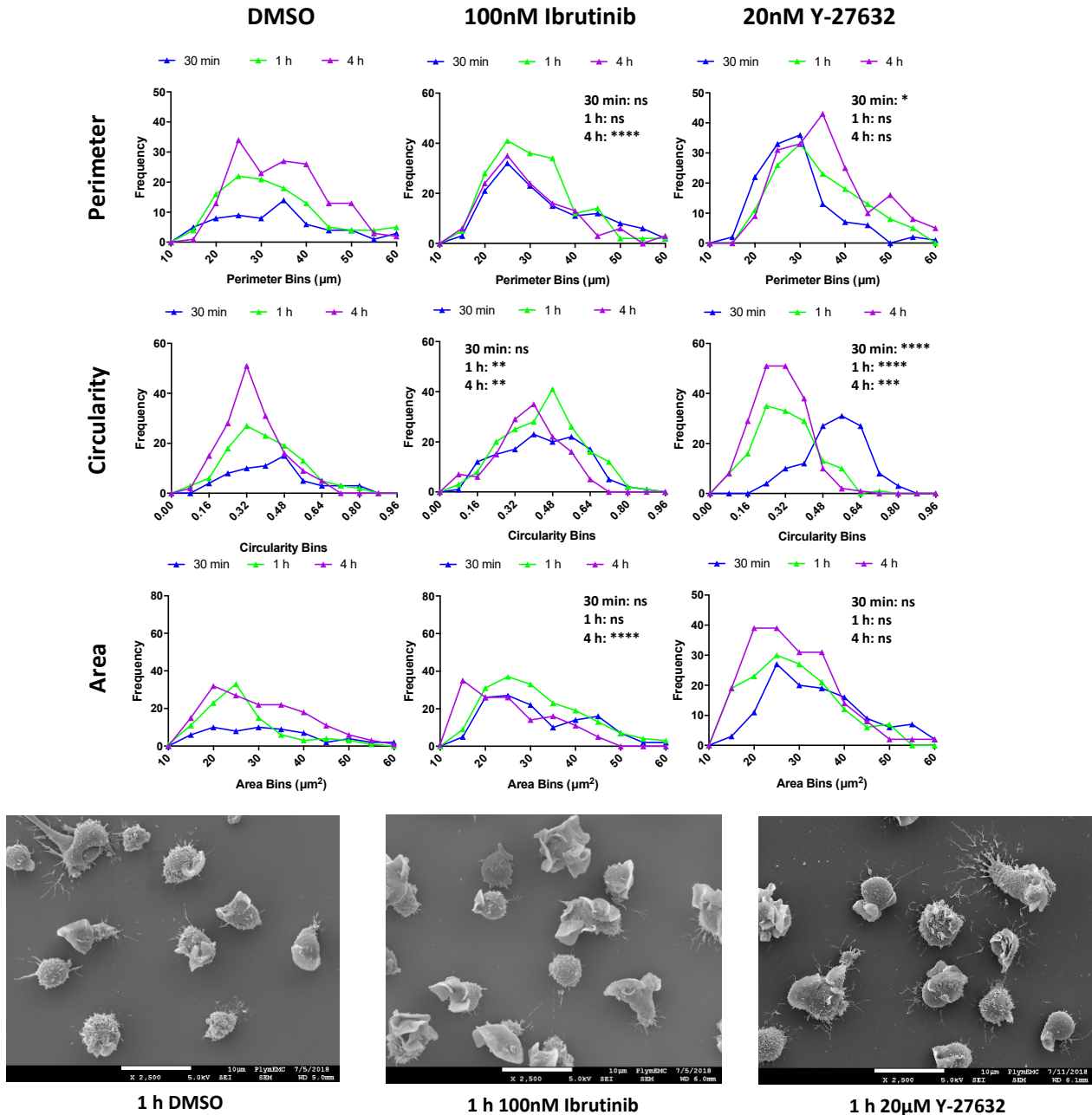
Figure 3.11: Effects of small molecule inhibitors on CLL-03 cell shape. Case CLL-03 was treated with signal inhibitors for 30 min, 1 h and 4 h, and then fixed. Cells were observed using a JEOL 7001 F SEM at 1000x and 2500x, and images were captured using supporting software. Binary images were generated from 1000x .tif images using ImageJ, and the perimeter, circularity and area of cells measured. Frequency distribution histograms were created using GraphPad Prism. *p*-values for DMSO vs treatments for each time point were calculated using the Mann-Whitney U test. ****$p < 0.0001$; ***$p < 0.001$; **$p < 0.01$; *$p < 0.05$; not significant (ns) $p > 0.05$. Imatinib was not available at the time that CLL-03 cells were treated.

Table 3.2: Perimeter - summary of the changes in CLL cell shape following small molecule inhibitor treatment.

Case	Time	Conditions	*p*-value[†]	Increase/decrease in perimeter compared to DMSO control
CLL-01	30 min	DMSO vs 100nM Ibrutinib	0.0389 *	Increase
		DMSO vs 20µM Y-27632	<0.0001 ****	Increase
		DMSO vs 10µM Imatinib	0.1190 ns[‡]	N/A[§]
	1 h	DMSO vs 100nM Ibrutinib	<0.0001 ****	Decrease
		DMSO vs 1µM Ibrutinib	<0.0001 ****	Decrease
		DMSO vs 20µM Y-27632	<0.0001 ****	Increase
		DMSO vs 10µM Imatinib	0.0002 ***	Decrease
	4 h	DMSO vs 100nM Ibrutinib	<0.0001 ****	Decrease
		DMSO vs 20µM Y-27632	<0.0001 ****	Decrease
		DMSO vs 10µM Imatinib	<0.0001 ****	Decrease
CLL-02	1 h	DMSO vs 100nM Ibrutinib	<0.0001 ****	Decrease
		DMSO vs 20µM Y-27632	0.2644 ns	N/A
		DMSO vs 10µM Imatinib	<0.0001 ****	Decrease
	4 h	DMSO vs 100nM Ibrutinib	0.0238 *	Decrease
		DMSO vs 20µM Y-27632	0.6868 ns	N/A
		DMSO vs 10µM Imatinib	<0.0001 ****	Decrease
CLL-03	30 min	DMSO vs 100nM Ibrutinib	0.8499 ns	N/A
		DMSO vs 20µM Y-27632	0.0333 *	Decrease
	1 h	DMSO vs 100nM Ibrutinib	0.1080 ns	N/A
		DMSO vs 20µM Y-27632	0.1602 ns	N/A
	4 h	DMSO vs 100nM Ibrutinib	<0.0001 ****	Decrease
		DMSO vs 20µM Y-27632	0.1621 ns	N/A

[†] *p*-values were determined using the non-parametric Mann-Whitney U test for unpaired data sets.

[‡] ns, not significant.

[§] N/A, not applicable.

Table 3.3: Circularity - summary of the changes in CLL cell shape following small molecule inhibitor treatment.

Case	Time	Conditions	*p*-value[†]	Increase/decrease in circularity compared to DMSO control
CLL-01	30 min	DMSO vs 100nM Ibrutinib	<0.0001 ****	Increase
		DMSO vs 20µM Y-27632	<0.0001 ****	Decrease
		DMSO vs 10µM Imatinib	<0.0001 ****	Increase
	1h	DMSO vs 100nM Ibrutinib	<0.0001 ****	Increase
		DMSO vs 1µM Ibrutinib	0.0018 **	Increase
		DMSO vs 20µM Y-27632	<0.0001 ****	Decrease
		DMSO vs 10µM Imatinib	0.0036 **	Increase
	4h	DMSO vs 100nM Ibrutinib	<0.0001 ****	Increase
		DMSO vs 20µM Y-27632	<0.0001 ****	Increase
		DMSO vs 10µM Imatinib	<0.0001 ****	Increase
CLL-02	1h	DMSO vs 100nM Ibrutinib	<0.0001 ****	Increase
		DMSO vs 20µM Y-27632	0.0728 ns[‡]	N/A[§]
		DMSO vs 10µM Imatinib	<0.0001 ****	Increase
	4h	DMSO vs 100nM Ibrutinib	0.0342 *	Increase
		DMSO vs 20µM Y-27632	0.6937 ns	N/A
		DMSO vs 10µM Imatinib	<0.0001 ****	Increase
CLL-03	30 min	DMSO vs 100nM Ibrutinib	0.7036 ns	N/A
		DMSO vs 20µM Y-27632	<0.0001 ****	Increase
	1h	DMSO vs 100nM Ibrutinib	0.0017 **	Increase
		DMSO vs 20µM Y-27632	<0.0001 ****	Decrease
	4h	DMSO vs 100nM Ibrutinib	0.0034 **	Increase
		DMSO vs 20µM Y-27632	0.0003 ***	Decrease

[†] *p*-values were determined using the non-parametric Mann-Whitney U test for unpaired data sets.

[‡] ns, not significant.

[§] N/A, not applicable.

Table 3.4: Area - summary of the changes in CLL cell shape following small molecule inhibitor treatment.

Case	Time	Conditions	*p*-value[†]	Increase/decrease in area compared to DMSO control
CLL-01	30 min	DMSO vs 100nM Ibrutinib	<0.0001 ****	Increase
		DMSO vs 20µM Y-27632	<0.0001 ****	Increase
		DMSO vs 10µM Imatinib	<0.0001 ****	Increase
	1h	DMSO vs 100nM Ibrutinib	<0.0001 ****	Decrease
		DMSO vs 1µM Ibrutinib	<0.0001 ****	Decrease
		DMSO vs 20µM Y-27632	<0.0001 ****	Increase
		DMSO vs 10µM Imatinib	0.0005 ***	Decrease
	4h	DMSO vs 100nM Ibrutinib	<0.0001 ****	Decrease
		DMSO vs 20µM Y-27632	<0.0001 ****	Decrease
		DMSO vs 10µM Imatinib	<0.0001 ****	Decrease
CLL-02	1h	DMSO vs 100nM Ibrutinib	<0.0001 ****	Decrease
		DMSO vs 20µM Y-27632	0.7273 ns[‡]	N/A[§]
		DMSO vs 10µM Imatinib	0.0005 ***	Decrease
	4h	DMSO vs 100nM Ibrutinib	0.2500 ns	N/A
		DMSO vs 20µM Y-27632	0.8024 ns	N/A
		DMSO vs 10µM Imatinib	<0.0001 ****	Decrease
CLL-03	30 min	DMSO vs 100nM Ibrutinib	0.9973 ns	N/A
		DMSO vs 20µM Y-27632	0.3039 ns	N/A
	1h	DMSO vs 100nM Ibrutinib	0.1903 ns	N/A
		DMSO vs 20µM Y-27632	0.7681 ns	N/A
	4h	DMSO vs 100nM Ibrutinib	<0.0001 ****	Decrease
		DMSO vs 20µM Y-27632	0.2718 ns	N/A

[†] *p*-values were determined using the non-parametric Mann-Whitney U test for unpaired data sets.

[‡] ns, not significant.

[§] N/A, not applicable.

An unexpected observation from this experiment, was the distinctly different morphology of the CLL-03 case (Figure 3.11). The unusual morphology of control CLL-03 cells (large, irregular cells with numerous ruffles and distinct front-tail morphology) compared to control cell from the other two CLL cases (small, globular cells with short microvilli) may have been due differences in treatment status and/or cytogenetics (Table 4.1-2). CLL-01 and CLL-02 were treatment-naïve, M-CLL cases and although CLL-01 carried a del(13q), this mutation is associated with a favourable prognosis.[9] In contrast, CLL-03 had received previous chemotherapy and exhibited the unfavourable del(11q).[9] In addition, CLL-03 exhibited unmutated *IGHV*. UM-CLL cases typically have a more aggressive disease than M-CLL cases.[18,19]

3.6. DISCUSSION

Given that ibrutinib yields complete responses in only 10% of R/R CLL patients,[210] understanding the mechanism underlying the cellular sensitivity of CLL to BTKi and other small molecule inhibitors is of particular importance. To achieve this, the work described in this chapter involved the development, implementation, and evaluation of tools for the quantitative assessment of cytoskeletal changes in CLL cells *in vitro*. In the following chapters of this thesis, these tools were used to determine the specific behavioural responses of neoplastic cells during treatment with clinically relevant therapeutic interventions.

Of the techniques tested in this chapter, SEM proved to be the optimum method for studying changes in cell shape. Despite providing both qualitative and quantitative data on the distribution of F-actin within leukaemic cells and being a relatively quick and simple technique (when compared to SEM), Texas-Red™-X staining resulted in binary images lacking all but the largest cytoskeletal protrusions due to varying staining intensity between the cortex and fine

filopodia. Likewise, weak, or inconsistent staining of filopodial projections with monoclonal antibodies targeting plasma membrane proteins CD20, CD40, CD45 lead to loss of cytoskeletal protrusions during image processing. In contrast to confocal microscopy, which produced a cross-sectional image, SEM produced high-resolution, grey-scale 3D images, which when converted to binary images using ImageJ, displayed the full range of cytoskeletal structures observed on the B lymphocyte's cell surface. Changes in the frequency and size of filopodia, microvilli and ruffles could best be appreciated using SEM. This additional structural detail provided by SEM allowed prominent morphological differences between CLL cases to be identified. However, further cases need to be tested to confirm whether the behavioural differences observed were related to clinical features (e.g., *IGHV* mutational status, previous treatments, chromosomal alterations) of cases (discussed in Chapter 4).

Using SEM and binary image generation, it was possible to quantitatively evaluate changes in the perimeter, area, and circularity of CLL cells *in vitro*. These measures then allowed the graphical representation of different morphological populations formed following treatment with small molecule inhibitors, allowing cytoskeletal-mediated behaviour, such as motility, adhesion, or cell-to-cell communication, to be evaluated. Given that ibrutinib, Y-27632 and imatinib target different signalling pathways, it was assumed that different cytoskeletal changes would be observed following treatment.

Selective inhibition of ROCK1 by Y-27632 resulted in irregular cells with numerous non-polarised peripheral ruffles and networks of extended filopodia, suggesting that retraction of cytoplasmic processes and, subsequently, effective cell migration, had been impaired.[267] This loss of cytoskeletal asymmetry following Y-27632 treatment is entirely consistent with the importance of ROCK1, which is a downstream signalling effector of RhoA, in permitting

cellular transmigration by simultaneously impairing Rac1-induced extension of the plasma membrane, except at the leading edge, and promoting actomyosin-mediated retraction of the lagging tail.[147,316,317]

In contrast, imatinib-treated cells displayed morphologies similar to that of control cells, with numerous densely packed microvilli on the cell surface. However, the cells were predominantly smaller and more globular, suggesting that cellular polarisation had been impaired. Indeed, the ABL family kinase ABL1 is known to coordinate actin remodelling and extension of lamellipodia in lymphocytes.[283] The formation of microvillus structures on lymphocytes is independent of ABL1 and its downstream effector proteins WASP/WAVE2[318] and, therefore, is not affected by imatinib treatment. Despite its key role in filopodia formation,[283] ABL1 inhibition failed to completely remove filopodial projections from the surface of all cells; suggesting that alternative pathways for filopodia formation may exist.

CLL cells treated with ibrutinib typically became more circular with a suggestion of decreased polarity and fewer surface projections. Cells move both by elongated-type directed motility, but also by amoeboid motility which requires weak integrin-mediated attachment to the substratum and can even be integrin-independent.[319] The shape changes observed in ibrutinib-treated cells may, therefore, represent a switch to amoeboid motility. This is in keeping with the observed BTKi-induced increase in CLL motility and migration seen in clinical trials,[212] which is thought to be related to reduced integrin $\alpha4\beta1$-mediated retention of the neoplastic cells within the TME.[235] The altered motility and cell-to-cell interactions of ibrutinib-treated B-lymphocytes suggested in this initial experiment required further detailed assessment and confirmation using additional methods (discussed in Chapter 4).

Although cytoskeletal alterations following signal inhibition were observed at different time points depending on the CLL case, distinct morphological changes were generally apparent following 1 h drug treatments in all cases. Thus, for all future microscopy-based experiments an incubation time of 1 h was selected. The major reason behind this decision was to significantly decrease the time needed for sample processing and image acquisition.

This chapter demonstrated that SEM, in conjunction with ImageJ morphometric analysis, can be used as a tool for quantitatively assessing the morphological response(s) of CLL cells to clinically relevant small molecule inhibitors *in vitro*. Major disadvantages of electron microscopy (cost and time-consuming sample preparation) can be minimised by utilising the culture conditions (1 h incubation) optimised during these experiments. The changes in cell behaviour observed using SEM were distinct, with ROCK1 inhibition causing impaired retraction of filopodia and loss of polarity, and ABL1 inhibition resulting in a uniform globular cell population. In contrast, loss of BTK had no significant effects on cytoskeletal features but produced a more uniform population of more globular cells perhaps favouring changes in the mechanism of cell motility. An awareness of the different pathways that together coordinate cytoskeletal-mediated motility and cell-to-cell interactions within the TME is highly relevant for understanding resistance mechanisms and the development of novel combinational therapeutic strategies.

CHAPTER 4 – QUANTITATIVE ASSESSMENT OF CYTOSKELETAL-MEDIATED MALIGNANT B-LYMPHOCYTE BEHVIOUR AND COMPARISON BETWEEN CLINICAL SUB-GROUPS

4.1. INTRODUCTION

CLL is a clinically heterogeneous disease, with survival ranging from several months despite early therapeutic intervention to decades of treatment-free survival.[9–12] An ever expanding understanding of CLL pathogenesis has helped identify a number of biological features of particular prognostic significance, by which CLL cases can be placed into distinct disease subgroups.

CLL can be divided into two main categories which are distinguished by whether CLL cells have undergone SHM in the IGHV genes or whether the *IGHV* resembles that of germline.[18,320] CLL patients with unmutated *IGHV* (i.e., those exhibiting *IGHV* with ≥98% homology to the germline sequence) have a more progressive disease and significantly shorter survival (95 months compared with 293 months) than patients with mutated *IGHV* (i.e., those displaying *IGHV* with <98% homology to the germline sequence).[19] The sole exception being cases using *IGHV3-21*, which despite being mutated in most cases, is associated with poor survival similar to that seen in UM-CLL.[321,322]

Furthermore, enhanced BCR activation is typically observed in *IGHV*-unmutated CLL, with 80% of UM-CLL cases displaying IgM-mediated increased global tyrosine phosphorylation, whereas only 20% of M-CLL cases responded to IgM ligation.[23] CLL cells exhibiting mutated *IGHV* are believed to be in a state of cellular exhaustion (also known as anergy) due to chronic engagement of antigen-specific transmembrane immunoglobulins, independent of

appropriate T-lymphocyte stimulation. These anergic M-CLL cells are less likely to proliferate in response to BCR signalling initiation within lymphoid tissues than 'activated' UM-CLL cells, which may (at least in part) explain the less aggressive disease frequently observed in patients displaying mutated *IGHV*.[13] UM-CLL cells also generally express ZAP-70 in contrast to their mutated counterparts or normal B-lymphocytes. ZAP-70+ leukaemic cells demonstrate greater levels of activated BLNK, an adaptor protein linking BCR signalling to the cytoskeleton via recruitment of VAV, following IgM ligation than CLL cells lacking ZAP-70.[24] Interestingly, the interaction of CD38 on the surface of CLL cells with BMSC- and NLC-expressed CD31 can also activate ZAP-70 and subsequent downstream pro-survival signalling pathways.[94,95] This suggests that ZAP-70+ CLL cases may be more sensitive to therapies targeting leukaemic cell interactions within the TME than ZAP-70- cases.

Additionally, the presence of specific chromosomal abnormalities is a robust prognostic indictor of treatment-free survival and OS. Conventionally cytogenetic analyses have revealed chromosomal alterations in approximately 80% of CLL cases.[9] The most recurrent lesions identified were del(13q14), del(11q), trisomy 12 and del(17p). These abnormalities act as independent prognostic markers, identifying patients with rapidly progressing disease and an adverse clinical outcome, or a favourable prognosis. The minimal deleted region of each of these aberrations have been found to contain within them putative CLL leukaemogenesis drivers: *mir-15a/16-1* in del(13q14),[31,32] *TP53* in del(17p)[35,43] and *ATM* and *BIRC3* in del(11q).[35,38,39,81] Although UM-CLL and M-CLL display the same chromosomal aberrations, the incidence of high-risk abnormalities is higher in UM-CLL.[30]

With the growing number therapeutic possibilities, understanding the heterogeneous biological features of CLL subgroups, and how these unique characteristics may contribute to

drug resistance, has become a priority to ensure that the maximum clinical benefit is observed. Thus, using techniques developed and optimised in Chapter 3, this chapter aimed to produce a quantitative description and comparison of cytoskeletal-mediated responses of CLL subgroups to specific small molecule inhibitors, aiming to offer a fresh perspective on our approach to the management of CLL and to suggest rational drug combinations in this disease.

Utilising the MCL cell lines REC-1 (ibrutinib-sensitive) and G519 (ibrutinib-resistant) as a surrogate model for BTKi sensitivity in CLL, the effect(s) of ibrutinib resistance on mechanical responses was also evaluated following signal inhibition. Both CLL and MCL patients exhibit a concurrent PB lymphocytosis and reduction in tumour burden with ibrutinib induction,[212,229] suggesting that BCR signalling is essential for the trafficking of malignant B-lymphocytes to lymphoid organs and their retention within these supportive niches in both diseases. Thus, MCL cell lines can provide novel insight into the cellular behaviour underlying ibrutinib resistance, which may, ultimately, aid in the development of therapeutic strategies to combat the appearance of resistance in CLL and MCL.

4.2. SUMMARY OF EXPERIMENTAL METHODS

The methods employed in this chapter involved the extraction of genomic DNA from CLL cases and the amplification of the IGHV genes by multiplex PCR (section 2.10.1-2). The resulting bands were visualised by agarose gel electrophoresis and excised to allow the extraction of DNA from the gel (section 2.10.3-4). Purified DNA was analysed by Sanger Sequencing and the *IGHV* mutational status determined using Unipro UGENE and IMGT/V-QUEST (section 2.10.5).

Additional methods included the general culture of patient-derived CLL cells *ex vivo* (section 2.2.1) and MCL cell lines (section 2.2.3). These cells were adhered to fibronectin-coated coverslips (section 2.3.1-2), treated with small molecule inhibitors (section 2.3.9) and their cytoskeletal features assessed by SEM (2.3.10) combined with morphometric ImageJ analyses (2.3.11). The optimised methods for quantitatively describing CLL shape changes using SEM and ImageJ are described in detail within Chapter 3.

The effects of signal inhibition on CLL cellular interactions were determined using DBSCAN analyses, carried out via R and RStudio (section 2.4)

Changes in the migration of CLL and MCL cells to CXCL12 following signal inhibition were determined using the Transwell migration assay (section 2.5).

All data generated through ImageJ, RStudio and FlowJo analyses were exported to GraphPad Prism™ Version 5 software for graphical representation and statistical analysis (section 2.3.12, section 2.4.4, and section 2.5.4, respectively). The specific statistical tests employed are described in the figure legends of each experiment.

4.3. ESTABLISHING THE *IGHV* MUTATIONAL STATUS OF CLL CASES

Using an optimised PCR multiplex PCR method, twenty-seven CLL cases could be successfully classified as either having mutated *IGHV* or *IGHV* sequences that resemble those of germline.

4.3.1. OPTIMISING THE AMPLIFICATION OF THE IGVH GENES BY MULTIPLEX PCR

Before the *IGHV* mutational status of CLL cases could be determined, the amplification of the IGHV genes by multiplex PCR was optimised by varying the annealing temperature. Although the protocol listed 59°C as the optimal annealing temperature (section 2.10.2), annealing

temperatures of 60°C and 62°C were also tested to allow for differences in the calibration of instruments.
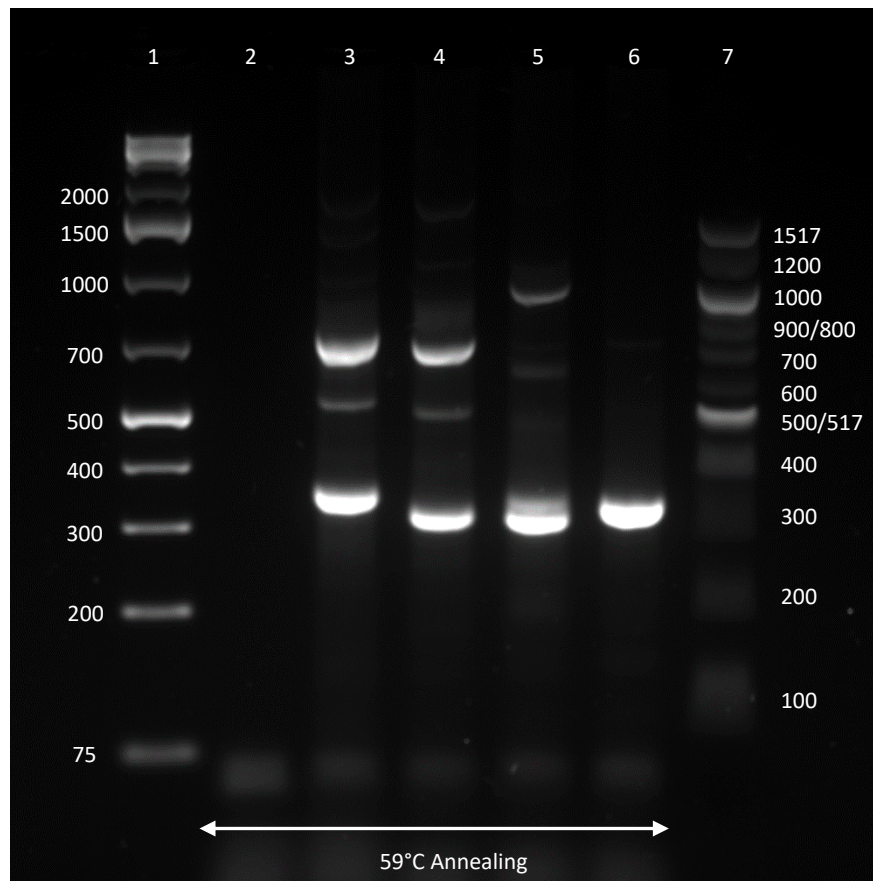
Figure 4.1: Amplification of CLL Ig V_H genes using an annealing temperature of 59°C. DNA extracted from four CLL cases was amplified by multiplex PCR using an annealing temperature of 59°C. PCR products were separated by agarose gel electrophoresis using a 2% gel [with a 1 in 50,000 dilution of GelRed® Nucleic Acid Gel Stain (41003, Biotinum) added] and 0.5% TBE buffer at 150V. The PCR products were observed using a Syngene PXi 4 system (with supporting GeneSys software) and images captured. The predicted product sizes of the seven primer pairs ranged from approximately 250-400bp. The GeneRuler 1Kb Plus Ladder (SM1333, Thermo Fisher Scientific; Lane 1) and Quick-Load 100bp Ladder (N04673S, New England Biolabs; Lane 7) were included as references. Lane 2, negative control; Lane 3, CLL-06; Lane 4, CLL-04; Lane 5, CLL-27; Lane 6, CLL-05.
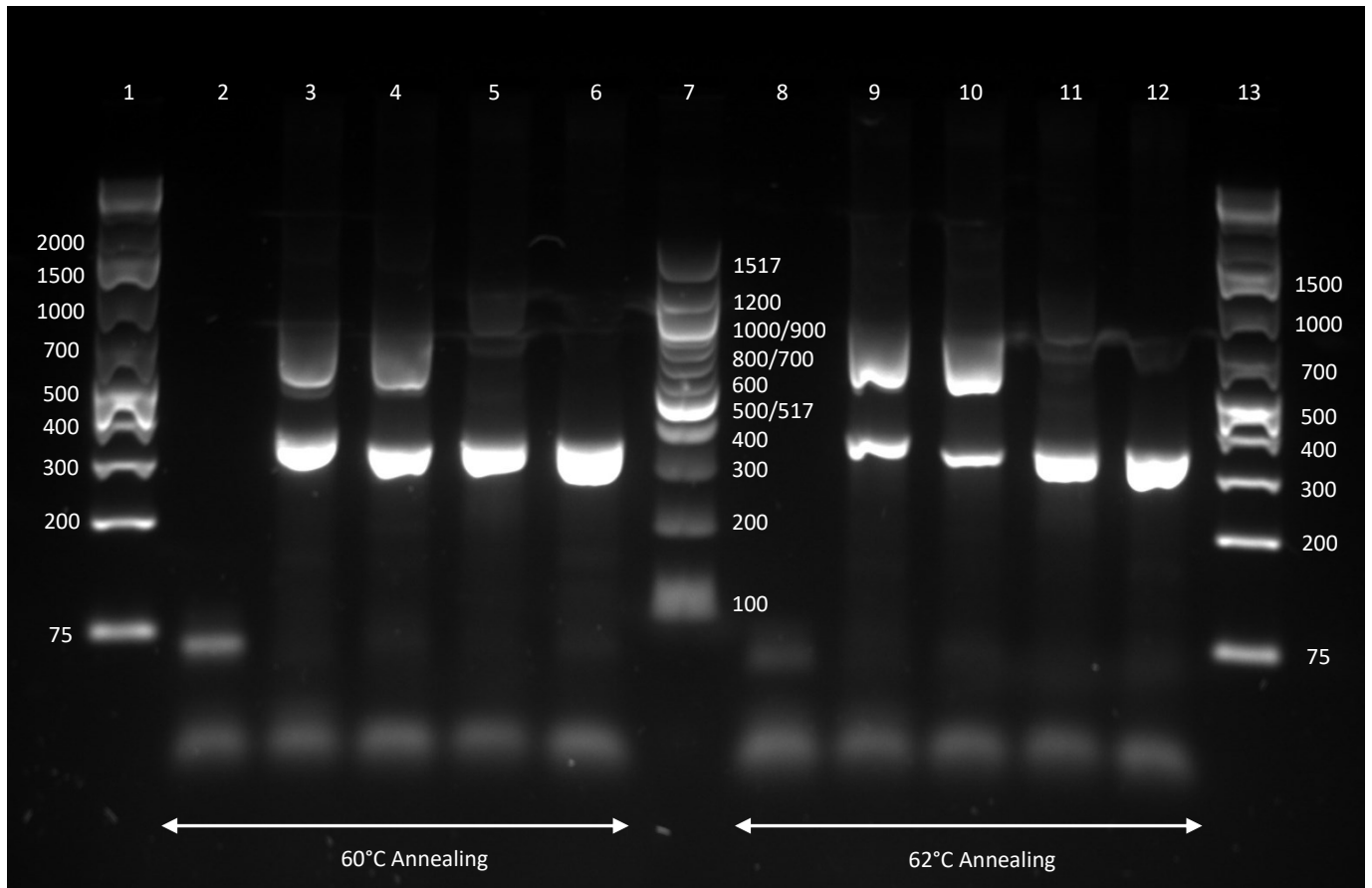
Figure 4.2: Amplification of CLL Ig V_H genes using annealing temperatures of 60°C and 62°C. DNA extracted from four CLL cases was amplified by multiplex PCR using annealing temperatures of 60°C and 62°C. PCR products were separated by agarose gel electrophoresis using a 2% gel [with a 1 in 50,000 dilution of GelRed® Nucleic Acid Gel Stain (41003, Biotinum) added] and 0.5% TBE buffer at 150V. The PCR products were observed using a Syngene PXi 4 system (with supporting GeneSys software) and images captured. The predicted product sizes of the seven primer pairs ranged from approximately 250-400bp. The GeneRuler 1Kb Plus Ladder (SM1333, Thermo Fisher Scientific; Lanes 1 and 13) and Quick-Load 100bp Ladder (N04673S, New England Biolabs; Lane 7) were included as references. Lanes 2 and 8, negative control; Lanes 3 and 9, CLL-06; Lanes 4 and 10, CLL-04; Lanes 5 and 11, CLL-27; Lanes 6 and 12, CLL-05.

Annealing temperatures of 59°C and 62°C both generated strong bands for all four CLL cases within the size range predicted for the seven primer pairs (approximately 250-400bp) (Figure 4.1-2). However, non-specific bands of >500bp were also observed for three of the cases, with strong non-specific bands of approximately 700bp being seen in CLL-06 and CLL-04 lanes. In contrast, an annealing temperature of 60°C maintained strong amplification of the *IGHV* while decreasing the intensity of all non-specific products. Thus, an annealing temperature of 60°C was selected for all subsequent PCR reactions due to the greater stringency of primer annealing.

4.3.2. CLINICAL AND CYTOGENETIC FEATURES OF CLL CASES

DNA was extracted and successfully analysed by Sanger Sequencing for seven females and twenty males with classical B-lymphocyte CLL (Table 4.1-2). Twenty cases were untreated and seven had received one or more previous therapies. The cytogenetics of most cases were not determined as the patients had stable disease and/or it was not clinically indicated. However, mutations/deletions involving *ATM* were found in two patients. Three patients had mutations/deletions affecting *TP53*. Deletions at 13q14 were found in three patients. All eight cases had a mutation or deletion as a single abnormality at the time of sample collection.

Table 4.1: Characteristics of patients with CLL whose V$_H$ genes showed ≥98% sequence homology with the nearest germline V$_H$ gene.

ID	Sex[†]	VH Gene	Percentage Sequence Homology	Treatment Status[‡]	Additional Cytogenetics[§]
CLL-03	M	V4-30	100	FCR	Del(11q)
CLL-05	M	V3-21	100	UT	TP53 WT
CLL-07	F	V4-39	100	UT	TP53 deletion
CLL-11	M	V3-33	100	UT	TP53 WT
CLL-15	M	V3-15	99.18	UT	N/D
CLL-19	M	V1-02	99.18	UT	N/D
CLL-21	M	V3-11	100	Ibrutinib	N/D
CLL-22	F	V1-69	100	Ibrutinib	N/D
CLL-24	M	V3-09	100	UT	Del(13q); TP53 WT
CLL-25	F	V3-33	100	UT	TP53 mutation
CLL-26	M	V1-69	100	UT	TP53 WT
CLL-27	M	V3-48	100	UT	TP53 WT

[†] M, male; F, female.

[‡] FCR, fludarabine, cyclophosphamide and rituximab chemotherapy; UT, untreated.

[§] Del(11q), deletion of the long arm of chromosome 11; TP53, tumour protein 53; WT, wild-type; N/D; not determined.

DNA was extracted and PCR amplification attempted for an additional sixteen CLL cases. However, the *IGHV* mutational status could not be determined for these cases due to low-quality DNA inhibiting primer annealing and/or the PCR product yield being insufficient for Sanger Sequencing (i.e., <75ng of extracted DNA). Additionally, the *IGHV* mutational status could not be determined using Unipro UGENE for two patients due to the presence of two bands at approximately 300bp, resulting in a heterogeneous DNA sequence which could not accurately be compared to the germline sequence (Figure 4.3). To successfully assign these patients to a *IGHV* mutational status subgroup, PCR amplification of DNA with individual

primer sets (e.g., Vh1 FR1 and JH, Vh2 FR1 and JH, etc.) would need to be carried out to try to identify the bands being produced by the two different primer sets. However, this additional analysis could not be achieved during the time frame of this study.

Table 4.2: Characteristics of patients with CLL whose V$_H$ genes showed <98% sequence homology with the nearest germline V$_H$ gene.

ID	Sex[†]	VH Gene	Percentage Sequence Homology	Treatment Status[‡]	Additional Cytogenetics[§]
CLL-01	M	V3-48	97.94	UT	Del(13q)
CLL-02	F	V3-23	95.12	UT	N/D
CLL-04	M	V3-07	88.46	UT	N/D
CLL-06	F	V2-05	94.12	FCR	Del(13q)
CLL-08	M	V3-53	95.47	UT	N/D
CLL-09	M	V3-33	90.61	UT	TP53 mutation
CLL-10	M	V3-15	97.64	UT	ATM deletion
CLL-12	M	V3-21	85.43	T	N/D
CLL-13	F	V3-33	95.98	UT	N/D
CLL-14	F	V2-23	94.54	UT	N/D
CLL-16	M	V3-48	91.87	UT	N/D
CLL-17	M	V3-21	97.38	Chemoimmunotherapy	N/D
CLL-18	M	V3-21	88.64	UT	N/D
CLL-20	M	V1-02	96.55	Ibrutinib	N/D
CLL-23	M	V2-05	92.50	UT	N/D

[†] M, male; F, female.

[‡] FCR, fludarabine, cyclophosphamide and rituximab chemotherapy; UT, untreated; T, treated.

[§] Del(11q), deletion of the long arm of chromosome 11; TP53, tumour protein 53; N/D; not determined; ATM, ataxia telangiectasia mutated gene.
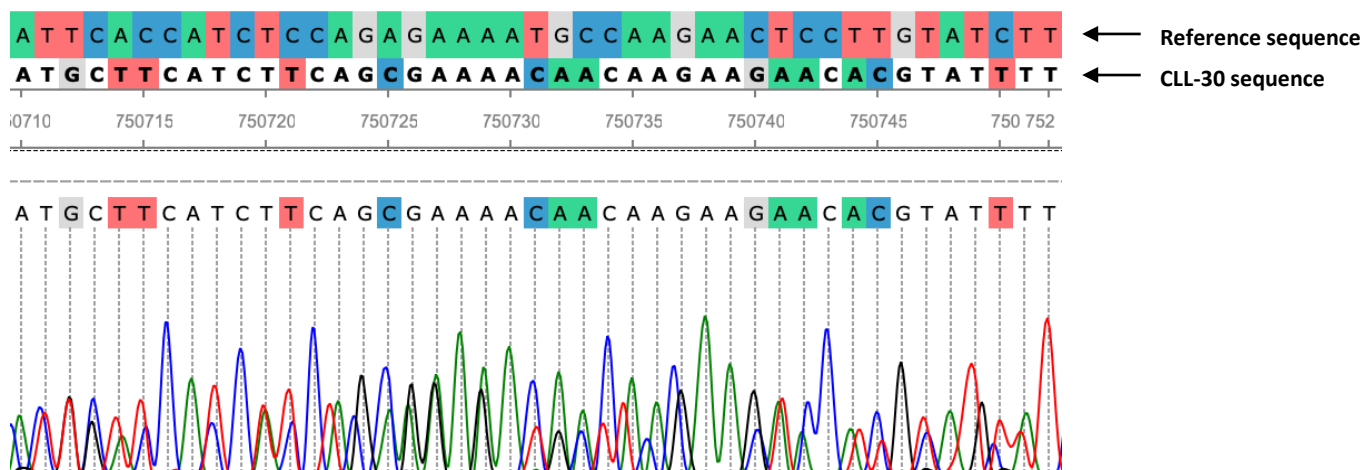
Figure 4.3: Sanger Sequencing data analysis for a CLL case with a heterogeneous *IGHV* sequence. Following Sanger Sequencing of purified PCR fragments from CLL-30 and alignment against the reference sequence using Unipro UGENE (version 36), two *IGHV* sequences were observed. This was caused by the presence of two bands of similar molecular weight, which could not be excised individually, following PCR amplification of extracted DNA.

4.4 DETERMING THE EFFECTS OF *IGHV* MUTATIONAL STATUS ON SIGNAL INHIBITOR-MEDIATED MORPHOLOGICAL RESPONSES

Distinct shape changes were observed following treatment of CLL cases with signal inhibitors. Cytoskeletal-mediated morphological changes and associated behavioural responses were largely independent of *IGHV* mutational status.

4.4.1. COMPARING CLL SHAPE CHANGES FOLLOWING TREATMENT WITH SMALL MOLECULE INHIBITORS

To determine if *IGHV* mutational status effects the morphological response(s) of CLL cells to clinically relevant small molecule inhibitors, four UM-CLL and three M-CLL cases (Table 4.1-2) were fixed at 1 h and examined using SEM and graphical representation of shape parameters. For representative images of the shape changes observed following drug treatments for each CLL case see Figure 4.5-6. The histograms being discussed in this section are shown in Figure

4.7-9. Exact *p*-values for DMSO vs small molecule inhibitor treatment for each case are listed in Table 4.3-5.

Resting morphology: CLL cases demonstrated varying phenotypic features on SEM analyses (Figure 4.4). These morphological differences were independent of *IGHV* mutational status, with DMSO-treated (control) cells from both subsets (*IGHV*-unmutated: CLL-11 and CLL-26; *IGHV*-mutated: CLL-01) forming characteristic bi-modal distributions of cell shapes. Cells within these populations were predominantly small and globular with densely packed microvilli. Larger, more irregular cells were also present and generally represented motile cells with distinct front-tail polarity and posterior attachment points. Microprojections were less frequently seen on the surface of migrating cells. Filopodia formation and distribution differed from cases-to-case, with case CLL-11 exhibiting particularly long, polarised filopodial projects. Greater variation in cell size, circularity and surface features was observed in the remaining four CLL cases examined.

Resting cells from case CLL-03 (*IGHV*-unmutated) were large and highly irregular, with numerous ruffles, filopodia and long microvilli. In addition, CLL-03 cells demonstrated distinct anterior-posterior morphology, indicating that cells were readily undergoing elongated-type motility.

Control CLL-27 (*IGHV*-unmutated) cells displayed notable cell spreading across the adhesive substratum and frequent filopodia. Villous structures were less densely packed on the CLL-27 cell surface.

The CLL-02 (*IGHV*-mutated) resting population was typically large and irregular, with 'ridge-like' profiles on the cell surface rather than villous structures. Fine filopodia were observed extending between adjacent CLL-02 cells.

Although case CLL-09 (*IGHV*-mutated) showed a relatively characteristic bi-modal distribution of cell area and perimeter, the circularity histogram formed an almost Gaussian (i.e., normal) distribution of values. Polarised filopodia were typically seen extending from posterior attachment points of motile cell, whereas non-polarised projects extended from large cells exhibiting cytoskeletal spreading. Microvilli were typically frequent on the CLL-09 cell surface; however, when absent, ridge-like profiles were the prominent cell surface features.
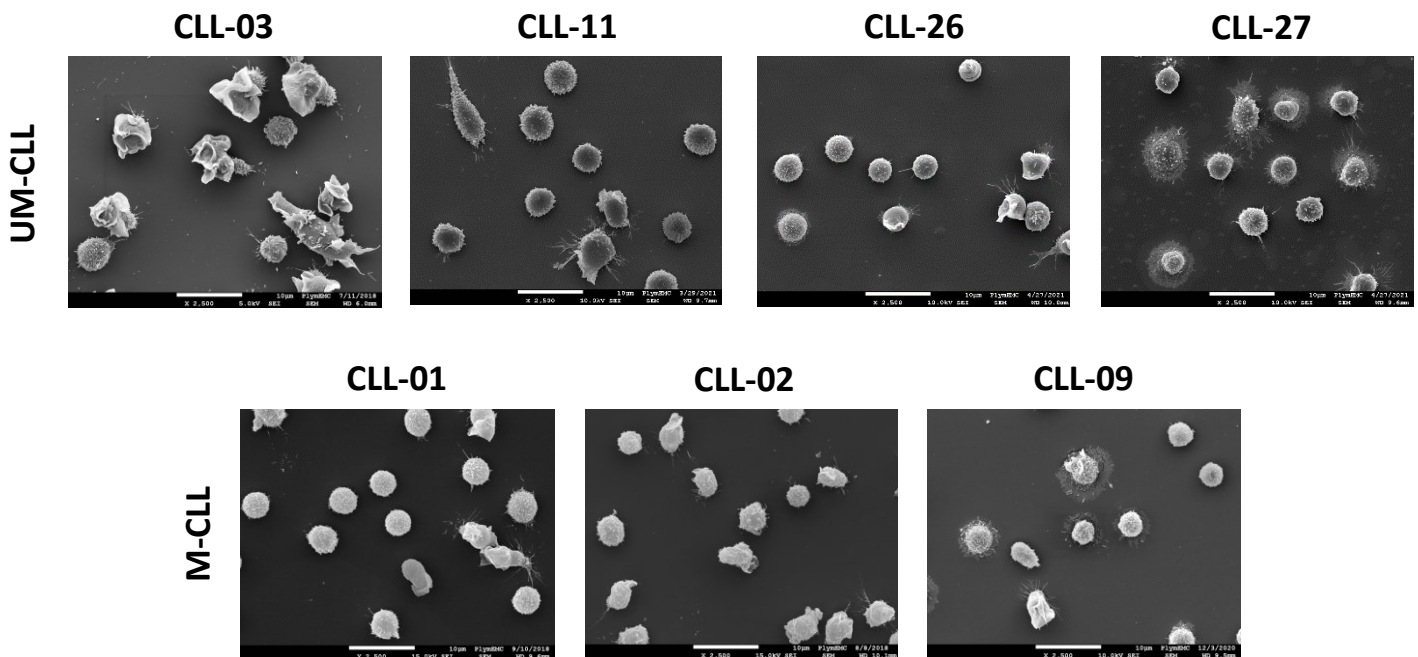
Figure 4.4: Resting morphology of UM-CLL and M-CLL cells. Following 6 days culture, CLL cases were treated with DMSO for 1 h, fixed and processed. Cells were observed using a JEOL 7001 F SEM at 2500x and images were captured using supporting software.

Ibrutinib treatment: Histograms showed a significant shift towards smaller (area and perimeter), globular cells with ibrutinib treatment in four of the CLL cases (*IGHV*-unmutated: CLL-26 and CLL-27; *IGHV*-mutated: CLL-01 and CLL-02) examined (Figure 4.7-9; Table 4.3-5). The reduction in cell spreading was particularly notable in case CLL-27 (Figure 4.5-6). The remaining cases (*IGHV*-unmutated: CLL-03 and CLL-11; *IGHV*-mutated: CLL-09) did not demonstrate any significant alterations in shaper parameters with ibrutinib exposure, with the exception of cases CLL-03 and CLL-11 which both exhibited a significant increase in circularity alone. Cell surface features of all cases were largely similar to control cells. Villous structures and filopodia were still present following ibrutinib treatment; however, their relative frequencies appeared to be reduced. Morphological responses to ibrutinib were independent of the presence/absence of *IGHV* mutations.

Y-27632 treatment: Non-polarised filopodial networks were seen within CLL populations following Y-27632 treatment; however, the size and complexity of these networks differed from case-to-case (Figure 4.5-6). In three of the Y-27632-treated CLL cases (*IGHV*-unmutated: CLL-11; *IGHV*-mutated: CLL-01 and CLL-09), changes in filopodia formation correlated with a significant increase in cell size and irregularity (Figure 4.7-9; Table 4.3-5). Y-27632-mediated alterations in filopodia formation were not reflected in shape parameter histograms for the remaining CLL cases. Case CLL-03 (*IGHV*-unmutated) displayed a significant decrease in circularity alone compared to control cells, whereas case CLL-27 (*IGHV*-unmutated) exhibited a significant decrease in cell size combined with an increase in circularity due to reduced cell spreading. No significant changes in shape parameter were observed in cases CLL-02 (*IGHV*-mutated) and CLL-26 (*IGHV*-unmutated) despite numerous filopodial projections and ruffles,

which were unusual in the case of CLL-26, being formed following Y-27632 treatment.

Morphological responses to Y-27632 were independent *IGHV* mutational status.
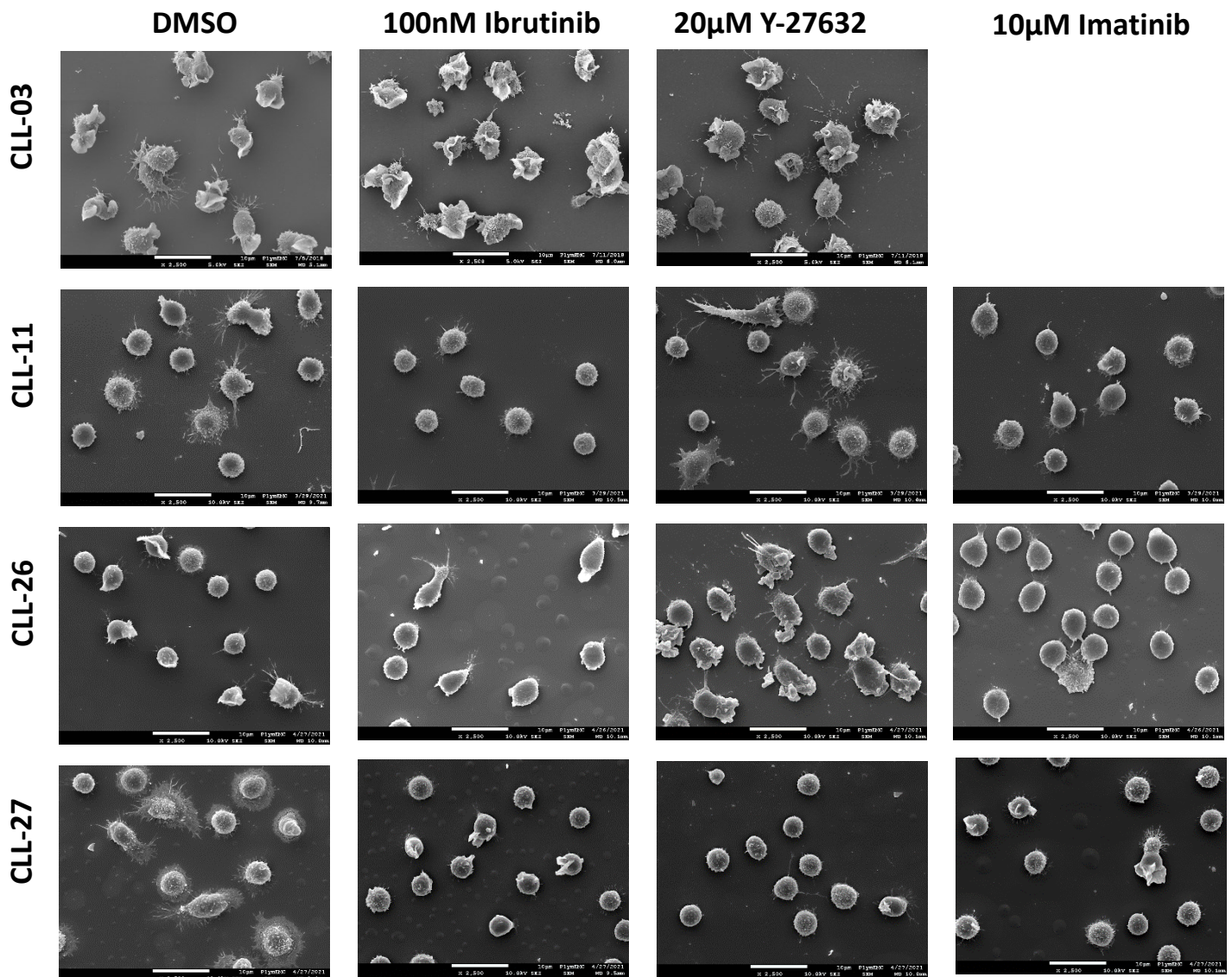
Figure 4.5: Effects of small molecule inhibitors on morphology of UM-CLL cells. Following 6 days culture, CLL cases were treated with either DMSO, ibrutinib, Y-27632 or imatinib for 1 h, fixed and processed. Cells were observed using a JEOL 7001 F SEM at 2500x and images were captured using supporting software. Imatinib was not available at the time that CLL-03 cells were treated.
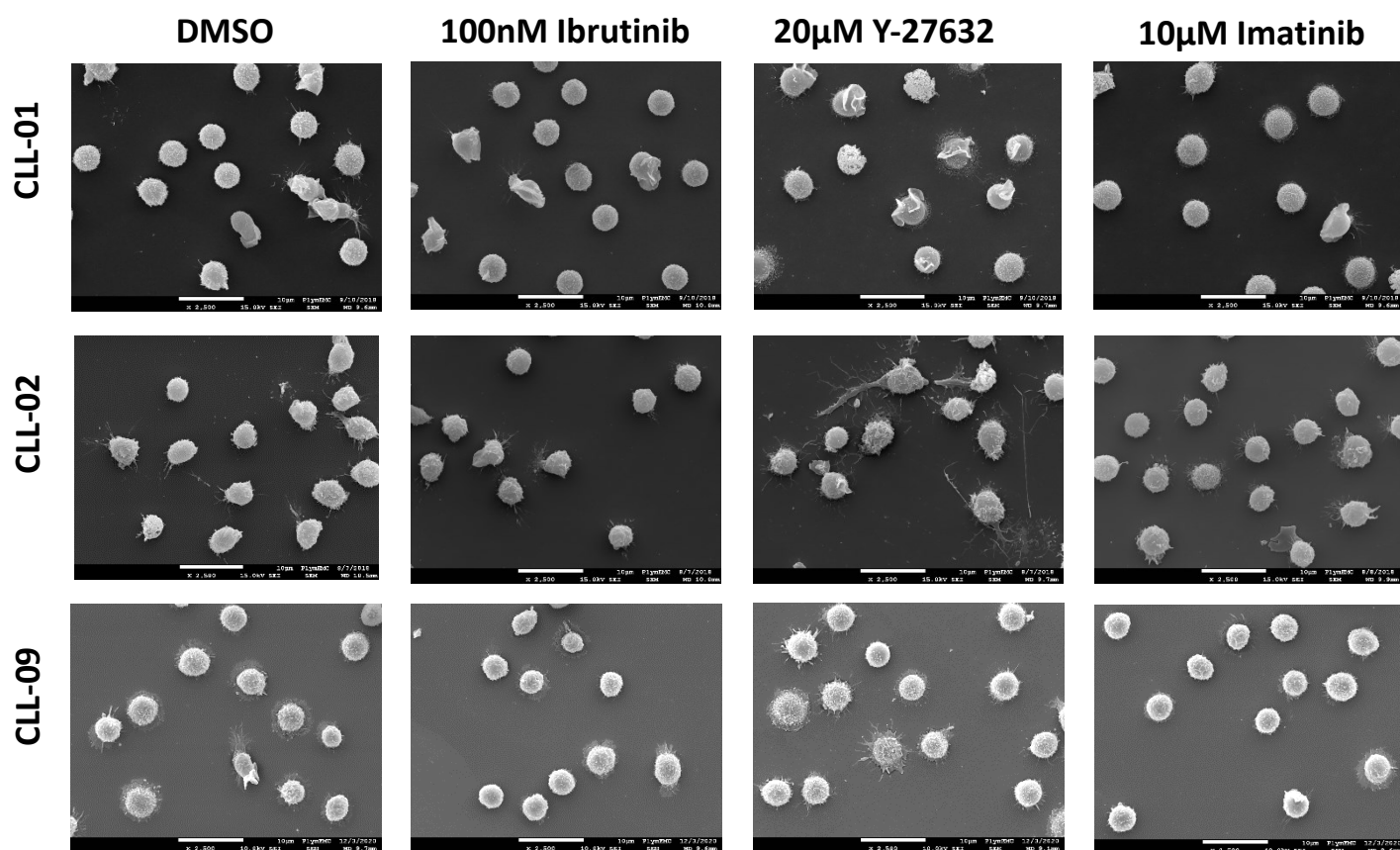
Figure 4.6: Effects of small molecule inhibitors on morphology of M-CLL cells. Following 6 days culture, CLL cases were treated with either DMSO, ibrutinib, Y-27632 or imatinib for 1 h, fixed and processed. Cells were observed using a JEOL 7001 F SEM at 2500x and images were captured using supporting software.
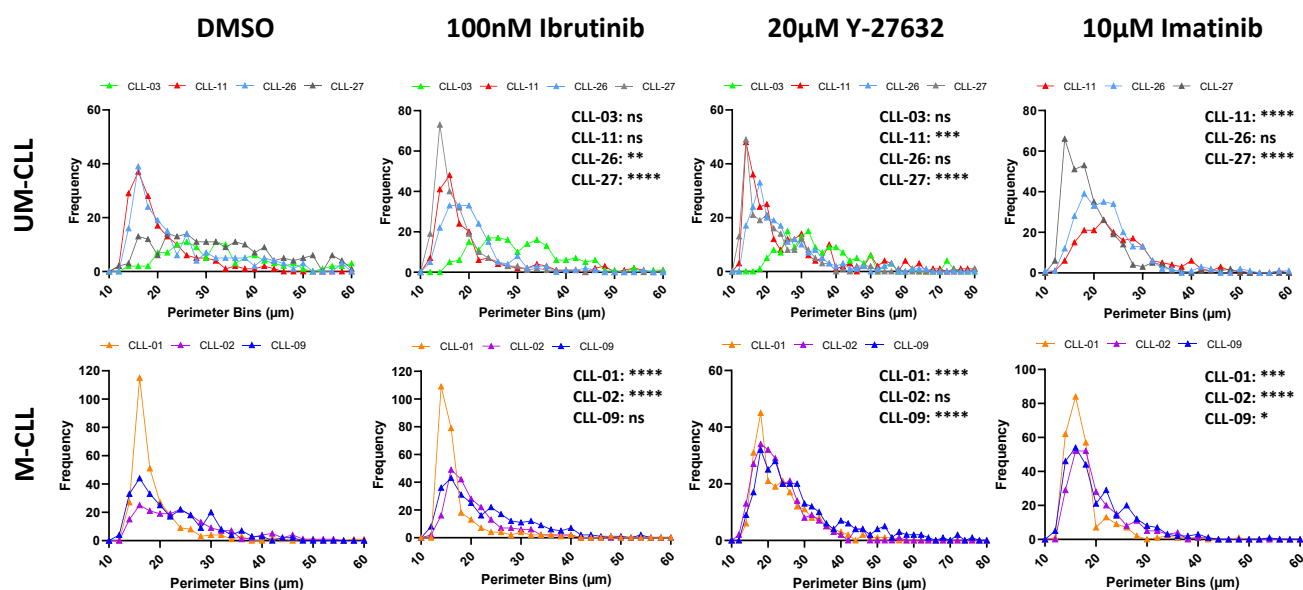
Figure 4.7: Effects of small molecule inhibitors on the perimeter of UM-CLL and M-CLL cells. Following 6 days culture, CLL cases were treated with either DMSO, ibrutinib, Y-27632 or imatinib for 1 h, fixed and processed. Cells were observed using a JEOL 7001 F SEM at 1000x and 2500x, and images were captured using supporting software. Binary images were generated from 1000x .tif images using ImageJ, and the perimeter of cells measured. Frequency distribution histograms were created using GraphPad Prism. p-values for DMSO vs treatments were calculated using the Mann-Whitney U test. ****$p < 0.0001$; ***$p < 0.001$; **$p < 0.01$; *$p < 0.05$; not significant (ns) $p > 0.05$. Imatinib was not available at the time that CLL-03 cells were treated.
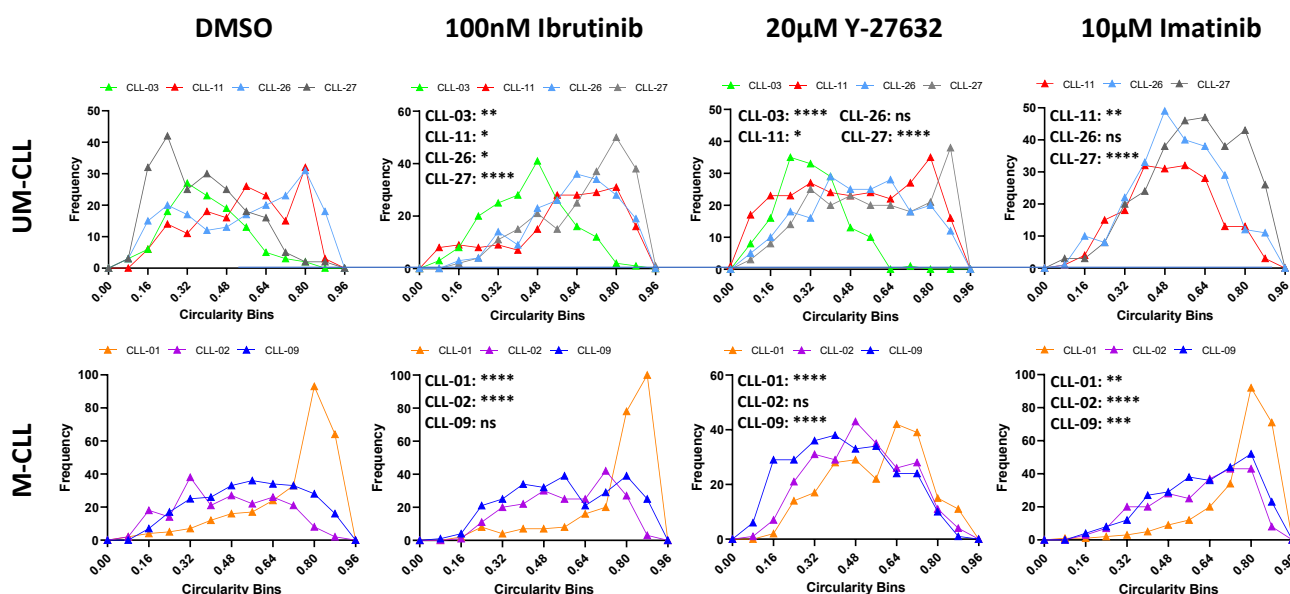
Figure 4.8: Effects of small molecule inhibitors on the circularity of UM-CLL and M-CLL cells. Following 6 days culture, CLL cases were treated with either DMSO, ibrutinib, Y-27632 or imatinib for 1 h, fixed and processed. Cells were observed using a JEOL 7001 F SEM at 1000x and 2500x, and images were captured using supporting software. Binary images were generated from 1000x .tif images using ImageJ, and the circularity of cells measured. Frequency distribution histograms were created using GraphPad Prism. *p*-values for DMSO vs treatments were calculated using the Mann-Whitney U test. ****$p < 0.0001$; ***$p < 0.001$; **$p < 0.01$; *$p < 0.05$; not significant (ns) $p > 0.05$. Imatinib was not available at the time that CLL-03 cells were treated.

Imatinib treatment: Imatinib treatment resulted in relatively uniform populations of small, globular cells in four of the cases (*IGHV*-unmutated: CLL-27; *IGHV*-mutated: CLL-01, CLL-02 and CLL-09) studied (Figure 4.5-6). Histograms demonstrated a significant increase in circularity combined with a decrease in both cell perimeter and area (Figure 4.7-9; Table 4.3-5). The exception being case CLL-09 which instead showed a significant decrease in perimeter but not area. The reduction in cell spreading following imatinib exposure was particular apparent in case CLL-27, with cells displaying a more characteristic B-lymphocyte morphology. Case CLL-26 (*IGHV*-unmutated) did not demonstrate any significant alterations in shape parameters with imatinib treatment and cell morphologies mimicked those observed in

control cells. Case CLL-11 (*IGHV*-unmutated) exhibited a significant increase in cell size (perimeter and area) and a decrease in circularity. Surface features in case CLL-11 were largely similar to control cells with imatinib treatment. Microvilli were the predominant surface feature in all CLL populations following imatinib treatment, with the exception of CLL-26 cells which lacked villous structures. Filopodia were present; however, they appeared to be shorter and fewer in number.
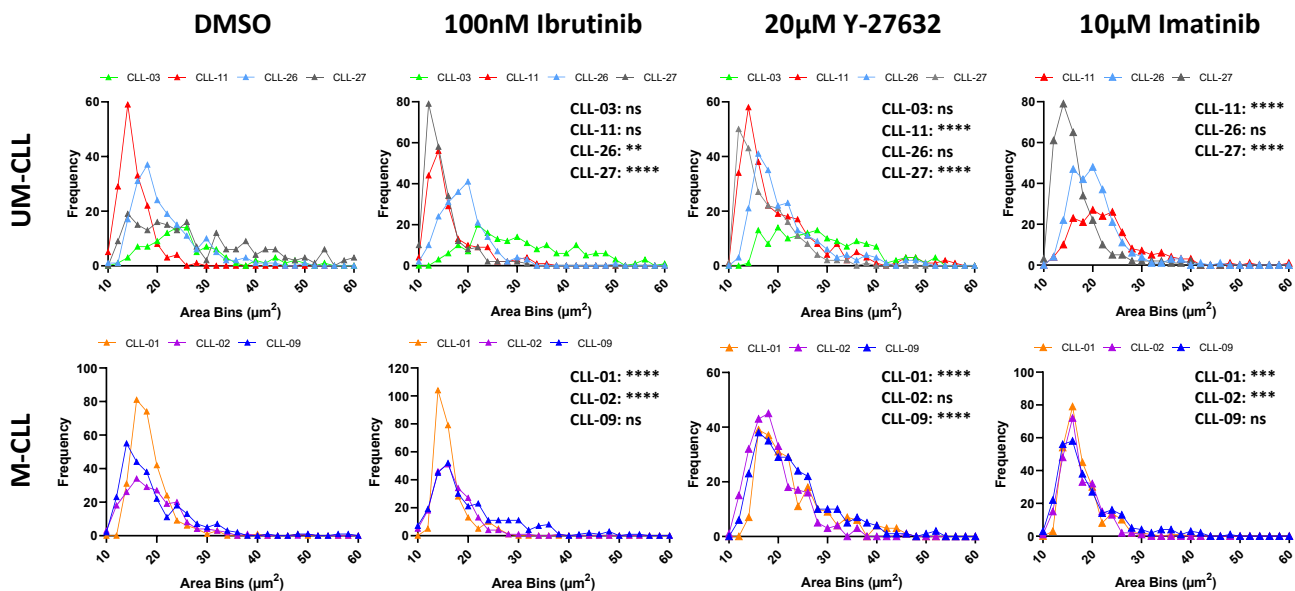
Figure 4.9: Effects of small molecule inhibitors on the area of UM-CLL and M-CLL cells. Following 6 days culture, CLL cases were treated with either DMSO, ibrutinib, Y-27632 or imatinib for 1 h, fixed and processed. Cells were observed using a JEOL 7001 F SEM at 1000x and 2500x, and images were captured using supporting software. Binary images were generated from 1000x .tif images using ImageJ, and the area of cells measured. Frequency distribution histograms were created using GraphPad Prism. *p*-values for DMSO vs treatments were calculated using the Mann-Whitney U test. ****$p < 0.0001$; ***$p < 0.001$; **$p < 0.01$; *$p < 0.05$; not significant (ns) $p > 0.05$. Imatinib was not available at the time that CLL-03 cells were treated.

Table 4.3: Perimeter - summary of the changes in shape of CLL subgroups following 1 h small molecule inhibitor treatment.

Case	IGHV status*	Conditions	p-value†	Increase/decrease in perimeter compared to DMSO control
CLL-01	M	DMSO vs 100nM Ibrutinib	<0.0001 ****	Decrease
		DMSO vs 20µM Y-27632	<0.0001 ****	Increase
		DMSO vs 10µM Imatinib	0.0002 ***	Decrease
CLL-02	M	DMSO vs 100nM Ibrutinib	<0.0001 ****	Decrease
		DMSO vs 20µM Y-27632	0.2644 ns‡	N/A§
		DMSO vs 10µM Imatinib	<0.0001 ****	Decrease
CLL-03	UM	DMSO vs 100nM Ibrutinib	0.1080 ns	N/A
		DMSO vs 20µM Y-27632	0.1602 ns	N/A
CLL-09	M	DMSO vs 100nM Ibrutinib	0.6200 ns	N/A
		DMSO vs 20µM Y-27632	<0.0001 ****	Increase
		DMSO vs 10µM Imatinib	0.0117 *	Decrease
CLL-11	UM	DMSO vs 100nM Ibrutinib	0.1633 ns	N/A
		DMSO vs 20µM Y-27632	0.0001 ***	Increase
		DMSO vs 10µM Imatinib	<0.0001 ****	Increase
CLL-26	UM	DMSO vs 100nM Ibrutinib	0.0022 **	Decrease
		DMSO vs 20µM Y-27632	0.4040 ns	N/A
		DMSO vs 10µM Imatinib	0.6872 ns	N/A
CLL-27	UM	DMSO vs 100nM Ibrutinib	<0.0001 ****	Decrease
		DMSO vs 20µM Y-27632	<0.0001 ****	Decrease
		DMSO vs 10µM Imatinib	<0.0001 ****	Decrease

* M, mutated IGHV; UM, unmutated IGHV.

† p-values were determined using the non-parametric Mann-Whitney U test for unpaired data sets.

‡ ns, not significant.

§ N/A, not applicable.

Table 4.4: Circularity - summary of the changes in shape of CLL subgroups following 1 h small molecule inhibitor treatment.

Case	*IGHV* status[*]	Conditions	*p*-value[†]	Increase/decrease in circularity compared to DMSO control
CLL-01	M	DMSO vs 100nM Ibrutinib	<0.0001 ****	Increase
		DMSO vs 20µM Y-27632	<0.0001 ****	Decrease
		DMSO vs 10µM Imatinib	0.0036 **	Increase
CLL-02	M	DMSO vs 100nM Ibrutinib	<0.0001 ****	Increase
		DMSO vs 20µM Y-27632	0.0728 ns[‡]	N/A[§]
		DMSO vs 10µM Imatinib	<0.0001 ****	Increase
CLL-03	UM	DMSO vs 100nM Ibrutinib	0.0017 **	Increase
		DMSO vs 20µM Y-27632	<0.0001 ****	Decrease
CLL-09	M	DMSO vs 100nM Ibrutinib	0.6653 ns	N/A
		DMSO vs 20µM Y-27632	<0.0001 ****	Decrease
		DMSO vs 10µM Imatinib	0.0001 ***	Increase
CLL-11	UM	DMSO vs 100nM Ibrutinib	0.0492 *	Increase
		DMSO vs 20µM Y-27632	0.0199 *	Decrease
		DMSO vs 10µM Imatinib	0.0082 **	Decrease
CLL-26	UM	DMSO vs 100nM Ibrutinib	0.0134 *	Increase
		DMSO vs 20µM Y-27632	0.1465 ns	N/A
		DMSO vs 10µM Imatinib	0.1428 ns	N/A
CLL-27	UM	DMSO vs 100nM Ibrutinib	<0.0001 ****	Increase
		DMSO vs 20µM Y-27632	<0.0001 ****	Increase
		DMSO vs 10µM Imatinib	<0.0001 ****	Increase

[*] M, mutated *IGHV*; UM, unmutated *IGHV*.

[†] *p*-values were determined using the non-parametric Mann-Whitney U test for unpaired data sets.

[‡] ns, not significant.

[§] N/A, not applicable.

Table 4.5: Area - summary of the changes in shape of CLL subgroups following 1 h small molecule inhibitor treatment.

Case	*IGHV* status[*]	Conditions	*p*-value[†]	Increase/decrease in area compared to DMSO control
CLL-01	M	DMSO vs 100nM Ibrutinib	<0.0001 ****	Decrease
		DMSO vs 20µM Y-27632	<0.0001 ****	Increase
		DMSO vs 10µM Imatinib	0.0005 ***	Decrease
CLL-02	M	DMSO vs 100nM Ibrutinib	<0.0001 ****	Decrease
		DMSO vs 20µM Y-27632	0.7273 ns[‡]	N/A[§]
		DMSO vs 10µM Imatinib	0.0005 ***	Decrease
CLL-03	UM	DMSO vs 100nM Ibrutinib	0.1903 ns	N/A
		DMSO vs 20µM Y-27632	0.7681 ns	N/A
CLL-09	M	DMSO vs 100nM Ibrutinib	0.0829 ns	N/A
		DMSO vs 20µM Y-27632	<0.0001 ****	Increase
		DMSO vs 10µM Imatinib	0.9331 ns	N/A
CLL-11	UM	DMSO vs 100nM Ibrutinib	0.7905 ns	N/A
		DMSO vs 20µM Y-27632	<0.0001 ****	Increase
		DMSO vs 10µM Imatinib	<0.0001 ****	Increase
CLL-26	UM	DMSO vs 100nM Ibrutinib	0.0013 **	Decrease
		DMSO vs 20µM Y-27632	0.6376 ns	N/A
		DMSO vs 10µM Imatinib	0.1125 ns	N/A
CLL-27	UM	DMSO vs 100nM Ibrutinib	<0.0001 ****	Decrease
		DMSO vs 20µM Y-27632	<0.0001 ****	Decrease
		DMSO vs 10µM Imatinib	<0.0001 ****	Decrease

[*] M, mutated *IGHV*; UM, unmutated *IGHV*.

[†] *p*-values were determined using the non-parametric Mann-Whitney U test for unpaired data sets.

[‡] ns, not significant.

[§] N/A, not applicable.

Summary: Although primary CLL cells exhibited pronounced differences in their resting morphology, distinct changes in shape parameters were observed, using high-resolution SEM and morphometric analyses, in leukaemic cell populations following signal inhibition, independent of *IGHV* mutational status. Ibrutinib-mediated BTK inhibition generally resulted in the formation of one main homotypic population of globular cells, suggesting that elongated-type cell migration had been impaired (Table 4.3-5). Likewise, imatinib-treated CLL cases typically displayed a shift towards a more globular phenotype, indicating that ABL1 inhibition may disrupt F-actin polarisation in a similar manner to BTK blockage. In contrast, CLL populations were composed of large leukemic cells with extensive, non-polarised cytoskeletal projections following ROCK inhibition. Impaired retraction of cellular protrusions and establishment of anterior-posterior morphology suggested that Y-27632-treated cells were unable to effectively migrate across the substratum.

The unique morphological changes observed here indicated that directional cell migration and cell-to-cell interactions were impaired with blockage of BTK, ABL1 and ROCK signalling pathways. However, SEM images and shape parameter histograms only allowed these behavioural alterations to be inferred. Additional investigations were required to confirm the functional effect(s) of the disrupted cytoskeletal dynamics induced by signal inhibition.

4.4.2. COMPARING HOMOTYPIC CELLULAR INTERACTIONS FOLLOWING TREATMENT WITH SMALL MOLECULE INHIBITORS

To establish if *IGHV* mutational status effects homotypic cellular interactions (i.e., binding of a cell to one or more similar cells) between CLL cells treated with clinically relevant signal inhibitors, three UM-CLL and four M-CLL cases (Table 4.1-2) were fixed at 1 h and examined using immunofluorescence staining and DBSCAN analyses. An example of the output of DBSCAN analyses is shown in Figure 4.10.
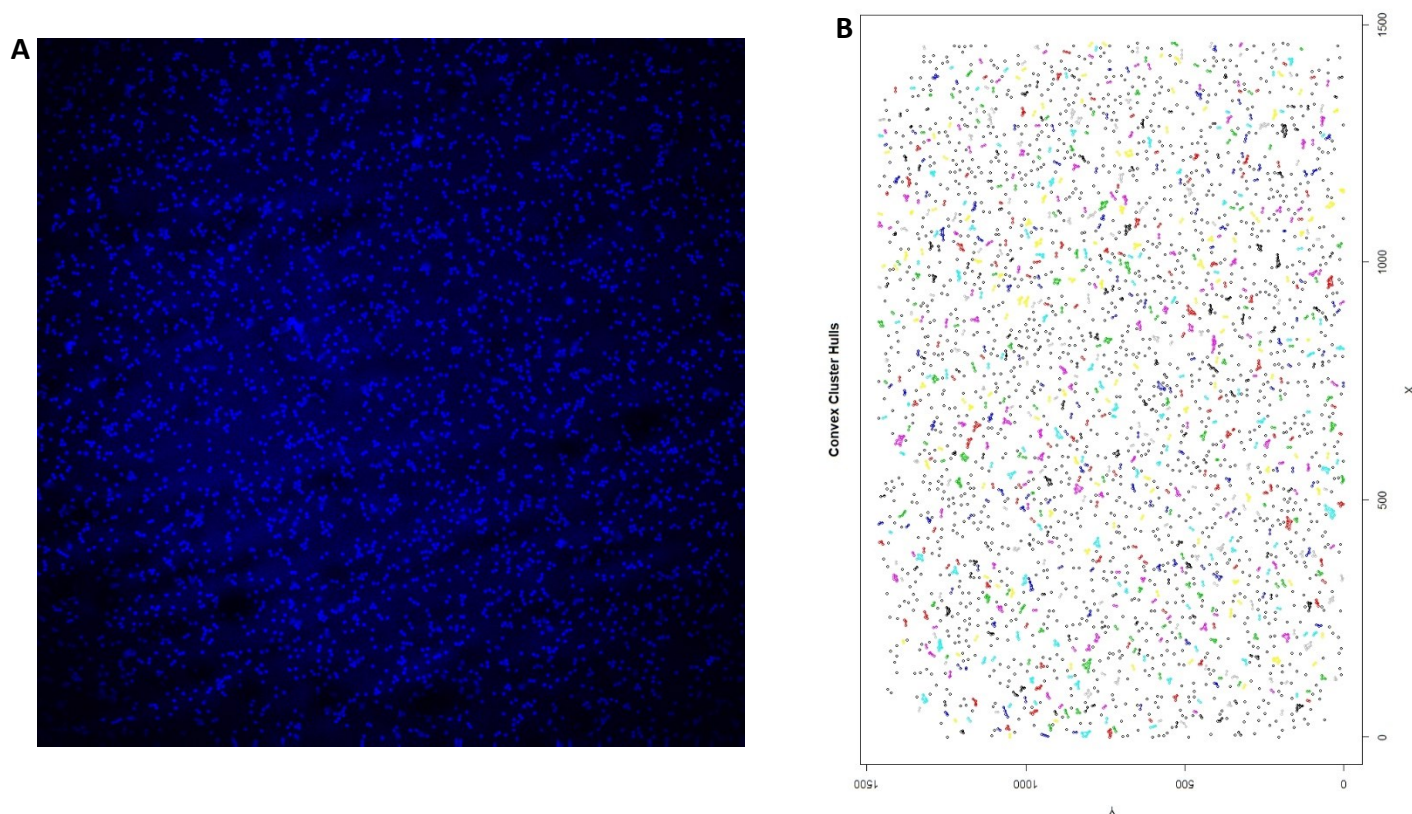
Figure 4.10: DBSCAN analysis of control homotypic CLL cell interactions. (A) Following 6 days culture, CLL-04 cells were treated with DMSO for 1 h, fixed and the DNA stained with DAPI (blue). The image was acquired using a Leica SE Confocal Microscope with the use of a 10x dry objective. Within ImageJ, the DAPI image was converted to a black-and-white image and, using the 'Watershed' tool, clumps of cells were split into individual cells. An image containing single points which represented individual lymphocyte nuclei was then created using the 'Ultimate points' tool and the x- and y-coordinate of each point determined. (B) Coordinates were exported as a .cvs file which could be directly used in R for DBSCAN clustering analysis. The analysis was exported as a hull plot for visualisation of homotypic cellular interactions within the CLL population, and as a .cvs file for graphical representation and statical analysis in GraphPad Prism.

The results being discussed in this section are shown in Figure 4.11-12. Exact *p*-values for DMSO vs small molecule inhibitor treatment for each case are listed in Table 4.6.

Control cells: The DMSO-treated (control) populations of both UM-CLL and M-CLL cases were predominantly comprised of single cells and cells in duplets (i.e., two cells interacting). Clusters containing three or more cells were less frequent. Interestingly, case CLL-02 (*IGHV*-mutated) had a larger proportion of cells forming clusters of all sizes compared to other CLL cases.

Ibrutinib treatment: Following ibrutinib treatment, all four CLL cases exhibiting mutated *IGHV* showed a significant decrease in the proportion of cells forming clusters compared to control populations, indicating that cellular interactions had been reduced in this CLL sub-group. However, this decrease was less apparent in the case of CLL-06.

In contrast, the *IGHV*-unmutated CLL populations exhibited varying changes in cellular interactions with ibrutinib treatment. The proportion of CLL-03 and CLL-05 cells establishing clusters was significantly increased following ibrutinib treatment, suggesting cellular interactions had been promoted. Indeed, the proportion of CLL-03 cell assembling into clusters of 5 or more cells was similar to the proportion of single cells after ibrutinib exposure. Case CLL-11 showed no significant changes in the proportion of cells forming clusters with ibrutinib treatment.
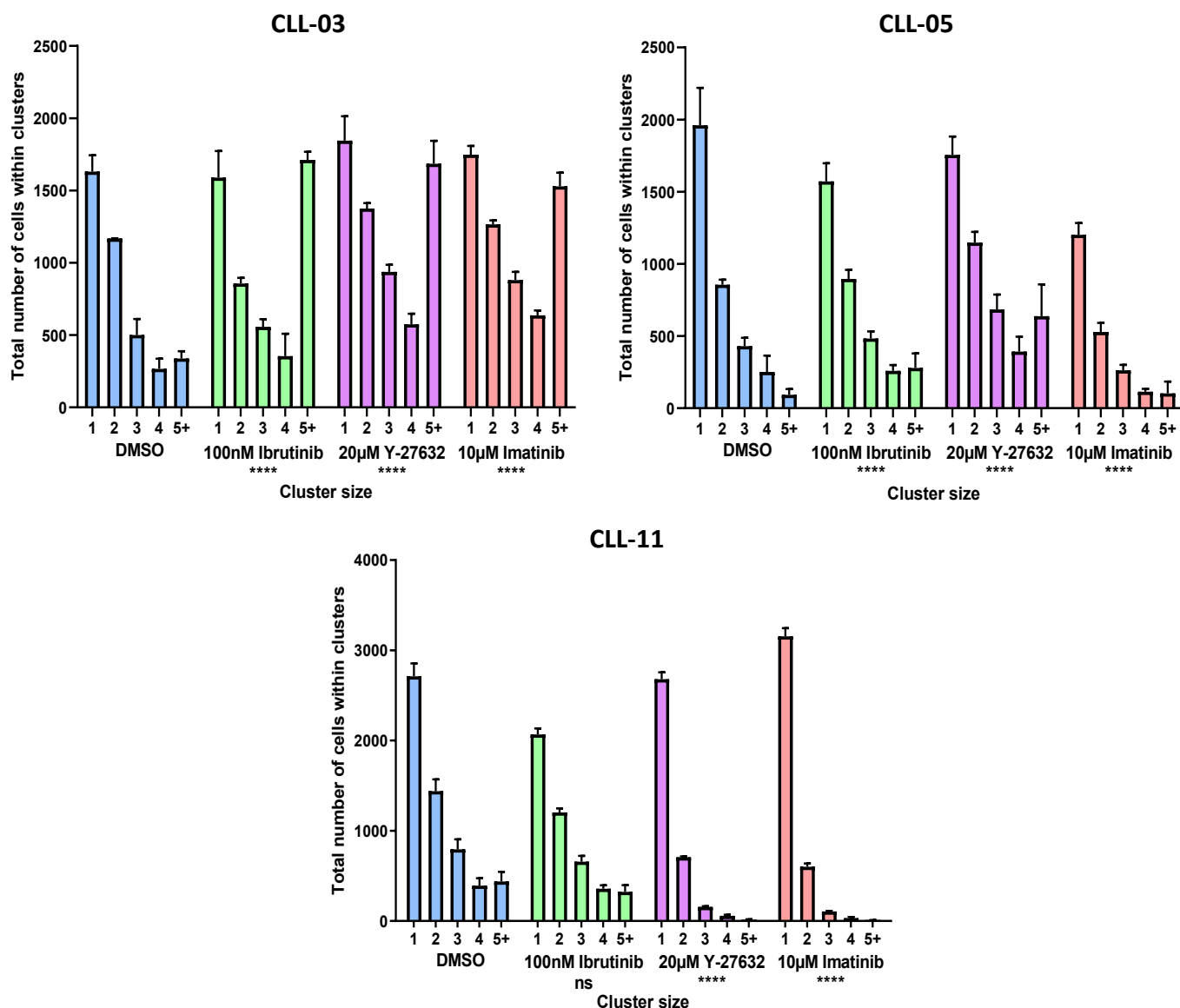
Figure 4.11: Effects of small molecule inhibitors on homotypic cellular interactions of UM-CLL cells. Following 6 days culture, UM-CLL cases were treated with either DMSO, ibrutinib, Y-27632 or imatinib for 1 h, fixed and stained. Cells within three fields of view were observed using a Leica SE Confocal Microscope with the use of a 10x dry objective. 'Ultimate point' images containing single points which represented individual lymphocyte nuclei were created using the DAPI (blue) channel and ImageJ. DBSCAN analyses were carried out using the R and RStudio programs with the Dbscan and tidyverse packages. Bar graphs showing the number of cells within clusters were created using GraphPad Prism. *p*-values for DMSO vs treatments were calculated using the Chi-square test. ****$p < 0.0001$; ***$p < 0.001$; **$p < 0.01$; *$p < 0.05$; not significant (ns) $p > 0.05$. Error bars represent standard error of the mean. For each CLL case n = 3.

Figure 4.12: Effects of small molecule inhibitors on homotypic cellular interactions of M-CLL cells. Following 6 days culture, M-CLL cases were treated with either DMSO, ibrutinib, Y-27632 or imatinib for 1 h, fixed and stained. Cells within three fields of view were observed using a Leica SE Confocal Microscope with the use of a 10x dry objective. 'Ultimate point' images containing single points which represented individual lymphocyte nuclei were created using the DAPI (blue) channel and ImageJ. DBSCAN analyses were carried out using the R and RStudio programs with the Dbscan and tidyverse packages. Bar graphs showing the number of cells within clusters were created using GraphPad Prism. p-values for DMSO vs treatments were calculated using the Chi-square test. ****$p < 0.0001$; ***$p < 0.001$; **$p < 0.01$; *$p < 0.05$; not significant (ns) $p > 0.05$. Error bars represent standard error of the mean. For each CLL case n = 3.

Y-27632 treatment: Varying shifts in homotypic cellular interaction were seen with Y-27632 treatment, independent of *IGHV* mutational status. The proportion of *IGHV*-mutated CLL-02 and CLL-09 cells establishing clusters was significantly decreased following Y-27632 treatment compared to control populations, with the formation of clusters of four or more cells being particularly decreased in both cases. However, Y-27632-treated CLL-06 (*IGHV*-mutated) cells exhibited a significant increase in the proportion of cells assembling into clusters of all sizes, but particularly clusters of five or more cell. The proportion of *IGHV*-mutated CLL-04 cells forming clusters was not significantly altered with Y-27632 exposure.

IGHV-unmutated cases CLL-03 and CLL-05 also showed a significant increase in the proportion of cells establishing clusters compared to control populations with Y-27632 treatment. Indeed, the proportion of CLL-03 cells forming clusters of five or more cells was similar to that of single cells. In contrast, CLL-11 cells (*IGHV*-unmutated) displayed a significant decrease in the proportion of cells forming clusters of all sizes. The formation of clusters of four or more cells was particularly decreased in CLL-11 populations following Y-27632 treatment.

Imatinib treatment: Imatinib-treated UM-CLL and M-CLL populations generally showed a significant decrease in the formation of clusters, particularly those comprised of four or more cells. The exceptions being CLL-03 (*IGHV*-unmutated) and CLL-06 (*IGHV*-mutated) which both displayed a significant increase in the proportion of cells establishing clusters with imatinib exposure. Within the CLL-03 population the proportion of cells forming clusters of five or more cells resembled that of individual cells.

Table 4.6: Summary of the changes in homotypic cellular interaction of CLL subgroups following 1 h small molecule inhibitor treatment.

Case	*IGHV* status[*]	Conditions	*p*-value[†]	Increase/decrease in cluster formation compared to DMSO control
CLL-02	M	DMSO vs 100nM Ibrutinib	<0.0001 ****	Decrease
		DMSO vs 20µM Y-27632	<0.0001 ****	Decrease
		DMSO vs 10µM Imatinib	<0.0001 ****	Decrease
CLL-03	UM	DMSO vs 100nM Ibrutinib	<0.0001 ****	Increase
		DMSO vs 20µM Y-27632	<0.0001 ****	Increase
		DMSO vs 10µM Imatinib	<0.0001 ****	Increase
CLL-04	M	DMSO vs 100nM Ibrutinib	<0.0001 ****	Decrease
		DMSO vs 20µM Y-27632	0.4896 ns[‡]	N/A[§]
		DMSO vs 10µM Imatinib	<0.0001 ****	Decrease
CLL-05	UM	DMSO vs 100nM Ibrutinib	<0.0001 ****	Increase
		DMSO vs 20µM Y-27632	<0.0001 ****	Increase
		DMSO vs 10µM Imatinib	<0.0001 ****	Decrease
CLL-06	M	DMSO vs 100nM Ibrutinib	0.0305 *	Decrease
		DMSO vs 20µM Y-27632	<0.0001 ****	Increase
		DMSO vs 10µM Imatinib	<0.0001 ****	Increase
CLL-09	M	DMSO vs 100nM Ibrutinib	<0.0001 ****	Decrease
		DMSO vs 20µM Y-27632	<0.0001 ****	Decrease
		DMSO vs 10µM Imatinib	<0.0001 ****	Decrease
CLL-11	UM	DMSO vs 100nM Ibrutinib	0.0702 ns	N/A
		DMSO vs 20µM Y-27632	<0.0001 ****	Decrease
		DMSO vs 10µM Imatinib	<0.0001 ****	Decrease

[*] M, mutated *IGHV*; UM, unmutated *IGHV.*

[†] *p*-values were determined using the Chi-square test.

[‡] ns, not significant.

[§] N/A, not applicable.

Summary: There was an overall trend for small molecular inhibitors targeting ABL1 and ROCK to interfere with the formation of homotypic groups within CLL populations, independent of the presence/absence of *IGHV* mutations (Table 4.6). These findings provided further evidence of the key role of the B-lymphocyte cytoskeleton in mediating CLL cell migration, adhesion, and cellular interactions. In contrast, ibrutinib impaired cell-to-cell contact in M-CLL cases specifically, suggesting that leukaemic cells displaying unmutated *IGHV* may favour alternative BTK-independent pathways for sustaining cellular transmigration and interactions.

4.4.3. COMPARING CXCL12-DRIVEN MIGRATION FOLLOWING TREATMENT WITH SMALL MOLECULE INHIBITORS

To determine if *IGHV* mutational status effects CXCL12-mediated migration of CLL cells follow treatment with clinically relevant small molecule inhibitors, three UM-CLL and five M-CLL cases (Table 4.1-2) were examined using the Transwell migration assay. The results being discussed in this section are shown in Figure 4.13. Exact *p*-values are included within the figure.

Ibrutinib treatment: Overall, the mean CXCL12-driven migration of both M-CLL and UM-CLL cases was not significantly altered with ibrutinib treatment compared to control (DMSO-treated) cells. Although not statistically significant, possibly due to the small sample sizes used in this study and a large degree of variation between individual responses, there was a general trend for the migration of individual UM-CLL cases to be increased with ibrutinib treatment, whereas the migration of individual M-CLL cases was reduced (mean cell migration relative to control cells of approximately 1.50 and 0.65 for UM-CLL and M-CLL cases, respectively). However, there were exceptions to these trends, particularly within the *IGHV*-mutated CLL

subgroup which showed a greater degree of variability than the *IGHV*-unmutated CLL subset (range of relative migration values of 0.63 and 1.11 for UM-CLL and M-CLL cases, respectively). For example, *IGHV*-mutated case CLL-12 displayed an approximately 1.2-fold increase in cell migration following ibrutinib treatment compared to control cells. In contrast, the migration of *IGHV*-mutated CLL-02 cells was decreased approximately ten-fold compared to control cells with ibrutinib exposure.

Y-27632 treatment: Following Y-27632 treatment, the mean relative CXCL12-driven migration of CLL cells exhibiting mutated *IGHV* was significantly reduced compared to control cells. Overall, the chemokine-mediated migration of *IGHV*-unmutated CLL cases was not significantly altered with Y-27632 exposure. There was a large degree of variability in both subgroups (range of UM-CLL and M-CLL relative migration values was 1.78 and 0.92, respectively). Case CLL-05 (*IGHV*-unmutated) exhibited an approximately two-fold increase in migration with Y-27632 treatment, whereas CLL-03 and CLL-24, both also UM-CLL, displayed a greater than two-fold decrease in cell migration. Similar variability was observed in *IGHV*-mutated CLL cases, with three cases (CLL-02, CLL-05 and CLL-09) all showing a greater than five-fold decrease in migration compared to DMSO-treated cells with Y-27632 exposure. In contrast, the migration of CLL-12 (*IGHV*-mutated CLL) was largely similar to that of control cells following Y-27632 treatment.
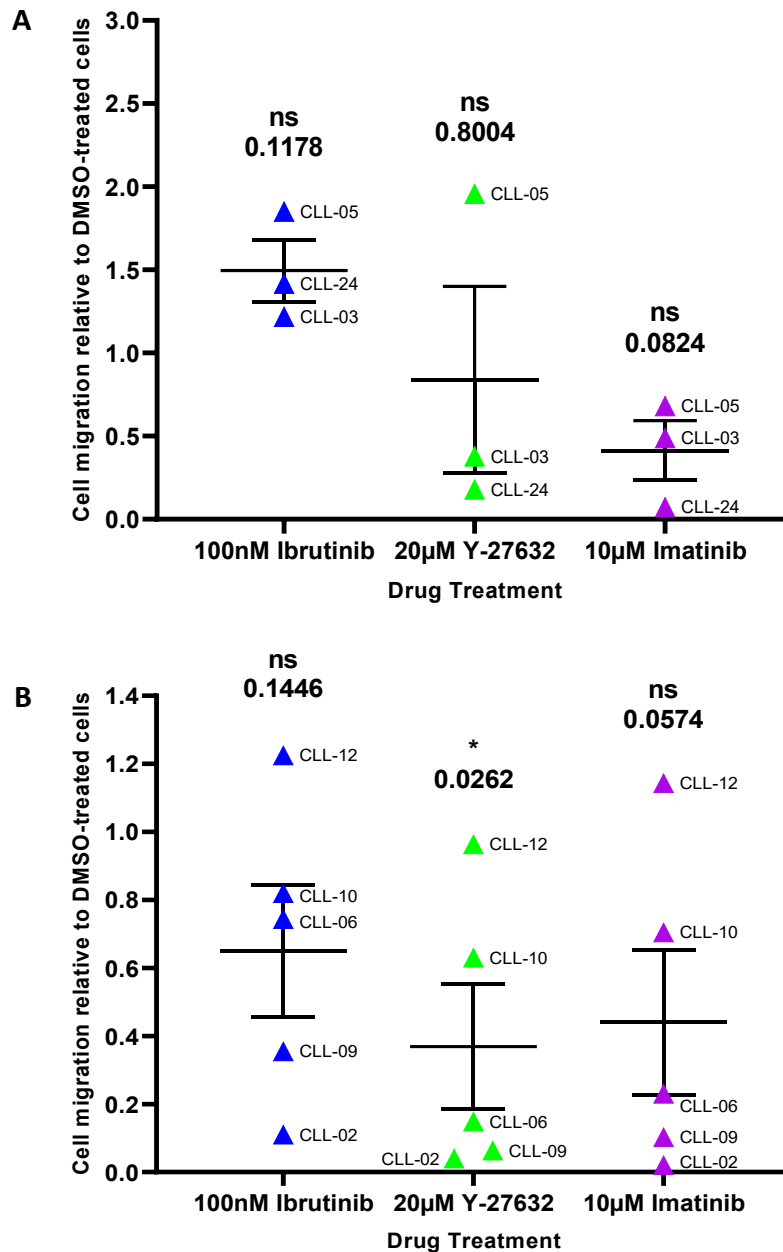
Figure 4.13: Effects of small molecule inhibitors on CXCL12-driven UM-CLL and M-CLL cell migration. Following 6 days culture, CLL cases were pre-treated with either DMSO, ibrutinib, Y-27632 or imatinib for 30 min and then transferred to Transwell inserts. Chemokine gradients were created by adding signal inhibitors at the concentrations stated above and 200ng/mL CXCL12 into each well. Cells were allowed to migrate for 4 h, and then the content of the wells collected and fixed. Migrating cells were counted using a BD Accuri™ C6 flow cytometer and FlowJo software. Scatter plots showing the relative CXCL12-driven migration of (A) UM-CLL and (B) M-CLL cells were created using GraphPad Prism. *p*-values of DMSO vs treatments were calculated using the parametric t-test for unpaired data sets with Welch's correction. ****$p < 0.0001$; ***$p < 0.001$; **$p < 0.01$; *$p < 0.05$; not significant (ns) $p > 0.05$. Error bars represent standard error of the mean. UM-CLL: n = 3; M-CLL: n = 5.

Imatinib treatment: The relative CXCL12-facilitated migration of UM-CLL and M-CLL subgroups collectively was not significantly altered with imatinib treatment compared to control cells. Despite this, there was a general trend for the migration of both subgroups to be reduced following imatinib exposure. The mean cell migration of both UM-CLL and M-CLL cases relative to DMSO-treated cells was approximately 0.4. Variation in behavioural responses to imatinib was primarily seen in *IGHV*-mutated cases (range of UM-CLL and M-CLL relative migration values was 0.61 and 1.12, respectively), with three cases (CLL-02, CLL-05 and CLL-09) all showing an approximately five-fold or greater decrease in cell migration, whereas the migration of CLL-12 (*IGHV*-mutated) cells was largely similar to that of control cells following imatinib treatment.

Summary: Generally, the CXCL12-driven migration of CLL cells was not significantly altered with small molecular inhibitor treatment, independent of *IGHV* mutational status (Figure 4.13). The one exception being M-CLL cases which displayed significantly reduced chemotactic responses following Y-27632-mediated ROCK inhibition (Figure 4.13B). This suggested that *IGHV*-unmutated CLL cells utilise alternative ROCK-independent pathways to permit cellular migration.

4.5. DETERMING THE EFFECTS OF BTKI RESISTANCE ON SIGNAL INHIBITOR-MEDIATED MORPHOLOGICAL RESPONSES

Unique shape changes were observed following treatment of REC-1 and G519 cells with small molecule inhibitors. Ibrutinib-induced changes in cell morphology and CXCL12-driven migration appeared to be associated with BTKi resistance.

4.5.1. COMPARING REC-1 AND G519 SHAPE CHANGES FOLLOWING TREATMENT WITH SMALL MOLECULE INHIBITORS

To establish the effects of BTKi resistance on neoplastic cell shape changes observed following treatment with clinically relevant small molecule inhibitors, the MCL cell lines REC-1 and G519 were utilised. REC-1 cells are sensitive to BTKi, whereas the G519 cell line is inherently resistant.[323] The results being discussed in this section are shown in Figure 4.14-15. Exact *p*-values are included within figures and summarised within Table 4.7.

Firstly, due to the larger size of REC-1 and G519 cells compared to patient-derived CLL cells, the bin sizes of frequency distribution histograms optimised in Chapter 3 had to be altered. Bins of 50µm and 50µm^2 were used for perimeter and area, respectively and bins of 0.02 were used for circularity. Re-optimising the bin sizes ensured that the distinct MCL cell populations formed with signal inhibition could be identified graphically.

Resting morphology: At 1 h, the DMSO-treated (control) REC-1 population was primarily composed of large (perimeter and area approximately 200µm and 150µm^2, respectively), highly irregular cells (circularity approximately 0.06-0.08). SEM images demonstrated asymmetrical REC-1 cells producing extensive fine filopodia which were typically non-polarised in their distribution. Cell surface features were varied; some REC-1 cells were relatively smooth, whereas other exhibited undulating surfaces with peripheral ridge-like

structures. Microvilli were infrequently seen even on the surface of smaller, more globular cells within the REC-1 population. Motile REC-1 cells with distinct front-tail polarity and peripheral ruffles were also present.

Control G519 cells also formed one main population comprised of large (approximately 150μm and 100μm^2, respectively), highly irregular cells (circularity approximately 0.06). SEM images of G519 cells showed a range of different morphologies, from large, relatively flat cells which had spread thinly across the adhesive surface to smaller, more globular cells with frequent microprojections. The surface of large spread cells was typically smooth, although microvilli and peripheral ridges were also observed. Filopodial projects were seen extending from G519 cells; however, they were less extensive and shorter than those observed in the control REC-1 population. Motile G519 cells with distinct front-tail polarity and peripheral ruffles were also observed.

Ibrutinib treatment: Despite being sensitive to BTKi, REC-1 cells showed no significant changes in cell perimeter or area with ibrutinib treatment. Large cells with numerous filipodia and surface features resembling those demonstrated by control REC-1 cells were observed with ibrutinib treatment. However, histograms displayed a significant increase in circularity, indicating that BTK inhibition may have caused REC-1 cells to become more globular. Although ibrutinib did not impair filopodia formation in REC-1 cells, projections appeared to be shorter and less frequent than in control cells.

The BTKi resistant MCL cell line G519 showed no significant changes in shape parameters following ibrutinib treatment, and morphological features mimicked those observed in control cells.
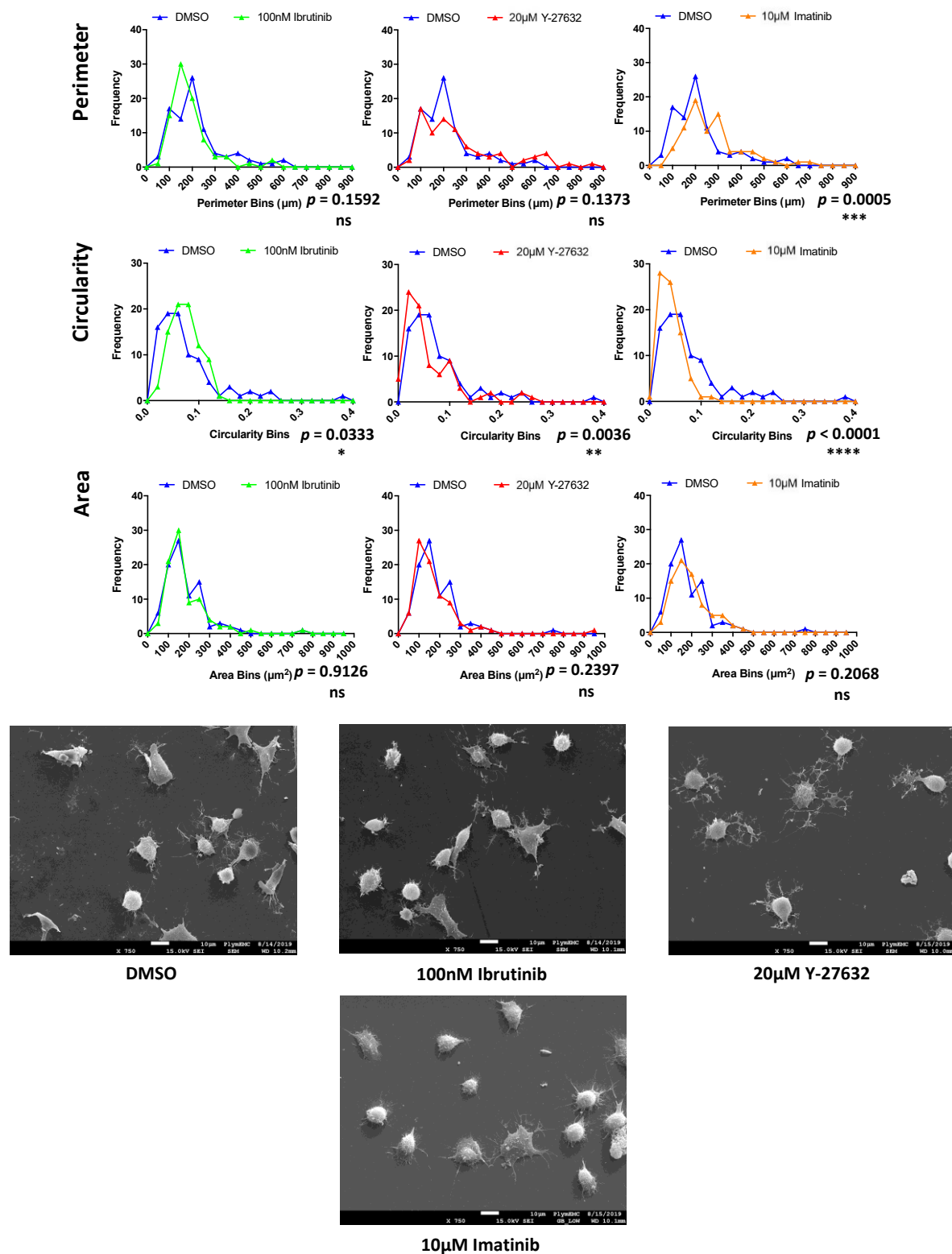
Figure 4.14: Effects of small molecule inhibitors on REC-1 cell shape. REC-1 cells were treated with signal inhibitors for 1 h and then fixed. Cells were observed using a JEOL 7001 F SEM at 450x and 750x, and images were captured using supporting software. Binary images were generated from 450x .tif images using ImageJ, and the perimeter, circularity and area of cells measured. Frequency distribution histograms were created using GraphPad Prism. *p*-values for DMSO vs treatments for each time point were calculated using the Mann-Whitney U test. Images were taken at 750x so that cytoskeletal features could be seen in detail.

156
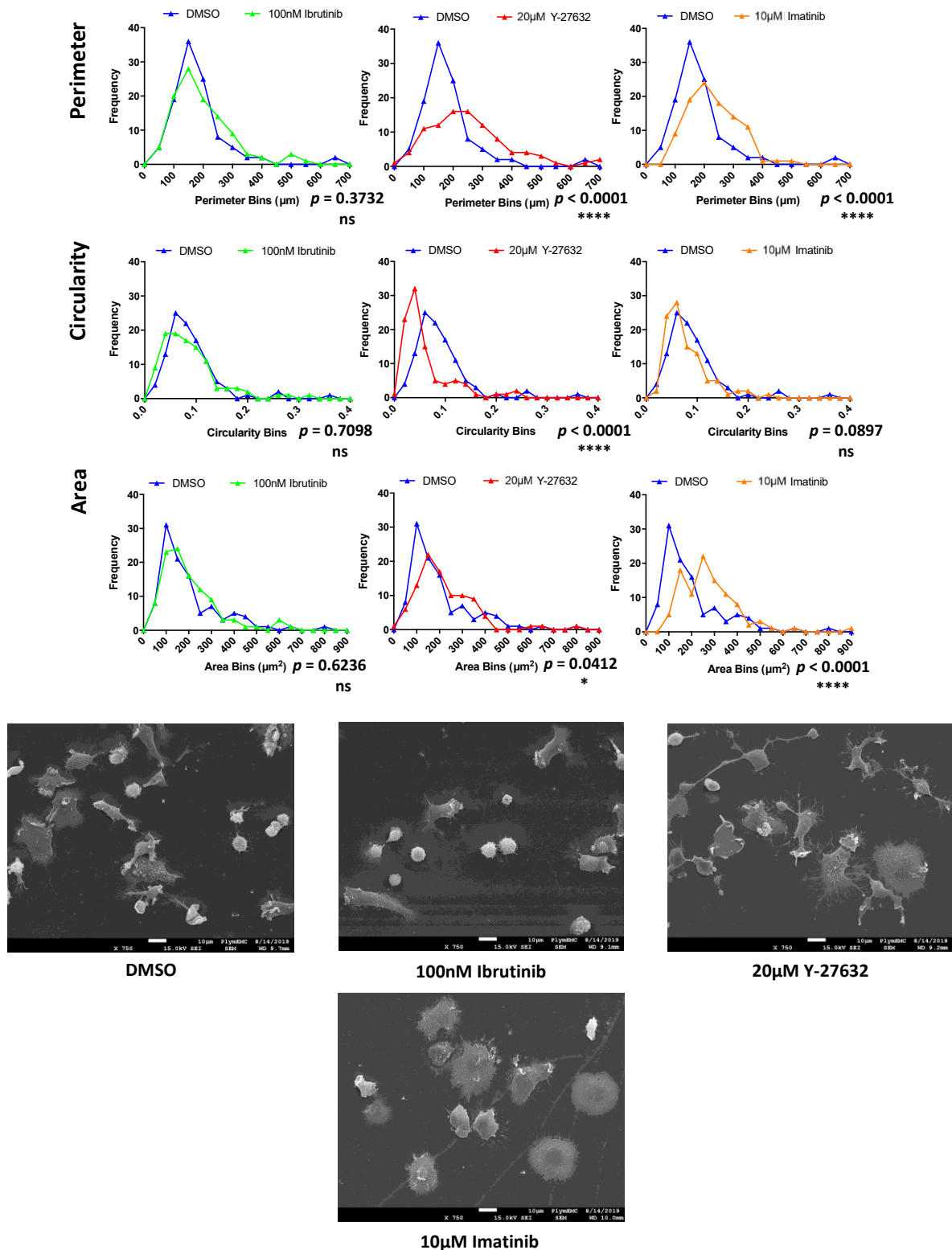
Figure 4.15: Effects of small molecule inhibitors on G519 cell shape. G519 cells were treated with signal inhibitors for 1 h and then fixed. Cells were observed using a JEOL 7001 F SEM at 450x and 750x, and images were captured using supporting software. Binary images were generated from 450x .tif images using ImageJ, and the perimeter, circularity and area of cells measured. Frequency distribution histograms were created using GraphPad Prism. *p*-values for DMSO vs treatments for each time point were calculated using the Mann-Whitney U test. Images were taken at 750x so that cytoskeletal features could be seen in detail.

Y-27632 treatment: Following exposure to Y-27632, REC-1 cells showed no significant alterations in cell perimeter or area despite the formation of large, non-polarised filopodial networks comprised of thicker projections than those seen in control cells. However, impaired retraction of cytoskeletal projections was combined with a significant decrease in circularity. The surface of Y-27632-treated REC-1 cells was either relatively smooth or undulating with peripheral ridge-like structures. Microvilli and peripheral ruffles were typically absent. Interestingly, in some case, 'nodule-like' cytoskeletal formations could be observed within networks of filopodia.

Histograms showed a significant shift towards larger (perimeter and area), more irregular G519 cells with Y-27632 treatment. Contractibility of the G519 cytoskeleton had been effectively impaired as indicated by an increase in cell spreading observed in some cells, in addition to the complex, and in some cases long (filopodia greater than 30μm in length), 'stalk-like' filopodial networks observed in SEM images. Nodule-like processes were also observed within G519 filopodial networks, typically at the ends of projection, with Y-27632 exposure. The surface of G519 cells was generally smooth, with some peripheral ridges and villous structures.

Imatinib treatment: Histograms showed a significant shift towards larger (perimeter), more irregular REC-1 cells with imatinib treatment. This was unexpected given that imatinib-treated REC-1 cells appeared more globular, with frequent microvilli and peripheral ridges in SEM images. Despite the role of ABL1 in filopodia formation, fine non-polarised filopodial projects were frequently seen with imatinib treatment and likely contributed to the observed increase in perimeter and decrease in circularity.

Table 4.7: Summary of the changes in shape of MCL cell lines following 1 h small molecule inhibitor treatment.

MCL cell line	Shape parameter	Conditions	p-value[†]	Increase/decrease in shape parameter compared to DMSO control
REC-1	Perimeter	DMSO vs 100nM Ibrutinib	0.1592 ns[‡]	N/A[§]
		DMSO vs 20µM Y-27632	0.1373 ns	N/A
		DMSO vs 10µM Imatinib	0.0005 ***	Increase
	Circularity	DMSO vs 100nM Ibrutinib	0.0333 *	Increase
		DMSO vs 20µM Y-27632	0.0036 **	Decrease
		DMSO vs 10µM Imatinib	<0.0001 ****	Decrease
	Area	DMSO vs 100nM Ibrutinib	0.9126 ns	N/A
		DMSO vs 20µM Y-27632	0.2397 ns	N/A
		DMSO vs 10µM Imatinib	0.2068 ns	N/A
G519	Perimeter	DMSO vs 100nM Ibrutinib	0.3732 ns	N/A
		DMSO vs 20µM Y-27632	<0.0001 ****	Increase
		DMSO vs 10µM Imatinib	<0.0001 ****	Increase
	Circularity	DMSO vs 100nM Ibrutinib	0.7098 ns	N/A
		DMSO vs 20µM Y-27632	<0.0001 ****	Decrease
		DMSO vs 10µM Imatinib	0.0897 ns	N/A
	Area	DMSO vs 100nM Ibrutinib	0.6236 ns	N/A
		DMSO vs 20µM Y-27632	0.0412 *	Increase
		DMSO vs 10µM Imatinib	<0.0001 ****	Increase

[†] p-values were determined using the non-parametric Mann-Whitney U test for unpaired data sets.

[‡] ns, not significant.

[§] N/A, not applicable.

G519 cells showed a significant increase in both perimeter and area with imatinib treatment compared to control cells. This change was reflected in SEM images which showed G519 cells that had spread thinly across large areas of the substratum. Despite G519 cells appearing rounder in SEM images, circularity was not significantly altered with imatinib treatment. Non-polarised filopodial projects were shorter and less frequent than those seen in control cell. Microvilli and peripheral ridges were also spare-to-absent from the surface of G519 cells following imatinib exposure.

Summary: Using MCL cell lines as a surrogate model for BTKi sensitivity in CLL, unique shape changes were demonstrated following blockage of BTK, ROCK and ABL1. Morphological responses resembled those observed in primary CLL cells, with BTKi-sensitive REC-1 cells displaying reduced cytoskeletal polarisation following ibrutinib treatment and both cell lines exhibiting impaired retraction of cytoskeletal projections with ROCK inhibition (Figure 4.14-15; Table 4.7). As expected, ibrutinib-resistant G519 cells showed no significant morphological alterations with BTK signalling blockade. Interestingly, both REC-1 and G519 cells demonstrated increased F-actin polymerisation and extension of the cytoskeleton with imatinib exposure. This contrasted with the predominantly globular morphology observed in imatinib-treated primary CLL populations and suggested that the role(s) of ABL1 in coordinating B-lymphocyte cytoskeletal dynamics may be disease-specific. As previously mentioned for CLL cells, behavioural changes can only be inferred from SEM images and morphometric analyses and, thus, further investigations were needed to confirm the altered motility of MCL cell lines following signal inhibition.

4.5.2. COMPARING CXCL12-DRIVEN REC-1 AND G519 CELL MIGRATION FOLLOWING TREATMENT WITH SMALL MOLECULE INHIBITORS

To determine the effects of BTKi resistance on CXCL12-induced neoplastic cell migration following treatment with clinically relevant signal inhibitors, the Transwell migration assay was utilised. The results being discussed in this section are shown in Figure 4.16. Exact p-values are included within the figure.

Ibrutinib treatment: The mean relative CXCL12-driven migration of REC-1 cells was significantly increased approximately 3.5-fold with ibrutinib treatment compared to control (DMSO-treated) cells.

In contrast, the BTKi resistant MCL cell line G519 showed no significant changes in relative chemokine-driven cell migration following ibrutinib treatment.

Y-27632 treatment: Following Y-27632 treatment the mean relative CXCL12-mediated migration of both REC-1 and G519 cells was significantly reduced compared to control cells. Indeed, the migration of G519 cells towards CXCL12 was decreased approximately ten-fold compared to DMSO-treated cells with Y-27632 exposure, whereas the migration of REC-1 cells was almost inhibited entirely.

Imatinib treatment: The mean relative chemokine-driven migration of both REC-1 and G519 cells was significantly reduced approximately ten-fold with imatinib treatment compared to control cells.
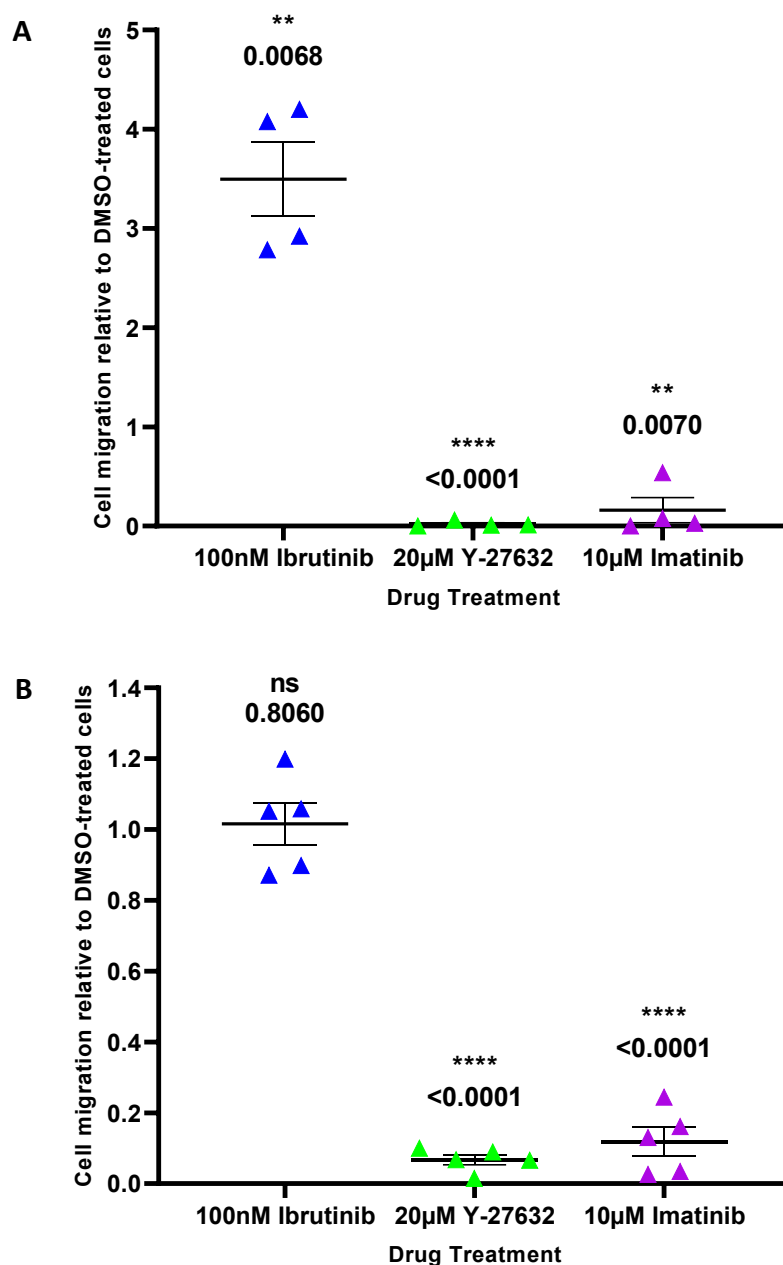
Figure 4.16: Effects of small molecule inhibitors on CXCL12-driven REC-1 and G519 cell migration. REC-1 and G519 cells were pre-treated with either DMSO, ibrutinib, Y-27632 or imatinib for 30 min and then transferred to Transwell inserts. Chemokine gradients were created by adding signal inhibitors at the concentrations stated above and 200ng/mL CXCL12 into each well. Cells were allowed to migrate for 4 h, and then the content of the wells collected and fixed. Migrating cells were counted using a BD Accuri™ C6 flow cytometer and FlowJo software. Scatter plots showing the relative CXCL12-driven migration of REC-1 (A) and G519 (B) cells were created using GraphPad Prism. *p*-values of DMSO vs treatments were calculated using the parametric t-test for unpaired data sets with Welch's correction. ****$p < 0.0001$; ***$p < 0.001$; **$p < 0.01$; *$p < 0.05$; not significant (ns) $p > 0.05$. Error bars represent standard error of the mean. REC-1 cells: n = 4; G519 cells: n = 5.

Summary: Morphological evidence of altered cytoskeletal dynamics with ROCK and ABL1 inhibition correlated with significantly reduced CXCL12-driven MCL cell migration, irrespective of BTKi sensitivity. In contrast, the impaired cytoskeletal polarisation noted in ibrutinib-treated REC-1 cells did not eliminate cellular transmigration. In fact, the chemotactic response of REC-1 cells was significantly increased with BTK inhibition. The CXCL12-induced migration of G519 cells was unaltered with ibrutinib, consistent with their lower dependency on BTK signalling.

4.6. DISCUSSION

4.6.1. RESTING MORPHOLOGY OF CLL SUBGROUPS

Characteristically, CLL populations consist of two morphological states: (i) small, globular cells with frequent microvilli; and (ii) irregular, polarised cells. Leukaemic cells periodically transition between these two morphological forms, undergoing an amoeboid (or crawling) cell migration across adhesive substratum[165]. Amoeboid motility is distinct from the elongated-type motility induced by chemokines and integrin adhesion and has been described in both normal B- and T-lymphocytes.[324–326] Furthermore, the two forms of cell movement have different signalling basis. Amoeboid motility is RhoA/cell division control protein 42 homolog (CDC42) controlled and typically occurs within three-dimensions; whereas elongated-type motility has been associated with Rac1-mediated signalling and enables direct movement in two-dimensions. These Rho proteins belong to the Ras superfamily and are small molecules that share structural homology. They are activated by binding of GTP and regulate various aspects of cytoskeletal organisation via downstream signalling pathways. Notably, RhoA mediates stress fibre contraction and focal adhesion,

whilst Rac1 and CDC42 facilitate lamellipodia extension and filopodium formation, respectively (revied in Parri and Chiarugi,[257] and Nguyen *et al.*[327]).

'Typical' morphology: Biphasic populations were clearly observed in three of the seven CLL cases, independent of *IGHV* mutational status. CLL populations were predominately small and globular with dense microvilli, whilst the remaining (minority) populations were polarised with distinct anterior-posterior morphology, indicating that cells were undergoing elongated-type movement.

Case CLL-01 (*IGHV*-mutated) carried a del(13q) mutation, the presence of which has been significantly associated with *IGHV* mutations and a favourable prognosis.[19] Interestingly, del(13q) as a sole abnormality is rare in CLL with atypical morphology.[19,328–331] Atypical morphology is a deleterious prognostic factor and is applied to cases in which there is >10% of peripheral lymphocytes with prolymphocyte features or a pleomorphic cell population (i.e., >15% of circulating lymphocytes exhibiting clefted nuclei and/or lymphoplasmacytoid features in patients whose predominant cell type was a small lymphocyte with coarsely clumped chromatin).[329,332] Although standard morphological analyses and the above definition of atypical were not utilised in this study, the 'typical' morphological features observed within the CLL-01 population were, therefore, not surprising. Detailed cytogenetic analysis had not been performed for the other two *IGHV*-unmutated CLL cases (CLL-11 and CLL-26), so their relatively typical morphology could not be attributed to a lack of adverse prognostic factors.

'Atypical' morphology: Distinct bi-modal distributions of cell shape parameters were not observed in the remaining four CLL cases These populations showed a greater degree of variability in cell size and circularity and, again, morphological features could not be

attributed to the presence/lack of *IGHV* mutations. Instead, unique morphologies, at least in two CLL cases, could possibly be linked to additional deleterious cytogenetic alterations.

As previously noted, CLL-03 cells (*IGHV*-unmutated) were large and highly irregular, with numerous peripheral ruffles and filipodia, and clear anterior-posterior morphology. This suggested that this CLL population favoured Rac1-mediated elongated-type motility over amoeboid cell movement. CLL-03 cells exhibited del(11q), which typically effects *ATM*. The protein kinase ATM is involved in cell cycle checkpoint signalling, initiating the repair of DNA double-strand breaks or apoptosis.[36] Interestingly, loss of ATM has been shown to elevate intracellular reactive oxygen species generation, leading to Rac1 activation via a noncanonical pathway, resulting in increased cellular spreading and motility. Antioxidant treatment eliminated Rac1 activity in ATM-null cells and reverted cell migration back to that observed in wild-type cells.[333] These findings suggest a role for Rac1 signalling in generating the unusual morphological features observed in CLL-03 cells under conditions of elevated oxidative stress due to loss of ATM function. Increased Rac1 activity due to *ATM*-mutation may, therefore, promote CLL cell homing to tissues in the del(13q) subgroup, leading to bulky lymphadenopathy and reduced OS as previously described.[9] Indeed, dysregulated Rac1 activity has been linked to a metastatic phenotype and drug resistance in several other malignancies (reviewed in Liang *et al.*[334]).

Case CLL-09 (*IGHV*-mutated) also demonstrated varied cell size and irregularity. However, variability in cell shape parameters was observed to a lesser extent than that seen in case CLL-03. CLL-09 cells displayed numerous microvilli, cellular spreading and although there was evidence of cytoskeletal polarisation, it was not the predominant morphological feature within the population. Case CLL-09 harboured a mutation in p53, which plays a crucial role in

the response of normal cells to genotoxic stress by activating pathways involved in cell-cycle arrest and DNA repair or apoptosis.[335] TP53 mutations are generally seen in advanced stages of malignancies and most likely have a driving role in the acquisition of features required for aggressive evolution of cancers (e.g., tissue invasion and metastasis).[336,337] In line with this, loss of p53 promoted Rac1-mediated hyperproliferation in B- and T-lymphoma cells and Rac1 inhibition was able to specifically delay p53-deficient lymphoma cell growth in murine transplantation models.[338] Furthermore, p53 deficiency was shown to increase Rac1 signalling in primary mouse fibroblasts, with this collaboration being sufficient to promote transformation of these cells.[339] These studies suggest a role of Rac1 in driving tumourigenesis and disease progression in p53-deficient malignancies. In contrast, p53-deficient mouse embryotic fibroblast demonstrated RhoA/ROCK-dependent amoeboid cell migration, corresponding to increased motility and invasion within 3D models. Interestingly, whilst levels of GTP-bound RhoA were increased in p53-null embryonic fibroblasts compared to wild-type, GTP-Rac1 and -Cdc42 levels were unaltered.[340] This finding indicates that alteration in TP53 promote tumour metastasis via increased RhoA/ROCK activation rather than Rac1.

It is worth noting that there is a reciprocal balance between RhoA and Rac1. The two molecules are spatially and temporally exclusive within mobile cells. Rac1 is almost exclusively active at the leading edge, whereas the majority of RhoA activity is seen posteriorly and induces retraction of the lagging tail, but RhoA activity can also be briefly observed at the leading edge, peaking before Rac1 activation. This exclusivity is the result of RhoA and Rac1 participating in a mutual inhibitory feedback loop. RhoA supresses Rac1 activity through the activation of ROCK-dependent mechanisms, while Rac1 reduces RhoA activation via p21-activated kinase-dependent processes (reviewed in Nguyen *et al.*[327]). Thus, activation and,

consequently, inhibition of both RhoA and Rac1 pathways in *TP53*-mutated CLL-09 may have prevented the formation of highly atypical morphological features, such as those observed in *ATM*-mutated CLL-03 cells.

4.6.2. MORPHOLOGICAL AND BEHAVIOURAL CHANGES INDUCED BY SIGNAL INHIBITION

The mononuclear, high-density culture preparations utilised in this study have previously been reported to replicate features of the *in vivo* response to signal inhibition.[166] In this chapter, distinct changes affecting CLL cell morphology, and subsequently, cellular behaviour were observed following inhibition of pathways controlling cytoskeletal organisation.

BTK inhibition: BCR activation induces reorganisation of the F-actin cytoskeleton; however, the mechanistic links between BCR signalling and the cytoskeleton are not well defined. BTK has been reported to be a linker protein connecting BCR signalling to F-actin dynamics via BTK-dependent activation of WASP, a haematopoietic cell-specific cytoskeletal regulator that coordinates F-actin polymerisation and branching by stabilising ARP2/3 complexes.[147]

BKT inhibition resulted in the formation of one main homotypic population of small, globular cells in four of the seven CLL cases examined, independent of *IGHV* mutational status. The rounder appearance of cells suggested that elongated-type motility had been impaired by ibrutinib treatment, likely by the reported reduction in adhesion molecule expression, particularly α4β1.[235–237] In line with evidence suggesting that CLL transmigration is impaired by ibrutinib, transient homotypic cellular interactions were significantly reduced in four of the seven CLL cases examined using DBSCAN analyses. However, reduced cellular interactions were observed only in CLL cases harbouring mutated *IGHV*. This indicated that *IGHV*-unmutated CLL cells, which demonstrated unaltered or increased homotypic cellular interactions following BTK inhibition, rapidly switched to integrin-independent amoeboid

transmigration to sustain cell-to-cell contact following inhibition of elongated-type motility. It also suggested that the mechanisms by which BTK controls cytoskeletal dynamics may differ between CLL subsets, with *IGHV*-unmutated leukaemic cells being less reliant on BTK signalling.

In contrast to the above findings, M-CLL and UM-CLL cases collectively displayed no alterations in chemokine-driven migration following ibrutinib treatment compared with control cells. If cases were examined individually, there was a suggestion of increased and decreased directional cell migration in ibrutinib-treated *IGHV*-unmutated and -mutated cases, respectively. However, a large degree of variation in individual responses ultimately led to these weak trends being unsignificant. Varying ibrutinib-induced alterations in CXCL12-driven migration have previously been reported, with Herman *et al.*[237] observing an almost 500-fold increase in directional migration in one primary CLL case, whereas the remaining eleven cases demonstrated unaltered or decreased cellular mobility. These finding further highlight the heterotypic nature of CLL.

The failure of ibrutinib to elicit responses in some CLL patients here may have been due to activation of additional BTK-independent signalling pathways, such as receptor tyrosine kinase like orphan receptor (ROR)1.[341,342] Wnt Family Member 5A (Wnt5a)-dependent activation of ROR1 (an oncoembryonic cell surface marker present on CLL cells) oligomerisation with ROR2, lead to activation of Rac1 and RhoA and, subsequently, enhanced leukemic cell survival, proliferation and chemotaxis. Wnt5a was present at relatively high levels in the plasma of CLL patients.[343] Interestingly, ibrutinib failed to inhibit Wnt5a-induced Rac1 activation within CLL cells; however, Rac1 activation could be blocked with cirmtuzumab, a first-in-class humanised anti-ROR1 monoclonal antibody,[344] indicating that

alternative pathways play a role in controlling cytoskeletal dynamics within CLL cells, independent of BTK signalling. The presence of mutations in BTK and PLCγ2, which are both associated with resistance to ibrutinib,[345] should also be considered.

ROCK inhibition: The Rho family GTPases and their downstream signalling effectors, which include ROCK, play an essential role in the organisation of the F-actin cytoskeleton.[327] RhoA stimulates ROCK, leading to increased MLC phosphorylation through inhibition of MLC phosphatase and direct phosphorylation of MLC, thus promoting actin-myosin II contraction.[259] In addition to participating in normal cellular activities, ROCK has been implicated in tumour motility, invasion and growth. The therapeutic benefits of ROCK inhibition on metastasis have been explored in several tumour models.[262–266]

ROCK inhibition markedly reduced directional polarisation in three of the seven CLL cases examined, with migrating cells losing their distinct anterior-posterior morphology, regardless of *IGHV* mutational status. This indicated that RhoA/ROCK-mediated retraction of cytoplasmic processes had been impaired. Unregulated extension of the cytoskeleton, facilitated via removal of the functional inhibition of Rac1 by RhoA/ROCK, resulted in long, stalk-like projections and extensive filopodial networks. Similarly, monocytes and prostate cancer cells demonstrated an accumulation of extremely long unretracted tails behind the main cell bodies following RhoA/ROCK inhibition, corresponding to impaired cell migration.[264,267]

Forward movement of cells is thought to be driven by actin polymerisation at the leading edge, leading to Rac1-induced extension of the lamellipodium. To successfully migrate towards stimuli, cells must coordinate this extension of the leading edge with RhoA/ROCK-mediated retraction of the lagging tail.[257] Indeed, monocytes continued forward crawling movement following RhoA/ROCK impairment; however, failure to retract lagging tails

ultimately drew the cells back to their original positions, eliminating any net cellular transmigration.[267] In line with this finding, impaired retraction of the trailing edge following Y-27632 treatment corresponded to significantly decreased homotypic cellular interactions in three of the seven CLL cases, independent of the presence/absence of *IGHV* mutations. Decreased chemokine-mediated cellular migration with RhoA/ROCK inhibition was specific to *IGHV*-mutated cases; further highlighting the existence of alternative mechanism of mediating cytoskeletal alteration within CLL patients, particularly those exhibiting unmutated *IGHV*. Interestingly, *TP53*-mutated CLL-09 cells (*IGHV*-mutated) demonstrated characteristic morphological and behavioural responses following Y-27632 treatment. These observations combined with evidence of increased RhoA/ROCK-dependent cell migration and invasion in p53 deficient cells,[340] suggest targeting of ROCK activity within this hard-to-treat CLL subset may have beneficial therapeutic effects.

Cases CLL-03 [*IGHV*-unmutated; del(11q)] and CLL-06 [*IGHV*-mutated; del(13q)] were amongst the CLL cases demonstrating partial and/or atypical responses to RhoA/ROCK inhibition. Despite both displaying reduced chemokine-induced migration with Y-27632 pre-treatment, homotypic cellular interactions were increased within populations. Additionally, CLL-03 cells exhibited a decrease in circularity alone. As previously described, ATM deficiency, such as in the case of del(11q), has been linked to dysregulated Rac1 signalling and increased motility.[333] However, cases CLL-03 and CLL-06 were the only patients included in this study which had previously received FCR therapy. The selection and expansion of CLL clones with atypical cytoskeletal dynamics, possibly resulting from chromosomal abnormalities or somatic mutations, may account for the unusual treatment responses of these CLL cases and should be explored further. Indeed, subclonal populations demonstrating numerous somatic

mutations, varied levels of drug resistance, and proliferation and repopulation rates have been identified in CLL.[346]

ABL1 inhibition: The ABL family kinases co-localise with F-actin and are known to play a key role in the control of cytoskeletal structures and cell migration in various cell types.[273] However, its role in lymphocytes is less well defined, due in part to the focus of research on the oncogenic properties of constitutively active ABL mutants, such as those produced by the *BCR-ABL* fusion gene in chronic myeloid leukaemia,[272] and partly due to the fact that germ-line deletions of ABL in mice lead to increased neonatal mortality,[281] with surviving mice exhibiting abnormalities in lymphocytes development.[282,347] Nevertheless, ABL1 is known to be highly expressed in CLL cells, and facilitates their survival *in vitro.*[280]

Following ABL1 inhibition, four of the six CLL cases retracted their large filopodial projections and reverted to a small, globular cell shape, independent of *IGHV* mutational status. This indicated that ABL1 activity was required for effective actin polymerisation and extension of lamellipodia in lymphocytes, as previously reported,[283] and inhibition of stress fibre formation. Consistent with these observation, the relocation of polymerised F-actin to a narrow cortical ring following imatinib treatment has been described.[165] Interestingly, another ABL family nonreceptor tyrosine kinase, the Arg protein, was shown to be essential for inhibition of RhoA-mediated contractility in fibroblast.[279] Arg-dependent phosphorylation of the Rho inhibitor p190RhoGAP-A (p190) promoted its binding to p120RasGAP (p120).[279,348–350] Formation of this p190-p120 complex was essential for p190 recruitment to the cell periphery and function, with *Arg*-null fibroblast demonstrating impaired p190 translocation and, consequently, significantly increased RhoA activity and stress fibre formation.

Reconstitution of these cells with wild-type Arg restored p190 re-localisation and reduced RhoA-mediated contractility of cells to normal levels.[279]

Global reduction in RhoA activity within cells, induced by ABL kinase signalling, likely permits cellular spreading and exploratory transmigration in lymphocytes. Indeed, homotypic cellular interactions were significantly decreased in five of the seven CLL populations examined with ABL1 inhibition, regardless of *IGHV* mutation status. Decreased spontaneous amoeboid motility and filopodial contact between neighbouring CLL cells following suppression of ABL kinase activity has been described,[165] in addition to impaired F-actin polymerisation at the IS, which plays a key part in T-lymphocyte interactions with antigen presenting cells.[283] Although ABL activity is crucial for amoeboid motility and cellular interactions within the immune environment, imatinib treatment does not appear to play a key role in elongated-type cell migration. Collectively *IGHV*-unmutated and -mutated CLL cases showed reduced, but not significantly altered chemotactic responses to CXCL12 with ABL1 inhibition, as previously reported.[165] Furthermore, although the proportion of CLL cells displaying distinct anterior-posterior morphology appeared to be reduced within imatinib-treated populations, prominent cell polarisation was still present. These findings provide further evidence of distinct signalling pathways for cytoskeletal reorganisation in CLL cells, with shape-changes associated with exploratory cell migration being ABL1-dependent while chemokine-induced cellular elongation is predominantly ABL1-independent.

As with other signal inhibitors, partial/atypical morphological and behavioural responses to imatinib were observed in CLL cases. In particular, CLL-03 [*IGHV*-unmutated; del(11q)] and CLL-06 [*IGHV*-mutated; del(13q)] cells both displayed increased cellular interactions with ABL1 inhibition, implying that culture-induced exploratory cell migration has been increased.

As mentioned above, further investigations are needed to explore the possible selection of subclonal populations with 'atypical' cytoskeletal dynamics by FCR therapy. Alternative signalling pathways controlling RhoA-mediated cytoskeletal contractility may also exist within resistant CLL populations. For example, Src family kinases, which act as switch molecules coupling the BCR to downstream signalling pathways,[201,205] are also required for integrin-dependent phosphorylation and activation of p190.[350,351]

4.6.3. THE EFFECT OF BTKI RESISTANCE ON B-LYMPHOCYTES MORPHOLOGY AND BEHAVIOUR

Despite the clinical efficacy of ibrutinib in CLL, both primary and acquired resistance to this BTKi has been described.[345,352] Gaining a greater understanding of the cellular behaviour(s) underlying ibrutinib resistance is, therefore, needed to aid in the development of novel therapeutic strategies to improve treatment efficacy and to bypass the appearance of BTKi resistance in CLL patients.

To determine the effects of ibrutinib resistance on the morphological and behavioural responses of malignant B-lymphocytes following signal inhibition, the MCL cell lines REC-1 and G519 were selected. REC-1 cells are sensitive to BTKi, whereas the G519 cell line is inherently resistant.[323] MCL cell lines were utilised instead of CLL cells for several reasons: (i) existing CLL cell lines typically have molecular features of high-risk CLL only, having *IGHV* unmutated disease and mutated *TP53*;[353,354] (ii) the addition of accessory cells or other B-lymphocyte activating stimuli are often needed to maintain CLL cell lines in culture;[165,167,171,172] and (iii) CD5 expression diminishes with continuous culture of CLL cell lines.[355,356] Resistance to viral transformation by Epstein-Barr virus[357–359] and the presence of numerous prognostically relevant karyotypes in CLL[9] have both contributed to the lack of

representative immortalised cell lines that accurately reflect the disease. In contrast, a comparative study of G519 and primary MCL tumours reported that this cell line has preserved its expression of genes that are up-regulated in primary MCL, as compared to normal B-lymphocytes.[360] Paired samples from patients who had initially responded to ibrutinib and gone on to develop resistance would been a superior option to cell lines; however, at the time of this study no such samples were available.

REC-1 cells exhibit unmutated *IGHV* and SRY-box transcription factor 11 (SOX11) expression consistent with the classic indolent forms of MCL,[361] whereas G519 cells behave like aggressive MCL disease. G519 was established from the PB of a patients with relapsed high-grade MCL in leukemic transformation, and cells display a blastoid phenotype with SOX11, unmutated *IGHV* and amplification of the pro-survival gene BCL2 apoptosis regulator.[362–364]

In line with clinical differences between the two MCL cell lines, REC-1 and G519 cells displayed varying morphological features. REC-1 cells predominantly displayed extensive, non-polarised, fine filopodia, whereas G519 cells typically demonstrated fewer cytoskeletal protrusions and a large degree of cellular spreading. Whether the morphological variation between REC-1 and G519 cells reflects differences in disease stage at the time of establishment, with the former being indolent MCL and the latter aggressive disease, remains to be established. Nevertheless, in contrast to the predominantly globular primary CLL cells, REC-1 and G519 populations typically consisted of large, highly irregular cells

BTK inhibition: As expected the ibrutinib-resistant cell line G519 showed no significant changes in shape parameters with ibrutinib treatment, and cell morphology resembling that of control cells. Chemokine-driven migration of G519 cells was also unaltered by ibrutinib exposure. These finding further highlight the lower dependency of G519 on BTK

signalling.[286,365] G519 cells may favour alternative mechanism for controlling cytoskeletal dynamics due to mutations in other pathways. Indeed, targeting of SYK and Src activity has demonstrated efficacy in R/R B-NHL.[230,366]

Ibrutinib-sensitive REC-1 cells displayed a significant increase in circularity, indicating that integrin-dependent directional cell migration had been impaired (at least in part), as described in primary CLL cell. A PB lymphocytosis combined with a reduction in tumour volume was seen in MCL patients with ibrutinib therapy,[229] indicating that tumour cells moved from lymph nodes into the peripheral circulation. Circulating MCL cells demonstrated reduced CXCR4 expression follow ibrutinib treatment[367] and levels of plasma chemokines were also reduced.[368] These finding indicated that ibrutinib impaired homing and retention of MCL cells within lymphoid tissues in a similar manner to that observed in CLL cells.[235–237] In contrast to this hypothesis, the chemotactic response of REC-1 cells to CXCL12 was increased following ibrutinib pre-treatment. A possible explanation for this unexpected finding could not be found in the literature. However, there is limited evidence suggesting that MCL exhibit varying responses to ibrutinib depending on *in vitro* culture conditions. BTK inhibition resulted in decreased and increased MCL cell migration through BMSC and lymph node barriers, respectively. Changes in tumour cell homing could not be fully attributed to involvement of the CXCR4-CXCL12 axis, with ibrutinib inducing CXCR4 upregulation on MCL cells co-cultured with BMSC and down-regulation of CXCR4 expression on tumour cells co-cultured with lymph node stromal cell.[369] Thus, MCL cells display context-dependent ibrutinib responses, which require further investigations.

ROCK inhibition: G519 cells demonstrated a significant shift towards larger, more irregular cell shapes following RhoA/ROCK inhibition, whereas REC-1 cells displayed a significant

175

decrease in circularity alone. Non-polarised filopodial networks were frequent in both MCL populations with Y-27632 treatment and, in the case of G519 cells, contained long stalk-like processes. These observations are consistent with previous observations of impaired retraction of cytoskeletal projections, combined with uncontrolled Rac1/CDC42-mediated extension of leading edges in various cell types[264,267] and primary CLL cells following disrupted RhoA/ROCK signalling. Furthermore, impaired reaction of the trailing edge correlated to significantly reduced chemokine-driven migration in both REC-1 and G519 cells in line with the literature[264,267] and *IGHV*-mutated primary CLL cells. These observations suggest that retraction of cytoskeletal processes, which is essential for directional cell migration, is potentially a BTK-independent processes, based on the lower dependency of G519 on BTK signalling,[286,365] Thus, targeting of ROCK activity could be incorporated into combinational therapies to disrupt trafficking of malignant B-lymphocytes to tissues niches in patients who are R/R to ibrutinib.

ABL1 inhibition: MCL cell lines exhibited a significant increase in cell size and, in the case of REC-1 cells, cytoskeletal polarisation following ABL1 inhibition. This contrasted with the small, globular populations typically seen in imatinib-treated CLL cases. Although ABL1 is recognised as playing a role in filopodia formation in cells of the immune system,[283] filopodia were still present within MCL populations. These finding suggest that, while primary CLL cells may be largely dependent on the activity of ABL kinases to alleviate RhoA-mediated contractility,[165,279] MCL cells utilise alternative signalling pathways to reduce stress fibre formation, and permit cellular spreading and exploratory transmigration. Furthermore, both MCL cell lines required ABL1 activity for effective directional motility, with CXCL12-driven migration being significant reduced. This contrasted with primary CLL cells which did not

require ABL1 for chemotactic response as previously reported.[20] These findings indicate that the roles of ABL1 in facilitating cytoskeletal alterations, particularly the coordinated relaxation of cortical tension needed for effective directional cell migration, are potentially disease-dependent.

As with CLL, the function(s) of ABL signalling in MCL have not been well described. *ABL* is not the primary driver oncogene in this disease; however, a translocation involving BCR and ABL is the sole genetic abnormality detected in newly diagnosed chronic myeloid leukaemia patients.[271,272] A literature search yielded case reports of MCL which developed in patients with chronic myeloid leukaemia following imatinib treatment and, therefore, a biological link between dysregulated ABL activity and MCL is plausible.[370,371] Indeed, a comparison of the expression levels of *BCR-ABL* and *cyclin D1* in the BM of chronic myeloid leukaemia patients demonstrated a significantly higher level of *cyclin D1* transcripts in the accelerated phase of the disease compared with the chronic phase.[372] Afar *et al.*[373] also demonstrated that the activated ABL oncogene could signal through cyclin D1 and induce malignant transformation. Collectively these findings indicate that dysregulated ABL1 signalling, through yet unknown mechanism, can lead to overexpression of cyclin D1 and, consequently, promote B-lymphocyte lymphomagenesis. Further studies are needed to elucidate the precise role of ABL1 in MCL.

CHAPTER 5 – DEVELOPING A THREE-DIMENSIONAL MODEL FOR THE STUDY OF CLL CELLULAR BEHAVIOUR VIA TEM

5.1. INTRODUCTION

These experiments aimed to develop a 3D model that could be used, in combination with TEM, to study changes in cellular morphology and protein localisation following treatment with clinically relevant stimuli or signal inhibitors.

This chapter is divided into a discussion of the relevance of 3D models for the study of CLL pathogenesis; a brief overview of the models currently in development; and the justification for the choice of model for this work followed by the sequential experiments performed to optimise this model for the study of behavioural and molecular aspects of CLL within a TME-like setting.

5.2. RATIONALE FOR IMPLEMENTING A 3D CULTURE SYSTEM

The specialised microenvironment within BM and lymph nodes modulates immune cell function and plays a crucial part in CLL leukemogenesis, providing supportive niches in which malignant B-lymphocytes are nourished and protected.[95] In lymphoid tissues, survival of CLL cells is heavily influenced by cellular and molecular interactions with non-malignant accessory cells.[94] CLL is a complex disease where malignant B-lymphocytes traffic between the PB, BM and secondary lymphoid organs, and undergo variable rates of proliferation and cell death within these anatomical sites. In particular, the lymph node has been identified as the primary site of cellular proliferation in CLL.[374,375] Furthermore, Pasikowska *et al.*[376] demonstrated that lymph node-derived CLL cells exhibit a unique phenotype, and enhanced capacity to activate T-lymphocytes and form IS. It is also interesting to notes that several novel therapeutic

interventions for CLL, such as ibrutinib, target the CLL-TME interactions in addition to intrinsic CLL survival pathways.[233–237] Therefore, based on the complexity of the interactions occurring within the TME and the cell heterogeneity present within these niches, it has been very challenging to reproduce *in vitro* the conditions promoting the mobilisation, retention and proliferation of CLL cells.

For many decades, the study of cancer biology and drugs screening has relied on 2D cell culture systems and animal models. However, it is generally recognised that despite being easy and convenient, the flat, stiff, artificial surfaces typically used for 2D monolayer culture poorly reflect the complex conditions found *in vivo*.[377] By definition, 2D models lack the 3D cell-cell and cell-ECM interactions considered essentially for control of proliferation, differentiation and mobility during cancer development.[378] Indeed, direct comparisons of cells grown as 2D monolayers and 3D cultures have highlighted differences in cell morphology, receptor expression, cellular architecture and expression of oncogenes[377] (Table 5.1). Although *in vivo* animal models can provide many advantages compared to 2D cultures (e.g., complete organ systems rather than cell monolayer), they are also associated with a number of limitations, including cost, ethical issues and a lack of correct immune activation.[379,380] Due to these differences the ability of 2D culture systems and animal models to adequately reproduce the features of human cancers or accurately predict therapeutic responses has been called into question. However, 3D *in vitro* culture models, which aim to mimic key tissue-specific structural features more accurately than 2D culture methods (Table 5.1), have gained popularity in the study of metastasis, invasion and cell-cell interactions in solid tumours, and could provide a third approach.[377] Given the differences in cellular interactions demonstrated in 2D and 3D systems, it would seem logical to attempt to develop

a 3D *in vitro* culture system that can be combined with the superior resolving power of electron microscopy for the study of CLL cell morphology within a TME-like setting.

5.3. AN OVERVIEW OF 3D MODELS IN CURRENT CELLULAR RESEARCH

In recent years, advances in culturing techniques and tissue engineering have allowed for the development of numerous 3D models for the study of complex human tissues and cancers. These 3D systems no longer rely on stiff culture surfaces and instead allow cells to proliferation, migration, and interaction in a more physiological manner.[379] In the broadest sense, 3D culture methods can be categorised into two main groups: (i) tumour spheroids; and (ii) matrix-embedded cultures.

5.3.1. SPHEROID-BASED CULTURE METHODS

Spheroid-based culture systems take advantage of the fact that many cell types are capable of anchorage-independent cell growth and, in the absence of a substratum to which they can adhere, self-assemble into large cellular aggregates known as 'spheroid'.[381] Spheroid can be produced by several methods, including hanging drop microplates,[382–384] forced floating,[385–387] or rotating culture flasks [388] (Figure 5.1).

Tumour spheroids, which can be homotypic (exclusively cancer cells) or heterotypic (cancer cells co-cultured with accessory cell types),[389–391] more accurately recapitulate the physiological conditions of tumours with regard to cell-cell communication and signalling pathways.[392] Varying proliferation rates, and oxygen and pH levels between cell layers within the spheroid (i.e., hypoxic, acidic core) have also been described as being responsible for the impaired therapeutic action of chemotherapy drugs.[393–395] Although spheroid-based culture systems are relatively quick and simple to generate as they do not require an external scaffold for aggregation, they typically lack essential cell-ECM interactions. Furthermore, in the

context of this project, the relative fragility of spheroids during the handling process, difficulty in controlling size uniformity, which is important to standardise drug exposure, and the requirement for specialist equipment to simultaneously rotate and incubate culture vessels may limit the use of spheroid-based methods.

5.3.2. MATRIX-EMBEDDED CULTURE METHODS

Matrix-embedded culture methods rely on cells migrating between the fibres of a physical structure and adhering to them. The cells then proliferate and colonise the interstices within the matrix, generating 3D structures. Soluble factors, such as cytokines and growth factors, can be added as required but ideally, cells cultured within the matrix produce and communicate with their own ECM molecules, thus mimicking *in vivo* cell-ECM interactions.[379,396] The most common matrix-embedded culture systems can be further categorised as synthetic or biological.

Prefabricated synthetic scaffold are made of hard polymers (e.g., glass microfibers) or hydrogels [e.g., gelatin, alginate, cellulose, polylactic acid, or poly(vinyl acetate)] that are not naturally found in human tissues, but have the advantage of being highly reproducible, relatively cheap, and having tuneable biochemical and mechanical properties. However, the major disadvantage of synthetic matrix-based systems is that cells interact with an artificial material and these matrices are, therefore, not as biologically relevant as their natural counterparts.[377,379,396]

Table 5.1: Brief comparison of 2D culture and 3D culture methods

Characteristic	2D cell culture	3D cell culture	References
Cell morphology	• Cells are often flat and elongated • Cells grow in monolayers • Cells are exposed to artificially high tensile stress, which can lead to altered cell shape, cytoskeleton arrangement and cell-cell adhesion • Cell differentiation is typically poor	• Cell morphology usually mimics that observed *in vivo* • Cells grow in 3D aggregates/spheroids • 3D models contain multiple cell layers • Cells are typically well differentiated	von der Mar *et al.*[397] Petersen *et al.*[398] Ghosh *et al.*[399] Kim[400] Costa *et al.*[392] Langhans[396]
Exposure to medium/soluble factors	• Cells are exposed to a uniform environment, which is not representative of the oxygen, nutrient and other soluble factor gradients observed *in vivo*	• Cells within aggregates/spheroid are exposed to gradients of oxygen, nutrients, and other soluble factors, mimicking the *in vivo* environment	Breslin and O'Driscoll[377] Costa *et al.*[392] Langhans[396]
Drug sensitivity	• Cells often have reduced resistance to drugs • Cells typically undergo drug-induced apoptosis more readily	• Cells typically have greater resistance to drugs • Cells usually exhibit greater resistance to drug-induced apoptosis, due to limited diffusion of drugs within 3D aggregates and/or the presence of supportive cells	Haisler *et al.*[401] Imamura *et al.*[402] Langhans[396]
Cell proliferation	• Cells can proliferation at an artificially rapid speed • Cells often proliferate at a uniform rate	• Cell proliferation rates can mimic what is observed *in vivo* depending on the culture system and cell type used • Cell layers display varying rates of proliferation	Ravi *et al.*[403] Langhans[396]
Expression levels	• Gene and protein expression levels can vary to that observed *in vivo*	• Gene and protein expression often mimics that observed *in vivo*	Costa *et al.*[392] Langhans[396]
Cost	• 2D models have lower costs, particularly for large-scale studies, and are relatively easy to set up	• 3D models are usually more expensive and labour intensive	Breslin and O'Driscoll[377] Ravi *et al.*[403] Bruce *et al.*[404] Mannino *et al.*[405]
Application and reproducibility	• 2D models are highly reproducible, can be easily combined with imaging techniques and results are easily interpreted • 2D models are typically more suitable for long-term culture	• 3D models are less reproducible, harder to combined with imaging techniques and results are more difficult to interpret	Breslin and O'Driscoll[377] Kapałczyńska *et al.*[406]
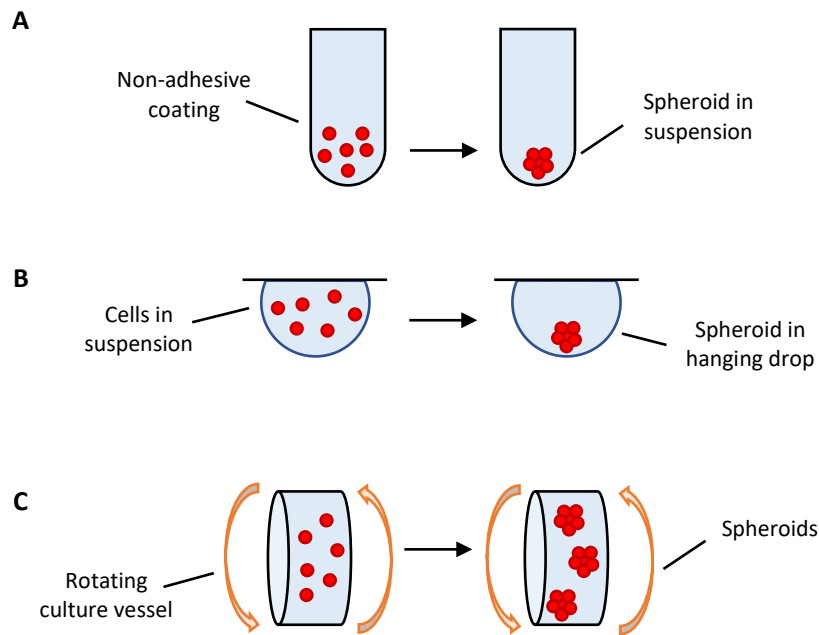
Figure 5.1: Overview of the common methods used for the generation of spheroids. (A) Forced floating of cells is a relatively simple method for generating 3D aggregates/spheroids by inhibiting their attachment to a culture surface. This is achieved using culture vessels with a modified surface (e.g., coated with 0.5% poly-2-hydroxyethyl methacrylate or 1.5% agarose).[385–387] Forced floating of cells in suspension promotes cell-cell contact due to the lack of interaction with the culture surface, which, in turn, encourages the formation of spheroids.[377] (B) The hanging drop method utilises a small aliquot of a cell suspension which is placed into a well of a microwell plate. The plate is then inverted, and the aliquot of cell suspension forms a hanging drop held in place by surface tension. The cells accumulate and proliferate at the liquid-air interface at the tip of the drop, ultimately forming spheroids due to cell-cell contact.[377,383,384] (C) Agitation-based approaches, which include spinner flask bioreactors and rotational culture systems, generate spheroids by keeping cell suspensions in constant motion by gently stirring the cell suspension or rotating the culture vessels. The continuous motion prevents cells from adhering to the culture vessel walls and instead promotes cell-cell interactions, leading to the formation of spheroid. Spinner flasks contain a stirring element to ensure the cell suspension is continuously mixed. In contrast, rotational culture bioreactors the culture vessel rotates on its horizontal axis, simulating microgravity and exerting a low sheer force on cells. The constant end-over-end mixing keeps cells in a gentle fluid orbit and promotes cell-cell contact.[377,388]

Biological matrix-based systems contain ECM components (e.g., amino acids, carbohydrates, lipids, hormones) present in human tissue and are, therefore, naturally adhesive and have sustained physiological cell functions.[396] This biocompatibility results in high cell viability, controlled proliferation and differentiation and, typically, cell phenotypes observed within the *in vivo* TME.[36,38,39,42] However, natural products often have heterogeneity in their composition between different lots/batches, limiting reproducibility within experimental settings and the additional growth factors may alter experiential results.[377]

Biological matrix-based systems can be produced using decellularised tissues or organs.[407,408] As the initiation of this model requires solid tissue samples and is thus, not applicable to peripheral blood samples obtained in this study, it will not be discussed further.

Alternatively, hydrogels of natural origin can be used as substitute supportive structures for 3D culture,[377,396] with one of the most commonly utilised biological hydrogel being Matrigel™. Matrigel™ is a soluble ECM derived from Engelbreth–Holm–Swarm mouse tumour sarcoma cells, and consists of basement membrane proteins such as collagen IV, laminin, matrix metalloproteinases-2, perlecan, entactin and growth factors. This liquid basement membrane extract polymerises to form a gel at 24-37°C. The gel does not readily redissolve on cooling; thus, the physical matrix is preserved during sample handling.[409] Cell can be seeded onto and allowed to migrate inside of the Matrigel™ structure or mixed with the liquid ECM extract prior to polymerisation. The later approach offers a simple solution to the major obstacle of all matrix-based culture systems, which is achieving a high seeding efficiency and the desired cellular distribution as cells may not migrate into or be retained within matrices. A growth-factor reduced formulation of Matrigel™ is available, allowing for generation of 3D models with more defined chemical properties.[409]

Both scaffold types have been used to reproduce lymphoid tissues, with the BM niche being particularly well investigated in acute myeloid leukaemia (AML) and multiple myeloma (MM). Bray et *al.*[410] designed a 3D BM TME by co-culturing AML cell with endothelial cells and mesenchymal stromal cells in a synthetic hydrogel and demonstrated significant greater resistance to chemotherapy in 3D co-cultures when compared to 2D models. Similarly, Braham *et al.*[411] established a 3D BM niche model in which multipotent mesenchymal stromal cells were co-cultured with endothelial progenitor cells within Matrigel™. These co-cultured cells formed pre-vascular networks within the 3D scaffold and supported the survival and proliferation of primary MM cells for up to 28 days. Within the 3D model, cellular interactions were reminiscent of that observed *in vivo* as demonstrated by the changes in mesenchymal stromal cells mineralisation capacity. Furthermore, using a microarray technology that enabled genome-wide analysis based on single-nucleotide polymorphisms, no genetic drift was observed within the cultured MM population; highlighting the 3D model's ability to accurately represent the genomic prolife of the primary cells at the time isolation.[411]

5.3.3. NOVEL 3D CULTURE METHODS

Emerging microfluidic technology, in which 3D structures are connected to synthetic microchannels to allow precise control over the mechanical properties of the matrix, nutrient delivery and fluidic sheer stress, offer new models to study various aspects of the TME. Indeed, microfluidic models have been applied to different cancer models, including AML.[404,412] A lymphoma-on-chip model for DLBCL has also been developed and allowed the study of crosstalk between malignant cells, immune cells and endothelial cells as well as treatment responses.[405] Although these novel models offer promising results, they require

specialised equipment and extensive optimisation. Microscopic analyses of the 3D cultures produced via these models may also be difficult.

5.4. JUSTIFICATION FOR SELECTING MATRIGEL™ FOR THIS STUDY

Matrigel™ has several qualities that make it suitable for testing in the context of this project:

- It contains ECM components and, thus, more accurately recapitulates the physiological conditions of the *in vivo* TME ('biomimicry of the tissue of origin').

- After re-constitution and polymerisation, it is translucent allowing easy visualisation of cells by light-microscopy and providing good contrast between colonising cells and the background matrix for TEM examination.

- Once polymerised, it does not readily redissolve upon cooling allowing the matrix to be easily handled during the fixation process.

- Cells can be mixed with the liquid ECM extract prior to polymerisation, overcoming issues relating to seeding efficiency and cellular distribution and, thus, avoiding extensive optimisation.

- Survival of cells and the formation of cell-cell interactions within Matrigel™ matrices does not require expensive culture equipment, such as rotating culture flasks or microfluidic technology.

Therefore, a series of experiments using Matrigel™ were designed to optimise the 3D culture of primary CLL cells.

5.5. PRACTICAL IMPLEMENTATION OF 3D CULTURE SYSTEMS

5.5.1. REAGENTS AND BUFFERS

Fibronectin (80µg/mL)

28µL of fibronectin (F2006, Sigma-Aldrich) stock solution at 1000µg/ml placed into 322µL of sterile 1X HBSS (14175046, Gibco™). Prepared fresh and kept on ice. Remaining solution discarded.

Matrigel Matrix mix [50% (v/v), 40µg/mL fibronectin]

A 400µL aliquot of Matrigel Basement Membrane Matrix (growth factor reduced, phenol red-free, lactose dehydrogenase elevating virus-free; 356231, Corning) was thawed overnight at 4°C in an insulated box full of ice, with the lid on. Once thawed the Matrigel Matrix was kept on ice at all times to prevent polymerisation.

350µL of thawed Matrigel Matrix placed into a chilled Eppendorf tube and made up to 700µL with chilled fibronectin (80µL/mL; final concentration 40µL/mL after 1:1 dilution with Matrigel Matrix). Prepared fresh and kept on ice. Remaining solution discarded.

Complete culture media [10% (v/v) FBS, 1% (v/v) penicillin-streptomycin]

50mL of FBS (16140071, Gibco™) and 5mL of penicillin-streptomycin (10,000 units/mL; 15140122, Gibco™) added into 445mL of RPMI 1640 growth media with GLUTAMAX™ (61870044, Gibco™).

1X PBS

1 tablet of PBS (12821680, Fisher BioReagents™) dissolved in 100mL of dH$_2$O.

1X Trypsin- EDTA

5mL of 10X trypsin-EDTA (0.5% trypsin, 5.3mM EDTA 4Na; 15400054, Gibco™) was diluted with 45mL of 1X sterile PBS.

1X Annexin V binding buffer

1mL of 10X Annexin V binding buffer (556454, BD Bioscience) added into 9mL of dH$_2$O.

0.2M PBS, pH 7.2

20.44g of sodium phosphate dibasic (BP332-500, Fisher BioReagents™) and 6.72g of sodium dihydrate phosphate monohydrate (011591.30, Thermo Scientific™) dissolved in 800mL of dH$_2$O, and pH adjusted to 7.4 with concentrated HCl or NaOH. Total volume brought up to 1000mL with dH$_2$O.

McDowell Trumps Fixative [4% (v/v) formaldehyde, 0.5% (v/v) glutaraldehyde, 0.1M PBS]

11mL of 37% formaldehyde (BP531-500, Fisher BioReagents™) and 2mL of 25% glutaraldehyde (BP2548-1, Fisher BioReagents™) added into 50mL of 0.2M PBS. Total volume brought up to 100mL with dH$_2$O.

2% (w/v) uranyl acetate solution

2g of uranyl acetate (AGR1260A, Agar Scientific) dissolved in 80mL of dH$_2$O. Total volume brought up to 100mL with dH$_2$O.

0.2M Sucrose

6.85g of sucrose (S0389-500, Sigma-Aldrich) dissolved in 100mL of dH$_2$O.

5.5.2. MATRIGEL CULTURE AND PLUG FORMATION

Patient-derived CLL cells were isolated from EDTA whole blood samples as described in section 2.2.1. All 3D cultures were performed in growth factor-reduced Matrigel™ 50% (supplemented with fibronectin to aid cell adhesion) diluted by an equal volume of complete culture media (section 5.5.1). Following isolation, the desired number of CLL cells were aliquoted and centrifuged at 200xg for 5 min. Cell pellets were resuspended in Matrigel 50% (v/v) and plugs of 50µL were made within sterile Eppendorf tubes or 24-well plates. Eppendorf tubes were utilised for culture because of their greater compatibility with sample processing for TEM (e.g., easier to trim away the tubes following embedding of 3D cultures within resin); however, it was not possible to microscopically examine cells cultured within Eppendorf tubes. Thus, plugs were also prepared within 24-well plates for the purpose of microscopic examination of cellular colonisation of 3D Matrigel™ matrices prior to TEM. Once polymerised, 500µL of complete culture media was added on top of the plugs. The media was topped up to approximately 500µL as required. The plugs were maintained in a humidified incubator at 37°C with 5% CO_2.

5.5.3. PHASE-CONTRAST MICROSCOPY

Following incubation, 24-well plates containing Matrigel™ plugs were sealed with parafilm. The plugs were immediately examined using phase-contrast microscopically and plates were kept out of the incubator no longer than 15 min. Images were acquired using a Leica DMI8 Microscope using supporting software and a HC PL APO x40/0.85 dry objective on a 1920x1440 pixel resolution format. Images were saved in a .lif file format.

5.5.4. LIVE-CELL IMAGING

For live-cell imaging of Matrigel™ cultures, plugs formation was performed as described in section 5.5.2 with the following exceptions: following resuspension of cell pellets in Matrigel™ 50% (v/v), plugs of 50µL were prepared in 8-well high glass bottom µ-slides (IB-80807, Thistle Scientific). Glass bottom slides were used for the microscopic examination of Matrigel™ plugs as they allowed the cultures to be visualised with high-resolution microscopy. Once polymerised, 300µL of complete culture media was added on top of the plugs. The media was topped up to approximately 300µL as required. The plugs were maintained in a humidified incubator at 37°C with 5% CO_2. Following incubation, phase-contrast microscopy was carried out as described in section 5.5.3 with the following exceptions: images were acquired using a Leica DMI8 Microscope using supporting software and a HC PL APO oil x63/1.40 objective on a 1920x1440 pixel resolution format. Images were taken every 10.27 seconds for a total of 10 min and saved in a .lif file format.

5.5.5. RELEASING CELLS FROM THE MATRIGEL™ MATRIX

Following 3D culture for 24h, 48h or 72h, cells were released from the Matrigel™ matrix plugs for viability testing. The complete culture media was removed and 500µL of 1X trypsin-EDTA (section 5.5.1) was added on top of plugs. The plugs were incubated at RT for approximately 10 min or until plugs had completed dissolved. The 1X trypsin-EDTA was periodically pipetted up and down gently to aid with the release of cells during incubation. Once the plugs had dissolved, the 1X trypsin-EDTA was neutralised with an equal volume of chilled complete culture media. Cells were pelleted by centrifugation at 200x*g* for 5 min and the supernatant removed. Cell pellets were resuspended in 500µL of chilled 1X PBS and centrifugation at 200x*g* for 5 min. The supernatant was removed, and cell pellets were resuspended in the required volume of 1X Annexin V binding buffer (section 5.5.1) to achieve a cell concentration

of $1x10^6$ cells/mL and kept on ice. The viability of cells was immediately assessed using Annexin V and flow cytometry.

5.5.6. ASSESSING CELL VIABILITY AFTER MATRIGEL™ MATRIX CULTURE

One hundred microlitres of cell suspension released form the Matrigel™ matrices ($1x10^5$ cell) was added into flow cytometry tubes. Five microlitres of Annexin V-FITC (556420, BD Biosciences) and 5μL of propidium iodide (PI; 556463, BD Biosciences) were added to the cell suspension, and incubated at RT for 15 min in the dark following gently vortexing. Four hundred microlitres of 1X Annexin V binding buffer (section 5.5.1) was added into each tube. Tubes were kept on ice and immediately analysed using a FACSAria II Flow Cytometer (BD Biosciences) and supporting software. The FITC signal detector and the PE signal detector were utilised for assessment of cell viability. Flow cytometry data was exported as .fcs files for analysis in FlowJo (version 10.4).

Using the FlowJo software, viable cells not undergoing measurable apoptosis (stain negative for both Annexin V-FITC and PI) were separately gated from dead cells (stain positive for both Annexin V-FITC and PI) and cells undergoing apoptosis (stain positive for Annexin V-FITC and negative for PI) within plots of FITC/PE fluorescence intensity. The percentage of viable cells within the total cell population was determined.

5.6. DEVELOPING TECHNIQUES TO IMAGE CELLS WITHIN 3D CULTURE SYSTEMS

5.6.1. INITIAL MICROSCOPIC EXAMINATION OF CELLULAR COLONISATION WITHIN MATRIGEL™ PLUGS

The aim of this chapter was to develop a 3D Matrigel™ model for the study of cellular behaviour and interactions in CLL. However, CLL cells rapidly undergo apoptosis without co-culture with accessory cells.[166] Additionally, shrinkage of Matrigel™ matrices can be observed

over time.[411] Therefore, initial optimisation experiments with CLL cells alone were limited to 72 h.

Major issues with any matrix-embedded 3D culture system include: (i) poor penetration of the matrix by cells; and (ii) low retention of cells within interstices, leading to colonisation of the base of the culture vessel.[413] To avoid these issues and reduce the time required for optimisation, cells were combined with the liquid ECM component prior to formation and polymerisation of matrices.

Microscopic phase-contrast examination of 3D Matrigel™ plugs demonstrated the formation of clusters of small, globular CLL cells after 72 h culture (Figure 5.2). Cluster were concentrated around the periphery of large spindle-shaped NLCs which had formed during the culture period, indicating that a TME-like environment had been established. Thin filopodial projections could also be observed extending between neighbouring CLL cells (arrows in Figure 5.2). Combining CLL cells with the liquid ECM prior to plug formation resulted in a large proportion of malignant cells being retained within the matrices. Indeed, only a small number of CLL cells were observed on the well floor rather than in the Matrigel™ plugs (images not shown). As expected, the distribution of cells within matrices was not uniform, with a greater number of both cell types being observed at the centre of the plugs than the matrix-growth medium interface. This indicated that cells were successfully able to adhere to and migrate through the interstices within the 3D structure. Successful migration was also demonstrated by sequential phase-contrast images showing CLL transiting between polarised and globular cell shapes as they move through the 3D matrix via amoeboid motility (Figure 5.3).
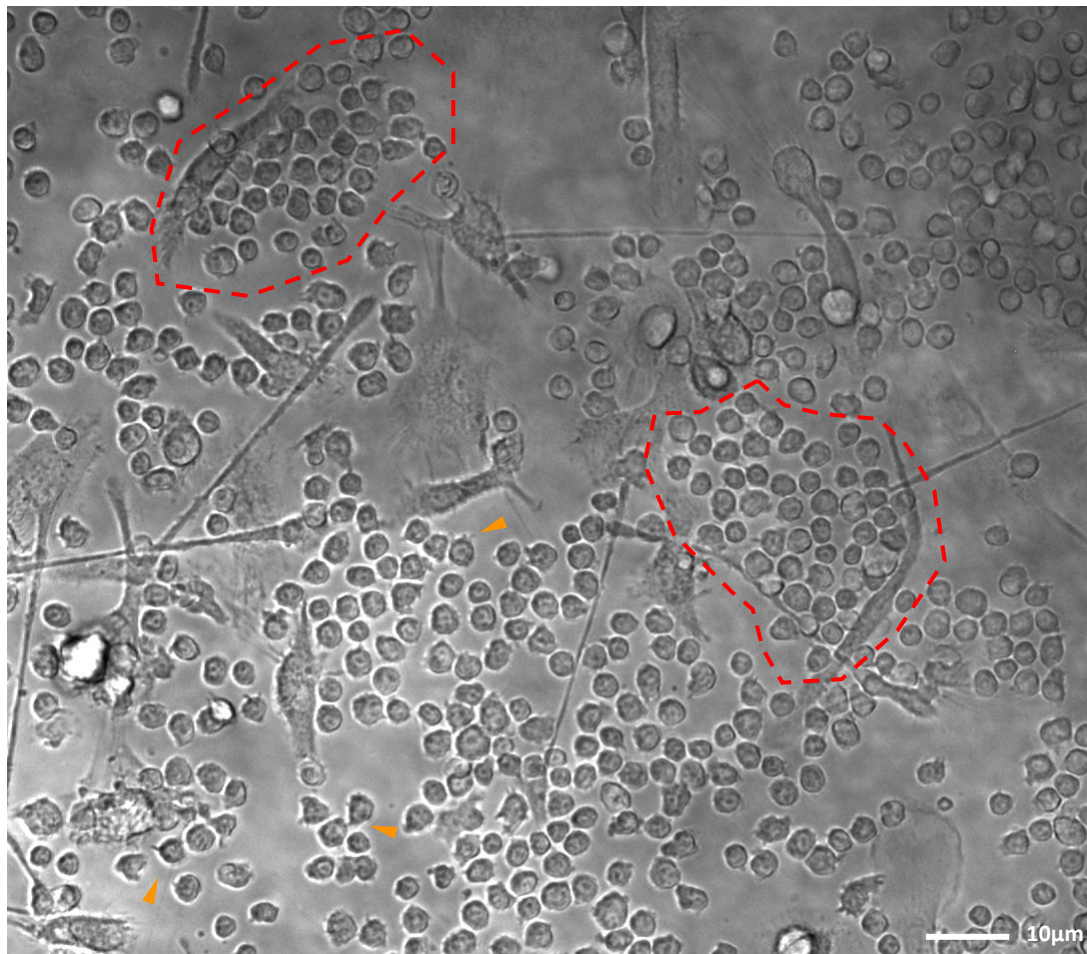
Figure 5.2: **Assessment of initial cellular colonisation within 3D Matrigel™ cultures.** CLL cells ($5x10^6$ cells) were resuspended in Matrigel 50% (v/v), and plugs cultured within a 24-well plate for 72 h. Following incubation, phase-contrast images were acquired using a Leica DMI8 Microscope with the use of a 40x dry objective. Red dashed lines represent large monocyte-derived NLCs surrounded by clusters of CLL. Thin filopodial projections extending between adjacent CLL cell could also be observed (orange arrows).
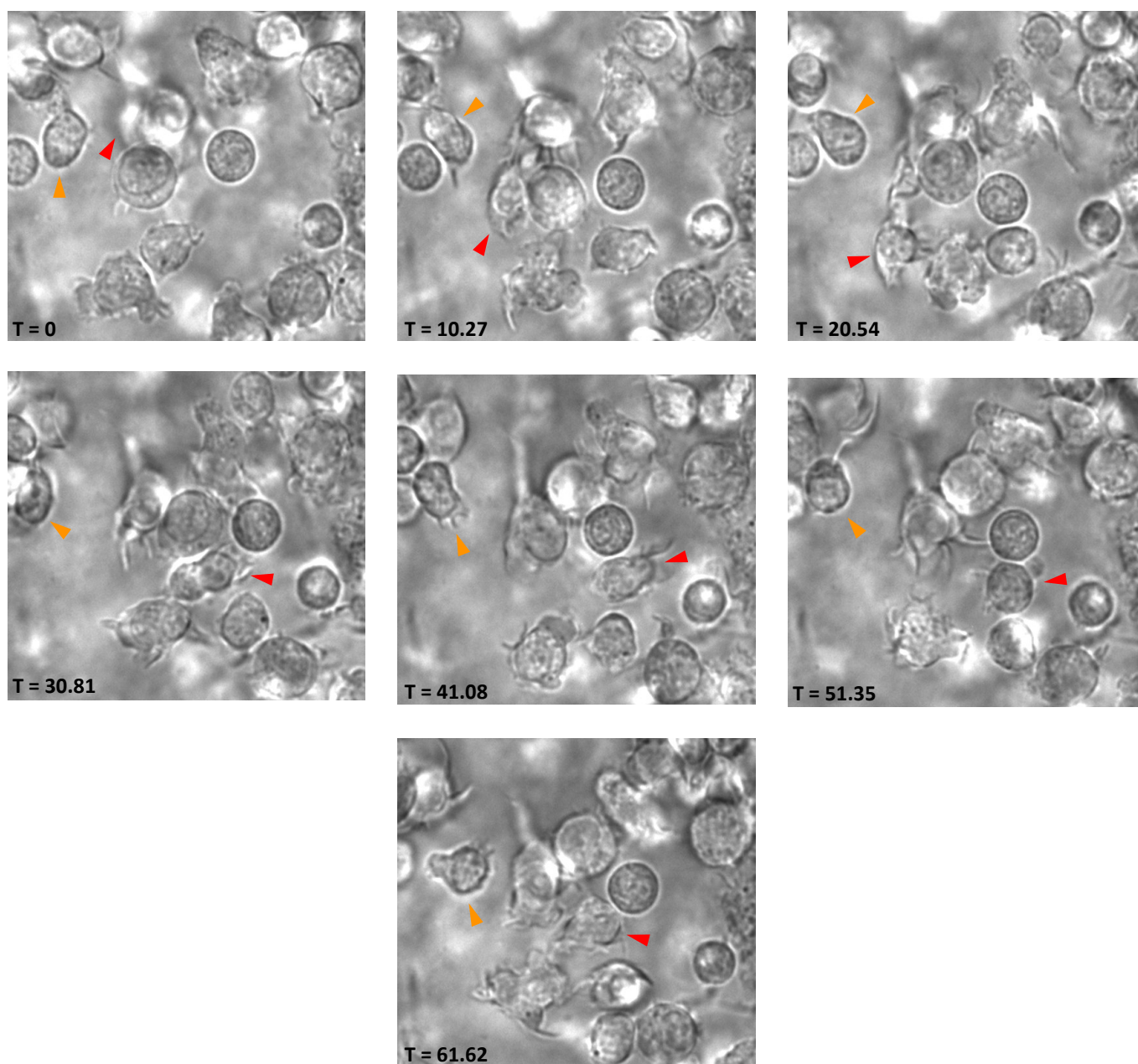
Figure 5.3: Initial evaluation of cellular interactions within 3D Matrigel™ cultures. CLL cells ($5x10^6$ cells) were resuspended in Matrigel 50% (v/v), and plugs cultured within an 8-well high glass bottom μ-slides for 72 h. Following incubation, time-lapse phase-contrast images were acquired using a Leica DMI8 Microscope with the use of a 63x oil objective. Images were taken every 10.27 sec. CLL cells periodically transitioning between polarised and globular morphologies as they underwent amoeboid motility were observed (orange and red arrows).

5.6.2. OPTIMISING SEEDING DENSITY AND CELL VIABILITY WITHIN 3D MATRIGEL™ MATRIX CULTURES

The major criterium for relevance of a TME-like model is survival of malignant cells. Thus, to further optimise the 3D matrix culture system, an experiment with a series of cell suspension densities was performed to establish the optimal seeding density. Three suspensions containing $1x10^6$, $5x10^6$ and $1x10^7$ cells were prepared in complete media and combined with liquid Matrigel™ matrix (50% v/v). After combining, 50µL plugs were formed within Eppendorf (lids open) or 24-well plates and maintained for up to 72 h. After the required incubation period, colonisation of the Matrigel™ matrices was assessed by phase-contrast microscopy. Matrigel™ plugs were also redissolved and the cells collected for viability testing via flow cytometry.

After 24 h incubation within 3D Matrigel™ matrix cultures, CLL cells seeded at $1x10^6$ cells/plug were typically observed forming small, distinct homotypic groups or surrounding accessory NLCs which had formed towards the centre of the plugs (Figure 5.4). Between these clusters of interacting cells were moderate-to-large areas of Matrigel™ containing few or no CLL cells. The low seeding density within these cultures likely promoted homotypic/heterotypic cellular interactions and the establishment of TME-like environment to support neoplastic cell survival. In contrast, CLL cells seeded at $5x10^6$ cells/plug displayed a more even distribution of cells within the centre of 3D models after 24 h incubation, with only small areas of the Matrigel™ being devoid of cells. Fewer distinct homotypic/heterotypic groups of cells were also observed, indicating that the higher seeding density may have promoted more transient cellular interactions within these 3D systems. Within Matrigel™ cultures seeded at $1x10^7$ cells/plug, near total colonisation of all interstices throughout the models was noted after 24 h. Areas of Matrigel™ containing few or no CLL cells were infrequent and small. Large

homotypic clusters of CLL cells were observed; however, these appeared to be the results of crowding within the interstices rather than cellular transmigration and interaction. Within all Matrigel™ cultures, regardless of seeding density, CLL cells were prominently globular with some polarised cells extending filopodial projections.

Following 48 h incubation, CLL seeded at $1x10^6$ cells/plug were still observed forming small homotypic clusters and interacting with NLCs at the centre of plugs (Figure 5.5). CLL cells were also still sparse-to-absent from large areas of the Matrigel™ culture. A larger proportion of polarised CLL cells were observed at 48 h than at the previous time point (Figure 5.4), suggesting that cells were readily undergoing amoeboid migration within the 3D models. The cellular distribution within cultures seeded at $5x10^6$ cells/plug after 48 h incubation (Figure 5.5) was a largely similar to that noted at 24 h (Figure 5.4); however, some relatively large homotypic groups had been established. The initial crowding noted within cultures seeded at $1x10^7$ cells/plug had been reduced following 48 h incubation, likely due to apoptosis (Figure 5.5). CLL cells demonstrated a more even distribution within high-density Matrigel™ models, with few sparsely colonised areas being observed.

Matrigel™ cultures seeded at $1x10^6$ and $5x10^6$ demonstrated similar large groups of interacting CLL cells around NLCs located towards the centre of plugs following 72 h culture (Figure 5.6). These clusters contained both small, globular cells and polarised cells extending filopodia towards neighbouring cells. The major difference between these 3D models at 72 h was the proportion of uncolonized Matrigel™, with larger areas of the matrices seeded at $1x10^6$ cells/plus containing few or no CLL cells as previously observed at earlier time points (Figure 5.4-5). Matrices seeded at $1x10^7$ cells/plug were still relatively crowded at 72 h (Figure 5.6) compared to cultures seeded at lower densities.

1x10^6 cells   **5x10^6 cells**   **1x10^7 cells**
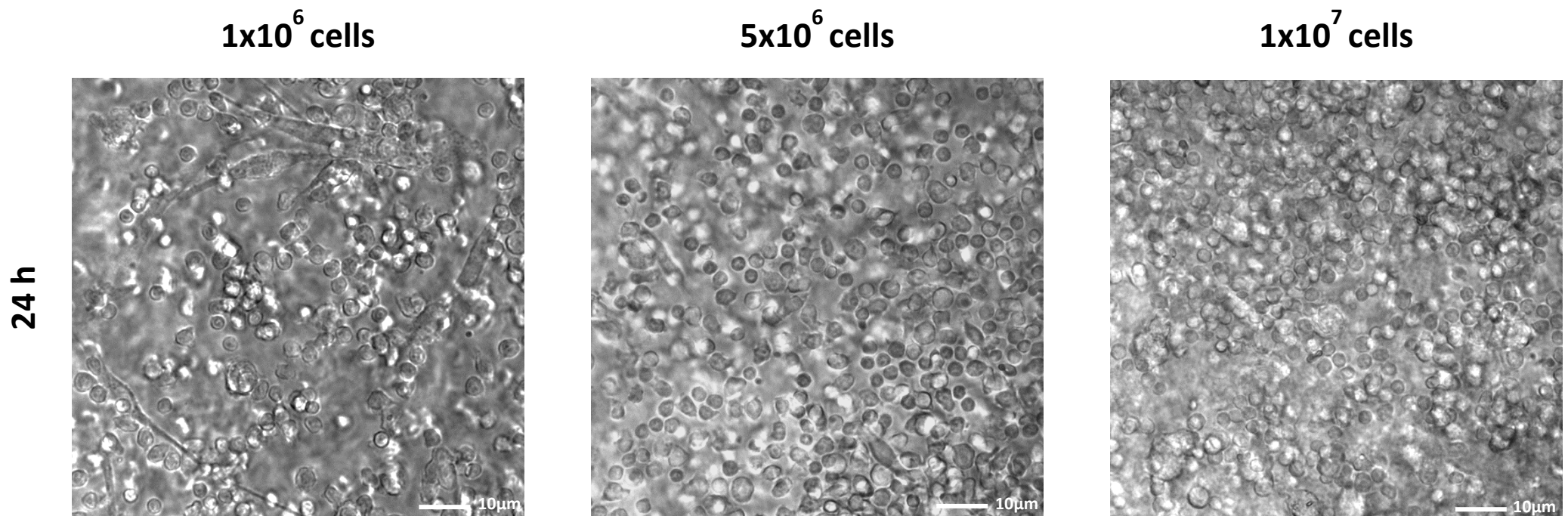
Figure 5.4: **Evaluation of cellular colonisation within 3D Matrigel™ cultures after 24 h incubation.** CLL cells ($1x10^6$, $5x10^6$ or $1x10^7$ cells) were resuspended in Matrigel 50% (v/v) and plugs cultured for 24 h. Following incubation, colonisation of the Matrigel™ plugs was assessed by phase-contrast microscopy using a Leica DMI8 Microscope with the use of a 40x dry objective.

1x10^6 cells **5x10^6 cells** **1x10^7 cells**

48 h
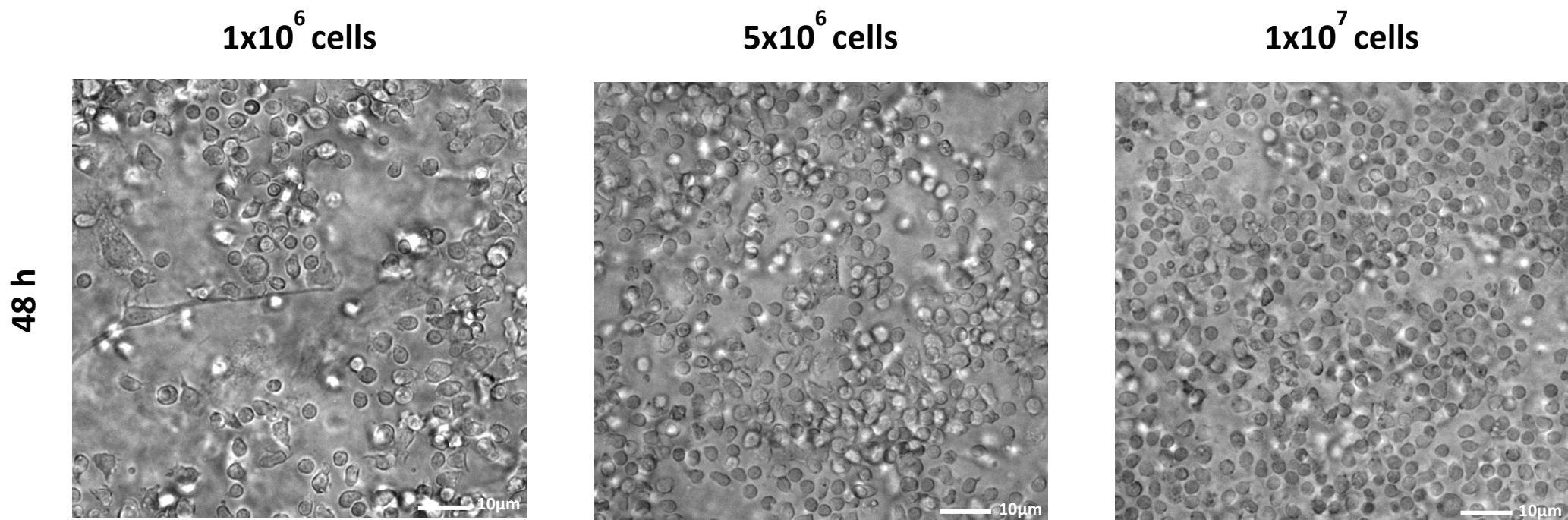
Figure 5.5: Evaluation of cellular colonisation within 3D Matrigel™ cultures after 48 h incubation. CLL cells (1x10^6, 5x10^6 or 1x10^7 cells) were resuspended in Matrigel 50% (v/v) and plugs cultured for 48 h. Following incubation, colonisation of the Matrigel™ plugs was assessed by phase-contrast microscopy using a Leica DMI8 Microscope with the use of a 40x dry objective.

72 h

1x10^6 cells   **5x10^6 cells**   **1x10^7 cells**
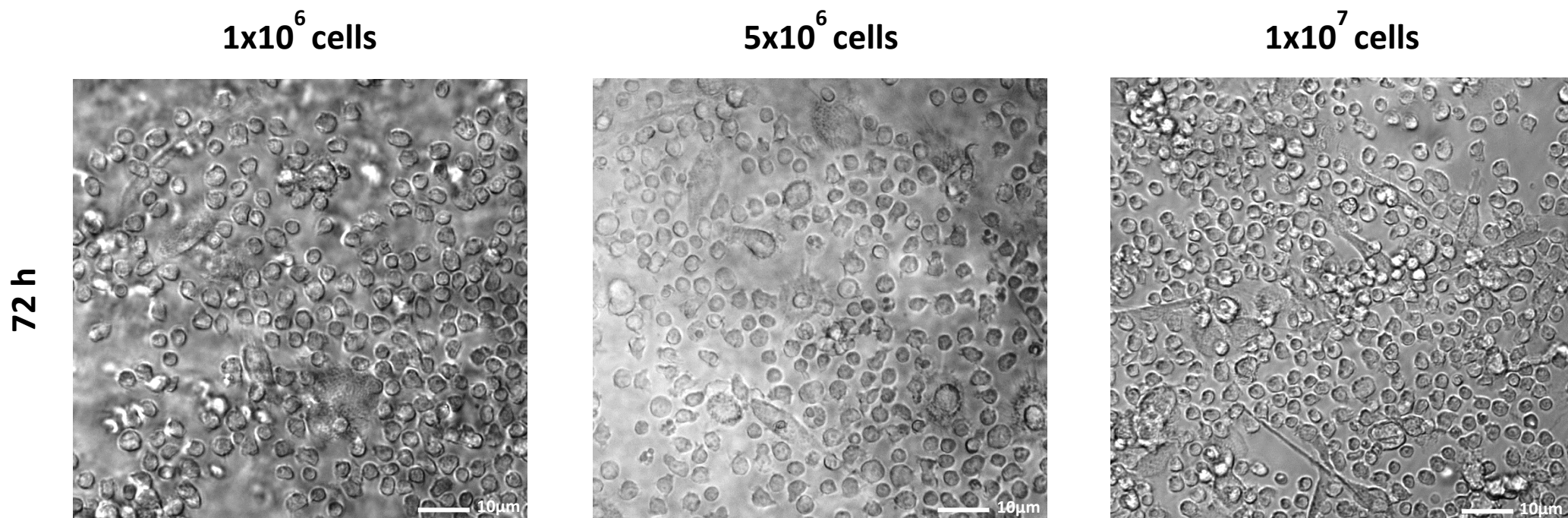
Figure 5.6: **Evaluation of cellular colonisation within 3D Matrigel™ cultures after 72 h incubation.** CLL cells (1x10^6, 5x10^6 or 1x10^7 cells) were resuspended in Matrigel 50% (v/v) and plugs cultured for 72 h. Following incubation, colonisation of the Matrigel™ plugs was assessed by phase-contrast microscopy using a Leica DMI8 Microscope with the use of a 40x dry objective.

An initial large decrease in mean CLL cell viability was observed after 24 h of cultures within 3D Matrigel™ systems seeded at 1×10^6 cells/plug (78.3% after 24 h incubation vs 98.5% at 0 h) (Figure 5.7). The mean cell viability within models seeded at 1×10^6 cells/plug gradually increased at later time points (80.8% and 80.9% following 48 and 72 h culture, respectively); however, it remained lower than that noted for models with higher seeding densities. Indeed, following initial small decreases in mean cells viability in matrices seeded at 5×10^6 and 1×10^7 cells/plug (94.1% and 96.0% at 24 h, respectively), relatively high mean cell viabilities were then sustained for up to 72 h of culture.
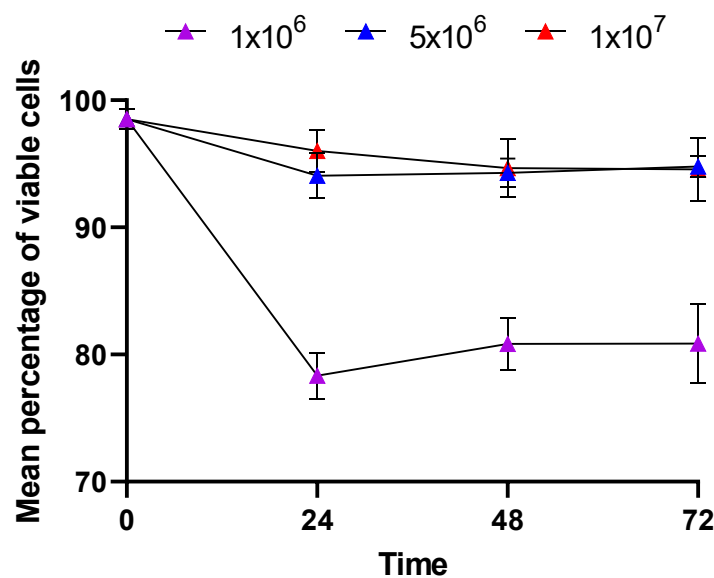
Figure 5.7: Assessment of cell viability within 3D Matrigel™ cultures. CLL cells (1×10^6, 5×10^6 or 1×10^7 cells) were resuspended in Matrigel 50% (v/v) and plugs cultured for 24, 48 or 72 h. Following incubation for the required period, cells were released from the plugs, stained with Annexin V-FITC and PI, and cell viability evaluated using a FACSAria II Flow Cytometer with supporting software. The percentage of viable (stain negative for both Annexin V-FITC and PI) was determined from FITC/PE fluorescence intensity plots using FlowJo. Line graphs showing the mean percentage of viable cells at 0, 24, 48 and 72 h 3D Matrigel™ culture were created using GraphPad Prism. Error bars represent standard error of the mean (n = 3).

Based on the above microscopic examination and evaluation of cell viability within 3D Matrigel™ cultures, a seeding density of 5×10^6 cells/plug was selected as the optimal concentration for subsequent investigations of CLL cell behaviour within a TME-like setting. A seeding density above this value (i.e., 1×10^7 cells/plug) resulted in significant crowding within interstices, which may lead to impaired 3D cell migration, whilst not providing any significant benefits in terms of cell viability. Although a low seeding density of 1×10^6 cells/plug possibly encouraged homotypic/heterotypic cellular interactions and amoeboid cell migration within the culture systems, mean CLL cell viability within these models was lower at all time points than that observed for higher seeding densities, with a particularly large decrease in viable cells being seen after 24 h culture. In contrast, a seeding density of 5×10^6 cells/plug provided a relatively even distribution of CLL cells towards the centre of plugs, allowing the microscopic examination of single cells interacting with their neighbours, and sustained high cell viability.

5.7. PROCESSING MATRIGEL™ MATRIX CULTURES FOR TEM

5.7.1. FIXATION METHODS FOR TEM

Following isolation, 5×10^6 cells were seeded into 50μL 50% Matrigel™ plugs and cultured for 72 h (section 5.5.2). Media was removed from Eppendorf tubes and 500μL of pre-warmed (37°C) McDowell Trumps fixative (section 5.5.1) carefully added on top of the plugs. The 3D Matrigel™ plugs were fixed at RT for 2-3 h and then carefully washed three times with sterile 1X PBS for 15 min each.

5.7.2. DEHYDRATION METHODS FOR TEM

The plugs were incubated at RT in 500μL of 0.2M sucrose twice for 15 min each and then rinsed briefly in 500μL of 1XPBS. Matrigel™ plugs were dehydrated further through an ethanol series, beginning with 30% and changing to solutions of 50%, 70%, 90% and two times 100%.

Plugs were left in each ethanol change for 15 min. At 70% ethanol, en-bloc staining was performed to enhance contrast if required (section 5.7.3). This step was optional and was not always performed depending on the SEM technician's judgement. The use of en-bloc staining is described in the figure legends of relevant experiments. If this step was omitted, the fixation of Matrigel™ plugs using the alcohol dehydration series 30/50/70/90 and 100% was performed as described above.

5.7.3. EN-BLOC STAINING (ENHANCING CONTRAST)

At 70% ethanol, the Matrigel™ plugs were en-bloc stained with 2% uranyl acetate (section 5.5.1) for 1 h at RT. Following incubation, the alcohol dehydration series (section 5.7.2.) was resumed, starting with 90% ethanol.

5.7.4. RESIN EMBEDDING AND SECTIONING

London White Resin (at a 50% ratio of resin to ethanol) (AGR1280, Agard Scientific) was added to each Eppendorf tube and incubated at RT for 1 h with rotation. The resin was removed, and fresh London White Resin (at a 70% ratio of resin to ethanol) was added to each Eppendorf tube and incubated at RT for 1 h with rotation. The resin was removed, and pure London White resin added to Eppendorf tubes. The resin was incubated at RT overnight with rotation. The resin was again removed, and fresh pure London White resin added to Eppendorf tubes. The resin was incubated at RT overnight with rotation. The resin was removed, and the plugs placed at the bottom of BEEM capsules (AGG360-1, Agard Scientific). The capsules were then filled with pure London White Resin to the brim and the resin polymerised at 50°C for 24 h.

The resin blocks were trimmed to locate the embedded cells using a glass knife and ultramicrotome, and subsequent semi-thin section (approximately 250nm in thickness) were

202

cut for microscopic examination of cell preservation and structure. Thin sections (approximately 90nm in thickness) were then cut using a diamond knife and ultramicrotome with a distilled water filled boat. Thin sections were then collected on nickel grids and left to dry overnight.

5.8. INITIAL EVALUATION OF MATRIGEL™ MATRIX SECTIONS USING TEM

TEM examination of Matrigel™ matrix sections demonstrated characteristic small, round B-lymphocytes with thin filopodial projections extending from the cell surface towards neighbouring cells (Figure 5.8). Within cell nuclei, electron-dense heterochromatin could be observed, in addition to lighter regions of euchromatin, a less compact, transcriptionally active form of chromatin.[414] Mitochondria and vacuoles could be distinguished within the cell cytoplasm (arrows in Figure 5.8); however, their visualisation was highly dependent of section quality. It was not possible to distinguish other organelles typically found in eukaryotic cells.
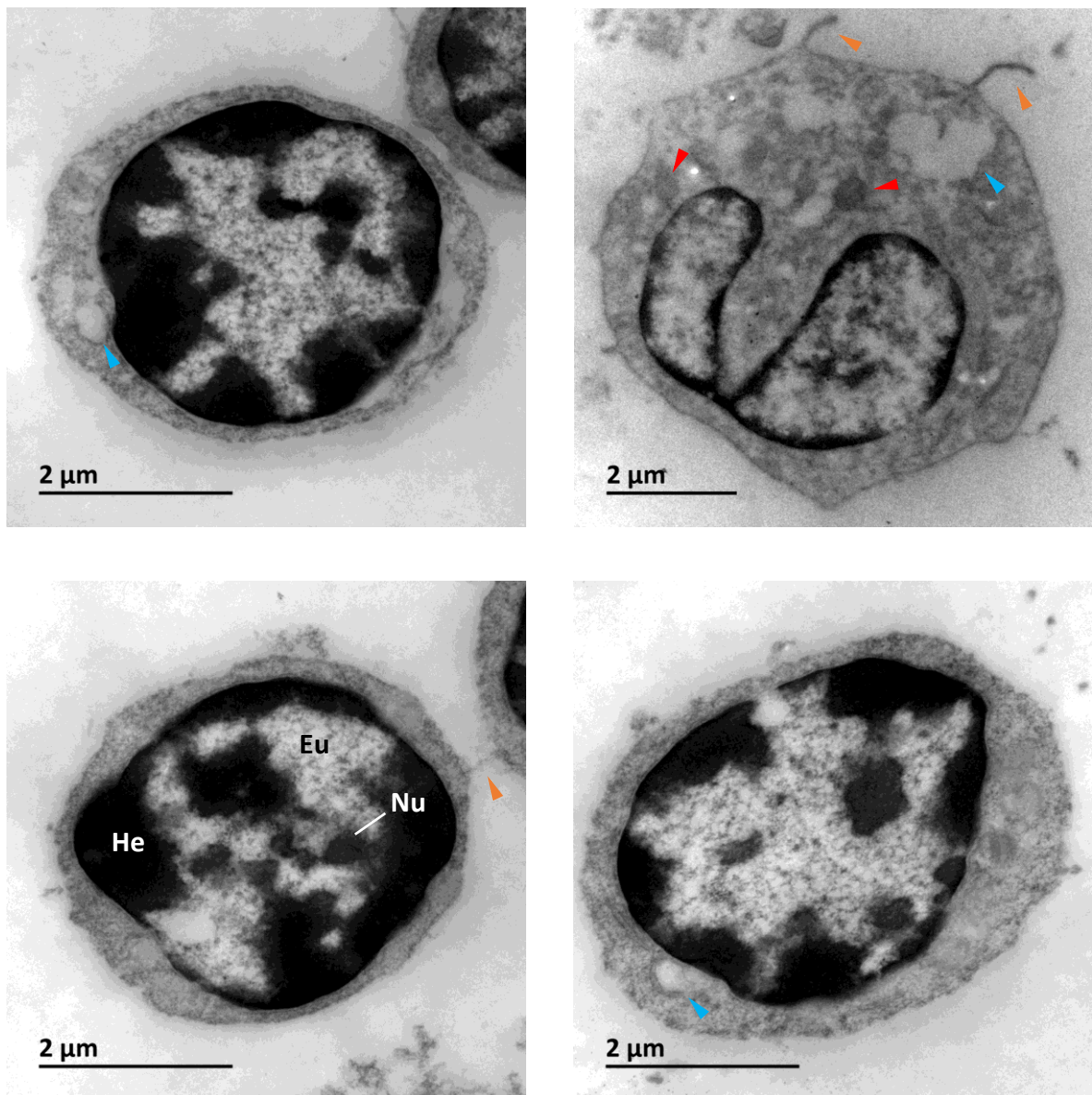
Figure 5.8: Evaluating CLL morphology within ultrathin sections prepared from 3D culture systems. CLL cells (5x10^6 cells/plug) were resuspended in Matrigel 50% (v/v), and plugs cultured for 72 h. Following incubation, plugs were fixed, processed and ultrathin sections prepared. Images were acquired at 15,000x using a JEOL 1400 TEM with supporting software. Mitochondria (red arrows) and vacuoles (blue arrows) could be distinguished within the CLL cell cytoplasm. Fine filapodial projections could also be seen extending between neighbouring cells (orange arrows). Eu, euchromatin; He, heterochromatin; Nu, nucleolus

5.9. DISCUSSION

In the BM and secondary lymphoid tissues, CLL engage in numerous cellular and molecular interactions with accessory cells and matrix.[94,95] Despite not yet being fully elucidated, studies have shown that this cross-talk between CLL cells and the TME modulates malignant B-lymphocyte survival and proliferation[167,171,172,179] and confers dug resistance,[74,113,415] which is possibly responsible for residual disease in some patients after conventional therapy. The BCR, which plays an integral part in the maintenance and expansion of the CLL clones through activation of downstream kinases such as BTK, SYK and PI3Kδ[193,197] is believed to play a crucial role in facilitating CLL-TME interactions by regulating rearrangement of the F-actin cytoskeleton[416] and cytokine production.[95] Indeed, molecular targeting of the BCR pathways via BTK and SYK inhibitors disrupts the interactions between CLL cells and the TME[212,230,235–238] and has shown promising results in clinical trials.[42,209,210,220,222,230] Thus, the CLL TME has become a highly dynamic translational field of research in recent decades.

The aim of this chapter was to develop a 3D Matrigel™ matrix culture system which could be combined with high-resolution EM for the subsequent study of behavioural and molecular aspects of CLL pathogenesis within a TME-like setting.

5.9.1. EVALUATING THE 3D MATRIGEL™MATRIX CULTURE SYSTEM

The *in vitro* 3D Matrigel™ system utilised in this study harboured characteristics of a representative TME model. The system permitted CLL cell migration, as demonstrated by live-cell imaging showing malignant B-lymphocytes rapidly transitioning between the two morphological states seen in RhoA/CDC42-controlled amoeboid motility.[165,257,327]

The model also supported the formation of large, spindle-like NLCs. Differentiation of NLCs from monocytes *in vitro* is contact-dependent, with CD14^{+} PBMCs co-cultured with CLL cells,

but separated by a Transwell membrane, displaying similar CD14 and CD33 levels to that of CD14^{+} PBMCs cultured alone. Down-modulation of CD14 and CD33 distinguishes the NLC phenotype from that of blood monocytes, monocyte-derived dendritic cells, or macrophages.[181] NLCs formation, therefore, indicated that CLL cells were able to interact directly with monocytes within the Matrigel™ model.

The establishment of clusters of leukemic cells around supportive NLCs was likely facilitated by CXCL12- and CXCL13-driven chemotaxis.[167,178] Thin filopodia were observed between CLL and NLCs, providing leukaemic cells with contact-dependent protection from spontaneous apoptosis as previously described by others.[179,180] The cellular interactions described here proved representative (at least in part) for the CLL TME, which is of great value for future mechanistic studies of this disease, as well as for evaluating treatment outcomes.

The 3D Matrigel™ model supported the survival of primary CLL cells for up to 72 h at high seeding densities. A similar 3D system has been used to encourage the growth of malignant B-lymphocytes for longer culture periods, with primary CD138^{+} MM cells surviving and proliferating for up to 28 days.[411] This model utilised a combination of endothelial progenitor cells and healthy allogeneic multipotent mesenchymal stromal cells to form pre-vascular niches which aided long-term culture. [411] Thus, the introduction of additional supportive cells, such as BMSCs which protect CLL cells from cytotoxic agents in a contact-dependent manner,[170,171] would have improved the bio-mimicry of the 3D model utilised here and permitted extended culture. However, co-culture of primary MCL cells and BMSCs requires irradiation of the BMSCs, once the desired confluency is achieved, to arrest stromal proliferation and prevent outgrowth of malignant B-lymphocytes.[286,413] Irradiation of BMSCs would have been incompatible with the pre-embedded method used here to ensure

colonisation of Matrigel™ matrices by CLL cells, as leukaemic cells would need to be omitted until after the BM cells had proliferated within the Matrigel™ interstices. Alternatively, irradiated BMSCs and CLL cells could be combined with liquid ECM, but the formation of supportive niches would likely be impaired due to the arrested proliferation of BM cells. Further studies are needed to establish a 3D tri-culture (i.e., CLL cell, NLC and BMSC) model for CLL.

The *in vitro* 3D TME-like culture system described here allowed CLL populations to be monitored using non-invasive time-lapse imaging and retrieved from culture, making this model suitable for mechanistic evaluation of CLL pathogenesis. Furthermore, morphologically recognisable CLL cells were well preserved in ultra-thin sections of the Matrigel™ matrix. Typical features of the eukaryotic subcellular architecture were clearly visible within sections following TEM examination, including nucleoli, mitochondria, and vacuoles. Fine filopodia were also observed extending between neighbouring cells, allowing the detailed examination of cell-to-cell contact. As such, this Matrigel™ model provides a relatively cheap and simple tool, avoiding expensive rotating culture vessels[377,388] or microfluidic systems,[404,412] to study the biology, interactions, and resistance of primary leukaemic cells within an artificial TME. Further investigations are required to increase the bio-mimicry of the tissue of origin, as well as show reproducible results from a heterogenous panel of primary CLL cells. However, due to time constraints this 3D model was deemed suitable for use in subsequent experiments to optimise immunogold labelling of proteins of interest (Chapter 6). Thus, allowing molecular alterations underlying the morphological and behavioural changes observed in CLL cells following signal inhibition to be characterised within a 3D TME-like setting.

CHAPTER 6 – APPLICATION OF 2D AND 3D CULTURE SYSTEMS TO EXPLORE NOTCH1 FUNCTION IN MATURE B-LYMPHOCYTE DISORDERS

6.1. INTRODUCTION

NOTCH1 is now recognised as one of the most frequently mutated genes in CLL.[47,53–56] These mutations typically generate a truncated protein that lacks the domains required for proteasomal degradation, leading to the accumulation of the N-ICD in CLL cells and aberrantly prolonged activation of downstream signalling pathways.[53,54,60,75,77–79] Interestingly, several lines of evidence indicate that NOTCH1 activation in CLL is under the control of the TME via ligand-dependent mechanisms. Jagged/Delta-like proteins, which are constitutively expressed by stromal cells in the BM and lymph nodes, increase NOTCH1 activation and promote CLL survival, independent *NOTCH1* mutational status.[74,77] Additionally, expression of the N-ICD in CLL cells was more pronounced in lymph nodes than surrounding soft tissue, regardless of NOTCH1 mutations.[417,418] Collectively, these reports highlight the importance of TME signals in inducing NOTCH1 activation in both *NOTCH1*-mutated and wild-type CLL patients.

The exact role of NOTCH1 in CLL pathogenesis is still largely unknown. However, mutated-*NOTCH1* has been identified in early haematopoietic progenitor cells of CLL patients.[49] Subsequent NGS studies revealed that *NOTCH1* mutations were present at the CD34$^+$/CD19$^-$ progenitor and CD34$^+$/CD19$^+$ pro-B cell levels in CLL.[419] These findings suggest that aberrant NOTCH1 signalling may contribute to CLL leukaemogenesis by facilitating the survival and proliferations of early CLL haematopoietic progenitors. Dysregulated NOTCH1 signalling within mature, malignant B-lymphocytes promoted CCL19- and CXCL12-mediated

homing,[86,88] indicating that *NOTCH1*-mutated CLL cells may favour recirculation to lymphoid organs, where interactions with accessory cells promote their survival in addition to further activating NOTCH1 signalling.

Recently, the BTKi ibrutinib has been shown to significantly reduce NOTCH1 activity in CLL patients. The presence of NOTCH1/BTK complexes, whose number was reduced after ibrutinib treatment was also confirmed. Downregulated NOTCH1 activity was restored at the at the point of relapse and remained activated in CLL patients resistant to ibrutinib.[420] Chemotaxis has been identified as one of the main NOTCH1-regulated processes in CLL cells[57,86,88] and, therefore, reduced integrin-mediated homing of leukemic cells to tissues, underlying the peripheral lymphocytosis observed in CLL patients receiving ibrutinib,[212,235] may be caused by decreased crosstalk between BTK and NOTCH1 signalling pathways. Indeed, a combination of ibrutinib and GSIs (PF-03084014 and L-685,458) enhanced CLL cell apoptosis, irrespective of co-culture with protective stromal cells.[113] Therefore, combinational therapies incorporating BTKi and NOTCH1 inhibitors may have therapeutic benefits in this disease.

The aim of this chapter was to optimise immunogold labelling of activated NOTCH1 within the 3D Matrigel™ matrix culture system previously evaluated in Chapter 5. Thus, permitting characterisation of changes in protein localisation following signal inhibition, and allowing molecular alterations to be linked to morphological and behavioural changes observed in CLL cell within 2D culture systems. The MCL cell lines REC-1 (mutated *NOTCH1*) and G519 (unmutated *NOTCH1*) were also utilised to model the effect(s) of *NOTCH1* mutation on chemokine-driven migration following GSI pre-treatment. Finally, experiments were conducted to further characterise NOTCH1-protein interactions in malignant B-lymphocytes;

initially exploring interactions with previously unreported proteins using co-immunoprecipitation and liquid chromatography-mass spectrometry analyses of JURKAT cell lysate. The human T-ALL cell line JURKAT does not display activating mutations of *NOTCH1*; however, it has been shown to produce high levels of N-ICD compared to other T-ALL cell lines.[287]

NOTCH1 was selected for initial immunogold labelling optimisation experiments, and detailed examination of GSI-induced mechanical and molecular responses due to evidence linking it to the trafficking of CLL cells to tissues and to ibrutinib treatment response.[57,86,88] Therefore, gaining a greater understanding of the role of NOTCH1 signalling in CLL pathogenesis and in mediating BTKi treatment outcomes has the potential to suggest novel therapeutic regimes to combat resistance in B-lymphocyte malignancies.

6.2. SUMMARY OF EXPERIMENTAL METHODS

The methods employed in this chapter involved the general culture of patient-derived CLL cells *ex vivo* (section 2.2.1), and MCL and JURKAT cell lines (section 2.2.3). These cells were adhered to fibronectin-coated coverslips (section 2.3.1-2), treated with small molecule inhibitors (section 2.3.9) and their cytoskeletal features assessed by SEM (2.3.10) combined with morphometric ImageJ analyses (2.3.11). The optimised methods for quantitatively describing CLL shape changes using SEM and ImageJ are described in detail within Chapter 3.

Changes in the migration of CLL and MCL cells to CXCL12 following signal inhibition were determined using the Transwell migration assay (section 2.5).

All data generated through ImageJ and FlowJo analyses were exported to GraphPad Prism™ Version 5 software for graphical representation and statistical analysis (section 2.3.12 and

section 2.5.4, respectively). The specific statistical tests employed are described in the figure legends of each experiment.

The optimised method for culturing primary CLL cells within 3D Matrigel™ models is described in detail within Chapter 5. Following incubation, Matrigel™ plugs were fixed (section 5.7.1), dehydrated (section 5.7.2), embedded in resin, and ultra-thin sections prepared (section 5.7.4) for TEM examination. The optimisation of immunogold labelling of NOTCH1 within CLL cells cultured within a 3D TME-like setting is described below (section 6.3-4).

NOTCH1 binding partners were investigated using biochemical assays of Co-IP (section 2.6.1-4), western blotting and immunohybridisation (section 2.7.1-2). Identification of NOTCH1-protein interactions was determined using liquid chromatography-mass spectrometry analyses of co-precipitated proteins (section 2.8.1-5 and 2.9). Functional relationships of the proteins identified using mass spectrometry were determined using the STRING (Search Tool for the Retrieval of Interacting Genes/Proteins) database (https://string-db.org/), using high confidence analysis (predicted significance >0.7).

6.3. PRACTICAL IMPLEMENTATION OF IMMUNOGOLD LABELLING OF NOTCH1

6.3.1. REAGENTS AND BUFFERS

1X PBS

1 tablet of PBS (12821680, Fisher BioReagents™) dissolved in 100mL of dH_2O.

0.05M Glycine

187.68mg of glycine (BP381-1, Fisher BioReagents™) dissolved in 50mL of 1X PBS.

10X TBS, pH 7.6

24.2g Tris base and 80.06g NaCl dissolved in 800mL dH$_2$O and pH adjusted to 7.6 with concentrated HCl. Total volume brought up to 100mL with dH$_2$O.

Wash buffers

1X TBST: 100mL of 10X TBS (pH 7.6) and 1mL of Tween-20 (BP337-100; Fischer BioReagents™) added into 900mL of dH$_2$O.

Electron microscopy (EM) Incubation buffer [1% (v/v) goat serum, 1% (w/v) BSA]

0.4mL of heat inactivated goat serum (092939249, MP Biomedicals) and 0.4g of BSA dissolved in 30mL of 1X TBST. Total volume brought up to 40mL with 1X TBST.

3% EM Blocking buffer [3% (v/v) goat serum, 2% (w/v) BSA]

1.2mL of heat inactivated goat serum and 0.8g of BSA dissolved in 30mL of 1X TBST. Total volume brought up to 40mL with 1X TBST.

5% EM Blocking buffer [5% (v/v) goat serum, 2% (w/v) BSA]

2mL of heat inactivated goat serum and 0.8g of BSA dissolved in 30mL of 1X TBST. Total volume brought up to 40mL with 1X TBST.

6.3.2. STANDARD METHOD FOR IMMUNOGOLD LABELLING OF TEM SECTIONS

Grids were incubated (section side down) on top of 50μL droplets of 0.05M glycine (section 6.3.1) at RT for 15 min and then blotted (section side up) on filter paper. The grids were rinsed twice on 50μL droplets of EM incubation buffer (section 6.3.1) for 15 min each and blotted. The grids were incubated on top of 50μL droplets of 3% EM blocking buffer (section 6.3.1) at RT for 30 min, blotted and then rinsed twice on droplets of EM incubation buffer for 5 min each. The grids were blotted and then incubated on 50μL droplets of primary antibody

212

(diluted in EM incubation buffer) at 4°C overnight. Following blotting and four rinses on droplets of EM incubation buffer for 5 min each, the grids were incubated on 50μL droplets of a secondary antibody conjugated to gold nanoparticles (diluted in EM incubation buffer) at RT for 1 h. The grids were blotted, rinsed five times on droplets of EM incubation buffer for 5 min each and then rinsed twice on droplets of 1X PBS for 5 min. The grids were blotted, rinsed twice on droplets of dH$_2$O and then left to air dry at RT for approximately 30 min before being analysed using a JEOL 1400 TEM with supporting software. Images were saved in a .tif file format.

6.3.3. EVALUATING IMMUNOGOLD LABELLING OF 3D MATRIGEL™ MODEL SECTIONS

One proteins of interest, NOTCH1, was selected for optimisation of immunogold labelling of sections prepared from 3D Matrigel™ culture systems. NOTCH1 signalling, which is initiated following proteolytic cleavage of the NOTCH1 transmembrane receptor and translocation of the active N-ICD to the nucleus,[60] is constitutively activated in CLL and promotes neoplastic cell survival and resistance to apoptosis.[73] In addition to this proteins being important in CLL leukemogenesis, an antibody directed against activated NOTCH1 has previously been utilised for immunogold labelling of TEM sections.[421]

Immunogold labelling of activated NOTCH1 within Matrigel™ matrix sections resulted in extensive staining throughout the cytoplasm and nuclei of CLL cells, with no observable clustering or patterns of gold particles (Figure 6.1A). Staining of Matrigel™ ECM was also seen (arrows in Figure 6.1A). In contrast, no staining (of CLL cells or Matrigel™) was present in control sections labelled with the secondary gold-conjugated antibody alone (Figure 6.1B). These findings suggested that the anti-activated NOTCH1 antibody was binding non-specifically to both CLL cells and the Matrigel™ at the recommended concentration and

further optimisation of the immunogold labelling procedure was necessary. Attempts to reduce non-specific signal by decreasing the primary antibody concentration and/or increasing the length of wash steps were not successful (images not shown). Based on the advice of technical staff, the decision was made to continue the optimisation of NOTCH1 immunogold labelling within sections prepared from CLL cell pellets (5×10^6 cells/pellet) instead of Matrigel™ models. Removing the Matrigel™ and, consequently, non-specific labelling of the ECM would simplify the optimisation process. The 3D Matrigel™ matrix would be reintroduced once specific NOTCH1 signal had been obtained.
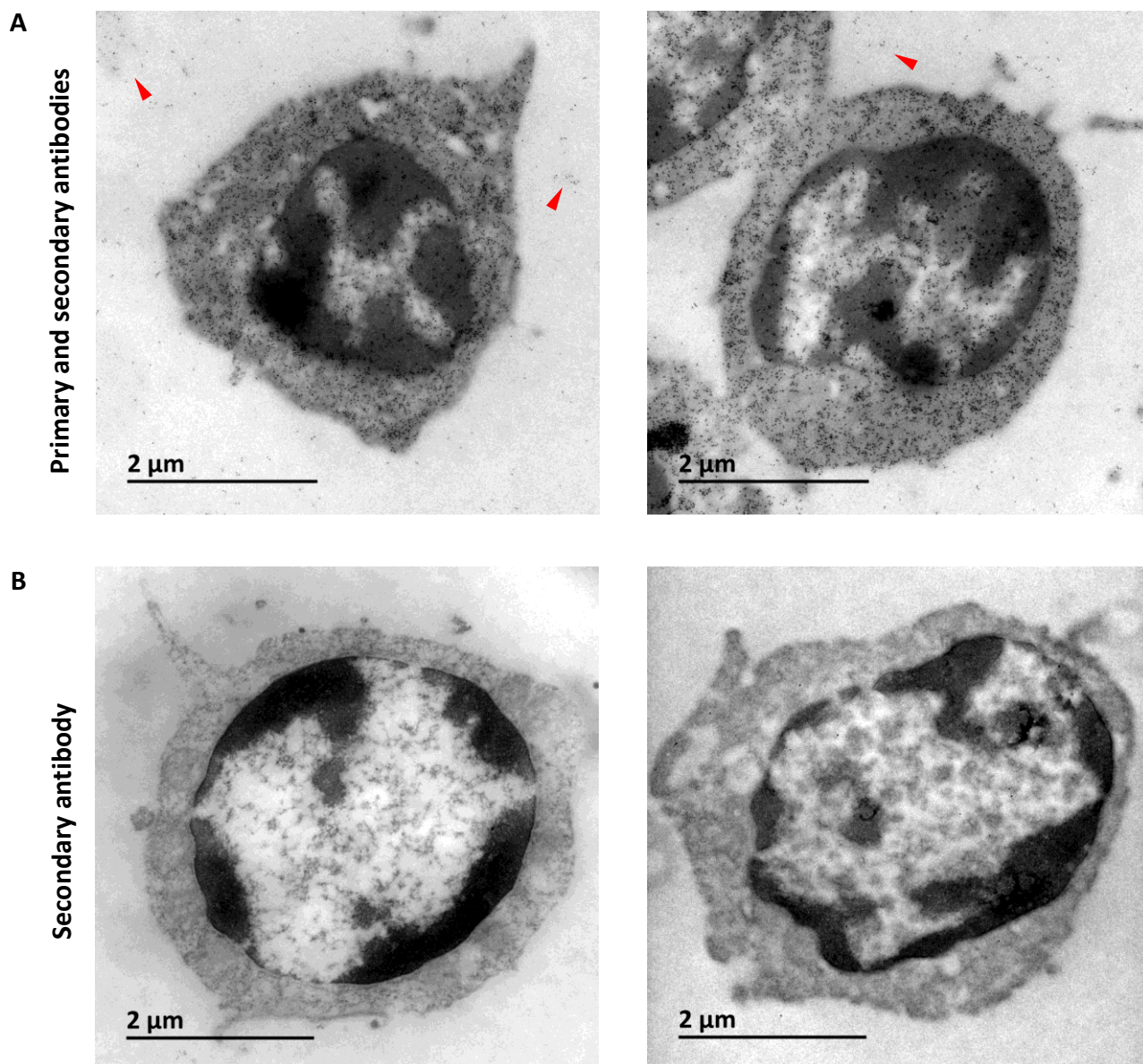
Figure 6.1: Evaluating immune-gold labelling of NOTCH1 within TEM sections. CLL cells (5×10^6 cells/plug) were resuspended in Matrigel 50% (v/v), and plugs cultured for 72 h. Following incubation, plugs were fixed, processed and ultrathin sections prepared. Sections were blocked in 3% EM blocking solution and (A) stained with the monoclonal anti-activated NOTCH1 antibody (ab8925, Abcam) (1 in 400 dilution) overnight at 4°C, followed by staining with the anti-rabbit IgG gold (10nm)-conjugated antibody (G7401, Sigma-Aldrich) (1 in 10 dilution) for 1 h at RT, or (B) with the anti-rabbit IgG gold-conjugated antibody alone. Images were acquired at 15,000x using a JEOL 1400 TEM with supporting software. Non-specific labelling of the Matrigel™ matrix could also be observed (red arrow).

6.4. GENERAL CELL PELLET CULTURE

6.4.1. PREPARING CELL PELLETS

Patient-derived CLL cells were isolated from EDTA whole blood samples as described in section 2.2.1 and cultured in complete culture media (section 5.5.1). Following isolation, $5x10^6$ cells were aliquoted into sterile Eppendorf tubes and the total volume made up to 1mL with complete culture media. The cells were incubated at 37°C with 5% CO_2 for 4 h to allow cells to gently settle to the bottom of Eppendorf tubes.

6.4.2. FIXATION, DEHYDRATION, EMBEDDING AND SECTIONING

The fixation, dehydration, embedding and sectioning of CLL cell pellets was performed as described in section 5.7.1-4.

6.4.3. ALTERED METHOD FOR IMMUNOGOLD LABELLING OF TEM SECTIONS

Immunogold labelling of NOTCH1 within TEM sections obtained from cell pellets was performed as described in section 6.3.2 with the following exception: (i) grids were incubated on top of 50μL droplets of 3% or 5% EM blocking buffer (section 6.3.1) at RT for 2 h, 4 h or overnight, blotted and then rinsed twice on droplets of EM incubation buffer for 5 min each; and (ii) grids were incubated on 50μL droplets of primary antibody (diluted in EM incubation buffer) at RT for 2 h or 4 h, or overnight at 4°C.

6.4.4. ESTABLISHING AN OPTIMAL BLOCKING TIME FOR IMMUNOGOLD LABELLING OF CELL PELLET SECTIONS

To reduce non-specific immunolabelling of activated NOTCH1 within sectioned CLL cells, blocking of TEM sections with 3% EM blocking buffer was increased from 30 min to 2 h, 4 h or overnight incubation at RT (Figure 6.2). Increasing the blocking time to 2 h resulted in no noticeable reductions in non-specific staining, with large amounts of gold nanoparticles being

observed throughout all CLL cells (Figure 6.2A). However, a blocking time of 4 h did appear to reduce the amount of random signal and some clusters of activated NOTCH1 could be observed, particularly at the plasma membrane, the primary location of NOTCH1 prior to activation via proteolytic cleavage, and within the less condensed areas of the nucleus. However, the large quantities of gold nanoparticles seen within cells suggested that some non-specific binding was still taking place. Overnight blocking appeared to reduce the amount of random signal to a similar level as blocking for 4 h, with clustering of gold molecules at the cell periphery and within the nucleus being observed as previously described. Although non-specific immunogold labelling could not be eliminated by increasing the blocking time of TEM sections alone, reductions in the amount of staining were noted with 4 h and overnight incubations. As there were no discernible benefits of overnight blocking when compared to 4 h blocking, an incubation time of 4 h was used for subsequent optimisation experiments to limit the time needed to prepare sections for imaging.

To further reduce random immunogold labelling of TEM sections, the concentration of the EM blocking buffer (section 6.3.1) was also increased to 5% (v/v) goat serum with 2% (w/v) BSA. Increasing the blocking solution resulted in largely similar levels of non-specific staining to that observed with the 3% EM blocking solution at all incubation lengths (images not shown). Thus, the 3% EM blocking buffer was used for all future experiments.
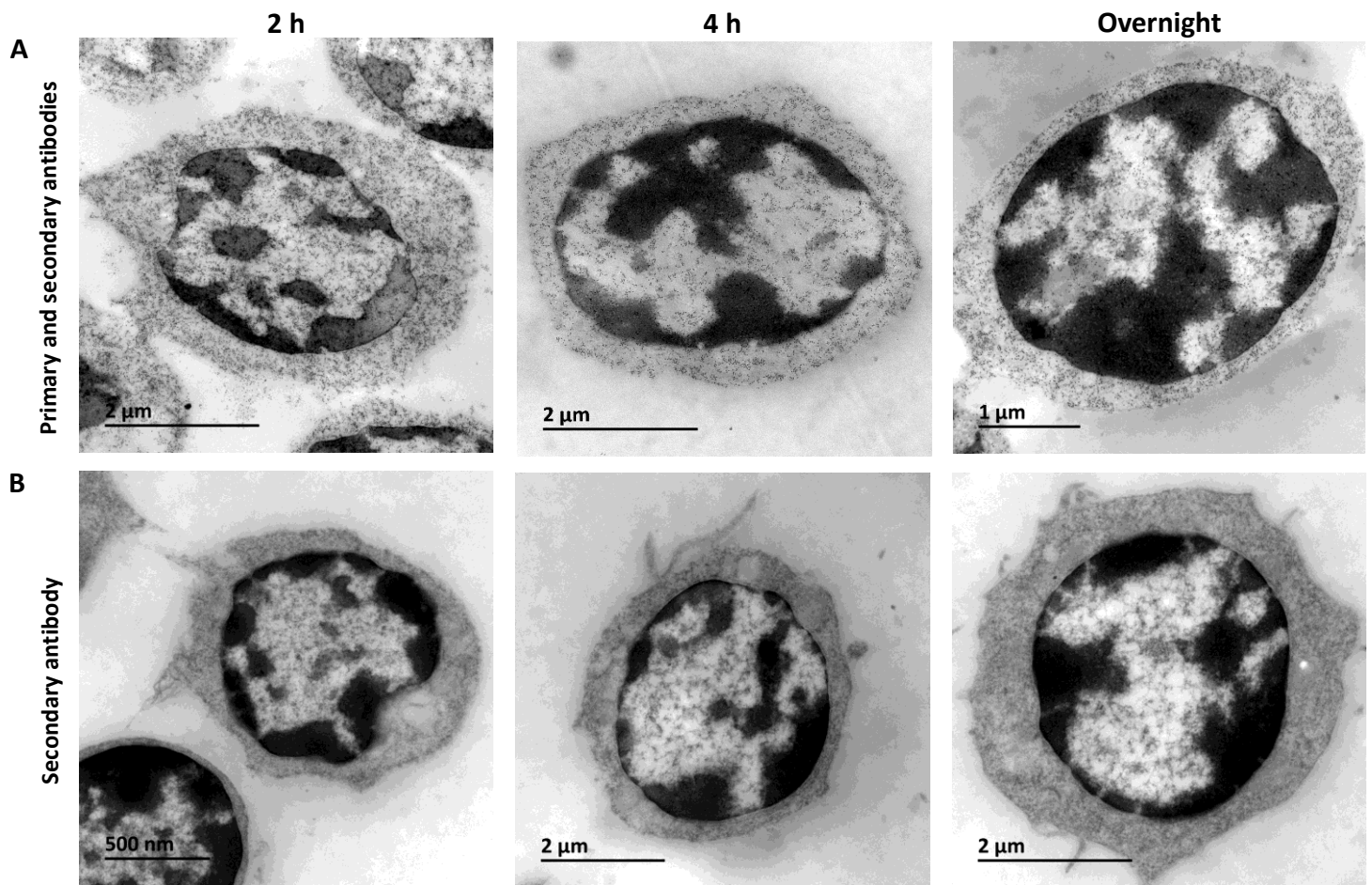
Figure 6.2: Immunogold labelling of NOTCH1 within CLL cells after blocking for 2 h, 4 h and overnight. Following isolation, CLL cells (5×10^6 cells) were collected and allow to settle to the bottom of Eppendorf tubes for 4 h. The cell pellets were then fixed, processed and ultrathin sections prepared. Sections were then blocked in 3% EM blocking buffer for 2 h, 4 h or overnight before being (A) stained with the monoclonal anti-activated NOTCH1 antibody (ab8925, Abcam) (1 in 400 dilution) overnight at 4°C, followed by staining with the anti-rabbit IgG gold (10nm)-conjugated antibody (G7401, Sigma-Aldrich) (1 in 10 dilution) for 1 h at RT, or (B) with the anti-rabbit IgG gold-conjugated antibody alone. Images were acquired at 15,000x using a JEOL 1400 TEM with supporting software.

6.4.5. ESTABLISHING AN OPTIMAL PRIMARY ANTIOBDY INCUBATION TIME FOR IMMUNOGOLD LABELLING OF CELL PELLET SECTIONS

The primary antibody incubation time was decreased from overnight at 4°C to 4 h or 2 h at RT to further reduce non-specific staining of CLL cells within TEM sections (Figure 6.3). However, microscopic examination revealed similar levels of signal at 4 h to that seen in sections incubated with the anti-activated NOTCH1 antibody overnight. Background labelling was present throughout the cytoplasm and nuclei of CLL cells; however, some clustering of gold nanoparticles was observed (Figure 6.3A). In contrast, reducing the primary antibody incubation period to 2 h dramatically decreased the amount of staining observed throughout CLL cells. Small clusters of gold nanoparticles could be seen at the plasma membrane and within the cytoplasm. Interestingly, groups of gold particles appeared to congregate at pores in the nuclear envelope (arrows in Figure 6.3A), suggesting that the staining represented activated NOTCH1 proteins translocating from the cell periphery to the nucleus to induce transcription of target genes. Clusters of gold nanoparticles were infrequent within CLL cell nuclei and were typically seen towards the perimeter of nuclei. Based on the finding of this experiment a primary antibody incubation time of 2 h at RT was selected for future immunogold labelling of CLL cells within TEM sections.

	2 h	4 h	Overnight

A Primary and secondary antibodies

B Secondary antibody
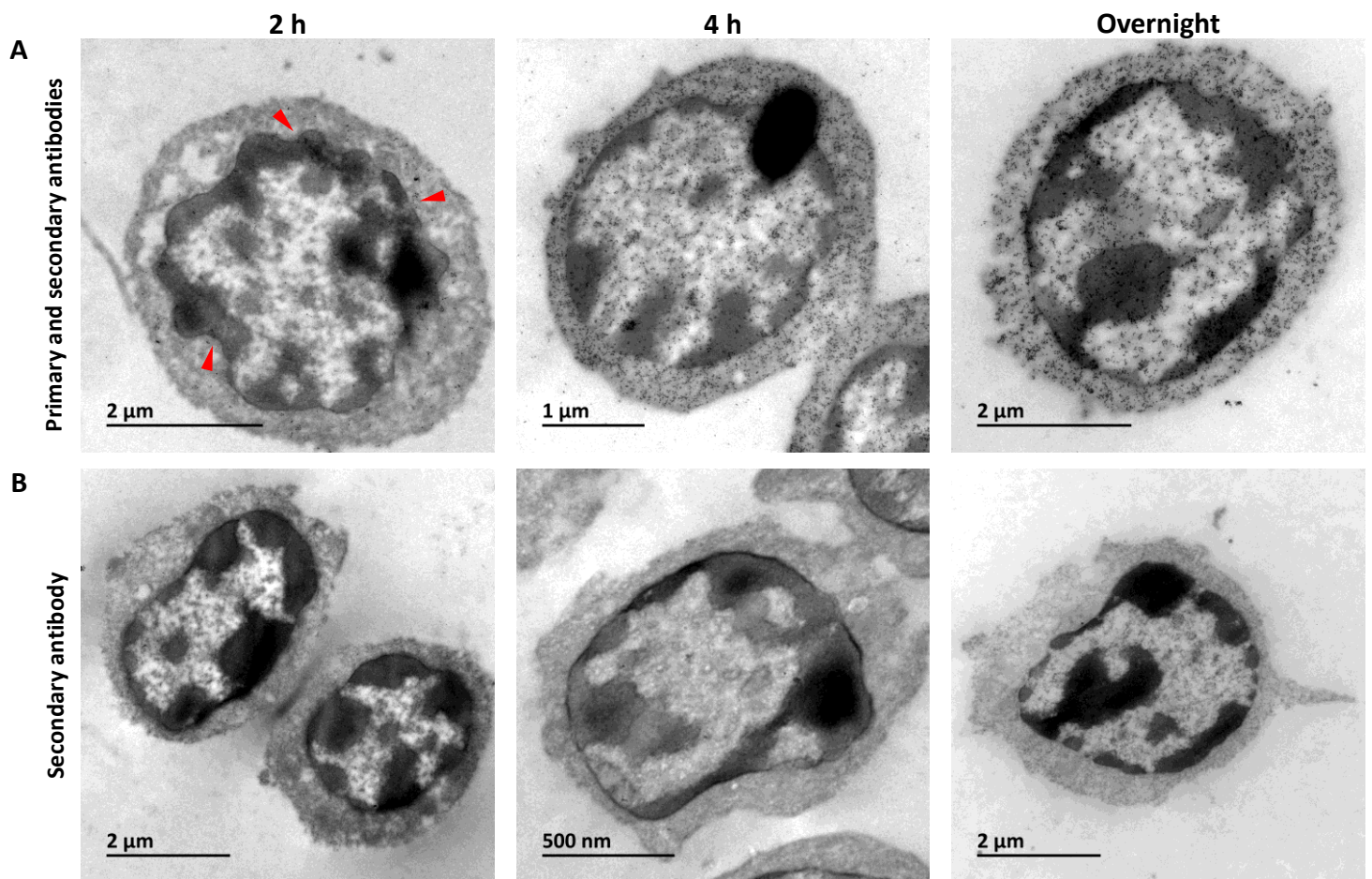
Figure 6.3: Immunogold labelling of NOTCH1 within CLL cells after 2 h, 4 h and overnight incubation with the primary antibody. Following isolation, CLL cells (5×10^6 cells) were collected and allow to settle to the bottom of Eppendorf tubes for 4 h. The cell pellets were then fixed, processed and ultrathin sections prepared. Sections were blocked in 3% EM blocking buffer and (A) stained with the monoclonal anti-activated NOTCH1 antibody (ab8925, Abcam) (1 in 400 dilution) for 2 h or 4 h at RT, or overnight at 4°C, followed by staining with the anti-rabbit IgG gold (10nm)-conjugated antibody (G7401, Sigma-Aldrich) (1 in 10 dilution), or (B) with the anti-rabbit IgG gold-conjugated antibody alone. Images were acquired at 15,000x using a JEOL 1400 TEM with supporting software. Clusters of gold particles appeared to congregate at pores in the nuclear envelope (red arrows).

6.5 DETERMING THE EFFECTS OF NOTCH1 INHIBITION ON B-LYMPHOCYTE BEHAVIOUR WITHIN 2D CULTURES

The aim of developing a 3D TME-like model for CLL was to primarily evaluate changes in NOTCH1 localisation following treatment with clinically relevant inhibitors with possible effects on CLL-TME interactions. An additional aim was to assess morphological and behavioural changes induced by signal inhibition within a 3D system; however, before this could be achieved, CLL responses needed to be demonstrated within a 2D setting to allow a direct comparison to be made. Chapter 4 described the morphological and behavioural changes induced by BTK, ALB1 and ROCK inhibition within a 2D culture system. The morphological and functional responses of malignant B-lymphocytes to impaired NOTCH1 signalling had yet to be established and, thus, were assessed here.

6.5.1. COMPARING MORPHOLOGICAL RESPONSES OF CLL CELLS FOLLOWING TREATMENT WITH NOTCH1 INHIBITORS

To evaluate the morphological response(s) of CLL cells to NOTCH1 inhibitors, PF-03084014 and R04929097, three CLL cases (Table 4.1-2) were fixed following 72 h treatment and examined using SEM and graphical representation of shape parameters. For representative images of the shape changes observed following drug treatments for each CLL case, see Figure 6.4. The results being discussed in this section are shown in Figure 6.5. Exact *p*-values for DMSO vs GSI for each case are listed in Table 6.1-3.

Resting morphology: CLL cases exhibited largely similar morphological features (Figure 6.4), with populations forming characteristic bi-modal distributions of most shape parameters (Figure 6.5). Interestingly, cases CLL-11 (*IGHV*-unmutated) and CLL-26 (*IGHV*-unmutated) both exhibited an almost Gaussian distribution of circularity values, indicating that larger proportions of these populations were undergoing directional cell migration compared to the

predominantly globular CLL-09 (*IGHV*-mutated) cells. Fine filopodial projections and peripheral ruffles were frequently seen extending from polarised cells, whereas villous structures were typically observed on globular cells. Cases CLL-26 appeared to display fewer surface microvilli on the cell surface compared to the other CLL populations.
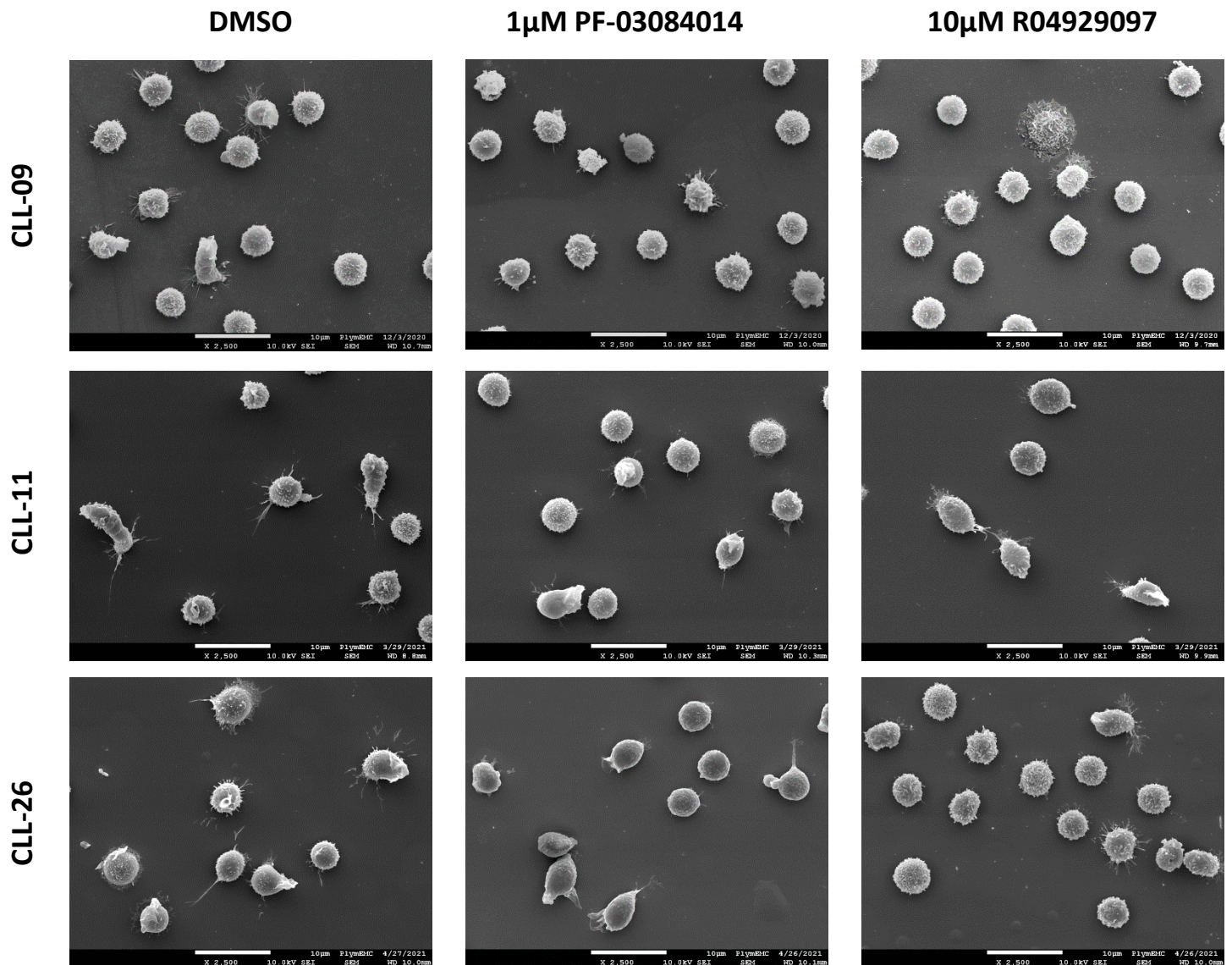
Figure 6.4: Effects of NOTCH1 inhibitors on morphology of CLL cells. Following 24 h culture, CLL cases were treated with either DMSO, PF-03084014 or R04929097 for 72 h, fixed and processed. Cells were observed using a JEOL 7001 F SEM at 2500x and images were captured using supporting software.
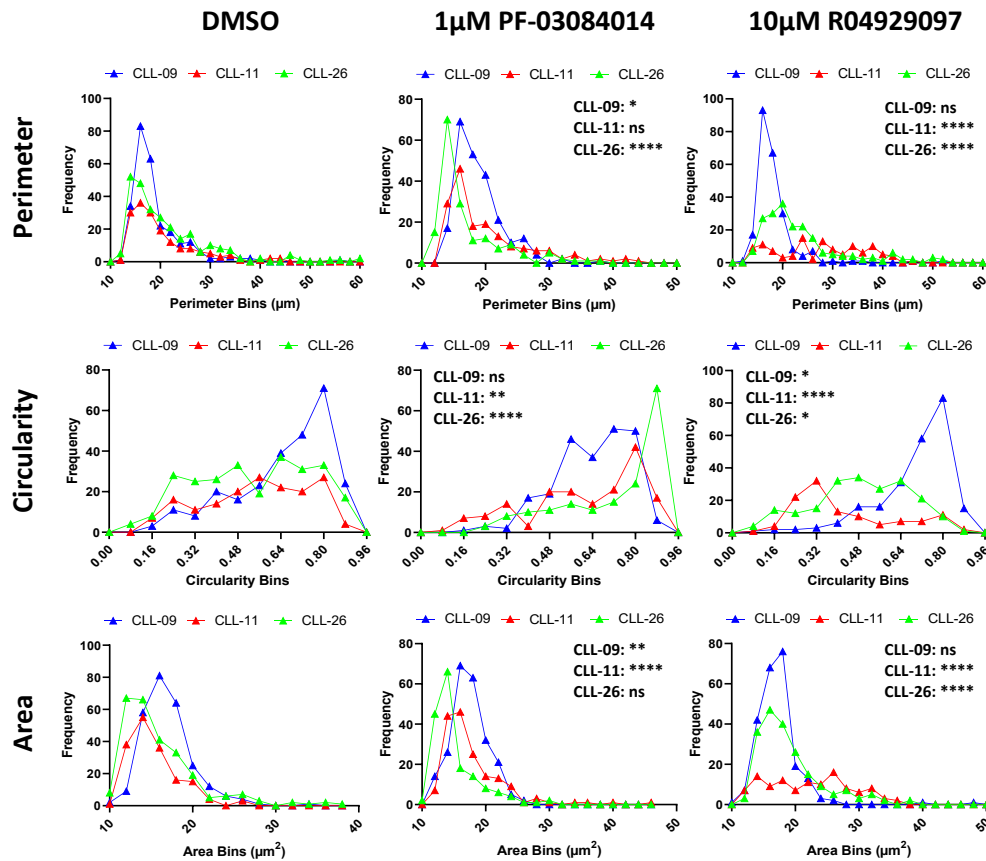
Figure 6.5: Effects of NOTCH1 inhibitors on CLL cell shape. Following 24 h culture, CLL cases were treated with either DMSO, PF-03084014 or RO4929097 for 72 h, fixed and processed. Cells were observed using a JEOL 7001 F SEM at 1000x and images were captured using supporting software. Binary images were generated from .tif images using ImageJ, and the perimeter, circularity and area of cells measured. Frequency distribution histograms were created using GraphPad Prism. *p*-values for DMSO vs treatments were calculated using the Mann-Whitney U test. ****$p < 0.0001$; ***$p < 0.001$; **$p < 0.01$; *$p < 0.05$; not significant (ns) $p > 0.05$.

PF-03084014 treatment: CLL cases demonstrated variable changes in cell shape following PF-03084014 treatment (Figure 6.4-5; Table 6.1-3). Cases CLL-09 (*IGHV*-mutated) and CLL-11 (*IGHV*-unmutated) demonstrated a significant increase in cell size with NOTCH1 inhibition. Cytoskeletal polarisation was decreased within the CLL-11 population, with cell shifting to a characteristic bi-modal distribution of circularity. The circularity of CLL-09 cells was not significantly altered following PF-03084014 treatment. Filopodia formation appeared to be slightly reduced in both CLL-09 and CLL-11 populations, whereas microvilli were reduced on the surface of CLL-11 cells alone.

In contrast, case CLL-26 (*IGHV*-unmutated) shifted towards one main homotypic population of small (perimeter), globular cells with PF-03084014 treatment. The rounder appearance of these cells suggested that elongated-type motility had been impaired to a degree with NOTCH1 inhibition. Cytoskeletal projections were absent from surface of CLL-26 cells and although peripheral ruffles were still present, they were typically small and poorly formed. Lagging tails were observed trailing behind the main cell bodies of migrating CLL-26 cells following PF-03084014 treatment; however, mobile cells represented a minority fraction of the treated cell population.

RO4929097 treatment: CLL cases displayed varying responses to RO4929097 treatment (Figure 6.4-5; Table 6.1-3). Cases CLL-11 (*IGHV*-unmutated) and CLL-26 (*IGHV*-unmutated) exhibited a significant increase in cell size and irregularity, suggesting that cytoskeletal polarisation had increased. Cytoskeletal projections appeared to be reduced within the CLL-11 population with NOTCH1 inhibition, while case CLL-26 displayed densely packed, long microvilli and frequent filopodia.

Case CLL-09 (*IGHV*-mutated) showed no alterations in cell size; however, circularity was significantly increased following R04929097 treatment. CLL-09 cells were predominantly globular, suggesting that directional cell migration had been impaired with NOTCH1 inhibition, and typically lacked filopodial projects. Villous structures on the surface of these cells also appeared to be reduced.

Table 6.1: Perimeter - summary of the changes in shape of CLL subgroups following 72 h NOTCH1 inhibitor treatment.

Case	*IGHV* status[*]	Conditions	*p*-value[†]	Increase/decrease in perimeter compared to DMSO control
CLL-09	M	DMSO vs 1µM PF-03084014	0.0347 *	Increase
		DMSO vs 10µM R04929097	0.3383 ns[‡]	N/A[§]
CLL-11	UM	DMSO vs 1µM PF-03084014	0.7469 ns	N/A
		DMSO vs 10µM R04929097	<0.0001 ****	Increase
CLL-26	UM	DMSO vs 1µM PF-03084014	<0.0001 ****	Decrease
		DMSO vs 10µM R04929097	<0.0001 ****	Increase

[*] M, mutated *IGHV*; UM, unmutated *IGHV*.

[†] *p*-values were determined using the non-parametric Mann-Whitney U test for unpaired data sets.

[‡] ns, not significant.

[§] N/A, not applicable.

Table 6.2: Circularity - summary of the changes in shape of CLL subgroups following 72 h NOTCH1 inhibitor treatment.

Case	IGHV status[*]	Conditions	p-value[†]	Increase/decrease in circularity compared to DMSO control
CLL-09	M	DMSO vs 1µM PF-03084014	0.0651 ns[‡]	N/A[§]
		DMSO vs 10µM R04929097	0.0141 *	Increase
CLL-11	UM	DMSO vs 1µM PF-03084014	0.0020 **	Increase
		DMSO vs 10µM R04929097	<0.0001 ****	Decrease
CLL-26	UM	DMSO vs 1µM PF-03084014	<0.0001 ****	Increase
		DMSO vs 10µM R04929097	0.0125 *	Decrease

[*] M, mutated *IGHV*; UM, unmutated *IGHV*.

[†] *p*-values were determined using the non-parametric Mann-Whitney U test for unpaired data sets.

[‡] ns, not significant.

[§] N/A, not applicable.

Table 6.3: Area - summary of the changes in shape of CLL subgroups following 72 h NOTCH1 inhibitor treatment.

Case	IGHV status[*]	Conditions	p-value[†]	Increase/decrease in area compared to DMSO control
CLL-09	M	DMSO vs 1µM PF-03084014	0.0075 **	Increase
		DMSO vs 10µM R04929097	0.1263 ns[‡]	N/A[§]
CLL-11	UM	DMSO vs 1µM PF-03084014	<0.0001 ****	Increase
		DMSO vs 10µM R04929097	<0.0001 ****	Increase
CLL-26	UM	DMSO vs 1µM PF-03084014	0.1363 ns	N/A
		DMSO vs 10µM R04929097	<0.0001 ****	Increase

[*] M, mutated *IGHV*; UM, unmutated *IGHV*.

[†] *p*-values were determined using the non-parametric Mann-Whitney U test for unpaired data sets.

[‡] ns, not significant.

[§] N/A, not applicable.

Summary: Primary CLL cases demonstrated varying shape changes with NOTCH1 inhibition (Table 6.1-3). The formation of large, polarised cells, or uniform globular populations was case/GSI-dependent, possibly indicating differences in patient-specific activation of NOTCH1, or off-target effects due to concurrent inhibition of other NOTCH molecules.

6.5.2. EVALUATING CXCL12-DRIVEN MIGRATION FOLLOWING TREATMENT WITH NOTCH1 INHIBITORS

To determine the effects of NOTCH1 inhibition on CXCL12-driven migration of CLL cells, four cases (Table 4.1-2) were examined using the Transwell migration assay. The effects of *NOTCH1* mutational status on chemokine-mediated migration following GSI pre-treatment were also explored by utilising the MCL cell lines REC-1 (*NOTCH1*-mutated) and G519 (*NOTCH1*-unmutated). The results being discussed in this section are shown in Figure 6.6. Exact *p*-values are included within the figure.

PF-03084014 treatment: Overall, the mean chemokine-induced migration of CLL cases was significantly increased approximately 14-fold with PF-03084014 pre-treatment compared to control (DMSO-treated) cells (Figure 6.6A). *NOTCH1*-mutated REC-1 cells also demonstrated a significant increase in chemokine-driven transmigration with PF-03084014 exposure (mean cell migration relative to control cells of approximately 45) (Figure 6.6B). However, *NOTCH1*-unmutated G519 cells displayed no significant alterations in cell migration with PF-03084014 treatment (Figure 6.6C).

R04929097 treatment: Following R04929097 treatment, the mean relative CXCL12-driven migration of CLL cases was significantly increased approximately 40-fold compared to control cells (Figure 6.6A). Likewise, the migration of *NOTCH1*-mutated REC-1 cells towards CXCL12 was significant increased with R04929097 exposure (mean cell migration relative to control

cells of approximately 59) (Figure 6.6B). In contrast, *NOTCH1*-unmutated G519 cells displayed

a significant 2.3-fold decrease in chemokine-induced migration following R04929097

treatment compared to control cells (Figure 6.6C).
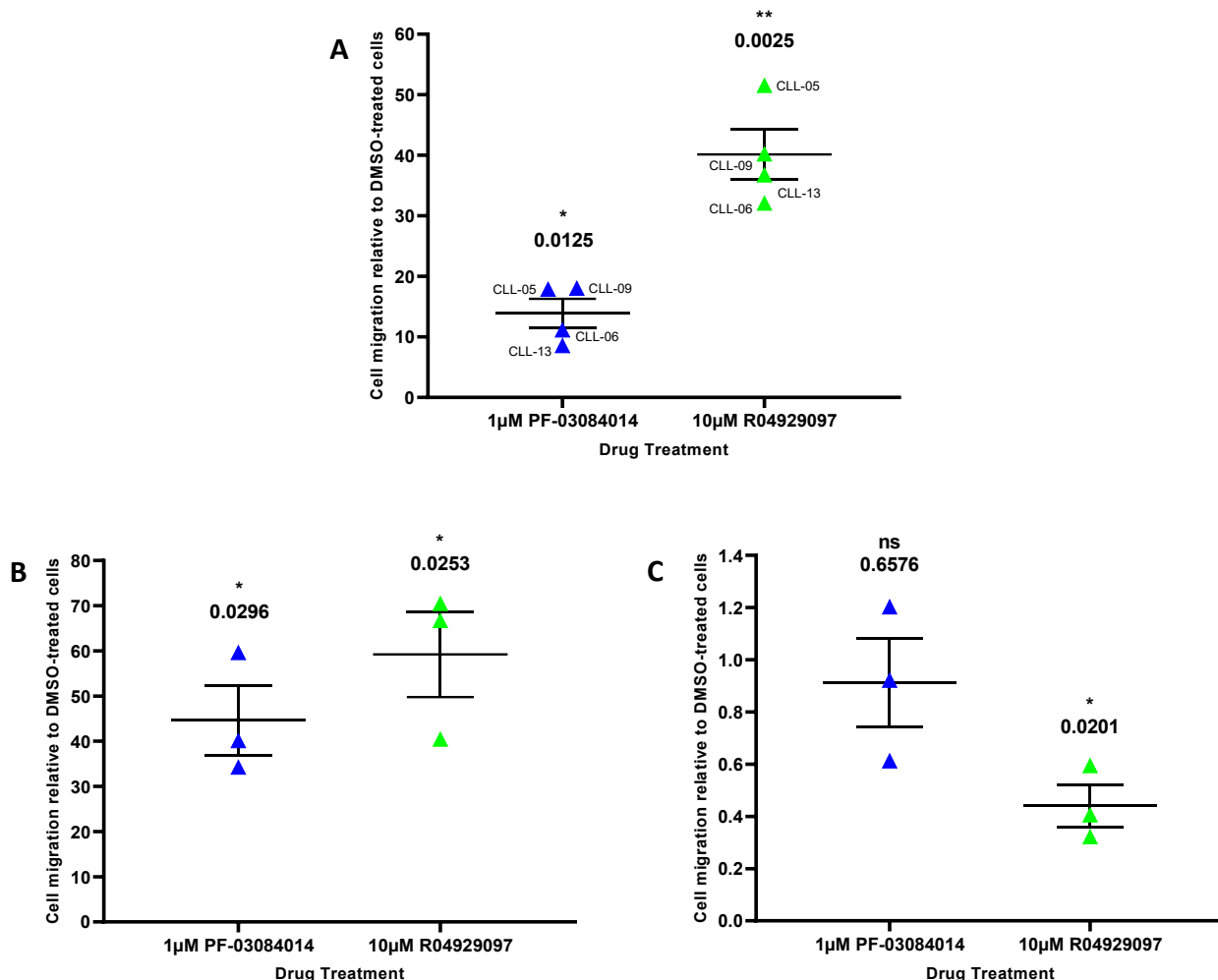
Figure 6.6: Effects of NOTCH1 inhibitors on CXCL-12 driven CLL and MCL cell migration. Following 24 h culture, CLL and MCL cells were pre-treated with either DMSO, PF-03084014 or R04929097 for 72 h and then transferred to Transwell inserts. Chemokine gradients were created by adding signal inhibitors at the concentrations stated above and 200ng/mL CXCL12 into each well. Cells were allowed to migrate for 4 h, and then the content of the wells collected and fixed. Migrating cells were counted using a BD Accuri™ C6 flow cytometer and FlowJo software. Scatter plots showing the relative CXCL12-driven migration of (A) CLL, (B) REC-1 and (C) G519 cells were created using GraphPad Prism. *P*- values of DMSO vs treatments were calculated using the parametric t-test for unpaired data sets with Welch's correction. ****$p < 0.0001$; ***$p < 0.001$; **$p < 0.01$; *$p < 0.05$; not significant (ns) $p > 0.05$. Error bars represent standard error of the mean. CLL cells: n = 4; REC-1 cells: n = 3; G519 cells: n = 3.

Summary: Chemotactic responses of both primary CLL cells and *NOTCH1*-mutated REC-1 cells were significantly increased with GSI treatment, suggesting that directional cell migration was stimulated despite the role of NOTCH1 signalling in regulating chemokine-induced transmigration. *NOTCH1*-unmutated G519 cells demonstrated decreased CXCL12-induced migration with R04929097 pre-treatment alone, again suggesting the involvement of off-target effects.

6.6. INVESTIGATING NOTCH1-PROTEIN INTERACTIONS IN CLL

Studies have indicated that NOTCH1 activity is linked to ibrutinib therapy responses in CLL patients. BTKi treatment significantly reduced NOTCH1 cleavage and phosphorylation of eIF4E, a downstream target of NOTCH1 signalling in CLL cases. The percentage of leukemic cells displaying cytoplasmic N-ICD/BTK complexes, confirmed using the *in situ* proximity ligation assay, was also significantly decreased with ibrutinib exposure. Interestingly, NOTCH1 activity was restored at relapse and persisted in ibrutinib-resistant CLL patients,[420] indicating that NOTCH1 signalling contributes to the anti-leukaemic effects of ibrutinib and may represent a novel mechanism of BTKi resistant. Cross-talk between BTK and NOTCH1 signalling pathways, therefore, suggests a high potential of NOTCH1 inhibitors in overcoming ibrutinib resistance in this disease.

Indeed, a combination of ibrutinib and GSIs enhanced the cytotoxicity of CLL cells co-cultured with protective stromal cells. Additionally, the combinational therapy was effective in decreasing CXCR4 expression and, consequently, CXCL12-induced leukaemic cell migration.[113] Understanding the complex interplay between pro-survival signalling pathways in CLL has the potentially to further improve treatment outcomes and allow the implementation of targeted therapeutic regimes against NOTCH1-associated resistance. Thus, investigations were

undertaken to further characterise NOTCH1-protein interactions in CLL; initially exploring interactions with previously unreported proteins using co-immunoprecipitation and liquid chromatography–mass spectrometry.

A table of antibodies used in this section is shown below (Table 6.4), accompanied with the antibody dilutions relating to the application in which they were used.

Table 6.4: Antibodies used for the assessment of NOTCH1-protein interactions.

Antibody	Species	Application*	Product number	Supplier[†]	Concentration
Anti-cleaved NOTCH1 (Val1744) (B3B8)	Rabbit	IP WB	4147	CST	1 in 200 1 in 1000
Anti-NOTCH1 (D1E11) XP®	Rabbit	IP WB	3609	CST	1 in 50 1 in 1000
Normal Rabbit IgG[§]	Rabbit	IP (with B3B8) IP (with D1E11)	2729	CST	1 in 218 1 in 227
Anti-rabbit immunoglobulins-HRP	Goat	WB	P0448	Dako	1 in 2000

*WB, western blotting; IP, immunoprecipitation.

[†] CST, Cell Signalling Technology.

[§] The normal rabbit IgG antibody was used at the same final concentrations as the anti-NOTCH1 antibodies.

6.6.1. ESTABLISHING AN OPTIMAL NOTCH1 ANTIBODY FOR CO-IMMUNOPRECIPITATION

Prior to mass spectrometry analysis of protein-protein interactions, an optimal primary antibody for immunoprecipitation of NOTCH1 needed to be established. Two antibodies, both of which detected cleaved (i.e., active) NOTCH1, were selected for Co-IP studies (Table 6.4).

The anti-cleaved NOTCH1 (Val1744) (D3B8) primary antibody is able to detect levels of the N-ICD when released by γ-secretase-mediated cleavage, whereas the anti-NOTCH1 (D1E11) XP® primary antibody is able recognise both the full-length NOTCH1 and the cleaved N-TMIC subunit.

As varied levels of N-ICD expression could be detected by immunoblot analysis in only approximately 51% of primary CLL cases exhibiting wild-type *NOTCH1*,[57] the JURKAT cell line was instead utilised for initial optimisation of Co-IP and mass spectrometry analyses. JURKAT is a T-ALL cell line which has been shown to display wild-type *NOTCH1* and express high levels of the N-ICD compared to other cell lines.[287]

Co-IP with the anti-cleaved NOTCH1 (Val1744) (D3B8) primary antibody resulted in partial precipitation of activation NOTCH1 as demonstrated by the presence of a bands at approximately 110kDa in both the specific precipitate and PIP-fraction (Figure 6.75A). This indicated that the efficiency of NOTCH1 precipitation with this antibody was low.
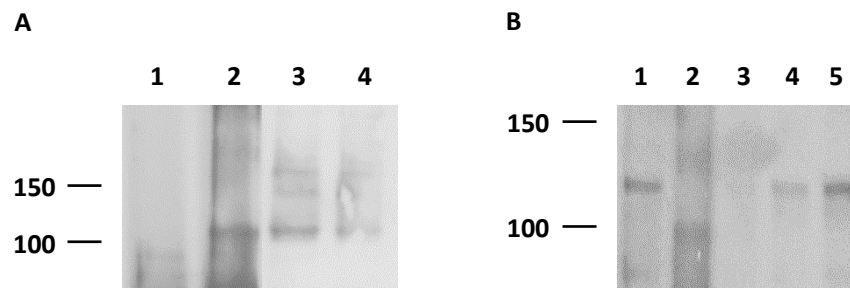
Figure 6.7: Determining the efficiency of NOTCH1 immunoprecipitation from JURKAT cell lysate.
JURKAT cell lysate (600µg) was incubated with either the (A) anti-cleaved NOTCH1 (Val1744) (D3B8) primary antibody (1 in 200 dilution; 4147, CST), (B) anti-NOTCH1 (D1E11) XP® primary antibody (1 in 50 dilution; 3608, CST) or the normal rabbit IgG (i.e., control) antibody (2729, CST) overnight at 4°C. Following incubation, the lysate-antibody mixtures were added to pre-washed Dynabeads™ (10003D, Invitrogen) and incubated at RT for 20 min. Precipitates were analysed by SDS-PAGE to ensure immunoprecipitation was successful. Membranes were incubated with an anti-NOTCH1 antibody (D3B8: 1 in 1000 dilution or D1E11 XP®: 1 in 1000 dilution) overnight at 4°C. Membranes were then incubated with the mouse anti-rabbit secondary antibody-HRP (1 in 2000 dilution; P0448, Dako) for 1 h prior to detection of bands. (A) Lane 1, control antibody precipitate; Lane 2, anti-cleaved NOTCH1 (Val1744) (D3B8) antibody precipitate; Lane 3, control antibody P-IP fraction; Lane 4, anti-cleaved NOTCH1 (Val1744) (D3B8) antibody P-IP fraction. (B) Lane 1, anti-NOTCH1 (D1E11) XP® antibody precipitate; Lane 2, control antibody precipitate; Lane 3, anti-NOTCH1 (D1E11) XP® antibody P-IP fraction; Lane 4, control antibody P-IP fraction; Lane 5, JURKAT cell lysate prepared with RIPA buffer (30µg).

In contrast, the specific precipitate prepared using the anti-NOTCH1 (D1E11) XP® primary antibody contained a distinct band at approximately 120kDa (Figure 6.7B). A 120kDa band was also present within the PIP fraction; however, it was extremely faint, demonstrating that activated NOTCH1 was almost fully precipitated.

Approximately 110/120kDa bands were presence in the control P-IP fractions and absent from the control precipitates from both experiments (Figure 6.7), indicating that precipitation of activated NOTCH1 by the anti-cleaved NOTCH1 (Val1744) (D3B8) and anti-NOTCH1 (D1E11) XP® primary antibodies was not due to non-specific interactions.

Based on the higher efficiency of NOTCH1 precipitation achieved with the anti-NOTCH1 (D1E11) XP® primary antibody, this antibody was selected for use in optimisation of mass spectrometry-based analysis of NOTCH1-protein interactions.

6.6.2. NOTCH1-PROTEIN INTERACTIONS IDENTIFIED BY MASS SPECTROMETRY

NOTCH1-protein precipitates were prepared from JURKAT cell lysate using the anti-NOTCH1 (D1E11) XP® antibody and IgG control antibody (both antibodies were used at the same final concentration). The denatured precipitates were run on a 7% resolving gel prepared under sterile conditions and each Co-IP lane cut into 2 gel segments (section 2.8, Figure 2.6). The gel was left stained as the ProtoBlue Safe Colloidal Coomassie Blue stain is compatible with mass spectrometry analyses; however, excess stain was removed by repeatedly rinsing with dH$_2$O. The preparation of protein precipitates for liquid chromatography was carried out using protocols (section 2.8.2-5) kindly supplied by Dr Vikram Sharma (University of Plymouth, UK). Liquid chromatography-mass spectrometry and data analyses by MaxQuant (section 2.9) was also performed by Dr Vikram Sharma.

Using liquid chromatography-mass spectrometry and proteomics analyses, a number of proteins precipitated by the antibody directed against NOTCH1, but not the IgG control, were identified (Table 6.5). Unfortunately, the specificity of these protein-protein interactions could not be confirmed since the NOTCH1 protein itself was not found in the precipitate where the specific antibody was used. Repeat Co-IP and mass spectrometry experiments using the same (600µg) or larger quantities of JURKAT lysate (800µg or 1000µg) were also unable to identity the NOTCH1 protein (results not shown) despite previous immunoblot evidence of successful precipitation (Figure 6.7). It was, therefore, possible that the identified proteins were co-precipitated by chance by the anti-NOTCH1 antibody and not the IgG control. Thus, the clinical relevance of any NOTCH1-protein interactions identified here cannot be explored further until their specificity is confirmed. Unfortunately, further optimisation of the NOTCH1 Co-IP and mass spectrometry analyses was not possible in the time available for this study.

Table 6.5: Proteins identified via mass spectrometry analysis of NOTCH1 precipitates

Protein Name	Protein Function*
Caspase-8 (CASP8)	Participates in the signalling cascade responsible for initiating cell death
Plastin-3 (PLS3)	Actin-bundling protein found in intestinal microvilli, hair cell stereocilia and fibroblast filopodia
Small subunit ribosomal protein sae (RPSA)	Facilitates ribosome assembly
Pyruvate kinase m1/2 (PKM)	Glycolytic enzyme catalysing the generation of ATP
Eukaryotic initiation factor 4A-I (EIF4A1)	Facilitates mRNA binding to the ribosome
T-complex protein 1 subunit beta (CCT2)	Assists in the folding of actin and tubulin
Stress-induced-phosphoprotein 1 (STIP1)	Acts as a co-chaperone for HSP90AA1
ATP synthase subunit beta, mitochondrial (ATP5B)	Facilitates the production of ATP in the presence of a proton gradient across the mitochondrial membrane
Fructose-bisphosphate aldolase A (ALDOA)	Participates in glycolysis and gluconeogenesis
ATP synthase subunit alpha, mitochondrial (ATP5A1)	Facilitates the production of ATP in the presence of a proton gradient across the mitochondrial membrane
Glyceraldehyde-3-phosphate dehydrogenase (GAPDH)	Participates in glycolysis, nuclear events, and organisation of the cytoskeleton
Protein S100-A8 (S100AB)	Induces neutrophil chemotaxis and adhesion via modulation of the tubulin-dependent cytoskeleton
Tubulin beta-4B chain (TUBB4B)	Major constituent of microtubules
Neuroblast differentiation-associated protein AHNAK (AHNAK)	May participate in neuronal cell differentiation
Heat shock protein 90 alpha family class B member 1 (HSP90AB1)	Promotes maturation, structural maintenance and regulation of proteins involved in cell cycle control and signal transduction
Coiled-coil domain-containing protein 38 (CCDC38)	Not determined
Uncharacterized protein KIAA2026 (KIAA2026)	Not determined
NUAK family SNF1-like kinase 2 (NUAK2)	Stress-activated kinase involved in tolerance to glucose starvation and cell-cell detachment

*Protein function information was taken from the STRING database.

Nevertheless, to visualise any functional relationships between the precipitated proteins, mass spectrometry results were exported to the STRING database. The STRING database is an online resource aiming to integrate all organism-wide known and predicated physical associations in addition to functional interactions. To achieve this, STRING combines and scores evidence form a range of sources, including text mining of the scientific literatures and databases of experimentally determined protein interactions.[422] All high confidence interactions were included in the analysis (Figure 6.8). Single proteins without linkage most likely represented non-specific associations or unreported interactions.
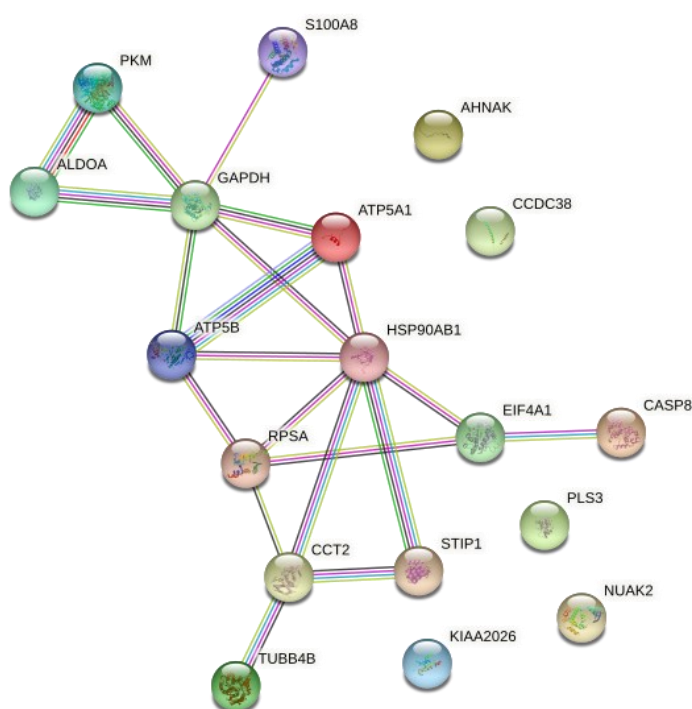
Figure 6.8: STRING analysis of high confidence protein-protein associations. Proteins specifically precipitated by the anti-NOTCH1 antibody were exported to the STRING database to identify known and predicted associations. High levels of protein-protein interactions were suggested for some of the precipitated proteins. Single proteins without linkage most likely represented non-specific associations or unreported interactions.

Although the specificity of the protein-protein interactions identified remains to be confirmed, it was interesting to note that the proteins potentially precipitated by the anti-NOTCH1 antibody belonged to three main functional groups: (i) cytoskeletal components and regulation; (ii) cellular metabolism; and (iii) ribosomal assembly and mRNA translation (Table 6.5 and Figure 6.8).

6.7. DISCUSSION

NOTCH1 is now recognised as one of the most frequently mutated genes in CLL.[47,53–56] The mutated NOTCH1 protein typically lacks the domains required for FBXW7-induced proteasomal degradation, resulting in an increase in the N-ICD half-life and aberrantly prolonged activation of downstream signalling pathways promoting leukaemic cell survival, BCR activation, trafficking to lymphoid organs and treatment resistance.[53,54,60,75,77–79] Thus, all *NOTCH1* mutations have been associated with a poor prognosis compared to wild-type patients.[47,53–55,80,81] Despite playing a role in the clinical course of CLL, the specific function(s) of NOTCH1 in leukaemogenesis remains poorly understood. However, early haematopoietic progenitor cells of CLL patients display mutated *NOTCH1*.[49,419]

Transcriptional signature analyses have identified chemotaxis as one of the primary NOTCH1-regulated processes in mature B-lymphocytes of CLL, with signalling activation leading to increased CCR7 and CXCR4 expression.[57,86] As such, *NOTCH1*-mutated CLL specifically demonstrated stimulated chemokine-induced trafficking,[86,88] suggesting that deregulated NOTCH1 signalling may promote homing of CLL cells to protective lymphoid tissues. Indeed, NOTCH1 ligands are constitutively expressed by stromal cells in the BM and lymph nodes and activate NOTCH1 signalling, thus, promoting leukaemic cell survival, regardless of mutational

status.[74,77] These findings further emphasise the key role of the TME in encouraging CLL cell survival via activation of NOTCH1 in addition to other signalling pathways.

Additionally, ibrutinib has been shown to significantly diminish NOTCH1 activity in CLL patients, with the number of NOTCH1/BTK complexes being significantly reduced within BTKi-sensitive cases and sustained in BTKi-resistant cases.[420] Given that chemotaxis has been confirmed as a NOTCH1-regulated process in CLL,[57,86,88] the impaired integrin-mediated homing of B-lymphocytes to tissue niches, underlying the lymphocytosis and alleviated tumour burden seen in CLL patients with ibrutinib,[94,217] may be the result of disrupted BTK-NOTCH1 interaction.

Thus, the aim of the chapter was to optimise immunogold labelling of NOTCH1 within CLL cells cultured in the previously evaluated 3D Matrigel™ matrix model (Chapter 5), allowing changes in protein localisation to be assessed following signal inhibition. Molecular alterations were linked to GSI-induced behavioural responses observed in CLL and MCL cells within 2D cultures. Novel NOTCH1-protein interactions were also characterised using co-immunoprecipitation and liquid chromatography-mass spectrometry analyses. Collectively, these investigations hoped to provide crucial insight into the role(s) of NOTCH1 signalling in CLL pathogenies and in mediating BTKi treatment outcomes.

6.7.1. OPTIMISATING IMMUNOGOLD LABELLING OF NOTCH1 WITHIN TEM SECTIONS

Immunogold labelling of endogenous proteins with specific antibodies combined with TEM is the only technique with sufficient resolution to determine molecular localisation at the ultrastructural level.[423,424] Due to their uniform size, giving a characteristic appearance that cannot be confused with other biological structures,[425,426] and countability, conjugates of 5-

25 nm in diameter can easily be visualised in ultrathin sections,[425,427] colloidal gold particles offer the possibility of identification and quantification of antigens within cells and tissues.[428–433] Thus, immunogold labelling can provide crucial insight into the function(s) of proteins. Additionally, the precision of gold particle engineering permits the production of antibodies conjugated with particles of different diameters for use in double/triple staining.[425]

There are several approaches to EM immunolabelling, each with advantages and limitations, that can be broadly placed into two categories: (i) pre-embedding methods (immunolabelling prior to resin embedding); and (ii) post-embedding methods (immunolabeling after resin embedding).[434] Conventional chemical fixation steps found in post-embedding methods can induce structural artifact and limit antigen availability.[423,435,436] In contrast, pre-embedding methods offer improved antigenicity but require permeabilisation of biological membrane to allow antibodies to reach internal epitopes. This is typically achieved with the use of a detergent; however, these reagents can modify membranes to varying degrees depending on the type of detergent used, its concentration and treatment time.[437] Furthermore, as only small gold particles are compatible with pre-embedding methods (large particles are unable to pass through permeabilised membranes), silver or gold enhancement is required to enlarge the gold particles for visualisation.[438,439] Protocols for high-pressure-freezing fixation of cryoprotected biological specimens and sectioning with a cryo-ultramicrotome prior to labelling have been established to circumvent issues relating to both pre- and post-embedding methods.[425,440,441] Although this more laborious procedure might be advantageous in some circumstances, not all materials are suitable for cryofixation and precise establishment of experimental conditions for each specimen is needed to prevent the formation of deleterious ice crystals.[423] A conventional post-embedding procedure was

selected for use in this study due to its superior preservation of the substructure of intracellular compartments, and relatively quick and simple protocol (when compared to pre-embedding and high-pressure-freezing methods).

Arguably the most crucial issue for any immunolabelling study is the specificity of the antibody used to label the protein of interest. Various validation methods exist (reviewed in Uhlen *et al.*[442] and Voskuil *et al.*[443]), but the simplest means of verifying the specificity of an antibody is to prepare a control specimen where the primary antibody is omitted. In these control sections, some background particles should be scattered randomly.[444] If a primary antibody is specific, clusters of signal should be observed at the expected subcellular site with high precision.

Immunolabelling of activated NOTCH1 resulted in extensive signal throughout all CLL cell compartments, with no distinct clustering of gold particles. Labelling of the Matrigel™ matrix was also observed. Nonspecific signal is generally caused by one of two issues: (i) cross-reactive antibodies binding to unintended epitopes within sections; and (ii) adsorption of the primary antibody to clear plastic resin.[445] Elimination of the ECM removed background labelling, with no alterations in signal within CLL cells, demonstrating that the primary antibody was cross-reacting with epitopes within the Matrigel™ and leukaemic cells rather than being absorbed by the resin. Thus, the ECM was omitted for subsequent optimisation experiments.

There are countless different epitopes within cells/tissues that antibodies can cross-react with. Thus, preincubation (or blocking) of biological specimens with 5-10% normal serum (sourced from the same species as the secondary antibody host species) prior to incubation with the primary antibody is essential for diminishing cross-reactivity and/or random ionic

and hydrophobic interactions.[446] Optimisation of specimen blocking included varying the preincubation time and concentration of goat serum. Blocking for 4 h slightly reduced non-specific signal, with no discernible differences between 3% and 5% buffers. To further eliminate undesirable labelling, the primary antibody incubation time was decreased as the rate of binding between antibody and antigen (known as the affinity constant) is affected by time in additional to other variables, such as temperature and pH.[447] Incubation for 2 h at RT dramatically reduced random labelling throughout cellular compartments. Clusters of signal were observed at the plasma membrane and pores within the nuclear envelope. This pattern of signal was indicative of genuine activated NOTCH1 labelling as following proteolytic cleavage of the extracellular NOTCH1 receptor, the N-ICD translocates to the nucleus to induce transcription of target genes.[60,64]

Further validation studies are required to fully establish the specificity of optimised NOTCH1 immunogold labelling prior to reintroduction of the Matrigel™ matrix. These studies would include the use of additional anti-activated NOTCH1 antibodies (if suitable for EM), and assessment of signal density following indirect (i.e., GSI treatment) and direct (i.e., NOTCH1 small interfering RNA transfection) inhibition of NOTCH1 activity.

6.7.2. MORPHOLOGICAL AND BEHAVIOURAL CHANGES INDUCED BY NOTCH1 INHIBITION

GSIs are small molecules developed for the treatment of malignancies driven by dysregulated NOTCH1 signalling.[448] Although the exact role of NOTCH1 in CLL leukaemogenesis still needs to be established, it is important to note that patients exhibiting NOTCH1 mutations display poor treatment outcomes,[47,53–55,80,81] more deleterious prognostic factors (e.g., unmutated *IGHV*) and higher risk of transformation to Richter Syndrome than wild-type NOTCH1

cases.[47,84] Thus, the relevance of NOTCH1 mutations in disease progression invites the possibility for new therapeutic options.

CLL cells: Morphological responses to NOTCH1 inhibition varied between CLL cases and GSI treatment. PF-03084014 resulted in the formation of significantly larger cells in two CLL cases [CLL-09 (*IGHV*-mutated; *TP53*-mutated) and CLL-11 (*IGHV*-unmutated)], whereas the CLL-26 (*IGHV*-unmutated) population was comprised of predominantly small, globular cells due to impaired cytoskeletal polarisation. RO4929097-treated CLL-11 and CLL-26 cells cases demonstrated a shift towards large, polarised cells. The CLL-09 population exhibited a significant decrease in cellular elongation alone with RO4929097 treatment. Varying responses to GSI therapy may indicate differences in NOTCH1 activity between CLL patients as previously described. Detectable levels of N-ICD expression were observed in approximately 51% of *NOTCH*-unmutated CLL cases only. Furthermore, levels of N-ICD expression varied amongst the N-ICD-positive panel, with *NOTCH*-mutated cases typically exhibiting higher levels than wild-type cases.[57]

Given that CLL cases demonstrated conflicting shape changes with PF-03084014 and RO4929097 treatment, off-target effects should also be considered. GSI are pan-NOTCH inhibitors, blocking the cleavage of all NOTCH receptors at varying (but often overlapping) drug concentions.[112] Indeed, severe gastrointestinal toxicity was described in T-ALL/AML patients receiving the oral GSI MK-0752,[115] due to simultaneous inhibition of both NOTCH1 and NOTCH2.[116,117]

Little has been published on the morphological and behavioural responses of CLL cells following *NOTCH1* inhibition. However, by comparing the transcriptional signature of CLL cells expressing unmutated *NOTCH1* to NOTCH1-null cells, chemotaxis was identified as a key

NOTCH1-dependent process.[86] In line with this, *NOTCH1*-mutated CLL cases specifically exhibited disrupted chemotactic responses following NOTCH1 inhibition.[88,114] T-ALL cells, which display NOTCH1 mutations in over 50% of cases,[72] also demonstrated reduced cell polarisation, migration and adhesion with impaired NOTCH1 signalling.[92] Interestingly, NOCTH1-depleted T-ALL cells showed a more rounded phenotype and lacked posterior tails. These phenotypic alterations were similar to those observed in case CLL-26 and CLL-09 with PF-03084014 and R04929097 treatment, respectively. T-ALL shape changes were linked to decreased NOTCH1-dependent RhoU activity. RhoU and RhoV constitute an atypical subfamily of Rho GTPases with extremely rapid intrinsic guanine nucleotide exchange activity, resulting in the proteins being predominantly in the GTP-loaded (i.e., active) configuration.[449–451] These GTPases facilitate cytoskeletal reorganisation in several cell types *in vitro*, leading to enhanced lamellipodia/filopodia formation, integrin-based focal adhesion,[452,453] and neural crest cell migration.[454] It remains to be established if NOTCH1-dependent RhoU activity is required for the effective adhesion, migration, and chemotaxis of CLL cells.

In contrast to the above finding, the CXCL12-driven migration of CLL cells was significantly increased by both PF-03084014 and R04929097 treatment. An explanation for these unexpected results could not be found in the literature. Varying mechanisms of resistance to NOTCH1 signalling blockade have been described in T-ALL, including loss of PTEN, AKT activation, mutations in the *FBW7* gene,[65,455] and alterations in transcriptomic and metabolic signatures, particularly glucose metabolism;[456,457] however, enhanced chemotactic responses have not been described in resistant leukemic cells.

MCL cells: Characterisation of the *NOTCH1* mutational status of CLL cases was not feasible in the timeframe of this investigation. Thus, MCL cell lines REC-1 and G519 were utilised to

determine the effects of NOTCH1 mutation on chemokine-driven migration following GSI treatment. REC-1 cells exhibit an intragenic deletion in exon 28 encoding a truncated NOTCH1 protein activated by γ-secretase in a ligand-independent fashion.[418,458] In contrast, G519 were demonstrated to express unmutated *NOTCH1* by targeting Sanger Sequencing of a comprehensive cohort of 103 primary MCL samples and 9 additional cell lines.[459]

REC-1 cells demonstrated significantly decreased cell proliferation and expression of NOTCH1 target genes following GSI treatment compared to most *NOTCH1*-unmuated MCL cells.[459] Additionally, REC-1 cells were confirmed to overexpress cleaved NOTCH1 independently of Delta-like protein 1-mediated activation.[459] Despite this previously reported sensitivity to NOTCH inhibition, the chemotactic response of *NOTCH1*-mutated REC-1 cells was significantly increased by both GSIs here. As with the increased directional cell migration observed in primary CLL cells with NOTCH1 inhibition, an explanation for this unusual observation could not be found in the literature.

In contrast, *NOTCH1*-unmutated G519 displayed unaltered CXCL12-driven chemotaxis with PF-03084014 treatment. This observation was in lines with previous reports that *NOTCH1*-unmuated MCL cell lines typically exhibit low sensitivity to γ-secretase impairment.[459,460] Indeed, OMP-52M51 impeded Delta-like protein 4-induced upregulation of genes related to apoptosis, adhesion, angiogenesis, and migration in *NOTCH1*-mutated Mino cells but not *NOTCH1*-unmutated JeKo-1 cells.[460] However, a significant decrease in G519 directional cell migration was observed following R04929097 pre-treatment. Once again, GSI are pan-NOTCH inhibitors, preventing the proteolysis of all NOTCH receptors at varying concentrations. Thus, simultaneous inhibition of both NOTCH1 and other NOTCH molecules may account for the decreased chemotactic response observed in G519 cells with R04929097 exposure;

particularly as the IC$_{50}$ values of R04929097 for NOTCH receptors are similar (e.g., 0.46-4.0nM for NOTCH1, 2.24nM for NOTCH2 and 3.4nM for NOTCH4).[112]

The predominantly atypical GSI-induced morphological and/or chemotactic responses of CLL and MCL cells described here need to be further corroborated with additional *in vitro* experiments.

6.7.3. INVESTIGATION OF NOTCH1-PROTEIN INTERACTIONS

Over the last few decades, mass spectrometry has emerged as the primary tool for high-throughput identification of proteins from biological samples containing a mixture of diverse biomolecules. Briefly, this technique involves the proteolytic cleavage of proteins to peptides, which are then typically pre-fractioned by capillary electrophoresis or using a chromatography technique (liquid or gas), ionised, fragmented into 'product ions', and separated based upon their *m/z* using an electrical or magnetic field within the mass analyser. Separated product ions travel either directly or indirectly (via collision cells) from the mass analyser(s) to the detector, where retention time, *m/z* values and relative intensities (or abundance) of product ions are recorded. The captured mass spectra, indicating the relationship between the *m/z* value of a product ion and its relative intensity, are then assigned to previously identified peptide sequences using database search engines, resulting in retrospective identification and quantification of proteins within the specimen (reviewed in detail in Noor *et al.*[461] and Baldwin[462]).

Ideally, assembly of the identified peptide sequences using protein inference algorithms would produce a final list containing all proteins within the original sample prior to enzymatic hydrolysis.[461,462] Unfortunately, this was not achieved here as despite immunoblot evidence of NOTCH1 precipitation, the protein could not be identified using a mass spectrometry-based

method, calling into question the validity of all other protein interactions identified by the Co-IP experiment. There are numerous variables that can lead to false-positive or -negative mass spectrometry results. Factors resulting in false-positive identification of proteins in mass spectrometry analyses include, but are not limited to, sub-optimal analyser setup, incorrect protein database choice and/or search parameters (e.g., low-stringency thresholds), variability in spectral matching and/or protein inference algorithms, and contamination.[461,463,464] Indeed, identification of plastin-3, an actin-bundling protein located in hair cell stereocilia, indicated that extraneous matter (e.g., hair and skin) had entered the sample despite the use of sterile conditions.

It is important to note that failure to identify a particular protein, in this case NOTCH1, does not definitively prove its absence from a specimen (i.e., false-negative). This is something that mass spectrometry is unable to confirm alone.[462] No peptide sequence inference may be due to the absence of a particular peptide, resulting from low quantities of the original protein in the sample, incomplete proteolysis due to incompatible pH, poor peptide extraction from gel pieces, poor pre-fractionation/separation of peptides, leading to competition for available protons during ionisation, or post-translational modification of the peptide, causing an unexpected m/z value.[462,463] Additionally, there are varying experimental limitations for the detection of extremely small or large peptides depending on the proteomic approach utilised (e.g., approximately 500-3000Da with bottom-up proteomics), a variable that cannot be controlled with a single enzymatic cleavage step.[463,465] Proteolytic digestion is most frequently achieved using the serine protease trypsin, which specifically cleaves the protein on the carboxyl-terminal side of lysine and arginine residues, unless the next amino acid in the sequence is a proline.[466] The selectivity of trypsin is essential for reproducible protein

hydrolysis; however, cleavage and, consequently, peptide size is dependent on the abundance of lysine and arginine residues within the protein.[462,465] Combining parallel or successive digests generated using multiple proteases of different specificities (e.g., trypsin and chymotrypsin) may increase protein coverage in future mass spectrometry analyses.[465,467]

Based on the information described above, numerous avenues could be explored in subsequent studies to improve the mass spectrometry-based evaluation of NOTCH1-protein interactions. Unfortunately, optimisation of protein identification was not possible in the time available for this study. However, an obvious first step would be to stimulate NOTCH1 activation via pre-treatment of JURKAT cells with recombinant ligands; consequently, increasing the quantity of N-ICD available for precipitation, extraction, and detection. Alternatively, equivalent segments from multiple gels should be combined and processed as if they were a single sample to increase NOTCH1 abundance. Failure to visualise the approximately 120kDa NOTCH1 band with the ProtoBlue Safe Colloidal Coomassie Blue stain (Figure 2.6) indicated that there was insufficient protein for confident identification.[463] A positive control (e.g., a high-abundance protein from the molecular weight standards) should be also be excised and processed in subsequent studies to confirm successful proteolytic digestion and extraction of peptides from gel fragments.[463] Finally, the specificity of the proteins identified by mass spectrometry here also needs to be confirmed by obtaining appropriate antibodies and demonstrating their presence within specific precipitates by western blotting.

Although the proteins identified via Co-IP and mass spectrometry are not known NOTCH1-binding partners, it was interesting to note that they belonged to three main functional

groups: (i) cytoskeletal components and regulation; (ii) cellular metabolism; and (iii) ribosomal assembly and mRNA translation. By comparing gene expression profiles of *NOTCH1*-mutated and *NOTCH1*-wildtype CLL cases, Pozzo *et al*.[468] previously demonstrated a NOTCH1 activation signature characterised by MYC-induced upregulation of genes involved in ribosome biogenesis, namely the nucleophosmin 1 gene and genes encoding ribosomal proteins. It was suggested that a link between NOTCH1 signalling and protein biosynthesis may provide proliferative advantages to CLL cells.[468]

Increased c-MYC transcription, facilitated by NOTCH1 activation, was also shown to contributes to the metabolic shift from oxidative phosphorylation to aerobic glycolysis induced in CLL cells by protective BMSCs,[415] potentially conferring increased cell growth and chemoresistance as described by the Warburg effect.[469] Stomal-facilitated upregulation of *c-MYC* and, consequently, the glycolytic switch in CLL cells were abolished by GSI treatment, confirming the involvement of NOTCH1-c-MYC signalling.[415] As previously mentioned, NOTCH1 signalling was demonstrated to regulate cytoskeletal polarisation in T-ALL cells via upregulation of *RHOU* and *RHOV*,[92] genes encoding atypical GTPases which promote lamellipodia/filopodia formation and focal adhesion.[452,453] NOTCH1- and RhoU-depleted T-ALL cells or leukaemic cells treated with GSIs exhibited a rounded phenotype in addition to impaired cell adhesion and chemotaxis.[92] Furthermore, *NOTCH1*-mutated CLL cells displayed reduced actin polymerisation, an essential processes for effective chemotactic responses, with PF-03084014 treatment.[88]

Taken together these findings suggest the upstream involvement of NOTCH1 signalling in regulating the key cellular functions highlighted within this mass spectrometry-based evaluation of NOTCH1-protein interactions. Interfering with the proteins linking this pathway

to protein synthesis, cellular metabolism, and cytoskeletal organisation could be therapeutically exploited for targeting CLL with deregulated NOTCH1 activity to overcome drug resistance in the disease.

CHAPTER 7 – DISCUSSION AND FUTURE WORK

Over the last few decades, substantial improvements in the treatment of CLL, a currently incurable lymphoproliferative disorder, have been made. In particular, the first-in-class irreversible BTKi, ibrutinib, has revolutionised the management of CLL, with clinical studies demonstrating overall and PFS benefits in several subgroups of CLL, including those with deleterious chromosomal aberrations.[209,210,222,223,226,227] However, a significant fraction of CLL patients develop resistance to BTKi, often characterised by aggressive relapse and disease progression.[243,244,249,352] Unfortunately, alternative therapeutic regimes are limited for R/R patients.[244] Thus, resistance remains a major challenge in the management of CLL. This thesis builds upon existing knowledge of the mechanisms underlying the sensitivity of CLL subgroups to clinically relevant small molecule inhibitors, aiming to provide novel insight into the morphological responses of leukemic cells and to suggest rational combination therapies.

7.1. MORPHOLOGY OF CLL CELLS IN VITRO

One of the most striking observations noted during this study, made using optimised SEM and ImageJ morphometric analyses, was the degree of morphological variation between CLL cells culture *in vitro.* This was not entirely surprising given that CLL is an extremely heterogeneous disease with numerous chromosomal alterations, somatic mutations, and miRNA and epigenetic changes contributing to disease pathology.[13] Furthermore, at the time of writing, a single driver event responsible for initiation and maintenance of CLL, such as the reciprocal translocation between chromosomes 9 and 22 in chronic myeloid leukaemia, resulting in the formation of the *BCR-ABL* oncogene,[271,272] has yet to be identified and the exact cellular origin(s) of CLL B-lymphocytes remains a matter of debate.[25]

To this effect, resting CLL cells exhibited marked morphological differences which could not be attributed to the presence/lack of *IGHV* mutations. There was some evidence of increased irregularity (i.e., larger, more polarised cells with abnormal cytoskeletal features) in *IGHV*-unmutated CLL cases; however, a larger sample cohort is needed to confirm this. The presence of additional adverse prognostic factors, with known effects on cell morphology and behaviour, also further complicated a direct comparison of CLL cases. For example, two of the cases with 'atypical' distributions of shape parameters, CLL-03 (*IGHV*-unmutated) and CLL-09 (*IGHV*-mutated), displayed del(11q) effecting *ATM* and mutated *TP53*, respectively. Loss of both ATM and TP53 activity has been linked to increased Rac1 activation in several cell types, resulting in increased cellular spreading, motility, and malignant transformation.[333,338,339] Thus, alterations in the mutual inhibitory loop between spatially and temporally exclusive Rac1 and RhoA molecules[327] likely contributed to altered cytoskeletal dynamics within these CLL cells, irrespective of *IGHV* mutational status. Larger studies are needed to confirm the association of deleterious chromosomal alterations with atypical morphology. Additionally, the precise role of Rac1 signalling in CLL subgroups needs to be fully elucidated. Targeting of Rac1 activity within CLL cases exhibiting disrupted ATM and TP53 function could be incorporated into a combination therapy to improve treatment outcomes in these hard-to-treat patients.

7.2. MORPHOLOGICAL RESPONSES TO SIGNAL INHIBITION IN CLL

Despite notable differences in the resting morphology of CLL cases, unique changes in shape parameters could be elicited (to varying degrees) in leukaemic cells following signal inhibition, independent of *IGHV* mutational status.

Ibrutinib-mediated inhibition of BTK, a linker protein connecting BCR signalling to the B-lymphocyte cytoskeleton via activation of WASP,[147] typically resulted in the formation of one main homotypic population of globular cells. Loss of anterior-posterior morphology indicated that elongated-type cell migration had been impaired due to decreased expression of adhesion molecules, such as integrin $\alpha 4\beta 1$, following BTK inhibition as previously described.[235–237] Rather than exerting a direct cytotoxic effect, ibrutinib is thought to reduce the tumour burden in CLL patients by impairing leukaemic cell retention within the TME and, consequently, depriving them of crucial pro-survival signals.[237] Similarly, CLL cells generally displayed a shift towards a more globular phenotype with blockage of ABL1 activity. ABL family kinases, such as ABL1, play a crucial role in facilitating cytoskeletal dynamics within lymphocytes, supporting filopodia formation and cell migration[165,273,283] by reducing stress fibre formation,[279,348–350] a prerequisite for cell spreading and exploratory transmigration. In contrast, disruption of the RhoA/ROCK pathway, which is responsible for the actomyosin-mediated retraction of cytoskeletal processes,[259] typically produced large leukemic cells with extensive, non-polarised cytoskeletal protrusions. Uninhibited extension of lamellipodia resulted from loss of ROCK-dependent RhoA suppression of Rac1 activity at leading edges.[257,264,267]

The morphological changes induced by BTK, ROCK and ABL1 inhibition generally correlated to reduced homotypic cellular interactions *in vitro*, further emphasising the key role of the B-lymphocyte cytoskeleton in facilitating CLL cell trafficking, adhesion, and cell-to-cell communication.[125,147,416] Interestingly, whilst Y-27632 and imatinib impaired cellular interaction within both *IGHV*-mutated and -unmutated subsets, ibrutinib reduced M-CLL cell-to-cell contact specifically. Likewise, blockage of RhoA/ROCK activity attenuated chemokine-

driven migration in cases exhibiting mutated *IGHV* alone. Chemotactic responses were largely unaltered in CLL subsets with ABL1 inhibition, consistent with elongated-type motility being an ABL1-independent process,[165] whereas highly variable BTKi-induced alterations in CXCL12-driven migration were observed as previously described.[237]

These unexpected subgroup-specific finding suggested that CLL cases exhibiting unmutated *IGHV* may favour alternative integrin-independent pathways for sustaining cellular transmigration and interactions within TME niches, such as amoeboid motility. This lower dependency on elongated-type cell migration, which is regulated by BCR signalling,[147,416] may, therefore, contribute to the bulky disease and less favourable responses initially reported in UM-CLL compared to M-CLL with ibrutinib therapy. The 5-year PFS of TN CLL/SLL cases displaying unmutated and mutated *IGHV* receiving ibrutinib was estimated at 67% and 81%, respectively.[213] The 5-year PFS was 39% in R/R patients with unmutated *IGHV* and 53% in patients with mutated *IGHV*.[210] However, the final update from RESONATE, a phase III clinical study of ibrutinib in R/R CLL/SLL, showed similar median PFS in patients with mutated *IGHV* (48.4 months) and unmutated *IGHV* (49.7 months) disease.[470]

Although a significant interaction between *IGHV* mutational status and the effect of ibrutinib treatment on PFS and outcomes in CLL patients remains inconclusive, ibrutinib-induced changes in leukaemic cell-to-cell interactions appear to vary between subgroups. Thus, combinational therapies should not target CLL cell-specific mechanisms for controlling cytoskeletal dynamics alone but should be adjusted to specific subsets. Indeed, the atypical *TP53*-mutated case CLL-09 demonstrated significant morphological and behavioural alterations following inhibition of ROCK and ABL1, despite exhibiting no changes in shape parameters with blockage of BTK signalling. Ibrutinib therapy responses and outcomes in

patients with deleted or mutated *TP53* are known to be less robust than those achieved in patients with other high-risk cytogenetic abnormalities.[210,222]

The morphological and behavioural responses described here need to be fully corroborated in additional *in vitro* experiments, with particular focus on charactering the BTK-independent signalling pathways controlling cytoskeletal alterations within CLL subgroups, as targeting these networks may have substantial therapeutic benefits in BTKi-resistant diseases.

7.3. THE EFFECT OF RESISTANCE ON MORPHOLOGICAL RESPONSES

Drug resistance is a major issue in the treatment of many malignancies, including CLL. Although novel small molecule inhibitors such as ibrutinib, idelalisib (PI3K inhibitor) and venetoclax (BCL2 inhibitor) have proven their clinical efficacy as monotherapies as well as in various combinations, primary and acquired resistance to these agents has been described in CLL patients.[352,471] A greater understanding of the leukemic cell behavioural changes underlying treatment outcomes is needed to identify new or synergistic therapeutic regimes for R/R patients.

Utilising MCL cell lines as a surrogate model for BTKi sensitivity in CLL, distinct shape and behavioural changes were demonstrated following signal inhibition. Ibrutinib-resistant G519 showed no significant morphological or chemotactic responses following ibrutinib therapy, further emphasising the lower dependency of this cell line on BTK signalling[286,365] for cytoskeletal reorganisation. Ibrutinib-sensitive REC-1 cells displayed a significant increase in circularity, suggesting that polarisation of the B-lymphocyte cytoskeleton and, consequently, integrin-dependent elongated-type motility had been reduced in a similar manner to that observed in primary CLL cells. In contrast to these morphological observations, the

chemotaxis of REC-1 cells was increased with BTK inhibition. However, varying culture system-dependent chemotactic responses have previously been reported for MCL cells following BTK blockade, which could not be explained by ibrutinib-mediated alterations in the CXCR4-CXCL12 axis.[369]

Despite notable differences in ibrutinib-induced responses between G519 and REC-1 cells, inhibition of ROCK or ABL1 resulted in largely similar cytoskeletal and chemotactic alterations, irrespective of BTKi sensitivity. Loss of RhoA/ROCK activity impaired retraction of cytoskeletal processes and eliminated any net cellular migration achieved by unregulated Rac1-mediated extension of lamellipodia within both MCL cell lines as described for monocytes,[267] prostate cancer cells[264] and *IGHV*-mutated primary CLL cells. Interestingly, both G519 and REC-1 cell lines demonstrated a significant increase in extension of the F-actin cytoskeleton with ABL1 inhibition. This contrasted with the imatinib-induced globular morphology observed in CLL populations, and increased RhoA activity and contractility previously noted in *Arg*-null fibroblast.[279] Furthermore, despite evidence of chemotactic responses being largely ABL1-independent in CLL,[165] the CXCL12-induced migration of both cell lines was almost entirely abolished with imatinib pre-treatment. These unexpected findings suggested that the role(s) of ABL kinases in controlling B-lymphocyte cytoskeletal dynamics may be disease-specific.

Nevertheless, the behavioural observations described here further indicated that coordination polarisation and contraction of the cortical cytoskeleton, facilitated through ROCK and ABL1 activity, is essential for effective directional migration and, thus, B-lymphocyte trafficking to protective niches, regardless of BTKi sensitivity. Combining a ROCK or ABL1 inhibitor with ibrutinib therapy may, therefore, be a synergistic therapeutic option to disrupt the retention of CLL (or MCL) cells within tissues. Testing of cases with confirmed

primary and acquired BTKi resistance is required to begin establishing the efficacy of such a combinational therapy for overcoming resistance.

7.4. MORPHOLOGICAL RESPONSES TO NOTCH1 INHIBITORS

In recent years the role of *NOTCH1* in CLL leukaemogenesis has become a topic of active research. NOTCH1 signalling, initiated via interaction of transmembrane receptors with cognate ligands expressed by supportive cells,[74] promotes leukaemic cell survival, activation of BCR signalling, B-lymphocytes homing to lymphoid tissues and drug resistance.[60] Alterations in NOTCH1 signalling have also been implicated in the clinical activity of ibrutinib *in situ*, with reduced NOTCH1 activity and N-ICD/BTK complexes being demonstrated in CLL cases receiving ibrutinib. Relapse coincided with recovery of NOTCH1 signalling, whereas ibrutinib-resistant CLL cells exhibited sustained activation.[420] NOTCH1 activity potentially represents an additional mechanism of BTKi resistance in CLL patients. Thus, combinational regimes incorporating a GSIs may have synergistic effects, leading to improved outcomes in this disease.

Interestingly, primary CLL cases exhibited either a significant shift towards larger, polarised cells, or a uniform globular population, depending on the GSI used. Varying treatment responses potentially indicated differences in patient-specific activation of NOTCH1. Indeed, varied levels of N-ICD expression could be detected by immunoblot analysis in approximately 51% of *NOTCH1*-wild-type CLL cases only.[57] As GSI are pan-NOTCH inhibitors blocking the cleavage of NOTCH receptors 1-4 at varying but often overlapping drug concentions,[112] the involvement of off-target effects in mediating shape changes should also be considered.

Transcriptional signature analysis has shown that *CXCR4* expression is a direct target of NOTCH1 signalling.[57] Consequently, impaired leukemic cell migration towards CXCL12 following blockage of NOTCH1 signalling has been described. Disruption of chemotactic responses following NOTCH1 inhibition appears to be specific to *NOTCH1*-mutated CLL cases,[88,114] due likely to higher expression of N-ICD compared to wild-type samples.[57] In contrast to previous reports, chemokine-driven migration of CLL cases was significantly increased by both GSIs. This unexpected result possibly indicated that the CLL cases expressed unmutated *NOTCH1*; however, unaltered (not enhanced) CXCR4 expression and chemotaxis are typically described in wild-type CLL with NOTCH1 inhibition.[88,114]

Due to time constraints the *NOTCH1* mutational status of CLL patients could not be confirmed. Instead, REC-1 cells exhibiting a deletion in exon 28 encoding a truncated NOTCH1 protein[418,458] and *NOTCH1*-unmutated G519 cells[459] were utilised to model the effects of GSI sensitivity on chemotactic responses. Like primary CLL cells, *NOTCH1* -mutated MCL cell lines generally display greater sensitivity to NOTCH1 inhibition compared to most *NOTHC1*-unmutated MCL cells.[459,460] In contrast, the CXCL12-induced migration of REC-1 cells was significantly increased with both GSIs, whereas G519 cells displayed decreased chemotaxis with RO4929097 pre-treatment alone.

Before the role(s) of NOTCH1 activation in BTKi-mediated treatment outcomes can be explored, future investigations with additional CLL cases and MCL cell lines are required to clarify the unusual GSI-induced responses identified here and to excluded experimental errors. Focus should also be placed on determine whether MCL cells display varying culture condition-dependent chemotaxis towards CXCL12 following GSI therapy as has been reported with ibrutinib.[369]

7.5. DEVELOPING A 3D MODEL TO ASSESS CLL MORPHOLOGY AND NOTCH1 LOCALISATION

The development of a 3D culture system *ex vivo* for studying the pathogenesis of lymphoproliferative disorders is not a novel concept[410,411] However, the combination of a TME-like model with high-resolution TEM and immunogold labelling for the assessment of leukaemic cell morphology and NOTCH1 localisation has not previously been explored. As this method had not been tested in CLL, numerous variables needed to be optimised with limited time and materials.

Colonisation of a 3D Matrigel™ culture model was possible with both primary CLL cells and monocyte-derived NLCs using a pre-embedded method of cell seeding. Characteristic morphologies were observed using phase-contrast microscopy, with the establishment of discrete clusters of predominately globular lymphocytes surrounding flat, spindle-shaped NLCs.[167] Preservation of cell viability, a significant challenge with any culture system, was improved using higher seeding densities without the need for additional supportive cells or stimuli, such as BMSCs or CD40L. However, the incorporation and optimisation of these factors in future studies will undoubtable increase the biomimicry of this 3D model.

Morphologically recognisable CLL cells were well preserved in ultra-thin sections of the Matrigel™ matrix. However, significant issues relating to nonspecific signal were encountered with the antibody selected for immunolabelling of activated NOTCH1. Background signal was possibly eliminated in sections labelled with the anti-activated NOTCH1 antibody following optimisation of the staining method, but additional investigations are needed to confirm the specificity of this labelling before changes in protein localisation between CLL subsets or following signal inhibition can be assessed.

Importantly, this work demonstrated that it is possible to use high-resolution microscopy to observe CLL morphology and protein localisation within 3D settings, therefore, enabling future work to examine dynamic changes to cell shape, interactions, and protein distribution following signal inhibition. Furthermore, the effect(s) of NOTCH1 inhibition on N-ICD and BTK co-localisation[420] would be an interesting avenue to explore in subsequent double-labelling studies.

7.6. CONCLUSION

The development of novel small molecule inhibitors has increased the catalogue of drugs available for the management of CLL and provided new hope of achieving long-term complete remissions in the near future. Indeed, ibrutinib, and more recently second generation BTKi and venetoclax, have demonstrated safety and efficacy as monotherapies in TN and R/R CLL patients.[478] However, CLL is an extremely heterogenous disease with numerous chromosomal alterations and somatic mutations having been described. Thus, resistance to emerging therapies is a major concern.

The diversity amongst CLL patients was further highlighted using high-resolution morphological analysis of the limited sample cohort available to this study. Specific CLL subsets, such as those with disruption of ATM and TP53 activity, or unmutated *IGHV*, appeared to display altered cytoskeletal dynamics which may contribute to the less robust outcomes reported for conventional drugs. CLL is unlikely to be cured by a single-agent therapy and, thus, combinational treatments targeting several aspects of the pro-survival behaviour of leukemic B-lymphocytes, such as homing and cellular interactions, should be explored further. Indeed, the findings presented here suggested that directly targeting pathways responsible for balancing extension and contraction of the cortical cytoskeletal,

which is crucial for effective chemotaxis, may be incorporated into therapeutic regimes to overcome BTKi resistance.

Detailed characterisation of CLL subsets and the distinct pathways mediating altered cytoskeletal dynamics will be crucial for providing CLL patients with 'personalised medicine'. Identifying disease subgroups which, based on their genetics and transcriptomes, will benefit from specific therapeutic agents will undoubtedly improve treatment outcomes in CLL. The knowledge gained from in-depth morphological and molecular studies of CLL subsets could, ultimately, be combined with advancing global gene expression profiling techniques to identify adverse transcriptional and, subsequently, behavioural characteristics unique to the patient's malignancy, providing meaningful prognostic information.

REFERENCES

1. Matutes, E. *et al.* The immunological profile of B-cell disorders and proposal of a scoring system for the diagnosis of CLL. *Leukemia* **8**, 1640–1645 (1994).

2. Siegel, R. L., Miller, K. D. & Jemal, A. Cancer statistics, 2017. *CA. Cancer J. Clin.* **67**, 7–30 (2017).

3. Cancer Research UK. Chronic lymphocytic leukaemia (CLL) incidence statistics. *Cancer Research UK* https://www.cancerresearchuk.org/health-professional/cancer-statistics/statistics-by-cancer-type/leukaemia-cll/incidence#heading-Zero (2020).

4. Li, Y., Wang, Y., Wang, Z., Yi, D. & Ma, S. Racial differences in three major NHL subtypes: Descriptive epidemiology. *Cancer Epidemiol.* **39**, 8–13 (2015).

5. Pulte, D., Redaniel, M. T., Bird, J. & Jeffreys, M. Survival for patients with chronic leukemias in the US and Britain: Age-related disparities and changes in the early 21st century. *Eur. J. Haematol.* **94**, 540–545 (2015).

6. Hallek, M. Chronic lymphocytic leukemia: 2020 update on diagnosis, risk stratification and treatment. *Am. J. Hematol.* **94**, 1266–1287 (2019).

7. Cerhan, J. R. & Slager, S. L. Familial predisposition and genetic risk factors for lymphoma. *Blood* **126**, 2265–2273 (2015).

8. Hallek, M. *et al.* Guidelines for the diagnosis and treatment of chronic lymphocytic leukemia: A report from the International Workshop on Chronic Lymphocytic Leukemia updating the National Cancer Institute-Working Group 1996 guidelines. *Blood* **111**, 5446–5456 (2008).

9. Döhner, H. *et al.* Genomic Aberrations and Survival in Chronic Lymphocytic Leukemia. *N. Engl. J. Med.* **343**, 1910–1916 (2000).

10. Stilgenbauer, S. *et al.* Gene mutations and treatment outcome in chronic lymphocytic leukemia: Results from the CLL8 trial. *Blood* **123**, 3247–3254 (2014).

11. Fischer, K. *et al.* Long-term remissions after FCR chemoimmunotherapy in previously untreated patients with CLL: Updated results of the CLL8 trial. *Blood* **127**, 208–215 (2016).

12. Wierda, W. G. *et al.* Multivariable model for time to first treatment in patients with chronic lymphocytic leukemia. *J. Clin. Oncol.* **29**, 4088–4095 (2011).

13. Kipps, T. J. *et al.* Chronic lymphocytic leukaemia. *Nat. Rev. Dis. Prim.* **3**, 16096 (2017).

14. Lydyard, P., Whelan, A. & Fanger, M. *BIOS Instant Notes in Immunology*. (Taylor & Francis, Abingdon, 2011).

15. Odegard, V. H. & Schatz, D. G. Targeting of somatic hypermutation. *Nat. Rev. Immunol.* **6**, 573–583 (2006).

16. Di Noia, J. M. & Neuberger, M. S. Molecular mechanisms of antibody somatic hypermutation.

Annu. Rev. Biochem. **76**, 1–22 (2007).

17. Klein, U. & Dalla-Favera, R. Germinal centres: Role in B-cell physiology and malignancy. *Nat. Rev. Immunol.* **8**, 22–33 (2008).

18. Damle, R. N. *et al.* Ig V gene mutation status and CD38 expression as novel prognostic indicators in chronic lymphocytic leukemia. *Blood* **94**, 1840–1847 (1999).

19. Hamblin, T. J., Davis, Z., Gardiner, A., Oscier, D. G. & Stevenson, F. K. Unmutated Ig V(H) genes are associated with a more aggressive form of chronic lymphocytic leukemia. *Blood* **94**, 1848–1854 (1999).

20. Damle, R. N. *et al.* Telomere length and telomerase activity delineate distinctive replicative features of the B-CLL subgroups defined by immunoglobulin V gene mutations. *Blood* **103**, 375–382 (2004).

21. Rosenwald, A. *et al.* Relation of gene expression phenotype to immunoglobulin mutation genotype in B cell chronic lymphocytic leukemia. *J. Exp. Med.* **194**, 1639–1648 (2001).

22. Stilgenbauer, S. *et al.* Clonal evolution in chronic lymphocytic leukemia: Acquisition of high-risk genomic aberrations associated with unmutated VH, resistance to therapy, and short survival. *Haematologica* **92**, 1242–1245 (2007).

23. Chen, L. *et al.* ZAP-70 directly enhances IgM signaling in chronic lymphocytic leukemia. *Blood* **105**, 2036–2041 (2005).

24. Lanham, S. *et al.* Differential signaling via surface IgM is associated with VH gene mutational status and CD38 expression in chronic lymphocytic leukemia. *Blood* **101**, 1087–1093 (2003).

25. Chiorazzi, N. & Ferrarini, M. Cellular origin(s) of chronic lymphocytic leukemia: Cautionary notes and additional considerations and possibilities. *Blood* **117**, 1781–1791 (2011).

26. Agathangelidis, A. *et al.* Stereotyped B-cell receptors in one-third of chronic lymphocytic leukemia: a molecular classification with implications for targeted therapies. *Blood* **119**, 4467–4475 (2012).

27. Kipps, T. J. *et al.* Developmentally restricted immunoglobulin heavy chain variable region gene expressed at high frequency in chronic lymphocytic leukemia. *Proc. Natl. Acad. Sci. U. S. A.* **86**, 5913–5917 (1989).

28. Fais, F. *et al.* Chronic lymphocytic leukemia B cells express restricted sets of mutated and unmutated antigen receptors. *J. Clin. Invest.* **102**, 1515–1525 (1998).

29. Widhopf, G. F. *et al.* Chronic lymphocytic leukemia B cells of more than 1% of patients express virtually identical immunoglobulins. *Blood* **104**, 2499–504 (2004).

30. Kröber, A. *et al.* VH mutation status, CD38 expression level, genomic aberrations, and survival in chronic lymphocytic leukemia. *Blood* **100**, 1410–1416 (2002).

31. Calin, G. A. *et al.* Nonlinear partial differential equations and applications: Frequent deletions and down-regulation of micro- RNA genes miR15 and miR16 at 13q14 in chronic lymphocytic leukemia. *Proc. Natl. Acad. Sci.* **99**, 15524–15529 (2002).

32. Klein, U. *et al.* The DLEU2/miR-15a/16-1 cluster controls B cell proliferation and its deletion leads to chronic lymphocytic leukemia. *Cancer Cell* **17**, 28–40 (2010).

33. Stilgenbauer, S. *et al.* Subcutaneous alemtuzumab in fludarabine-refractory chronic lymphocytic leukemia: Clinical results and prognostic marker analyses from the CLL2H study of the German chronic lymphocytic leukemia study group. *J. Clin. Oncol.* **27**, 3994–4001 (2009).

34. Zenz, T. *et al.* Detailed analysis of p53 pathway defects in fludarabine-refractory chronic lymphocytic leukemia (CLL): Dissecting the contribution of 17p deletion, TP53 mutation, p53-p21 dysfunction, and miR34a in a prospective clinical trial. *Blood* **114**, 2589–2597 (2009).

35. Zenz, T., Mertens, D., Küppers, R., Döhner, H. & Stilgenbauer, S. From pathogenesis to treatment of chronic lymphocytic leukaemia. *Nat. Rev. Cancer* **10**, 37–50 (2010).

36. Lavin, M. F. Ataxia-telangiectasia: From a rare disorder to a paradigm for cell signalling and cancer. *Nat. Rev. Mol. Cell Biol.* **9**, 759–769 (2008).

37. Mulligan, C. S., Thomas, M. E. & Mulligan, S. P. Monoclonal B-cell lymphocytosis and chronic lymphocytic leukemia. *N. Engl. J. Med.* **359**, 2065–2066 (2008).

38. Rossi, D. *et al.* Disruption of BIRC3 associates with fludarabine chemorefractoriness in TP53 wild-type chronic lymphocytic leukemia. *Blood* **119**, 2854–2862 (2012).

39. Rossi, D. *et al.* Integrated mutational and cytogenetic analysis identifies new prognostic subgroups in chronic lymphocytic leukemia. *Blood* **121**, 1403–1412 (2013).

40. Rose-Zerilli, M. J. J. *et al.* ATM mutation rather than BIRC3 deletion and/or mutation predicts reduced survival in 11q-deleted chronic lymphocytic leukemia: Data from the UK LRF CLL4 trial. *Haematologica* **99**, 736–742 (2014).

41. Barrio, S. *et al.* Genomic characterization of high-count MBL cases indicates that early detection of driver mutations and subclonal expansion are predictors of adverse clinical outcome. *Leukemia* **31**, 170–176 (2017).

42. Hallek, M. *et al.* Addition of rituximab to fludarabine and cyclophosphamide in patients with chronic lymphocytic leukaemia: A randomised, open-label, phase 3 trial. *Lancet* **376**, 1164–1174 (2010).

43. Döhner, H. *et al.* p53 Gene deletion predicts for poor survival and non-response to therapy with purine analogs in chronic B-cell leukemias. *Blood* **85**, 1580–1589 (1995).

44. Stilgenbauer, S. & Zenz, T. Understanding and managing ultra high-risk chronic lymphocytic leukemia. *Hematol. Am. Soc. Hematol. Educ. Progr.* **2010**, 481–488 (2010).

45. Zenz, T. *et al.* Monoallelic TP53 inactivation is associated with poor prognosis in chronic lymphocytic leukemia: Results from a detailed genetic characterization with long-term follow-up. *Blood* **112**, 3322–3329 (2008).

46. Else, M., Wade, R., Oscier, D. & Catovsky, D. The long-term outcome of patients in the LRF CLL4 trial: The effect of salvage treatment and biological markers in those surviving 10 years. *Br. J. Haematol.* **172**, 228–237 (2016).

47. Fabbri, G. *et al.* Analysis of the chronic lymphocytic leukemia coding genome: Role of NOTCH1 mutational activation. *J. Exp. Med.* **208**, 1389–1401 (2011).

48. Wang, L. *et al.* SF3B1 and other novel cancer genes in chronic lymphocytic leukemia. *N. Engl. J. Med.* **365**, 2497–2506 (2011).

49. Damm, F. *et al.* Acquired initiating mutations in early hematopoietic cells of CLL patients. *Cancer Discov.* **4**, 1088–1101 (2014).

50. Logan, C. Y. & Nusse, R. The Wnt signaling pathway in development and disease. *Annu. Rev. Cell Dev. Biol.* **20**, 781–810 (2004).

51. Patel, S., Alam, A., Pant, R. & Chattopadhyay, S. Wnt signaling and its significance within the tumor microenvironment: Novel therapeutic insights. *Front. Immunol.* **10**, 2872 (2019).

52. Diop, F. *et al.* Biological and clinical implications of BIRC3 mutations in chronic lymphocytic leukemia. *Haematologica* **105**, 448–456 (2020).

53. Puente, X. S. *et al.* Non-coding recurrent mutations in chronic lymphocytic leukaemia. *Nature* **526**, 519–524 (2015).

54. Puente, X. S. *et al.* Whole-genome sequencing identifies recurrent mutations in chronic lymphocytic leukaemia. *Nature* **475**, 101–105 (2011).

55. Weissmann, S. *et al.* Prognostic impact and landscape of NOTCH1 mutations in chronic lymphocytic leukemia (CLL): A study on 852 patients. *Leukemia* **27**, 2393–2396 (2013).

56. Rossi, D. *et al.* Mutations of NOTCH1 are an independent predictor of survival in chronic lymphocytic leukemia. *Blood* **119**, 521–529 (2012).

57. Fabbri, G. *et al.* Common nonmutational NOTCH1 activation in chronic lymphocytic leukemia. *Proc. Natl. Acad. Sci. U. S. A.* **114**, E2911–E2919 (2017).

58. Lobry, C., Oh, P., Mansour, M. R., Look, A. T. & Aifantis, I. Notch signaling: switching an oncogene to a tumor suppressor. *Blood* **123**, 2451–2459 (2014).

59. Blaumueller, C. M., Qi, H., Zagouras, P. & Artavanis-Tsakonas, S. Intracellular cleavage of Notch leads to a heterodimeric receptor on the plasma membrane. *Cell* **90**, 281–291 (1997).

60. Rosati, E. *et al.* NOTCH1 aberrations in Chronic lymphocytic leukemia. *Front. Oncol.* **8**, 229 (2018).

61. De Joussineau, C. *et al.* Delta-promoted filopodia mediate long-range lateral inhibition in Drosophila. *Nature* **426**, 555–559 (2003).

62. Renaud, O. & Simpson, P. scabrous modifies epithelial cell adhesion and extends the range of lateral signalling during development of the spaced bristle pattern in Drosophila. *Dev. Biol.* **240**, 361–376 (2001).

63. Shah, S. *et al.* Nicastrin functions as a γ-secretase-substrate receptor. *Cell* **122**, 435–447 (2005).

64. Andersson, E. R., Sandberg, R. & Lendahl, U. Notch signaling: Simplicity in design, versatility in function. *Development* **138**, 3593–3612 (2011).

65. O'Neil, J. *et al.* FBW7 mutations in leukemic cells mediate NOTCH pathway activation and resistance to γ-secretase inhibitors. *J. Exp. Med.* **204**, 1813–1824 (2007).

66. Thompson, B. J. *et al.* The SCFFBW7 ubiquitin ligase complex as a tumor suppressor in T cell leukemia. *J. Exp. Med.* **204**, 1825–1835 (2007).

67. Ye, X. *et al.* Recognition of phosphodegron motifs in human cyclin E by the SCF (Fbw7) ubiquitin ligase. *J. Biol. Chem.* **279**, 50110–50119 (2004).

68. Fryer, C. J., White, J. B. & Jones, K. A. Mastermind recruits CycC:CDK8 to phosphorylate the Notch ICD and coordinate activation with turnover. *Mol. Cell* **16**, 509–520 (2004).

69. Mo, J.-S. *et al.* Integrin-linked kinase controls Notch1 signaling by down-regulation of protein stability through Fbw7 ubiquitin ligase. *Mol. Cell. Biol.* **27**, 5565–5574 (2007).

70. Ellisen, L. W. *et al.* TAN-1, the human homolog of the Drosophila Notch gene, is broken by chromosomal translocations in T lymphoblastic neoplasms. *Cell* **66**, 649–661 (1991).

71. Pear, W. S. *et al.* Exclusive development of T cell neoplasms in mice transplanted with bone marrow expressing activated Notch alleles. *J. Exp. Med.* **183**, 2283–2291 (1996).

72. Weng, A. P. *et al.* Activating mutations of NOTCH1 in human T cell acute lymphoblastic leukemia. *Science* **306**, 269–271 (2004).

73. Rosati, E. *et al.* Constitutively activated Notch signaling is involved in survival and apoptosis resistance of B-CLL cells. *Blood* **113**, 856–865 (2009).

74. Kamdje, A. H. N. *et al.* Role of stromal cell-mediated Notch signaling in CLL resistance to chemotherapy. *Blood Cancer J.* **2**, e73 (2012).

75. Ianni, M. Di *et al.* A new genetic lesion in B-CLL: A NOTCH1 PEST domain mutation. *Br. J. Haematol.* **146**, 689–691 (2009).

76. Sportoletti, P. *et al.* NOTCH1 PEST domain mutation is an adverse prognostic factor in B-CLL. *Br. J. Haematol.* **151**, 404–406 (2010).

77. Arruga, F. *et al.* Functional impact of NOTCH1 mutations in chronic lymphocytic leukemia. *Leukemia* **28**, 1060–1070 (2014).

78. Quesada, V. *et al.* Exome sequencing identifies recurrent mutations of the splicing factor SF3B1 gene in chronic lymphocytic leukemia. *Nat. Genet.* **44**, 47–52 (2012).

79. D'Agaro, T. *et al.* NOTCH1 mutational status in chronic lymphocytic leukaemia: clinical relevance of subclonal mutations and mutation types. *Br. J. Haematol.* **182**, 597–602 (2018).

80. Jeromin, S. *et al.* SF3B1 mutations correlated to cytogenetics and mutations in NOTCH1, FBXW7, MYD88, XPO1 and TP53 in 1160 untreated CLL patients. *Leukemia* **28**, 108–117 (2014).

81. Nadeu, F. *et al.* Clinical impact of clonal and subclonal TP53, SF3B1, BIRC3, NOTCH1, and ATM mutations in chronic lymphocytic leukemia. *Blood* **127**, 2122–2130 (2016).

82. Bittolo, T. *et al.* Mutations at 3' untranslated region (3'UTR) of NOTCH1 are associated with low CD20 expression levels in chronic lymphocytic leukemia. *Blood* **128**, 306–306 (2016).

83. Rossi, D., Spina, V. & Gaidano, G. Biology and treatment of Richter syndrome. *Blood* **131**, 2761–2772 (2018).

84. Balatti, V. *et al.* NOTCH1 mutations in CLL associated with trisomy 12. *Blood* **119**, 329–331 (2012).

85. Baliakas, P. *et al.* Recurrent mutations refine prognosis in chronic lymphocytic leukemia. *Leukemia* **29**, 329–336 (2015).

86. Arruga, F. *et al.* Mutations in NOTCH1 PEST domain orchestrate CCL19-driven homing of chronic lymphocytic leukemia cells by modulating the tumor suppressor gene DUSP22. *Leukemia* **31**, 1882–1893 (2017).

87. Buggins, A. G. S. *et al.* Evidence for a macromolecular complex in poor prognosis CLL that contains CD38, CD49d, CD44 and MMP-9. *Br. J. Haematol.* **154**, 216–222 (2011).

88. López-Guerra, M. *et al.* The γ-secretase inhibitor PF-03084014 combined with fludarabine antagonizes migration, invasion and angiogenesis in NOTCH1-mutated CLL cells. *Leukemia* **29**, 96–106 (2015).

89. Heinhuis, B. *et al.* Interleukin 32 (IL-32) contains a typical α-helix bundle structure that resembles focal adhesion targeting region of focal adhesion kinase-1. *J. Biol. Chem.* **287**, 5733–5743 (2012).

90. Sai, J., Raman, D., Liu, Y., Wikswo, J. & Richmond, A. Parallel phosphatidylinositol 3-kinase (PI3K)-dependent and Src-dependent pathways lead to CXCL8-mediated Rac2 activation and chemotaxis. *J. Biol. Chem.* **283**, 26538–26547 (2008).

91. Niggli, V., Schlicht, D. & Affentranger, S. Specific roles of Rac1 and Rac2 in motile functions of HT1080 fibrosarcoma cells. *Biochem. Biophys. Res. Commun.* **386**, 688–692 (2009).

92. Bhavsar, P. J., Infante, E., Khwaja, A. & Ridley, A. J. Analysis of Rho GTPase expression in T-ALL identifies RhoU as a target for Notch involved in T-ALL cell migration. *Oncogene* **32**, 198–208

(2013).

93.   Cuesta-Mateos, C. *et al.* Analysis of migratory and prosurvival pathways induced by the homeostatic chemokines CCL19 and CCL21 in B-cell chronic lymphocytic leukemia. *Exp. Hematol.* **38**, 756-764 (2010).

94.   Burger, J. A. & Gribben, J. G. The microenvironment in chronic lymphocytic leukemia (CLL) and other B cell malignancies: Insight into disease biology and new targeted therapies. *Semin. Cancer Biol.* **24**, 71–81 (2014).

95.   Burger, J. A. Nurture versus nature: The microenvironment in chronic lymphocytic leukemia. *Hematology* **2011**, 96–103 (2011).

96.   Sorrentino, C., Cuneo, A. & Roti, G. Therapeutic targeting of notch signaling pathway in hematological malignancies. *Mediterr. J. Hematol. Infect. Dis.* **11**, e2019037 (2019).

97.   Wu, Y. *et al.* Therapeutic antibody targeting of individual Notch receptors. *Nature* **464**, 1052–1057 (2010).

98.   Sharma, A. *et al.* A novel monoclonal antibody against Notch1 targets leukemia-associated mutant Notch1 and depletes therapy resistant cancer stem cells in solid tumors. *Sci. Rep.* **5**, 1–18 (2015).

99.   Aste-Amézaga, M. *et al.* Characterization of notch1 antibodies that inhibit signaling of both normal and mutated notch1 receptors. *PLoS One* **5**, e9094 (2010).

100.   Agnusdei, V. *et al.* Therapeutic antibody targeting of Notch1 in T-acute lymphoblastic leukemia xenografts. *Leukemia* **28**, 278–288 (2014).

101.   Casulo, C. *et al.* Safety and preliminary efficacy results of a phase I first-in-human study of the novel Notch-1 targeting antibody Brontictuzumab (OMP-52M51) administered intravenously to patients with hematologic malignancies. *Blood* **128**, 5108 (2016).

102.   Smith, D. C. *et al.* A phase I dose escalation and expansion study of the anticancer stem cell agent demcizumab (anti-DLL4) in patients with previously treated solid tumors. *Clin. Cancer Res.* **20**, 6295–6303 (2014).

103.   Chiorean, E. G. *et al.* A phase I first-in-human study of enoticumab (REGN421), a fully human delta-like ligand 4 (DLL4) monoclonal antibody in patients with advanced solid tumors. *Clin. Cancer Res.* **21**, 2695–2703 (2015).

104.   Roti, G. *et al.* Complementary genomic screens identify SERCA as a therapeutic target in NOTCH1 mutated cancer. *Cancer Cell* **23**, 390–405 (2013).

105.   Roti, G. *et al.* Leukemia-specific delivery of mutant NOTCH1 targeted therapy. *J. Exp. Med.* **215**, 197–216 (2018).

106.   Baldoni, S. *et al.* Bepridil exhibits anti-leukemic activity associated with NOTCH1 pathway

inhibition in chronic lymphocytic leukemia. *Int. J. Cancer* **143**, 958–970 (2018).

107. Moellering, R. E. *et al.* Direct inhibition of the NOTCH transcription factor complex. *Nature* **462**, 182–188 (2009).

108. Weber, D. *et al.* Pharmacological activity of CB-103: An oral pan-NOTCH inhibitor with a novel mode of action. *Ann. Oncol.* **28**, 137 (2017).

109. Spriano, F. *et al.* Targeting lymphomas with the novel first-in-class pan-NOTCH transcription inhibitor CB-103. *Mol. Cancer Ther.* **17**, B061 (2018).

110. Perez Garcia, J. M. *et al.* First-in-human phase 1-2A study of CB-103, an oral Protein-Protein Interaction Inhibitor targeting pan-NOTCH signalling in advanced solid tumors and blood malignancies. *J. Clin. Oncol.* **36**, TPS2619 (2018).

111. Barten, D. M., Meredith, J. E., Zaczek, R., Houston, J. G. & Albright, C. F. γ-secretase inhibitors for Alzheimer's disease: Balancing efficacy and toxicity. *Drugs R. D.* **7**, 87–97 (2006).

112. McCaw, T. R. *et al.* Gamma secretase inhibitors in cancer: A current perspective on clinical performance. *Oncologist* **26**, e608–e621 (2021).

113. Secchiero, P. *et al.* The γ-secretase inhibitors enhance the anti-leukemic activity of ibrutinib in B-CLL cells. *Oncotarget* **8**, 59235–59245 (2017).

114. López-Guerra, M. *et al.* Specific NOTCH1 antibody targets DLL4-induced proliferation, migration, and angiogenesis in NOTCH1-mutated CLL cells. *Oncogene* **39**, 1185–1197 (2020).

115. Deangelo, D. J. *et al.* A phase I clinical trial of the notch inhibitor MK-0752 in patients with T-cell acute lymphoblastic leukemia/lymphoma (T-ALL) and other leukemias. *J. Clin. Oncol.* **24**, 6585–6585 (2006).

116. Milano, J. *et al.* Modulation of Notch processing by γ-secretase inhibitors causes intestinal goblet cell metaplasia and induction of genes known to specify gut secretory lineage differentiation. *Toxicol. Sci.* **82**, 341–358 (2004).

117. Wu, Y. *et al.* Therapeutic antibody targeting of individual Notch receptors. *Nature* **464**, 1052–1057 (2010).

118. Papayannidis, C. *et al.* A Phase 1 study of the novel gamma-secretase inhibitor PF-03084014 in patients with T-cell acute lymphoblastic leukemia and T-cell lymphoblastic lymphoma. *Blood Cancer J.* **5**, e350 (2015).

119. Paganin, M. & Ferrando, A. Molecular pathogenesis and targeted therapies for NOTCH1-induced T-cell acute lymphoblastic leukemia. *Blood Rev.* **25**, 83–90 (2011).

120. Knoechel, B. *et al.* Complete hematologic response of early T-cell progenitor acute lymphoblastic leukemia to the γ-secretase inhibitor BMS-906024: genetic and epigenetic findings in an outlier case. *Mol. Case Stud.* **1**, a000539 (2015).

121.	Zweidler-McKay, P. A. *et al.* The safety and activity of BMS-906024, a gamma secretase inhibitor (GSI) with anti-Notch activity, in patients with relapsed T-cell acute lymphoblastic leukemia (T-ALL): Initial results of a phase 1 trial. *Blood* **124**, 968–968 (2014).

122.	Cullion, K. *et al.* Targeting the Notch1 and mTOR pathways in a mouse T-ALL model. *Blood* **113**, 6172–6181 (2009).

123.	Real, P. J. *et al.* γ-secretase inhibitors reverse glucocorticoid resistance in T cell acute lymphoblastic leukemia. *Nat. Med.* **15**, 50–58 (2009).

124.	Fletcher, D. A. & Mullins, R. D. Cell mechanics and the cytoskeleton. *Nature* **463**, 485–492 (2010).

125.	Vicente-Manzanares, M. & Sánchez-Madrid, F. Role of the cytoskeleton during leukocyte responses. *Nat. Rev. Immunol.* **4**, 110–122 (2004).

126.	Lanzi, G. *et al.* A novel primary human immunodeficiency due to deficiency in the WASP-interacting protein WIP. *J. Exp. Med.* **209**, 29–34 (2012).

127.	Thrasher, A. J. New insights into the biology of Wiskott-Aldrich syndrome (WAS). *Hematol. Am. Soc. Hematol. Educ. Progr.* **2009**, 132–138 (2009).

128.	Pfajfer, L. *et al.* WIP deficiency severely affects human lymphocyte architecture during migration and synapse assembly. *Blood* **130**, 1949–1953 (2017).

129.	Sullivan, K. E., Mullen, C. A., Blaese, R. M. & Winkelstein, J. A. A multiinstitutional survey of the Wiskott-Aldrich syndrome. *J. Pediatr.* **125**, 876–885 (1994).

130.	Stewart, D. M., Tian, L. & Nelson, D. L. Mutations that cause the Wiskott-Aldrich syndrome impair the interaction of Wiskott-Aldrich syndrome protein (WASP) with WASP interacting protein. *J. Immunol.* **162**, 5019–24 (1999).

131.	Chhabra, E. S. & Higgs, H. N. The many faces of actin: Matching assembly factors with cellular structures. *Nat. Cell Biol.* **9**, 1110–1121 (2007).

132.	Chesarone, M. A., Dupage, A. G. & Goode, B. L. Unleashing formins to remodel the actin and microtubule cytoskeletons. *Nat. Rev. Mol. Cell Biol.* **11**, 62–74 (2010).

133.	Pruyne, D. *et al.* Role of formins in actin assembly: Nucleation and barbed-end association. *Science* **297**, 612–615 (2002).

134.	Paul, A. S. & Pollard, T. D. Energetic requirements for processive elongation of actin filaments by FH1FH2-formins. *J. Biol. Chem.* **284**, 12533–12540 (2009).

135.	Mizuno, H. *et al.* Rotational movement of the formin mDia1 along the double helical strand of an actin filament. *Science* **331**, 80–83 (2011).

136.	Breitsprecher, D. *et al.* Rocket launcher mechanism of collaborative actin assembly defined by single-molecule imaging. *Science* **336**, 1164–1168 (2012).

137. Michelot, A. *et al.* The formin homology 1 domain modulates the actin nucleation and bundling activity of arabidopsis FORMIN1. *Plant Cell* **17**, 2296–2313 (2005).

138. Harris, E. S., Rouiller, I., Hanein, D. & Higgs, H. N. Mechanistic differences in actin bundling activity of two mammalian formins, FRL1 and mDia2. *J. Biol. Chem.* **281**, 14383–14392 (2006).

139. Harris, E. S., Li, F. & Higgs, H. N. The mouse gormin, FRLα, slows actin filament Bbrbed end elongation, competes with capping protein, accelerates polymerization from monomers, and severs filaments. *J. Biol. Chem.* **279**, 20076–20087 (2004).

140. Chhabra, E. S. & Higgs, H. N. INF2 is a WASP homology 2 motif-containing formin that severs actin filaments and accelerates both polymerization and depolymerization. *J. Biol. Chem.* **281**, 26754–26767 (2006).

141. Campellone, K. G. & Welch, M. D. A nucleator arms race: Cellular control of actin assembly. *Nat. Rev. Mol. Cell Biol.* **11**, 237–251 (2010).

142. Mullins, R. D., Heuser, J. A. & Pollard, T. D. The interaction of Arp2/3 complex with actin: Nucleation, high affinity pointed end capping, and formation of branching networks of filaments. *Proc. Natl. Acad. Sci. U. S. A.* **95**, 6181–6186 (1998).

143. Theriot, J. A. & Mitchison, T. J. Actin microfilament dynamics in locomoting cells. *Nature* **352**, 126–131 (1991).

144. Mallavarapu, A. & Mitchison, T. Regulated actin cytoskeleton assembly at filopodium tips controls their extension and retraction. *J. Cell Biol.* **146**, 1097–1106 (1999).

145. Wang, Y. L. Exchange of actin subunits at the leading edge of living fibroblasts: Possible role of treadmilling. *J. Cell Biol.* **101**, 597–602 (1985).

146. Rzadzinska, A. K., Schneider, M. E., Davies, C., Riordan, G. P. & Kachar, B. An actin molecular treadmill and myosins maintain stereocilia functional architecture and self-renewal. *J. Cell Biol.* **164**, 887–897 (2004).

147. Tolar, P. Cytoskeletal control of B cell responses to antigens. *Nat. Rev. Immunol.* **17**, 621–634 (2017).

148. Morone, N. *et al.* Three-dimensional reconstruction of the membrane skeleton at the plasma membrane interface by electron tomography. *J. Cell Biol.* **174**, 851–862 (2006).

149. Fritzsche, M., Lewalle, A., Duke, T., Kruse, K. & Charras, G. Analysis of turnover dynamics of the submembranous actin cortex. *Mol. Biol. Cell* **24**, 757–767 (2013).

150. Zheng, J. Q., Wan, J. J. & Poo, M. M. Essential role of filopodia in chemotropic turning of nerve growth cone induced by a glutamate gradient. *J. Neurosci.* **16**, 1140–1149 (1996).

151. Galbraith, C. G., Yamada, K. M. & Galbraith, J. A. Polymerizing actin fibers position integrins primed to probe for adhesion sites. *Science* **315**, 992–995 (2007).

152. Singer, I. I. *et al.* CCR5, CXCR4, and CD4 are clustered and closely apposed on microvilli of human macrophages and T cells. *J. Virol.* **75**, 3779–3790 (2001).

153. Kaksonen, M., Toret, C. P. & Drubin, D. G. Harnessing actin dynamics for clathrin-mediated endocytosis. *Nat. Rev. Mol. Cell Biol.* **7**, 404–414 (2006).

154. Kaksonen, M., Toret, C. P. & Drubin, D. G. A modular design for the clathrin- and actin-mediated endocytosis machinery. *Cell* **123**, 305–320 (2005).

155. Billington, N., Wang, A., Mao, J., Adelstein, R. S. & Sellers, J. R. Characterization of three full-length human nonmuscle myosin II paralogs. *J. Biol. Chem.* **288**, 33398–33410 (2013).

156. Vicente-Manzanares, M., Ma, X., Adelstein, R. S. & Horwitz, A. R. Non-muscle myosin II takes centre stage in cell adhesion and migration. *Nat. Rev. Mol. Cell Biol.* **10**, 778–790 (2009).

157. Murrell, M., Oakes, P. W., Lenz, M. & Gardel, M. L. Forcing cells into shape: The mechanics of actomyosin contractility. *Nat. Rev. Mol. Cell Biol.* **16**, 486–498 (2015).

158. Jarvis, S. C. *et al.* Human lymphocyte motility: normal characteristics and anomalous behavior of chronic lymphocytic leukemia cells. *Blood* **48**, 717–729 (1976).

159. Cohen, H. J. Human lymphocyte surface immunoglobulin capping. Normal characteristics and anomalous behavior of chronic lymphocytic leukemic lymphocytes. *J. Clin. Invest.* **55**, 84–93 (1975).

160. Caligaris-Cappio, F. *et al.* Cytoskeleton organization is aberrantly rearranged in the cells of B chronic lymphocytic leukemia and hairy cell leukemia. *Blood* **67**, 233–239 (1986).

161. Frezzato, F. *et al.* Leukaemic cells from chronic lymphocytic leukaemia patients undergo apoptosis following microtubule depolymerization and Lyn inhibition by nocodazole. *Br. J. Haematol.* **165**, 659–672 (2014).

162. Vilpo, J. A., Koski, T. & Vilpo, L. M. Selective toxicity of vincristine against chronic lymphocytic leukemia cells in vitro. *Eur. J. Haematol.* **65**, 370–378 (2000).

163. Johansson, P. *et al.* Percentage of smudge cells determined on routine blood smears is a novel prognostic factor in chronic lymphocytic leukemia. *Leuk. Res.* **34**, 892–898 (2010).

164. Brown, M. J., Hallam, J. A., Colucci-Guyon, E. & Shaw, S. Rigidity of circulating lymphocytes is primarily conferred by vimentin intermediate filaments. *J. Immunol.* **166**, 6640–6646 (2001).

165. Hutchinson, C. V *et al.* Lymphocytes from chronic lymphocytic leukaemia undergo ABL1-linked amoeboid motility and homotypic interaction as an early adaptive change to ex vivo culture. *Exp. Hematol. Oncol.* **3**, 7 (2014).

166. Schulz, A. *et al.* Inflammatory cytokines and signaling pathways are associated with survival of primary chronic lymphocytic leukemia cells in vitro: A dominant role of CCL2. *Haematologica* **96**, 408–416 (2011).

167. Burger, J. A. *et al.* Blood-derived nurse-like cells protect chronic lymphocytic leukemia B cells from spontaneous apoptosis through stromal cell-derived factor-1. *Blood* **96**, 2655–2663 (2000).

168. Herishanu, Y. *et al.* The lymph node microenvironment promotes B-cell receptor signaling, NF-κB activation, and tumor proliferation in chronic lymphocytic leukemia. *Blood* **117**, 563–574 (2011).

169. Sugiyama, T., Kohara, H., Noda, M. & Nagasawa, T. Maintenance of the hematopoietic stem cell pool by CXCL12-CXCR4 chemokine signaling in bone marrow stromal cell niches. *Immunity* **25**, 977–988 (2006).

170. Kurtova, A. V *et al.* Diverse marrow stromal cells protect CLL cells from spontaneous and drug-induced apoptosis: Development of a reliable and reproducible system to assess stromal cell adhesion-mediated drug resistance. *Blood* **114**, 4441–4450 (2009).

171. Panayiotidis, P., Jones, D., Ganeshaguru, K., Foroni, L. & Hoffbrand, A. V. Human bone marrow stromal cells prevent apoptosis and support the survival of chronic lymphocytic leukaemia cells in vitro. *Br. J. Haematol.* **92**, 97–103 (1996).

172. Burger, J. A., Burger, M. & Kipps, T. J. Chronic lymphocytic leukemia B cells express functional CXCR4 chemokine receptors that mediate spontaneous migration beneath bone marrow stromal cells. *Blood* **94**, 3658–3667 (1999).

173. Miyake, K., Hasunuma, Y., Yagita, H. & Kimoto, M. Requirement for VLA-4 and VLA-5 integrins in lymphoma cells binding to and migration beneath stromal cells in culture. *J. Cell Biol.* **119**, 653–661 (1992).

174. Ding, W. *et al.* Bi-directional activation between mesenchymal stem cells and CLL B-cells: Implication for CLL disease progression. *Br. J. Haematol.* **147**, 471–483 (2009).

175. Ding, W. *et al.* Platelet-derived growth factor (PDGF)-PDGF receptor interaction activates bone marrow-derived mesenchymal stromal cells derived from chronic lymphocytic leukemia: Implications for an angiogenic switch. *Blood* **116**, 2984–2993 (2010).

176. Goel, H. L. & Mercurio, A. M. VEGF targets the tumour cell. *Nat. Rev. Cancer* **13**, 871–882 (2013).

177. Lutzny, G. *et al.* Protein kinase C-β-dependent activation of NF-κB in stromal cells is indispensable for the survival of chronic lymphocytic leukemia B cells in vivo. *Cancer Cell* **23**, 77–92 (2013).

178. Bürkle, A. *et al.* Overexpression of the CXCR5 chemokine receptor, and its ligand, CXCL13 in B-cell chronic lymphocytic leukemia. *Blood* **110**, 3316–3325 (2007).

179. Nishio, M. *et al.* Nurselike cells express BAFF and APRIL, which can promote survival of chronic

lymphocytic leukemia cells via a paracrine pathway distinct from that of SDF-1α. *Blood* **106**, 1012–1020 (2005).

180. Deaglio, S. *et al.* CD38 and CD100 lead a network of surface receptors relaying positive signals for B-CLL growth and survival. *Blood* **105**, 3042–3050 (2005).

181. Tsukada, N. *et al.* Distinctive features of 'nurselike' cells that differentiate in the context of chronic lymphocytic leukemia. *Blood* **99**, 1030–1037 (2013).

182. Reinart, N. *et al.* Delayed development of chronic lymphocytic leukemia in the absence of macrophage migration inhibitory factor. *Blood* **121**, 812–822 (2015).

183. Troeger, A. *et al.* RhoH is critical for cell-microenvironment interactions in chronic lymphocytic leukemia in mice and humans. *Blood* **119**, 4708–4718 (2012).

184. Herishanu, Y. *et al.* The lymph node microenvironment promotes B-cell receptor signaling, NF-κB activation, and tumor proliferation in chronic lymphocytic leukemia. *Blood* **117**, 563–574 (2011).

185. Burger, J. A. *et al.* High-level expression of the T-cell chemokines CCL3 and CCL4 by chronic lymphocytic leukemia B cells in nurselike cell cocultures and after BCR stimulation. *Blood* **113**, 3050–3058 (2009).

186. Görgün, G., Holderried, T. A. W., Zahrieh, D., Neuberg, D. & Gribben, J. G. Chronic lymphocytic leukemia cells induce changes in gene expression of CD4 and CD8 T cells. *J. Clin. Invest.* **115**, 1797–1805 (2005).

187. Ramsay, A. G. *et al.* Chronic lymphocytic leukemia T cells show impaired immunological synapse formation. *J. Clin. Invest.* **118**, 2427–2437 (2008).

188. Riches, J. C. *et al.* T cells from CLL patients exhibit features of T-cell exhaustion but retain capacity for cytokine production. *Blood* **121**, 1612–1621 (2013).

189. Pascutti, M. F. *et al.* IL-21 and CD40L signals from autologous T cells can induce antigen-independent proliferation of CLL cells. *Blood* **122**, 3010–3019 (2013).

190. Buschle, M. Interferon gamma inhibits apoptotic cell death in B cell chronic lymphocytic leukemia. *J. Exp. Med.* **177**, 213–218 (1993).

191. Kitada, S., Zapata, J. M., Andreff, M. & Reed, J. C. Bryostatin and CD40-ligand enhance apoptosis resistance and induce expression of cell survival genes in B-cell chronic lymphocytic leukaemia. *Br. J. Haematol.* **106**, 995–1004 (1999).

192. Dancescu, M. Interleukin 4 protects chronic lymphocytic leukemic B cells from death by apoptosis and upregulates Bcl-2 expression. *J. Exp. Med.* **176**, 1319–1326 (1992).

193. Lebien, T. W. & Tedder, T. F. B lymphocytes: How they develop and function. *Blood* **112**, 1570–1580 (2008).

194. Burger, J. A. & Wiestner, A. Targeting B cell receptor signalling in cancer: Preclinical and clinical advances. *Nat. Rev. Cancer* **18**, 148–167 (2018).

195. Venkitaraman, A. R., Williams, G. T., Dariavach, P. & Neuberger, M. S. The B-cell antigen receptor of the five immunoglobulin classes. *Nature* **352**, 777–781 (1991).

196. Hombach, J., Tsubata, T., Leclercq, L., Stappert, H. & Reth, M. Molecular components of the B-cell antigen receptor complex of the IgM class. *Nature* **343**, 760–762 (1990).

197. Dal Porto, J. M. *et al.* B cell antigen receptor signaling 101. *Mol. Immunol.* **41**, 599–613 (2004).

198. Reth, M. Antigen receptor tail clue. *Nature* **338**, 383–384 (1989).

199. Cambier, J. C. New nomenclature for the Reth motif (or ARH1/TAM/ARAM/YXXL). *Immunol. Today* **16**, 110 (1995).

200. Rolli, V. *et al.* Amplification of B cell antigen receptor signaling by a Syk/ITAM positive feedback loop. *Mol. Cell* **10**, 1057–1069 (2002).

201. Yamamoto, T., Yamanashi, Y. & Toyoshima, K. Association of Src-Family Kinase Lyn with B-Cell Antigen Receptor. *Immunol. Rev.* **132**, 187–206 (1993).

202. Kurosaki, T. & Hikida, M. Tyrosine kinases and their substrates in B lymphocytes. *Immunol. Rev.* **228**, 132–148 (2009).

203. Woyach, J. A., Johnson, A. J. & Byrd, J. C. The B-cell receptor signaling pathway as a therapeutic target in CLL. *Blood* **120**, 1175–1184 (2012).

204. Baba, Y. *et al.* BLNK mediates Syk-dependent Btk activation. *Proc. Natl. Acad. Sci. U. S. A.* **98**, 2582–2586 (2001).

205. Rawlings, D. J. *et al.* Activation of BTK by a phosphorylation mechanism initiated by SRC family kinases. *Science* **271**, 822–825 (1996).

206. Liu, W., Tolar, P., Song, W. & Kim, T. J. Editorial: BCR signaling and B cell activation. *Front. Immunol.* **11**, 45 (2020).

207. Saci, A. & Carpenter, C. L. RhoA GTPase regulates B cell receptor signaling. *Mol. Cell* **17**, 205–214 (2005).

208. Pan, Z. *et al.* Discovery of selective irreversible inhibitors for Bruton's tyrosine kinase. *ChemMedChem* **2**, 58–61 (2007).

209. Advani, R. H. *et al.* Bruton tyrosine kinase inhibitor ibrutinib (PCI-32765) has significant activity in patients with relapsed/refractory B-cell malignancies. *J. Clin. Oncol.* **31**, 88–94 (2013).

210. O'Brien, S. *et al.* Single-agent ibrutinib in treatment-naïve and relapsed/refractory chronic lymphocytic leukemia: a 5-year experience. *Blood* **131**, 1910–1919 (2018).

211. Honigberg, L. A. *et al.* The Bruton tyrosine kinase inhibitor PCI-32765 blocks B-cell activation and is efficacious in models of autoimmune disease and B-cell malignancy. *Proc. Natl. Acad.*

Sci. U. S. A. **107**, 13075–13080 (2010).

212. Byrd, J. C. *et al.* Targeting BTK with ibrutinib in relapsed chronic lymphocytic leukemia. *N. Engl. J. Med.* **369**, 32–42 (2013).

213. Burger, J. A. *et al.* Long-term efficacy and safety of first-line ibrutinib treatment for patients with CLL/SLL: 5 years of follow-up from the phase 3 RESONATE-2 study. *Leukemia* **34**, 787–798 (2020).

214. McMullen, J. R. *et al.* Ibrutinib increases the risk of atrial fibrillation, potentially through inhibition of cardiac PI3K-Akt signaling. *Blood* **124**, 3829–3830 (2014).

215. Gao, W. *et al.* Selective antitumor activity of ibrutinib in EGFR-mutant non-small cell lung cancer cells. *J. Natl. Cancer Inst.* **106**, 204 (2014).

216. Harandi, A., Zaidi, A. S., Stocker, A. M. & Laber, D. A. Clinical efficacy and toxicity of anti-EGFR therapy in common cancers. *J. Oncol.* **567486**, 14 (2009).

217. Walter, H. S. *et al.* A phase 1 clinical trial of the selective BTK inhibitor ONO/GS-4059 in relapsed and refractory mature B-cell malignancies. *Blood* **127**, 411–419 (2016).

218. Byrd, J. C. *et al.* Acalabrutinib (ACP-196) in relapsed chronic lymphocytic leukemia. *N. Engl. J. Med.* **374**, 323–332 (2016).

219. Dolgin, E. Cancer's true breakthroughs. *Nat. Med.* **19**, 660–663 (2013).

220. Hillmen, P. *et al.* Alemtuzumab compared with chlorambucil as first-line therapy for chronic lymphocytic leukemia. *J. Clin. Oncol.* **25**, 5616–5623 (2007).

221. Pettitt, A. R. *et al.* Alemtuzumab in combination with methylprednisolone is a highly effective induction regimen for patients with chronic lymphocytic leukemia and deletion of TP53: Final results of the National Cancer Research Institute CLL206 Trial. *J. Clin. Oncol.* **30**, 1647–1655 (2012).

222. Byrd, J. C. *et al.* Up to 7 years of follow-up of single-agent ibrutinib in the phase 1b/2 PCYC-1102 trial of first line and relapsed/refractory patients with chronic lymphocytic leukemia/small lymphocytic lymphoma. *Blood* **132**, 3133 (2018).

223. Byrd, J. C. *et al.* Ibrutinib versus ofatumumab in previously treated chronic lymphoid leukemia. *N. Engl. J. Med.* **371**, 213–223 (2014).

224. Tedeschi, A. *et al.* Five-year follow-up of first-line ibrutinib for treatment of patients with chronic lymphocytic leukemia/small lymphocytic lymphoma. *Hematol. Oncol.* **37**, 103–104 (2019).

225. Shanafelt, T. D. *et al.* Ibrutinib–rituximab or chemoimmunotherapy for chronic lymphocytic leukemia. *N. Engl. J. Med.* **381**, 432–443 (2019).

226. Moreno, C. *et al.* Ibrutinib plus obinutuzumab versus chlorambucil plus obinutuzumab in first-

line treatment of chronic lymphocytic leukaemia (iLLUMINATE): a multicentre, randomised, open-label, phase 3 trial. *Lancet Oncol.* **20**, 43–56 (2019).

227. Woyach, J. A. *et al.* Ibrutinib regimens versus chemoimmunotherapy in older patients with untreated CLL. *N. Engl. J. Med.* **379**, 2517–2528 (2018).

228. Chanan-Khan, A. *et al.* Ibrutinib combined with bendamustine and rituximab compared with placebo, bendamustine, and rituximab for previously treated chronic lymphocytic leukaemia or small lymphocytic lymphoma (HELIOS): A randomised, double-blind, phase 3 study. *Lancet Oncol.* **17**, 200–211 (2016).

229. Wang, M. L. *et al.* Targeting BTK with ibrutinib in relapsed or refractory mantle-cell lymphoma. *N. Engl. J. Med.* **369**, 507–516 (2013).

230. Friedberg, J. W. *et al.* Inhibition of Syk with fostamatinib disodium has significant clinical activity in non-Hodgkin lymphoma and chronic lymphocytic leukemia. *Blood* **115**, 2578–2585 (2010).

231. Furman, R. R. *et al.* CAL-101, An isoform-selective inhibitor of phosphatidylinositol 3-kinase P110δ, demonstrates clinical activity and pharmacodynamic effects in patients with relapsed or refractory chronic lymphocytic leukemia. *Blood* **116**, 55 (2010).

232. Cheng, S. *et al.* Functional characterization of BTK C481S mutation that confers ibrutinib resistance: Exploration of alternative kinase inhibitors. *Leukemia* **29**, 895–900 (2015).

233. Herman, S. E. M. *et al.* Ibrutinib inhibits BCR and NF-κB signaling and reduces tumor proliferation in tissue-resident cells of patients with CLL. *Blood* **123**, 3286–3295 (2014).

234. Cheng, S. *et al.* BTK inhibition targets in vivo CLL proliferation through its effects on B-cell receptor signaling activity. *Leukemia* **28**, 649–657 (2014).

235. de Rooij, M. F. M. *et al.* The clinically active BTK inhibitor PCI-32765 targets B-cell receptor- and chemokine-controlled adhesion and migration in chronic lymphocytic leukemia. *Blood* **119**, 2590–2594 (2012).

236. Ponader, S. *et al.* The Bruton tyrosine kinase inhibitor PCI-32765 thwarts chronic lymphocytic leukemia cell survival and tissue homing in vitro and in vivo. *Blood* **119**, 1182–1189 (2012).

237. Herman, S. E. M. *et al.* Treatment with ibrutinib inhibits BTK- and VLA-4-dependent adhesion of chronic lymphocytic leukemia cells in vivo. *Clin. Cancer Res.* **21**, 4642–4651 (2015).

238. Niemann, C. U. *et al.* Disruption of in vivo chronic lymphocytic leukemia tumor-microenvironment interactions by ibrutinib - Findings from an investigator-initiated phase II study. *Clin. Cancer Res.* **22**, 1572–1582 (2016).

239. Dubovsky, J. A. *et al.* Ibrutinib is an irreversible molecular inhibitor of ITK driving a Th1-selective pressure in T lymphocytes. *Blood* **122**, 2539–2549 (2013).

240. Berg, L. J., Finkelstein, L. D., Lucas, J. A. & Schwartzberg, P. L. Tec family kinases in T lymphocyte development and function. *Annu. Rev. Immunol.* **23**, 549–600 (2005).

241. Ahn, I. E. *et al.* Clonal evolution leading to ibrutinib resistance in chronic lymphocytic leukemia. *Blood* **129**, 1469–1479 (2017).

242. Woyach, J. A. How I manage ibrutinib-refractory chronic lymphocytic leukemia. *Blood* **129**, 1270–1274 (2017).

243. Maddocks, K. J. *et al.* Etiology of ibrutinib therapy discontinuation and outcomes in patients with chronic lymphocytic leukemia. *JAMA Oncol.* **1**, 80–87 (2015).

244. Jain, P. *et al.* Outcomes of patients with chronic lymphocytic leukemia after discontinuing ibrutinib. *Blood* **125**, 2062–2067 (2015).

245. Jones, J. A. *et al.* Venetoclax for chronic lymphocytic leukaemia progressing after ibrutinib: an interim analysis of a multicentre, open-label, phase 2 trial. *Lancet Oncol.* **19**, 65–75 (2018).

246. Sharman, J. P. *et al.* Updated results on the clinical activity of entospletinib (GS-9973), a selective Syk inhibitor, in patients with CLL previously treated with an inhibitor of the B-Cell receptor signaling pathway. *Blood* **128**, 3225 (2016).

247. Mato, A. R. *et al.* Outcomes of CLL patients treated with sequential kinase inhibitor therapy: A real world experience. *Blood* **128**, 2199–2205 (2016).

248. Porcu, P. *et al.* Clinical activity of duvelisib (IPI-145), a phosphoinositide-3-kinase-δ,γ inhibitor, in patients previously treated with ibrutinib. *Blood* **124**, 3335 (2014).

249. Quinquenel, A. *et al.* Prevalence of BTK and PLCG2 mutations in a real-life CLL cohort still on ibrutinib after 3 years: A FILO group study. *Blood* **134**, 641–644 (2019).

250. Woyach, J. A. *et al.* Resistance mechanisms for the Bruton's tyrosine kinase inhibitor ibrutinib. *N. Engl. J. Med.* **370**, 2286–2294 (2014).

251. Furman, R. R. *et al.* Ibrutinib resistance in chronic lymphocytic leukemia. *N. Engl. J. Med.* **370**, 2352–2354 (2014).

252. Burger, J. A. *et al.* Clonal evolution in patients with chronic lymphocytic leukaemia developing resistance to BTK inhibition. *Nat. Commun.* **7**, 11589 (2016).

253. Gángó, A. *et al.* Dissection of subclonal evolution by temporal mutation profiling in chronic lymphocytic leukemia patients treated with ibrutinib. *Int. J. Cancer* **146**, 85–93 (2020).

254. Kanagal-Shamanna, R. *et al.* Targeted multigene deep sequencing of Bruton tyrosine kinase inhibitor–resistant chronic lymphocytic leukemia with disease progression and Richter transformation. *Cancer* **125**, 559–574 (2019).

255. Cosson, A. *et al.* Gain in the short arm of chromosome 2 (2p+) induces gene overexpression and drug resistance in chronic lymphocytic leukemia: Analysis of the central role of XPO1.

Leukemia **31**, 1625–1629 (2017).

256. Spina, V. *et al.* Mechanisms of adaptation to ibrutinib in high risk chronic lymphocytic leukemia. *Blood* **132**, 585 (2018).

257. Parri, M. & Chiarugi, P. Rac and Rho GTPases in cancer cell motility control. *Cell Commun. Signal.* **8**, 23 (2010).

258. Watanabe, N., Kato, T., Fujita, A., Ishizaki, T. & Narumiya, S. Cooperation between mDia1 and ROCK in Rho-induced actin reorganization. *Nat. Cell Biol.* **1**, 136–143 (1999).

259. Fukata, Y., Kaibuchi, K., Amano, M. & Kaibuchi, K. Rho–Rho-kinase pathway in smooth muscle contraction and cytoskeletal reorganization of non-muscle cells. *Trends Pharmacol. Sci.* **22**, 32–39 (2001).

260. Ishizaki, T. *et al.* Coordination of microtubules and the actin cytoskeleton by the Rho effector mDia1. *Nat. Cell Biol.* **3**, 8–14 (2001).

261. Amano, M., Nakayama, M. & Kaibuchi, K. Rho-kinase/ROCK: A key regulator of the cytoskeleton and cell polarity. *Cytoskeleton* **67**, 545–554 (2010).

262. Takamura, M. *et al.* Inhibition of intrahepatic metastasis of human hepatocellular carcinoma by Rho-associated protein kinase inhibitor Y-27632. *Hepatology* **33**, 577–581 (2001).

263. Genoa, T. *et al.* Cell motility mediated by Rho and Rho-associated protein kinase plays a critical role in intrahepatic metastasis of human hepatocellular carcinoma. *Hepatology* **30**, 1027–1036 (1999).

264. Somlyo, A. V. *et al.* Rho-kinase inhibitor retards migration and in vivo dissemination of human prostate cancer cells. *Biochem. Biophys. Res. Commun.* **269**, 652–659 (2000).

265. Bourguignon, L. Y. W., Zhu, H., Shao, L., Zhu, D. & Chen, Y. W. Rho-kinase (ROK) promotes CD44v(3,8-10)-ankyrin interaction and tumor cell migration in metastatic breast cancer cells. *Cell Motil. Cytoskeleton* **43**, 269–287 (1999).

266. Wicki, A. & Niggli, V. The RHO/RHO-kinase and the phosphatidylinositol 3-kinase pathways are essential for spontaneous locomotion of Walker 256 carcinosarcoma cells. *Int. J. Cancer* **91**, 763–771 (2001).

267. Worthylake, R. A., Lemoine, S., Watson, J. M. & Burridge, K. RhoA is required for monocyte tail retraction during transendothelial migration. *J. Cell Biol.* **154**, 147–160 (2001).

268. Hauert, A. B., Martinelli, S., Marone, C. & Niggli, V. Differentiated HL-60 cells are a valid model system for the analysis of human neutrophil migration and chemotaxis. *Int. J. Biochem. Cell Biol.* **34**, 838–854 (2002).

269. Alblas, J., Ulfman, L., Hordijk, P. & Koenderman, L. Activation of RhoA and ROCK are essential for detachment of migrating leukocytes. *Mol. Biol. Cell* **12**, 2137–2145 (2001).

270. Ai, S. *et al.* Rho-Rho kinase is involved in smooth muscle cell migration through myosin light chain phosphorylation-dependent and independent pathways. *Atherosclerosis* **155**, 321–327 (2001).

271. Rowley, J. D. A new consistent chromosomal abnormality in chronic myelogenous leukaemia identified by quinacrine fluorescence and Giemsa staining. *Nature* **243**, 290–293 (1973).

272. Soverini, S., Mancini, M., Bavaro, L., Cavo, M. & Martinelli, G. Chronic myeloid leukemia: The paradigm of targeting oncogenic tyrosine kinase signaling and counteracting resistance for successful cancer therapy. *Mol. Cancer* **17**, 1–15 (2018).

273. Bradley, W. D. & Koleske, A. J. Regulation of cell migration and morphogenesis by Abl-family kinases: Emerging mechanisms and physiological contexts. *J. Cell Sci.* **122**, 3441–3454 (2009).

274. Boyle, S. N., Michaud, G. A., Schweitzer, B., Predki, P. F. & Koleske, A. J. A critical role for cortactin phosphorylation by Abl-family kinases in PDGF-induced dorsal-wave formation. *Curr. Biol.* **17**, 445–451 (2007).

275. Plattner, R., Kadlec, L., Demali, K. A., Kazlauskas, A. & Pendergast, A. M. c-Abl is activated by growth factors and Src family kinases and has a role in the cellular response to PDGF. *Genes Dev.* **13**, 2400–2411 (1999).

276. Woodring, P. J. *et al.* c-Abl phosphorylates Dok1 to promote filopodia during cell spreading. *J. Cell Biol.* **165**, 493–503 (2004).

277. Miller, A. L., Wang, Y., Mooseker, M. S. & Koleske, A. J. The Abl-related gene (Arg) requires its F-actin-microtubule cross-linking activity to regulate lamellipodial dynamics during fibroblast adhesion. *J. Cell Biol.* **165**, 407–419 (2004).

278. Lapetina, S., Mader, C. C., Machida, K., Mayer, B. J. & Koleske, A. J. Arg interacts with cortactin to promote adhesion-dependent cell edge protrusion. *J. Cell Biol.* **185**, 503–519 (2009).

279. Bradley, W. D., Hernández, S. E., Settleman, J. & Koleske, A. J. Integrin signaling through Arg activates p190RhoGAP by promoting its binding to p120RasGAP and recruitment to the membrane. *Mol. Biol. Cell* **17**, 4827–4836 (2006).

280. Lin, K. *et al.* c-Abl expression in chronic lymphocytic leukemia cells: Clinical and therapeutic implications. *Cancer Res.* **66**, 7801–7809 (2006).

281. Tybulewicz, V. L. J., Crawford, C. E., Jackson, P. K., Bronson, R. T. & Mulligan, R. C. Neonatal lethality and lymphopenia in mice with a homozygous disruption of the c-abl proto-oncogene. *Cell* **65**, 1153–1163 (1991).

282. Schwartzberg, P. L. *et al.* Mice homozygous for the ablm1 mutation show poor viability and depletion of selected B and T cell populations. *Cell* **65**, 1165–1175 (1991).

283. Huang, Y. *et al.* The c-Abl tyrosine kinase regulates actin remodeling at the immune synapse.

Blood **112**, 111–119 (2008).

284. Aloyz, R. *et al.* Imatinib sensitizes CLL lymphocytes to chlorambucil. *Leukemia* **18**, 409–414 (2004).

285. Hallek, M. *et al.* iwCLL guidelines for diagnosis, indications for treatment, response assessment, and supportive management of CLL. *Blood* **131**, 2745–2760 (2018).

286. Thompson, H. P. Exploring the sensitivity of mantle cell lymphoma to inhibitors of bruton's tyrosine kinase. (University of Plymouth, 2018).

287. Rao, S. S. *et al.* Inhibition of NOTCH signaling by gamma secretase inhibitor engages the RB pathway and elicits cell cycle exit in T-cell acute lymphoblastic leukemia cells. *Cancer Res.* **69**, 3060–3068 (2009).

288. Jares, P., Colomer, D. & Campo, E. Genetic and molecular pathogenesis of mantle cell lymphoma: Perspectives for new targeted therapeutics. *Nat. Rev. Cancer* **7**, 750–762 (2007).

289. Raffeld, M. & Jaffe, E. S. Bcl-1, t(11;14), and mantle cell-derived lymphomas. *Blood* **78**, 259–263 (1991).

290. Frattini, A. *et al.* High variability of genomic instability and gene expression profiling in different HeLa clones. *Sci. Rep.* **5**, 1–9 (2015).

291. Nikitina, V. *et al.* Clonal chromosomal and genomic instability during human multipotent mesenchymal stromal cells long-term culture. *PLoS One* **13**, e0192445 (2018).

292. Liu, P. *et al.* Passage number is a major contributor to genomic structural variations in mouse iPSCs. *Stem Cells* **32**, 2657–2667 (2014).

293. Pankov, R. & Yamada, K. M. Fibronectin at a glance. *J. Cell Sci.* **115**, 3861–3863 (2002).

294. Debeb, B. G. *et al.* Pre-clinical studies of Notch signaling inhibitor RO4929097 in inflammatory breast cancer cells. *Breast Cancer Res. Treat.* **134**, 495–510 (2012).

295. Samon, J. B. *et al.* Preclinical analysis of the γ-secretase inhibitor PF-03084014 in combination with glucocorticoids in T-cell acute lymphoblastic leukemia. *Mol. Cancer Ther.* **11**, 1565–1575 (2012).

296. Wei, P. *et al.* Evaluation of selective γ-secretase inhibitor PF-03084014 for its antitumor efficacy and gastrointestinal safety to guide optimal clinical trial design. *Mol. Cancer Ther.* **9**, 1618–1628 (2010).

297. Huynh, C. *et al.* The novel gamma secretase inhibitor RO4929097 reduces the tumor initiating potential of melanoma. *PLoS One* **6**, (2011).

298. Campello, R. J. G. B., Moulavi, D. & Sander, J. Density-based clustering based on hierarchical density estimates. in *Lecture Notes in Computer Science* vol. 7819 (Springer, Berlin, 2013).

299. Hahsler, M., Piekenbrock, M. & Doran, D. dbscan: Fast density-based clustering with R. *J. Stat.*

Softw. **91**, 1–30 (2019).

300. Ester, M., Sander, J., Kriegel, H.-P. & Xu, X. A desity-based algorithm for discovering clusters. *Data Min. Knowl. Discov.* **2**, 169–194 (1998).

301. Bankhead, P. *Analyzing fluorescence microscopy images with ImageJ*. (Queen's University Belfast, Belfast, 2014).

302. Wickham, H. *et al.* Welcome to the Tidyverse. *J. Open Source Softw.* **4**, 1686 (2019).

303. Bonifacino, J. S., Dell'Angelica, E. C. & Springer, T. A. Immunoprecipitation. *Curr. Protoc. Mol. Biol.* **48**, 10.16.1-10.16.29 (1999).

304. Suarez-Cortes, P. *et al.* Comparative proteomics and functional analysis reveal a role of plasmodium falciparum osmiophilic bodies in malaria parasite transmission. *Mol. Cell. Proteomics* **15**, 3243–3255 (2016).

305. Cox, J. *et al.* Accurate proteome-wide label-free quantification by delayed normalization and maximal peptide ratio extraction, termed MaxLFQ. *Mol. Cell. Proteomics* **13**, 2513–2526 (2014).

306. van Dongen, J. J. M. *et al.* Design and standardization of PCR primers and protocols for detection of clonal immunoglobulin and T-cell receptor gene recombinations in suspect lymphoproliferations: Report of the BIOMED-2 concerted action BMH4-CT98-3936. *Leukemia* **17**, 2257–2317 (2003).

307. Brochet, X., Lefranc, M. P. & Giudicelli, V. IMGT/V-QUEST: the highly customized and integrated system for IG and TR standardized V-J and V-D-J sequence analysis. *Nucleic Acids Res.* **36**, W503-W508 (2008).

308. Stashenko, P., Nadler, L. M., Hardy, R. & Schlossman, S. F. Characterization of a human B lymphocyte-specific antigen. *J. Immunol.* **125**, 1678–1685 (1980).

309. Oettgen, H. C., Bayard, P. J., Van Ewijk, W., Nadler, L. M. & Terhorst, C. P. Further biochemical studies of the human B-cell differentiation antigens B1 and B2. *Hybridoma* **2**, 17–28 (1983).

310. Shrivastava, P., Katagiri, T., Ogimoto, M., Mizuno, K. & Yakura, H. Dynamic regulation of Src-family kinases by CD45 in B cells. *Blood* **103**, 1425–1432 (2004).

311. Postek, M. T. & Vladár, A. E. Does your SEM really tell the truth? How would you know? Part 4: Charging and its mitigation. *Proc. SPIE Int. Soc. Opt. Eng.* **9636**, 963605 (2015).

312. Electron Microscopy Sciences. Technical data sheet - Sputter coater principles. https://www.emsdiasum.com/microscopy/technical/datasheet/sputter_coating.aspx (2018).

313. Liu, C. *et al.* A balance of Bruton's tyrosine kinase and SHIP activation regulates B cell receptor cluster formation by controlling actin remodeling. *J. Immunol.* **187**, 230–239 (2011).

314. Ma, J. *et al.* Characterization of ibrutinib-sensitive and -resistant mantle lymphoma cells. *Br. J.*

Haematol. **166**, 849–861 (2014).

315. Amano, M. *et al.* Formation of actin stress fibers and focal adhesions enhanced by Rho- kinase. *Science* **275**, 1308–1311 (1997).

316. Nakayama, M. *et al.* Rho-kinase phosphorylates PAR-3 and disrupts PAR complex formation. *Dev. Cell* **14**, 205–215 (2008).

317. Pertz, O., Hodgson, L., Klemke, R. L. & Hahn, K. M. Spatiotemporal dynamics of RhoA activity in migrating cells. *Nature* **440**, 1069–1072 (2006).

318. Majstoravich, S. *et al.* Lymphocyte microvilli are dynamic, actin-dependent structures that do not require Wiskott-Aldrich syndrome protein (WASp) for their morphology. *Blood* **104**, 1396–1403 (2004).

319. Huttenlocher, A. & Horwitz, A. R. Integrins in cell migration. *Cold Spring Harb. Perspect. Biol.* **3**, 1–16 (2011).

320. Schroeder, H. W. & Dighiero, G. The pathogenesis of chronic lymphocytic leukemia: Analysis of the antibody repertoire. *Immunol. Today* **15**, 288–294 (1994).

321. Ghia, E. M. *et al.* Use of IGHV3-21 in chronic lymphocytic leukemia is associated with high-risk disease and reflects antigen-driven, post-germinal center leukemogenic selection. *Blood* **111**, 5101–5108 (2008).

322. Tobin, G. *et al.* Somatically mutated Ig VH3-21 genes characterize a new subset of chronic lymphocytic leukemia. *Blood* **99**, 2262–2264 (2002).

323. Balsas, P. *et al.* Activity of the novel BCR kinase inhibitor IQS019 in preclinical models of B-cell non-Hodgkin lymphoma. *J. Hematol. Oncol.* **10**, 80 (2017).

324. Carrasco, Y. R. Molecular and cellular dynamics at the early stages of antigen encounter: The B-cell immunological synapse. *Curr. Top. Microbiol. Immunol.* **340**, 51–62 (2010).

325. Doh, J. & Krummel, M. F. Immunological synapses within context: Patterns of cell-cell communication and their application in T-T interactions. *Curr. Top. Microbiol. Immunol.* **340**, 25–50 (2010).

326. Mempel, T. R., Henrickson, S. E. & Von Andrian, U. H. T-cell priming by dendritic cells in lymph nodes occurs in three distinct phases. *Nature* **427**, 154–159 (2004).

327. Nguyen, L. K., Kholodenko, B. N. & von Kriegsheim, A. Rac1 and RhoA: Networks, loops and bistability. *Small GTPases* **9**, 316–321 (2018).

328. Oscier, D. G., Thompsett, A., Zhu, D. & Stevenson, F. K. Differential rates of somatic hypermutation in V(H) genes among subsets of chronic lymphocytic leukemia defined by chromosomal abnormalities. *Blood* **89**, 4153–4160 (1997).

329. Matutes, E. *et al.* Trisomy 12 defines a group of CLL with atypical morphology: Correlation

between cytogenetic, clinical and laboratory features in 544 patients. *Br. J. Haematol.* **92**, 382–388 (1996).

330. Woessner, S., Solé, F., Pérez-Losada, A., Florensa, L. & Vilá, R. M. Trisomy 12 is a rare cytogenetic finding in typical chronic lymphocytic leukemia. *Leuk. Res.* **20**, 369–374 (1996).

331. Que, T. H. *et al.* Trisomy 12 in chronic lymphocytic leukemia detected by fluorescence in situ hybridization: analysis by stage, immunophenotype, and morphology. *Blood* **82**, 571–575 (1993).

332. Bennett, J. M. *et al.* Proposals for the classification of chronic (mature) B and T lymphoid leukaemias. *J. Clin. Pathol.* **42**, 567–584 (1989).

333. Tolbert, C. E., Beck, M. V., Kilmer, C. E. & Srougi, M. C. Loss of ATM positively regulates Rac1 activity and cellular migration through oxidative stress. *Biochem. Biophys. Res. Commun.* **508**, 1155–1161 (2019).

334. Liang, J. *et al.* Rac1, a potential target for tumor therapy. *Front. Oncol.* **11**, 1826 (2021).

335. Aubrey, B. J., Strasser, A. & Kelly, G. L. Tumor-suppressor functions of the TP53 pathway. *Cold Spring Harb. Perspect. Med.* **6**, a026062 (2016).

336. Mantovani, F., Collavin, L. & Del Sal, G. Mutant p53 as a guardian of the cancer cell. *Cell Death Differ.* **26**, 199–212 (2019).

337. Olivier, M., Hollstein, M. & Hainaut, P. TP53 mutations in human cancers: origins, consequences, and clinical use. *Cold Spring Harb. Perspect. Biol.* **2**, a001008 (2010).

338. Bosco, E. E. *et al.* Rac1 targeting suppresses p53 deficiency-mediated lymphomagenesis. *Blood* **115**, 3320–3328 (2010).

339. Guo, F. & Zheng, Y. Involvement of Rho family GTPases in p19Arf- and p53-mediated proliferation of primary mouse embryonic fibroblasts. *Mol. Cell. Biol.* **24**, 1426–1438 (2004).

340. Gadea, G., De Toledo, M., Anguille, C. & Roux, P. Loss of p53 promotes RhoA-ROCK-dependent cell migration and invasion in 3D matrices. *J. Cell Biol.* **178**, 23–30 (2007).

341. Widhopf, G. F. *et al.* ROR1 can interact with TCL1 and enhance leukemogenesis in Eμ-TCL1 transgenic mice. *Proc. Natl. Acad. Sci. U. S. A.* **111**, 793–798 (2014).

342. Fukuda, T. *et al.* Antisera induced by infusions of autologous Ad-CD154-leukemia B cells identify ROR1 as an oncofetal antigen and receptor for Wnt5a. *Proc. Natl. Acad. Sci. U. S. A.* **105**, 3047–3052 (2008).

343. Yu, J. *et al.* Wnt5a induces ROR1/ROR2 heterooligomerization to enhance leukemia chemotaxis and proliferation. *J. Clin. Invest.* **126**, 585–598 (2016).

344. Yu, J. *et al.* Cirmtuzumab inhibits Wnt5a-induced Rac1 activation in chronic lymphocytic leukemia treated with ibrutinib. *Leukemia* **31**, 1333–1339 (2017).

345. Puła, B., Gołos, A., Górniak, P. & Jamroziak, K. Overcoming ibrutinib resistance in chronic lymphocytic leukemia. *Cancers (Basel)* **11**, 1834 (2019).

346. Gutierrez, C. & Wu, C. J. Clonal dynamics in chronic lymphocytic leukemia. *Blood Adv.* **3**, 3759–3769 (2019).

347. Gu, J. J., Zhang, N., He, Y.-W., Koleske, A. J. & Pendergast, A. M. Defective T cell development and function in the absence of Abelson kinases. *J. Immunol.* **179**, 7334–7343 (2007).

348. Hu, K. Q. & Settleman, J. Tandem SH2 binding sites mediate the RasGAP-RhoGAP interaction: A conformational mechanism for SH3 domain regulation. *EMBO J.* **16**, 473–483 (1997).

349. Hernández, S. E., Settleman, J. & Koleske, A. J. Adhesion-dependent regulation of p190RhoGAP in the developing brain by the Abl-related gene tyrosine kinase. *Curr. Biol.* **14**, 691–696 (2004).

350. Roof, R. W. *et al.* Phosphotyrosine (p-Tyr)-dependent and -independent mechanisms of p190 RhoGAP-p120 RasGAP interaction: Tyr 1105 of p190, a substrate for c-Src, is the sole p-Tyr mediator of complex formation. *Mol. Cell. Biol.* **18**, 7052–7063 (1998).

351. Arthur, W. T., Petch, L. A. & Burridge, K. Integrin engagement suppresses RhoA activity via a c-Src-dependent mechanism. *Curr. Biol.* **10**, 719–722 (2000).

352. Zhang, S. Q., Smith, S. M., Zhang, S. Y. & Lynn Wang, Y. Mechanisms of ibrutinib resistance in chronic lymphocytic leukaemia and non-Hodgkin lymphoma. *Br. J. Haematol.* **170**, 445–456 (2015).

353. Hertlein, E. *et al.* Characterization of a new chronic lymphocytic leukemia cell line for mechanistic in vitro and in vivo studies relevant to disease. *PLoS One* **8**, e76607 (2013).

354. Stacchini, A. *et al.* MEC1 and MEC2: Two new cell lines derived from B-chronic lymphocytic leukaemia in prolymphocytoid transformation. *Leuk. Res.* **23**, 127–136 (1999).

355. Rosén, A. *et al.* Lymphoblastoid cell line with B1 cell characteristics established from a chronic lymphocytic leukemia clone by in vitro EBV infection. *Oncoimmunology* **1**, 18–27 (2012).

356. Wendel-Hansen, V. *et al.* Epstein-Barr virus (EBV) can immortalize B-CLL cells activated by cytokines. *Leukemia* **8**, 476–484 (1994).

357. Avila-Cariño, J. *et al.* B-CLL cells with unusual properties. *Int. J. Cancer* **70**, 1–8 (1997).

358. Takada, K., Yamamoto, K. & Osato, T. Analysis of the transformation of human lymphocytes by epstein-barr virus: II. Abortive response of leukemic cells to the transforming virus. *Intervirology* **13**, 223–231 (1980).

359. Walls, E. V. *et al.* Activation and immortalization of leukaemic B cells by epstein-barr virus. *Int. J. Cancer* **44**, 846–853 (1989).

360. Zaidi, A. R. S. Investigation of CCN1 role(s) in mantle cell lymphoma (MCL). (University of Plymouth, 2019).

361. Beà, S. *et al.* Landscape of somatic mutations and clonal evolution in mantle cell lymphoma. *Proc. Natl. Acad. Sci. U. S. A.* **110**, 18250–18255 (2013).

362. Queirós, A. C. *et al.* Decoding the DNA methylome of mantle cell lymphoma in the light of the entire B cell lineage. *Cancer Cell* **30**, 806–821 (2016).

363. Rudolph, C. *et al.* Molecular cytogenetic characterization of the mantle cell lymphoma cell line GRANTA-519. *Cancer Genet. Cytogenet.* **153**, 144–150 (2004).

364. Ek, S., Ortega, E. & Borrebaeck, C. A. K. Transcriptional profiling and assessment of cell lines as in vitro models for mantle cell lymphoma. *Leuk. Res.* **29**, 205–213 (2005).

365. Rauert-Wunderlich, H., Rudelius, M., Ott, G. & Rosenwald, A. Targeting protein kinase C in mantle cell lymphoma. *Br. J. Haematol.* **173**, 394–403 (2016).

366. Amrein, P. C. *et al.* Phase II study of dasatinib in relapsed or refractory chronic lymphocytic leukemia. *Clin. Cancer Res.* **17**, 2977–2986 (2011).

367. Furtado, M. *et al.* Ibrutinib-associated lymphocytosis corresponds to bone marrow involvement in mantle cell lymphoma. *Br. J. Haematol.* **170**, 131–134 (2015).

368. Chang, B. Y. *et al.* Egress of CD19+CD5+ cells into peripheral blood following treatment with the Bruton tyrosine kinase inhibitor, PCI-32765, in mantle cell lymphoma patients. *Blood* **118**, 954–954 (2011).

369. Katz, T. *et al.* Different sources of stromal cells diversely affect survival and trafficking of mantle cell lymphoma cells. *Blood* **126**, 2670 (2015).

370. Garzia, M. *et al.* Blastoid mantle cell lymphoma occuring in a patient in complete remission of chronic myelogenous leukemia. *Lab. Hematol.* **13**, 30–33 (2007).

371. Rodler, E. *et al.* Blastic mantle cell lymphoma developing concurrently in a patient with chronic myelogenous leukemia and a review of the literature. *Am. J. Hematol.* **75**, 231–238 (2004).

372. Liu, J. H. *et al.* Overexpression of cyclin D1 in accelerated-phase chronic myeloid leukemia. *Leuk. Lymphoma* **45**, 2419–2425 (2004).

373. Afar, D. E. H., Mclaughlin, J., Sherr, C. J., Witte, O. N. & Roussel, M. F. Signaling by ABL oncogenes through cyclin D1. *Proc. Natl. Acad. Sci. U. S. A.* **92**, 9540–9544 (1995).

374. Calissano, C. *et al.* In vivo intraclonal and interclonal kinetic heterogeneity in B-cell chronic lymphocytic leukemia. *Blood* **114**, 4832–4842 (2009).

375. Herndon, T. M. *et al.* Direct in vivo evidence for increased proliferation of CLL cells in lymph nodes compared to bone marrow and peripheral blood. *Leukemia* **31**, 1340–1347 (2017).

376. Pasikowska, M. *et al.* Phenotype and immune function of lymph node and peripheral blood CLL cells are linked to transendothelial migration. *Blood* **128**, 563–573 (2016).

377. Breslin, S. & O'Driscoll, L. Three-dimensional cell culture: The missing link in drug discovery.

Drug Discov. Today **18**, 240–249 (2013).

378. Kimlin, L., Kassis, J. & Virador, V. 3D in vitro tissue models and their potential for drug screening. *Expert Opin. Drug Discov.* **8**, 1455–1466 (2013).

379. Scielzo, C. & Ghia, P. Modeling the leukemia microenviroment in vitro. *Front. Oncol.* **10**, 2863 (2020).

380. Pampaloni, F., Reynaud, E. G. & Stelzer, E. H. K. The third dimension bridges the gap between cell culture and live tissue. *Nat. Rev. Mol. Cell Biol.* **8**, 839–845 (2007).

381. LaBarbera, D. V., Reid, B. G. & Yoo, B. H. The multicellular tumor spheroid model for high-throughput cancer drug discovery. *Expert Opin. Drug Discov.* **7**, 819–830 (2012).

382. Tung, Y. C. *et al.* High-throughput 3D spheroid culture and drug testing using a 384 hanging drop array. *Analyst* **136**, 473–478 (2011).

383. Kelm, J. M., Timmins, N. E., Brown, C. J., Fussenegger, M. & Nielsen, L. K. Method for generation of homogeneous multicellular tumor spheroids applicable to a wide variety of cell types. *Biotechnol. Bioeng.* **83**, 173–180 (2003).

384. Farinello, D. *et al.* A retinoic acid-dependent stroma-leukemia crosstalk promotes chronic lymphocytic leukemia progression. *Nat. Commun.* **9**, 1787 (2018).

385. Ivascu, A. & Kubbies, M. Rapid generation of single-tumor spheroids for high-throughput cell function and toxicity analysis. *J. Biomol. Screen.* **11**, 922–932 (2006).

386. Li, Q. *et al.* 3D models of epithelial-mesenchymal transition in breast cancer metastasis: High-throughput screening assay development, validation, and pilot screen. *J. Biomol. Screen.* **16**, 141–154 (2011).

387. Friedrich, J., Seidel, C., Ebner, R. & Kunz-Schughart, L. A. Spheroid-based drug screen: Considerations and practical approach. *Nat. Protoc.* **4**, 309–324 (2009).

388. Goodwin, T. J., Prewett, T. L., Wolf, D. A. & Spaulding, G. F. Reduced shear stress: A major component in the ability of mammalian tissues to form three-dimensional assemblies in simulated microgravity. *J. Cell. Biochem.* **51**, 301–311 (1993).

389. Rodríguez, C. E. *et al.* Cytotoxic effect of trastuzumab on macrophage-infiltrated human mammary tumor spheroids. *Exp. Mol. Ther.* **72**, 2881 (2012).

390. Correa de Sampaio, P. *et al.* A heterogeneous in vitro three dimensional model of tumour-stroma interactions regulating sprouting angiogenesis. *PLoS One* **7**, e30753 (2012).

391. Costa, E. C., Gaspar, V. M., Coutinho, P. & Correia, I. J. Optimization of liquid overlay technique to formulate heterogenic 3D co-cultures models. *Biotechnol. Bioeng.* **111**, 1672–1685 (2014).

392. Costa, E. C. *et al.* 3D tumor spheroids: an overview on the tools and techniques used for their analysis. *Biotechnol. Adv.* **34**, 1427–1441 (2016).

393. Minchinton, A. I. & Tannock, I. F. Drug penetration in solid tumours. *Nat. Rev. Cancer* **6**, 583–592 (2006).

394. Trédan, O., Galmarini, C. M., Patel, K. & Tannock, I. F. Drug resistance and the solid tumor microenvironment. *J. Natl. Cancer Inst.* **99**, 1441–1454 (2007).

395. Wojtkowiak, J. W., Verduzco, D., Schramm, K. J. & Gillies, R. J. Drug resistance and cellular adaptation to tumor acidic pH microenvironment. *Mol. Pharm.* **8**, 2032–2038 (2011).

396. Langhans, S. A. Three-dimensional in vitro cell culture models in drug discovery and drug repositioning. *Front. Pharmacol.* **9**, 6 (2018).

397. Von Der Mark, K., Gauss, V., Von Der Mark, H. & Müller, P. Relationship between cell shape and type of collagen synthesised as chondrocytes lose their cartilage phenotype in culture. *Nature* **267**, 531–532 (1977).

398. Petersen, O. W., Ronnov-Jessen, L., Howlett, A. R. & Bissell, M. J. Interaction with basement membrane serves to rapidly distinguish growth and differentiation pattern of normal and malignant human breast epithelial cells. *Proc. Natl. Acad. Sci. U. S. A.* **89**, 9064–9068 (1992).

399. Ghosh, S. *et al.* Three-dimensional culture of melanoma cells profoundly affects gene expression profile: A high density oligonucleotide array study. *J. Cell. Physiol.* **204**, 522–531 (2005).

400. Jong, B. K. Three-dimensional tissue culture models in cancer biology. *Semin. Cancer Biol.* **15**, 365–377 (2005).

401. Haisler, W. L. *et al.* Three-dimensional cell culturing by magnetic levitation. *Nat. Protoc.* **8**, 1940–1949 (2013).

402. Imamura, Y. *et al.* Comparison of 2D- and 3D-culture models as drug-testing platforms in breast cancer. *Oncol. Rep.* **33**, 1837–1843 (2015).

403. Ravi, M., Paramesh, V., Kaviya, S. R., Anuradha, E. & Paul Solomon, F. D. 3D cell culture systems: Advantages and applications. *J. Cell. Physiol.* **230**, 16–26 (2015).

404. Bruce, A. *et al.* Three-dimensional microfluidic tri-culture model of the bone marrow microenvironment for study of acute lymphoblastic leukemia. *PLoS One* **10**, e0140506 (2015).

405. Mannino, R. G. *et al.* 3D microvascular model recapitulates the diffuse large B-cell lymphoma tumor microenvironment in vitro. *Lab Chip* **17**, 407–414 (2017).

406. Kapałczyńska, M. *et al.* 2D and 3D cell cultures – a comparison of different types of cancer cell cultures. *Arch. Med. Sci.* **14**, 910–919 (2018).

407. Matoug-Elwerfelli, M. *et al.* Ex-vivo recellularisation and stem cell differentiation of a decellularised rat dental pulp matrix. *Sci. Rep.* **10**, 21553 (2020).

408. García-Gareta, E. *et al.* Decellularised scaffolds: just a framework? Current knowledge and

future directions. *J. Tissue Eng.* **11**, 2041731420942903 (2020).

409. Kleinman, H. K. & Martin, G. R. Matrigel: Basement membrane matrix with biological activity. *Semin. Cancer Biol.* **15**, 378–386 (2005).

410. Bray, L. J. *et al.* A three-dimensional ex vivo tri-culture model mimics cell-cell interactions between acute myeloid leukemia and the vascular niche. *Haematologica* **102**, 1215–1226 (2017).

411. Braham, M. V. J. *et al.* Cellular immunotherapy on primary multiple myeloma expanded in a 3D bone marrow niche model. *Oncoimmunology* **7**, e1434465 (2018).

412. Boussommier-Calleja, A., Li, R., Chen, M. B., Wong, S. C. & Kamm, R. D. Microfluidics: A new tool for modeling cancer–immune interactions. *Trends in Cancer* **2**, 6–19 (2016).

413. Tucker, D. Assessing the cellular and adhesive interactions in in vitro models of mantle cell lymphoma. (University of Plymouth, 2017).

414. Vos, J. G., Roholl, P. J. M. & Leene, W. Ultrastructural studies of peripheral blood lymphocytes in T cell-depleted rabbits - A scanning and transmission electron microscopic analysis. *Cell Tissue Res.* **213**, 221–235 (1980).

415. Jitschin, R. *et al.* Stromal cell-mediated glycolytic switch in CLL cells involves Notch-c-Myc signaling. *Blood* **125**, 3432–3436 (2015).

416. Li, J. *et al.* The coordination between B cell receptor signaling and the actin cytoskeleton during B cell activation. *Front. Immunol.* **10**, 3096 (2019).

417. Onaindia, A. *et al.* Chronic lymphocytic leukemia cells in lymph nodes show frequent NOTCH1 activation. *Haematologica* **100**, e200–e203 (2015).

418. Kluk, M. J. *et al.* Gauging NOTCH1 activation in cancer using immunohistochemistry. *PLoS One* **8**, 67306 (2013).

419. Quijada-Álamo, M. *et al.* Next-generation sequencing and FISH studies reveal the appearance of gene mutations and chromosomal abnormalities in hematopoietic progenitors in chronic lymphocytic leukemia. *J. Hematol. Oncol.* **10**, 83 (2017).

420. Del Papa, B. *et al.* Decreased NOTCH1 activation correlates with response to ibrutinib in chronic lymphocytic leukemia. *Clin. Cancer Res.* **25**, 7540–7553 (2019).

421. Radke, A. L. *et al.* Mature human eosinophils express functional Notch ligands mediating eosinophil autocrine regulation. *Blood* **113**, 3092–3101 (2009).

422. Szklarczyk, D. *et al.* The STRING database in 2021: Customizable protein-protein networks, and functional characterization of user-uploaded gene/measurement sets. *Nucleic Acids Res.* **49**, D605–D612 (2021).

423. Koster, A. J. & Klumperman, J. Electron microscopy in cell biology: Integrating structure and

function. *Nat. Rev. Mol. Cell Biol.* **4**, SS6-SS10 (2003).

424. Melo, R. C. N., Morgan, E., Monahan-Earley, R., Dvorak, A. M. & Weller, P. F. Pre-embedding immunogold labeling to optimize protein localization at subcellular compartments and membrane microdomains of leukocytes. *Nat. Protoc.* **9**, 2382–2394 (2014).

425. Jones, J. C. R. Pre- and post-embedding immunogold labelingof tissue sections. *Methods Mol. Biol.* **1474**, 291–307 (2016).

426. Frens, G. Controlled nucleation for the regulation of the particle size in monodisperse gold suspensions. *Nat. Phys. Sci.* **241**, 20–22 (1973).

427. De Mey, J., Moeremans, M., Geuens, G., Nuydens, R. & De Brabander, M. High resolution light and electron microscopic localization of tubulin with the IGS (immuno gold staining) method. *Cell Biol. Int. Rep.* **5**, 889–899 (1981).

428. Page Faulk, W. & Malcolm Taylor, G. Communication to the editors: An immunocolloid method for the electron microscope. *Immunochemistry* **8**, 1081–1083 (1971).

429. Romano, E. L. & Romano, M. Staphylococcal protein a bound to colloidal gold: A useful reagent to label antigen-antibody sites in electron microscopy. *Immunochemistry* **14**, 711–715 (1977).

430. Roth, J., Bendayan, M. & Orci, L. Ultrastructural localization of intracellular antigens by the use of protein A-gold complex. *J. Histochem. Cytochem.* **26**, 1074–1081 (1978).

431. Bendayan, M. Protein A-gold electron microscopic immunocytochemistry: Methods, applications, and limitations. *J. Electron Microsc. Tech.* **1**, 243–270 (1984).

432. Slot, J. W., Posthuma, G., Chang, L. -Y, Crapo, J. D. & Geuze, H. J. Quantitative aspects of immunogold labeling in embedded and in nonembedded sections. *Am. J. Anat.* **185**, 271–281 (1989).

433. Hansen, G. H., Wetterberg, L. L., Sjöström, H. & Norén, O. Immunogold labelling is a quantitative method as demonstrated by studies on aminopeptidase N in microvillar membrane vesicles. *Histochem. J.* **24**, 132–136 (1992).

434. Boykins, L. G., Jones, J. C. R., Estraño, C. E., Schwartzbach, S. D. & Skalli, O. Pre-embedding double-label immunoelectron microscopy of chemically fixed tissue culture cells. *Methods Mol. Biol.* **1474**, 217–232 (2016).

435. Eltoum, I., Fredenburgh, J., Myers, R. B. & Grizzle, W. E. Introduction to the theory and practice of fixation of tissues. *J. Histotechnol.* **24**, 173–190 (2001).

436. Eltoum, I., Fredenburgh, J. & Grizzle, W. E. Advanced concepts in fixation: 1. Effects of fixation on immunohistochemistry, reversibility of fixation and recovery of proteins, nucleic acids, and other molecules from fixed and processed tissues. 2. Developmental methods of fixation. *J. Histotechnol.* **24**, 201–210 (2012).

437. Koley, D. & Bard, A. J. Triton X-100 concentration effects on membrane permeability of a single HeLa cell by scanning electrochemical microscopy (SECM). *Proc. Natl. Acad. Sci. U. S. A.* **107**, 16783–16787 (2010).

438. Hainfeld, J. F. & Powell, R. D. New frontiers in gold labeling. *J. Histochem. Cytochem.* **48**, 471–480 (2000).

439. Humbel, B. M., Sibon, O. C., Stierhof, Y. D. & Schwarz, H. Ultra-small gold particles and silver enhancement as a detection system in immunolabeling and in situ hybridization experiments. *J. Histochem. Cytochem.* **43**, 735–737 (1995).

440. Mühlfeld, C. High-pressure freezing, chemical fixation and freeze-substitution for immuno-electron microscopy. *Methods Mol. Biol.* **611**, 87–101 (2010).

441. Studer, D., Graber, W., Al-Amoudi, A. & Eggli, P. A new approach for cryofixation by high-pressure freezing. *J. Microsc.* **203**, 285–294 (2001).

442. Uhlen, M. *et al.* A proposal for validation of antibodies. *Nat. Methods* **13**, 823–827 (2016).

443. Voskuil, J. L. A. *et al.* The Antibody Society's antibody validation webinar series. *MAbs* **12**, 1794421 (2020).

444. Hyatt, A. D. Protein A–gold: Nonspecific binding and cross-contamination. *Colloidal Gold* **2**, 19-32 (1989).

445. Kaur, R., Dikshit, K. L. & Raje, M. Optimization of immunogold labeling TEM: An ELISA-based method for evaluation of blocking agents for quantitative detection of antigen. *J. Histochem. Cytochem.* **50**, 863–873 (2002).

446. Daneshtalab, N., Doré, J. J. E. & Smeda, J. S. Troubleshooting tissue specificity and antibody selection: Procedures in immunohistochemical studies. *J. Pharmacol. Toxicol. Methods* **61**, 127–135 (2010).

447. Reverberi, R. & Reverberi, L. Factors affecting the antigen-antibody reaction. *Blood Transfus.* **5**, 227–240 (2007).

448. Rizzo, P. *et al.* Rational targeting of Notch signaling in cancer. *Oncogene* **27**, 5124–5131 (2008).

449. Aspenström, P., Ruusala, A. & Pacholsky, D. Taking Rho GTPases to the next level: The cellular functions of atypical Rho GTPases. *Exp. Cell Res.* **313**, 3673–3679 (2007).

450. Saras, J., Wollberg, P. & Aspenström, P. Wrch1 is a GTPase-deficient Cdc42-like protein with unusual binding characteristics and cellular effects. *Exp. Cell Res.* **299**, 356–369 (2004).

451. Shutes, A., Berzat, A. C., Cox, A. D. & Der, C. J. Atypical mechanism of regulation of the Wrch-1 rho family small GTPase. *Curr. Biol.* **14**, 2052–2056 (2004).

452. Aronheim, A. *et al.* Chp, a homologue of the GTPase CDc42Hs, activates the JNK pathway and is implicated in reorganizing the actin cytoskeleton. *Curr. Biol.* **8**, 1125–1129 (1998).

453. Chuang, Y. Y., Valster, A., Coniglio, S. J., Backer, J. M. & Symons, M. The atypical Rho family GTPase Wrch-1 regulates focal adhesion formation and cell migration. *J. Cell Sci.* **120**, 1927–1934 (2007).

454. Fort, P. *et al.* Activity of the RhoU/Wrch1 GTPase is critical for cranial neural crest cell migration. *Dev. Biol.* **350**, 451–463 (2011).

455. Palomero, T. *et al.* Mutational loss of PTEN induces resistance to NOTCH1 inhibition in T-cell leukemia. *Nat. Med.* **13**, 1203–1210 (2007).

456. Agnusdei, V. *et al.* Dissecting molecular mechanisms of resistance to NOTCH1-targeted therapy in T-cell acute lymphoblastic leukemia xenografts. *Haematologica* **105**, 1317–1328 (2020).

457. Herranz, D. *et al.* Metabolic reprogramming induces resistance to anti-NOTCH1 therapies in T cell acute lymphoblastic leukemia. *Nat. Med.* **21**, 1182–1189 (2015).

458. Ryan, R. J. H. *et al.* A B cell regulome links Notch to downstream oncogenic pathways in small B cell lymphomas. *Cell Rep.* **21**, 784–797 (2017).

459. Kridel, R. *et al.* Whole transcriptome sequencing reveals recurrent NOTCH1 mutations in mantle cell lymphoma. *Blood* **119**, 1963–1971 (2012).

460. Silkenstedt, E. *et al.* Notch1 signaling in NOTCH1-mutated mantle cell lymphoma depends on Delta-Like ligand 4 and is a potential target for specific antibody therapy. *J. Exp. Clin. Cancer Res.* **38**, 1–15 (2019).

461. Noor, Z., Ahn, S. B., Baker, M. S., Ranganathan, S. & Mohamedali, A. Mass spectrometry-based protein identification in proteomics - A review. *Brief. Bioinform.* **22**, 1620–1638 (2021).

462. Baldwin, M. A. Protein identification by mass spectrometry: Issues to be considered. *Mol. Cell. Proteomics* **3**, 1–9 (2004).

463. Gundry, R. L. *et al.* Preparation of proteins and peptides for mass spectrometry analysis in a bottom-up proteomics workflow. *Curr. Protoc. Mol. Biol.* **10**, Unit10.25 (2009).

464. Audain, E. *et al.* In-depth analysis of protein inference algorithms using multiple search engines and well-defined metrics. *J. Proteomics* **150**, 170–182 (2017).

465. Switzar, L., Giera, M. & Niessen, W. M. A. Protein digestion: An overview of the available techniques and recent developments. *J. Proteome Res.* **12**, 1067–1077 (2013).

466. Burkhart, J. M., Schumbrutzki, C., Wortelkamp, S., Sickmann, A. & Zahedi, R. P. Systematic and quantitative comparison of digest efficiency and specificity reveals the impact of trypsin quality on MS-based proteomics. *J. Proteomics* **75**, 1454–1462 (2012).

467. Clauser, K. R., Baker, P. & Burlingame, A. L. Role of accurate mass measurement (±10 ppm) in protein identification strategies employing MS or MS/MS and database searching. *Anal. Chem.* **71**, 2871–2882 (1999).

468.   Pozzo, F. *et al.* NOTCH1-mutated chronic lymphocytic leukemia cells are characterized by a MYC-related overexpression of nucleophosmin 1 and ribosome-associated components. *Leukemia* **31**, 2407–2415 (2017).

469.   Koppenol, W. H., Bounds, P. L. & Dang, C. V. Otto Warburg's contributions to current concepts of cancer metabolism. *Nat. Rev. Cancer* **11**, 325–337 (2011).

470.   Munir, T. *et al.* Final analysis from RESONATE: Up to six years of follow-up on ibrutinib in patients with previously treated chronic lymphocytic leukemia or small lymphocytic lymphoma. *Am. J. Hematol.* **94**, 1353–1363 (2019).

471.   Sedlarikova, L., Petrackova, A., Papajik, T., Turcsanyi, P. & Kriegova, E. Resistance-associated mutations in chronic lymphocytic leukemia patients treated with novel agents. *Front. Oncol.* **10**, 894 (2020).